Non-destructive material evaluation of a reinforced concrete viaduct: a practical methodology

Gert Wilgenburg

Rijkswaterstaat
Ministerie van Infrastructuur en Waterstaat

TUDelft

Delft University of Technology

Master's Thesis

Non-destructive material evaluation of a reinforced concrete viaduct: a practical methodology

Gert Wilgenburg

Committee

prof. dr. ir. Erik Schlangen	TU Delft
dr. ir. Penny Pipilikaki	Rijkswaterstaat
dr. Branko Šavija	TU Delft
ing. John van den Berg	TU Delft
dr. Dessi Koleva	TU Delft
dr. ir. Yugang Yang	TU Delft

A thesis submitted in fulfillment of the requirements
for the degree of Master of Science in

Civil Engineering

April 15, 2024

「石橋を叩いて渡る」

Knock on a stone bridge before crossing it.

Acknowledgements

I never imagined that a literature study at Rijkswaterstaat on non-destructive testing of reinforced concrete structures would lead me to such an amazing project, where I would have the opportunity to meet so many people. Following many meetings, emails and discussions, a suitable inspection location was found, and a methodology and safety plan were formulated, leading to the inspection of the Sluinerweg viaduct in November 2023. I gladly remained involved in the project until the demolition of the Sluinerweg viaduct in January this year. I will always treasure witnessing the demolition on that cold January night, alongside my father, both of us wearing borrowed PPE from Heijmans (my apologies to my colleagues with the white helmets).

Well, since this is the acknowledgments section, it's time for me to give away some words of thanks. This journey wouldn't have been possible without the time, effort, and enthusiasm of my supervisor at Rijkswaterstaat, Penny Pipilikaki. It was always a pleasure discussing the project with you, and I'm truly grateful for the opportunities you provided me. I'd like to thank the other committee members for their contribution to this project and for patiently listening to my lengthy presentations that always seemed to run over time: Erik Schlangen, Branko Šavija, John van den Berg, Dessi Koleva and Yuguang Yang. For John in particular, I want to express my gratitude for your involvement in the project. You were there on the testing days and always open to discussing some electrochemistry. Next, I would like to extend my thanks to the companies involved in the project inspection in one way or another: Heijmans, Nebest, Mourik-Salverda and Dikkerboom Betonboringen. The inspection wouldn't have been nearly as successful without the help from Ivo Verheijen of Newa. Thank you for providing me with training on NDTs, making your equipment available, and for your continued involvement in this project. I also want to express my gratitude to Rosaly Wiegmans and Markus Denton-Masih from Screaning Eagle Technologies for their expertise and presence at the inspection days back in November. Your assistance was truly invaluable. Then, I would like to thank my colleagues at Rijkswaterstaat for the enjoyable conversations at the office. In particular, I want to express my gratitude to Bryan de Jonge for taking me to different project sites at the A1, as well as Paul Spencer and Bas van Spanjen for their involvement in the project. I want to thank Marija Nedeljkovic for bringing her overwhelming enthusiasm to our inspections. Your energy is seriously inspiring, and I'm grateful for the chance you gave me to be a guest speaker at your workshop on advanced concrete recycling. I wish my successor, Zhi Xiang Zhong, the best of luck with the continuation of this project on the Ardeweg viaduct. Let's ensure that the enthusiasm towards NDTs only continues to grow from here!

And last but not least, to all my dear friends and my amazing parents who have always been there for me, thank you! I genuinely mean every word... Wait, what's with today?

Gert Wilgenburg
Delft, April 1st, 2024

Abstract

The use of non-destructive tests for assessing the material status of concrete structures in the Netherlands remains relatively uncommon, despite the growing demand for the preservation of existing structures under the VenR policy of Rijkswaterstaat. Skepticism towards NDTs is reflected in the scarcity of documented case studies in publicly available literature and in the absence of rules and guidelines.

In this research, following an extensive literature review on the current state of assessing the material status of reinforced concrete structures using NDTs, a large-scale non-destructive inspection was carried out on the Sluinerweg viaduct. The research aimed to address the practical challenges associated with these methods. These challenges serve to formulate a practical methodology to facilitate future inspections. Limitations include the use of specific NDTs: GPR, UPE, rebound hammer, UPV, half-cell potential, resistivity, and corrosion current density. Following the inspection, a data analysis was conducted, accompanied by a destructive verification of the methods.

The integration of GPR with UPE technology showed promise for tendon duct inspections. However, a 12 mm borehole used for destructive verification proved to be too small to make accurate judgments. Additionally, the absence of grouting defects made evaluation of the method challenging. GPR provided a more accurate estimation of the cover depth compared to previous measurements conducted on the Sluinerweg viaduct using a standard cover meter. However, it was impossible to measure through the cathodic protection coating. The data's correlation with the provided drawings is promising, especially given that drawings are often unavailable. The key finding regarding the estimation of compressive strength using the rebound hammer and UPV is the strong recommendation to avoid using SonReb models unless they are specifically calibrated for the structure under inspection. No active corrosion sites were found, which posed challenges to evaluating the methods. Resistivity values measured using the Proceq Resipod consistently showed lower readings than those obtained with the Gecor-10 Wenner probe. A laboratory investigation ruled out moisture content as the cause. Fortunately, the differences are less pronounced with corroded reinforcement; however, further investigation is necessary. The previous inspection regimes in the Liggerkoppen project were found to be suboptimal in some aspects but were deemed reasonable considering the complexity of the project.

This research demonstrated the effectiveness of several NDTs in-situ, which should help to build trust in the reliability of these methods for future inspections. Based on the findings of this research, it is strongly recommended to conduct further large-scale inspections to improve the practical methodology, gain further experience and develop improved codes and guidelines. While there is still much to accomplish, Rijkswaterstaat's support for investigations such as the one conducted for the Sluinerweg viaduct demonstrates their commitment to a better future.

Contents

List of Figures

List of Tables

List of Abbreviations

CASE	**C**osts **A**ccesibility **S**afety **E**xpertise
CP	**C**athodic **P**rotection
GGBFS	**G**round **G**ranulated **B**last-**F**urnace **S**lag
GPR	**G**round **P**enetrating **R**adar
HXRF	**H**andheld **X**-**r**ay **F**luorescence
KCG	**K**ristal **C**ement **G**raniet
NDT	**N**on-**D**estructive **T**esting
NDTs	**N**on-**D**estructive **T**est**s**
OCP	**O**pen **C**ircuit **P**otential
OPC	**O**rdinary **P**ortland **C**ement
RBK	**R**ichtlijnen **B**eoordeling **K**unstwerken
SonReb	**Son**ic **Reb**ound
UPV	**U**ltrasonic **P**ulse **V**elocity
UPE	**U**ltrasonic **P**ulse **E**cho
VenR	**V**ervanging **en R**enovatie
ZOAB	**Z**eer **O**pen **A**sfalt **B**eton

Chapter 1

Introduction

1.1 Background

The executive agency of the Ministry of Infrastructure and Water Management, known as *Rijkswaterstaat*, is undergoing a strategic shift in its policy focus towards "Vervanging en Renovatie" (Replacement and Renovation), abbreviated as VenR. This shift has become imperative due to growing challenges, including the *stikstofcrisis* (nitrogren emission crisis), personnel shortages, and material constraints. However the Netherlands is currently experiencing an exponential increase in the number of reinforced concrete structures requiring repair or replacement, with many of these structures dating back over half a century. Corrosion damage due to the ingress of chlorides in leaking joints is one of the most common durability issue these structures face. A particular Rijkswaterstaat project where this problem plays a significant role is the *Liggerkoppen* project. This project involves multiple structures constructed from prefabricated T-beams positioned either above or along the A1, A28, and A50 highways. In 2010, Royal Haskoning conducted recalculations for two viaducts within the Liggerkoppen project, assessing structural safety, including the loss of steel reinforcement and one prestressing bar tendon[1]. The recalculated results were extrapolated to other structures of the same type. It was demonstrated that, theoretically, the loss of one prestressing bar per beam in most structures does not endanger the structural safety. However, for structures with three or four prestressing bars, there is a potential for an unacceptable risk to the construction [1].

The *Sluinerweg viaduct* is one of the viaducts within the Liggerkoppen project. The scheduled demolition of the viaduct in February 2024, as part of the local widening of the A1, presented a unique opportunity to conduct an in-depth inspection for research purposes. The primary objective was to assess the material status using non-destructive testing methods. Non-destructive tests or NDTs have the capability to identify certain concrete defects without causing damage to the structure and are therefore preferred. However, there is limited experience with these methods in the Netherlands, and skepticism surrounds their use. Consequently, the Sluinerweg viaduct served as a testing ground for evaluating the material status through non-destructive testing.

For a more detailed description of the Liggerkoppen project and the Sluinerweg viaduct, refer to Chapter 3.

---

[1]The term *bar tendon* specifically refers to post-tensioned steel bars, as opposed to the more commonly used strand tendons.

1.2   Research significance

The use of NDTs in-situ to assess the material status of reinforced concrete structures remains relatively uncommon in the Netherlands, as evidenced by the scarcity of documented cases in publicly available literature. There is little experience with non-destructive testing beyond the use of a cover meter and potential measurements. Additionally, there is a lack of training programs and established rules or guidelines. This lack of familiarity with these devices, coupled with limited practical experience and prevailing skepticism, has prevented their widespread use. However, given the increasing number of vulnerable structures under the VenR policy, there is a growing demand for inspections involving NDTs.

Four factors can be identified that influence the decision making process for developing an inspection regime: costs, accessibility, safety and expertise. Conveniently, this can be abbreviated to **CASE**:

- **C**osts - The project budget and time-efficiency.
- **A**ccessibility - The accessibility of the test locations.
- **S**afety - The safety of the inspectors and all other involved parties.
- **E**xpertise - The expertise of the inspectors and the experience with certain inspection methods.

The relationships between safety, accessibility, expertise and costs are dynamic and interconnected as shown in Figure 1.1.
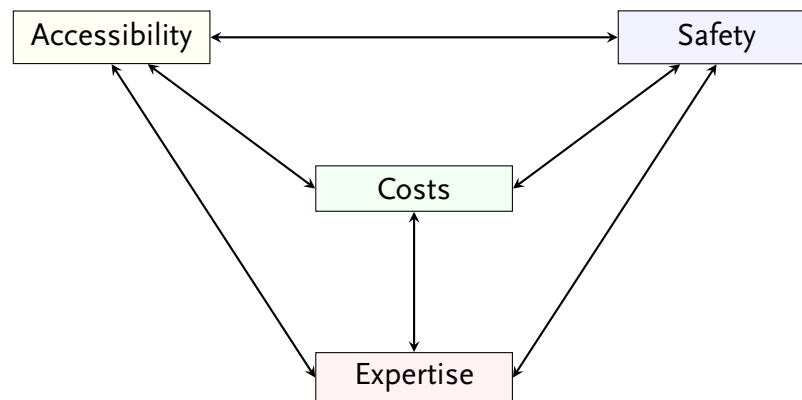
Figure 1.1: Interaction between costs, accessibility, safety and expertise in developing a suitable inspection regime.

Accessibility

- **Costs.** Poor accessibility can contribute to increased costs and extend the duration of the inspection, as additional resources and time are allocated to overcome limitations.
- **Safety.** Poor accessibility can directly impact safety, making it unsafe for inspection teams to reach certain areas. Adequate access planning is crucial for ensuring the safety of the inspection.
- **Expertise.** Poor accessibility may hinder the ability of even the most skilled inspectors to thoroughly assess certain areas. Specific areas may require specialized expertise for thorough evaluation.

Safety

- **Costs.** Applying stricter safety protocols may increase costs and extend the duration of the inspection. Investments in safety training, equipment, and procedures can be time-consuming and may lead to higher overall project expenses.
- **Accessibility.** Access to certain areas may be restricted during inspections due to safety protocols, potentially making it more challenging to assess specific critical points.
- **Expertise.** Investing in safety training and protocols ensures that inspectors are well-equipped and confident to handle potential risks, contributing to overall expertise.

Expertise

- **Costs.** Highly skilled inspectors can expedite the inspection process, potentially leading to cost and time savings. Although their expertise may incur higher initial costs, the efficiency they bring can contribute to a favorable cost-benefit ratio.
- **Accessibility.** An experienced inspection team can formulate innovative solutions to overcome accessibility challenges. Their expertise may contribute to the development of efficient access strategies. However, it's worth noting that certain specialised tests may demand improved accessibility.
- **Safety.** A highly skilled and knowledgeable inspection team is better equipped to implement and adhere to safety protocols. Expertise in structural assessment and safety go hand-in-hand for a comprehensive inspection process.

One can argue that the application of NDTs in-situ aligns with these parameters. NDTs may contribute to increased costs due to their time-consuming nature. The successful implementation of NDTs requires specialised expertise and a level of trust in the technology. Additionally, challenges in accessibility may limit the applicability of certain tests to specific structures. While NDTs may increase costs and require expertise, their non-intrusive nature can enhance safety. By identifying and addressing practical challenges associated with NDTs, this research aims to build trust in their application. The scientific significance of this research then lies in its contribution to bridging the gap between academic research and real-world applications in the field of non-destructive testing. This work can therefore be regarded as a tool for progressing towards the standardisation of using NDTs in-situ in the Netherlands.

1.3   Research objectives

The title of this research is *Non-destructive material evaluation of a reinforced concrete viaduct: a practical methodology*, which covers three main points:

- Evaluating the concrete and reinforcement using NDTs.
- Applying these tests in-situ on a concrete viaduct.
- Reporting the challenges when working in-situ with NDTs and extracting valuable lessons from these challenges for future projects of a similar nature.

Based on these points, the research objectives can be formulated to help increase trust in the use of NDTs in-situ in the Netherlands.

- Validate various NDTs in-situ and demonstrate their capabilities when used in combination with each other.
- Investigate the practical challenges associated with each method.
- Propose a practical methodology for the Netherlands for conducting in-situ measurements on concrete viaducts, either independently or in combination with destructive methods.

1.4   Research questions

The research objectives can be formulated into the main research question:

> *What is a practically feasible non-destructive inspection methodology for evaluating the material status of a reinforced concrete viaduct?*

Material status evaluation extends beyond assessing the durability and compressive strength of the concrete; it also encompasses the corrosion assessment of the reinforcement and the inspection of prestressing ducts. To answer the main research question, it has been subdivided into four sub-questions:

1. How can various NDTs, including GPR and UPE for locating reinforcement and identifying grouting defects, UPV and rebound hammer for assessing in-situ concrete compressive strength, and half-cell potential, resistivity, and corrosion current density for evaluating corrosion damage, be effectively correlated with each other for assessing the material status of a reinforced concrete viaduct?
2. How can the results obtained from NDTs be effectively validated and correlated with destructive measurements, such as those for compressive strength, carbonation depth, and chloride content?
3. What practical challenges arise when implementing non-destructive testing methods in-situ, and what insights can these challenges provide for future applications?
4. How effective are the earlier methods employed for evaluating the material status within the Liggerkoppen project, and to what extent do these methods align with current insights?

1.5   Scope and limitations

The scope is primarily determined by the measurements conducted on specific sections of the Sluinerweg viaduct, with two main limitations:

1. This research concentrates on assessing the material status using NDTs in-situ. Its scope does not extend to structural evaluation, nor does it aim to estimate the residual lifetime of the structure or provide advice for potential reuse.

2. The different types of NDTs that are used to evaluate the material status.

   - Ground penetrating radar.
   - Ultrasonic pulse echo.
   - Rebound hammer.
   - Ultrasonic pulse velocity.

- Half-cell potential.
- Resistivity (Wenner probe).
- Corrosion current density.

Despite these limitations, the obtained insights are undeniably valuable and can hold significant relevance for other concrete viaducts, particularly those associated with the Lig-gerkoppen project. Providing a general testing methodology however is difficult due to the unique characteristics of each structure, including factors such as age, dimensions, mix design, environment, and loading conditions.

1.6 Structure of the thesis

The thesis is structured as follows:

- **Chapter 2: Literature Review** - This chapter will delve into the relevant literature concerning electrochemical corrosion, non-destructive testing of concrete structures and the destructive evaluation of these tests.

- **Chapter 3: The Sluinerweg viaduct** - The focus of this chapter will be on the Sluinerweg viaduct, which serves as the main in-situ research location. This section will provide background information about the structure and about earlier inspections.

- **Chapter 4: In-situ measurements** - This chapter will be dedicated to the execution of various destructive and non-destructive tests on the Sluinerweg viaduct.

- **Chapter 5: Data processing** - This chapter will cover the processes involved in handling and processing the data collected during the testing phase and presents the findings based on this data.

- **Chapter 6: Discussion** - This chapter will be dedicated to the discussion of the findings and their implications.

- **Chapter 7: Conclusion and Recommendations** - In the final chapter, conclusions are drawn, a methodology for future inspections is proposed and recommendation are given for future research.

Chapter 2

Literature Review

2.1 Introduction

As outlined in the introduction, this research aims to advance the standardisation of using NDTs in-situ in the Netherlands. The first step is conducting a comprehensive literature review before proceeding to the testing phase. This literature review consists of the following sections:

- Section 2.2: Chloride-induced corrosion
- Section 2.3: Carbonation-induced corrosion
- Section 2.4: Corrosion thermodynamics
- Section 2.5: Corrosion kinetics
- Section 2.6: Mass transport
- Section 2.7: Non-destructive testing
- Section 2.8: Coring
- Section 2.9: Cathodic protection
- Section 2.10: Summary of literature findings

First, it is essential to discuss the basics of the corrosion process as the Liggerkoppen project is recognised for its issues with chloride-induced corrosion. Understanding corrosion thermodynamics and kinetics is important background knowledge for assessing corrosion using NDTs. Additionally, it's important to highlight the distinctions between chloride-induced corrosion and carbonation-induced corrosion. Section 2.6 explores mass transport mechanisms to gain deeper insight into the penetration of chloride ions into concrete. It also explains Fick's second law, which commonly serves as a modeling tool for chloride diffusion. The key part on NDTs is thereafter discussed in Section 2.7. This section specifically focuses on the NDTs outlined in the research scope. It delves into the fundamentals of these techniques, outlining the information they provide, external factors and concrete properties affecting their measurements, as well as the current applicable codes and guidelines. Section 2.8 provides general information on coring, including current codes and guidelines for determining in-situ compressive strength, carbonation depth, and chloride content. This information is important for the destructive verification of the in-situ measurements. Section 2.9 provides background information on cathodic protection, an integral aspect of the Liggerkoppen project. The final section provides a summary of the literature findings, with a primary focus on the insights gained in Section 2.7.

2.2 Chloride-induced corrosion

2.2.1 The corrosion process

Corrosion of reinforcement steel is a serious problem for reinforced concrete structures. This problem arises due to the failure of the passivation layer on the rebar, which is typically formed by the highly alkaline environment of the surrounding concrete. However, degradation mechanisms, such as carbonation, reduce the alkalinity of the concrete over time, leading to the breakdown of the passivation layer and the formation of electrical cells [3].

The corrosion process initiates when the reinforcement interacts with water and oxygen. While Figure 2.1 provides a general sketch of iron corrosion, it's important to note that the process is more complex and differs when reinforcement is embedded in concrete, as elaborated in Section 2.2.2. The primary anodic (oxidation) and cathodic (reduction) reactions are described in Equations 2.1 and 2.2, respectively.

$$Fe \rightarrow Fe^{2+} + 2\,e^- \tag{2.1}$$

$$O_2 + 2\,H_2O + 4\,e^- \rightarrow 4OH^- \tag{2.2}$$
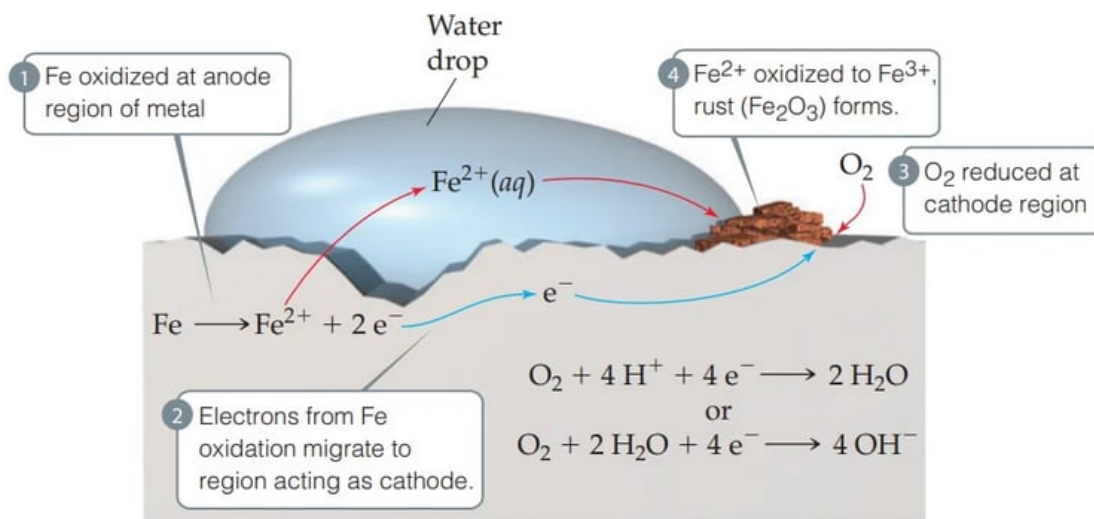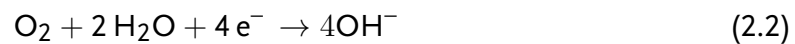
Figure 2.1: A schematic representation of the corrosion process of iron [4].

The corrosion process results in rust formation and the build-up of expansive pressure in the concrete. The expansive products formed at the steel-concrete interface, can occupy approximately $2-6$ times the volume of the original steel, as illustrated in Figure 2.2. This can result in cracking of the concrete which further facilitates the ingress of aggressive agents, ultimately contributing to concrete spalling. Moreover, the ongoing corrosion causes a reduction in the thickness of the reinforcement and weakens the bond between the concrete and the reinforcement.
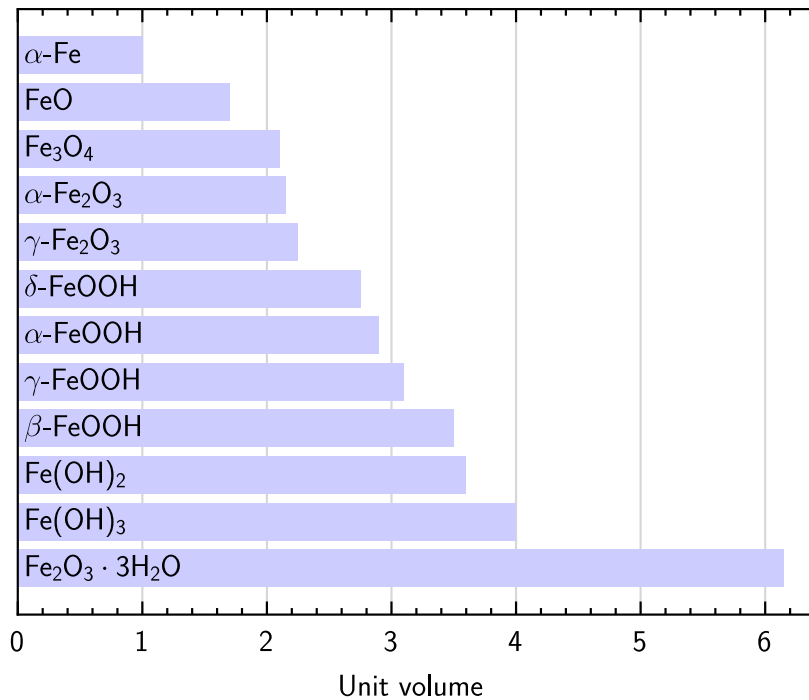
Figure 2.2: The relative volumes of iron corrosion products (adapted from [5]).

2.2.2 Pitting corrosion

Reinforced concrete structures, particularly concrete bridges and tunnels, face a substantial risk of corrosion, primarily due to the presence of chlorides, commonly referred to as chloride-induced corrosion. In the Netherlands, this is attributed to the widespread use of de-icing salts on roads, which can easily penetrate the porous *ZOAB* asphalt concrete. Expansion joints on bridges are locations that are susceptible for chlorides to enter and infiltrate the concrete. In the past, chlorides were sometimes intentionally added to the concrete mix, such as calcium chloride as an accelerating admixture.

The rate of chloride ion penetration through the cover zone is mainly determined by the permeability of the concrete. Once these chloride ions reach the steel reinforcement, they act as a catalyst in the local breakdown of the passivisation layer. This localised type of corrosion is called pitting corrosion. Chloride ions (Cl^-) migrate to the bottom of the pit where large amounts of iron(II) ions (Fe^{2+}) are present. There they can react to form iron chloride ($FeCl_2$) which is highly soluble in water. The hydrolysis of iron chloride results in local acidification due to the formation of hydrochloric acid according to Equation 2.3. At the surface oxygen reacts with water to produce hydroxyl ions (OH^-) [6].

$$2\,FeCl_2 + 2\,H_2O \rightarrow 2Fe(OH)_2 + 2\,HCl \tag{2.3}$$
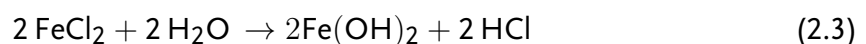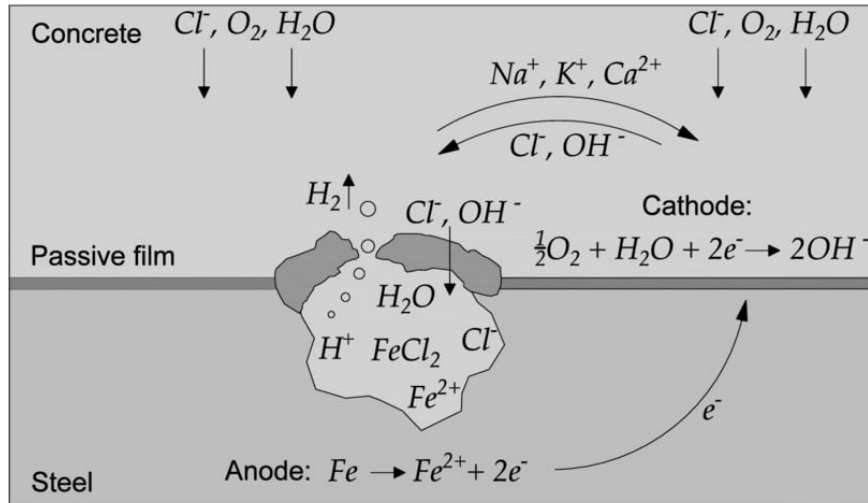
Figure 2.3: Chloride-induced pitting corrosion [7].

The chloride-induced corrosion process is auto-catalytic if a sufficient $[Cl^-]/[OH^-]$ ratio is reached [8]. A stable pit growth therefore depends on the concentration and mobility of both ions. An insufficient concentration of chloride ions will result in repassivation of the steel [9]. The pitting corrosion mechanism can swiftly lead to a local reduction in the reinforcement cross-section without being manifested by cracking or spalling of the concrete, making it difficult to detect through visual inspection [10].

2.3 Carbonation-induced corrosion

2.3.1 Chemical process

Carbonation is the chemical process where the calcium-bearing phases inside concrete react with carbon dioxide (CO_2) from the air resulting in the formation of calcium carbonate ($CaCO_3$).

$$CO_2 + H_2O \rightarrow HCO_3^- + H^+ \tag{2.4a}$$

$$HCO_3^- \rightarrow H^+ + CO_3^{2-} \tag{2.4b}$$

$$Ca(OH)_2 + 2\,H^+ + CO_3^{2-} \rightarrow CaCO_3 + 2\,H_2O \tag{2.4c}$$
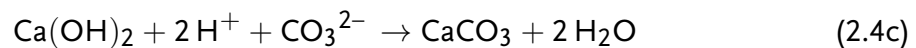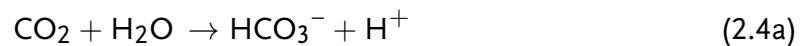
Calcium hydroxide or portlandite ($Ca(OH)_2$) is the main component that reacts with the CO_2, although carbonation of C-S-H can also occur with the depletion of calcium hydroxide. It must be noted that the carbonation of calcium hydroxide is an expansive reaction whereas carbonation of C-S-H results in shrinkage, this is important for blended cements with a lower $Ca(OH)_2$ content [10].

In order for the chemical reaction to initiate under optimal conditions, a relative humidity of 50% to 70% is required [3]. If the relative humidity is too low, the CO_2 will not dissolve, while if it is too high, water will block the pores. The carbonation front gradually reaches the steel surface, depending on the concentration of CO_2, the pore structure, and the relative humidity as mentioned above. As a result, the pH is lowered, leading to the breakdown of the steel passivation layer. Carbonation can result in a strength increase for

concrete structures made with portland cement since the process reduces the porosity of the concrete, however this benefit does generally not outweigh the increased corrosion risk.

The most common way to indicate the carbonation depth is by spraying a solution of phenolphthalein on a freshly broken face. A color change can be observed from fuchsia to colorless when the pH decreases below 8.5. Figure 2.4 provides an example of where the carbonation front has not reached the rebar.
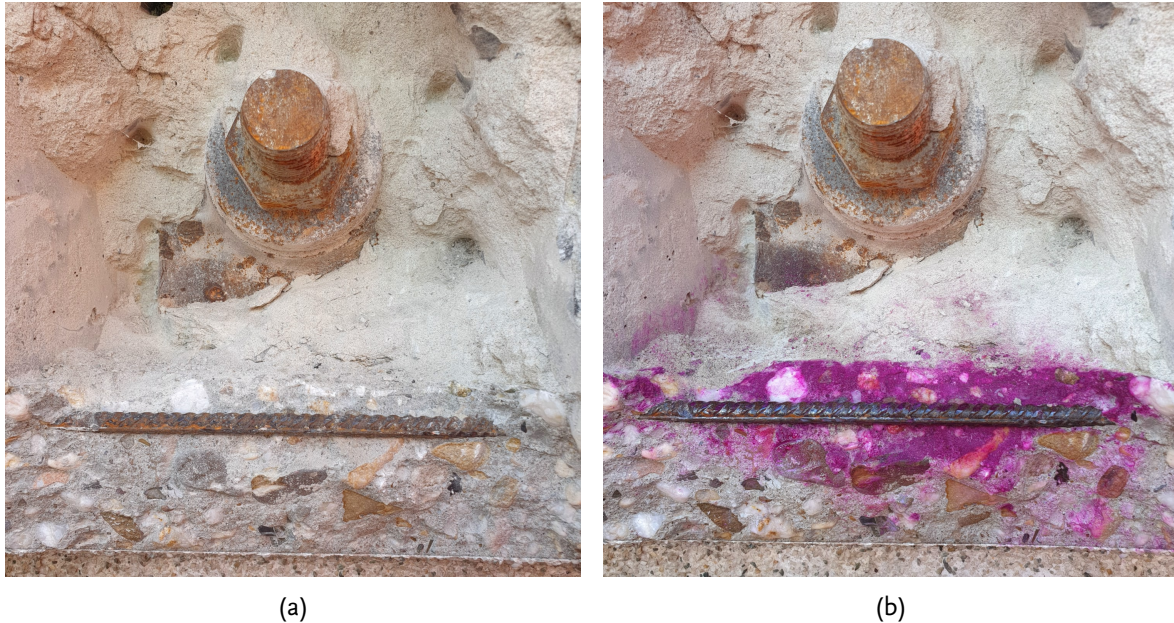
Figure 2.4: Before (a) and after (b) spraying with phenolphthalein.

2.3.2   Carbonation depth

The distance to which the carbonation front extends is referred to as the carbonation depth. This depth can be estimated using:

$$x(t) = K \cdot \sqrt{t} \tag{2.5}$$

where:

K = carbonation coefficient (mm/year$^{0.5}$)
t = time (s)

Equation 2.5 shows that the rate of carbonation decreases over time. This decrease can be attributed to the need for CO_2 to diffuse through the already carbonated concrete cover zone. Predicting K accurately in practice proves complex as the parameter can change in time or within different parts of a structure [10].

2.3.3   Factors influencing carbonation

The rate of carbonation is influenced by various factors, including environmental factors and factors related to concrete composition [10].

Relative humidity

As discussed in section 2.3.1, the rate of carbonation is strongly dependent on the relative humidity. The transport of CO_2 through water-filled pores is slow, therefore the diffusion of CO_2 decreases with an increase in relative humidity. However, the carbonation reaction can only occur with the presence of water and so the carbonation rate becomes negligible in dry concrete. This principle is illustrated in Figure 2.5.
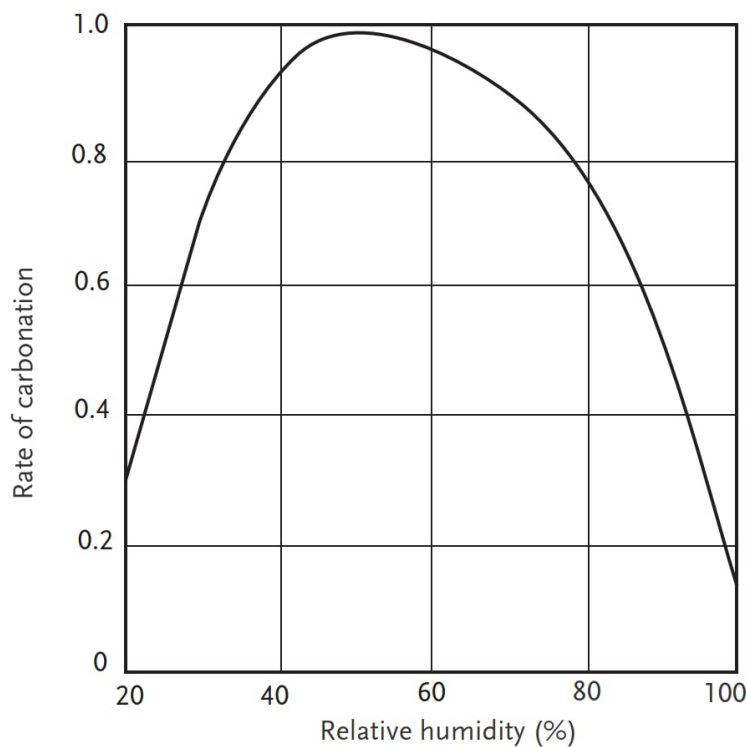
Figure 2.5: Rate of carbonation as a function of the relative humidity, under equilibrium conditions [11].

Temperature

According to [12], it was found that the carbonation depth demonstrates a linear increase with rising environmental temperature. Nevertheless, they observed a reduction in compressive strength following carbonation, specifically noting that this decrease was more pronounced in concrete with higher strength grades. This effect was attributed to potential increases in both the CO_2 transmission coefficient and chemical reaction coefficient at elevated temperatures.

Concentration of CO_2

In 2022, the global average concentration of CO_2 at the surface was 417.06 ppm and it has been increasing since the start of the measurements according to the *National Oceanic and Atmospheric Administration* [13]. Locally this concentration can vary under specific conditions, such as inside highway tunnels. A higher concentration of CO_2 in blast furnace slag concrete will result in a higher rate of carbonation of unreacted cement particles and it also increases the reaction with portlandite [14].

Concrete composition

The rate of carbonation in concrete is influenced by its permeability. A lower water-to-cement (w/c) ratio leads to reduced capillary porosity, resulting in a slower carbonation rate. Additionally, curing play a significant role; poor curing can accelerate carbonation, particularly in the cover zone. Finally, the type of cement used can also influence the carbonation rate. A lower $Ca(OH)_2$ may increase the carbonation rate due to the lower alkalinity. Nonetheless, this effect can be mitigated by the development of a denser structure through the hydration of blended cements when cured properly [10].

2.3.4 Chloride-contaminated carbonated concrete

When carbonated concrete is contaminated with chlorides, the corrosion process can intensify. Chloride contamination increases the ionic conductivity of the pore solution and facilitates moisture retention, leading to a lower resistivity [15]. Figure 2.6 shows the corrosion rate in carbonated mortars with varying chloride contents. It can be observed that in case of the absence of chlorides, the corrosion rate becomes negligible only when the external relative humidity drops below 70%. This threshold decreases to less than 40% in the case of a 1% chloride content.
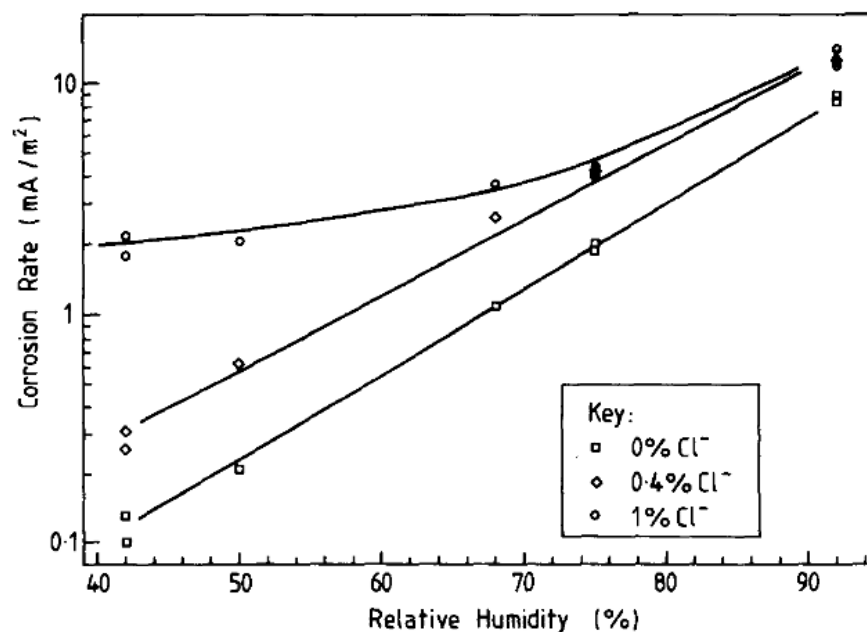
Figure 2.6: The relationship between relative humidity and corrosion rate obtained on polarisation resistance probes exposed to carbonated mortars containing 0, 0.4 and 1% chloride [15].

2.4 Corrosion thermodynamics

The corrosion process of reinforcement in concrete, as detailed in Section 2.2.1, is better understood when exploring its associated electrochemical aspects. Corrosion thermodynamics provides insights into the probability of corrosion in various environments. On the other hand, corrosion kinetics helps in evaluating the rate of corrosion, a crucial factor for designing effective maintenance strategies.

2.4.1   Electrochemical cells

Various types of electrochemical cells exist, including galvanic cells, electrolytic cells and concentration cells. In galvanic cells chemical energy is transformed into electrical energy, facilitated by the flow of electrons and current. In galvanic cells, electrochemical reactions occur spontaneously, driving the overall cell process. Electrolytic cells are designed to convert electrical energy into chemical energy. Unlike galvanic cells, the electrochemical reactions in electrolytic cells are non-spontaneous, requiring an external power source. Concentration cells represent a unique category, featuring equal half-cell conditions but with a distinct concentration gradient. Specifically, the concentration of a species is higher in the anode half-cell compared to its concentration in the cathodic counterpart [6].
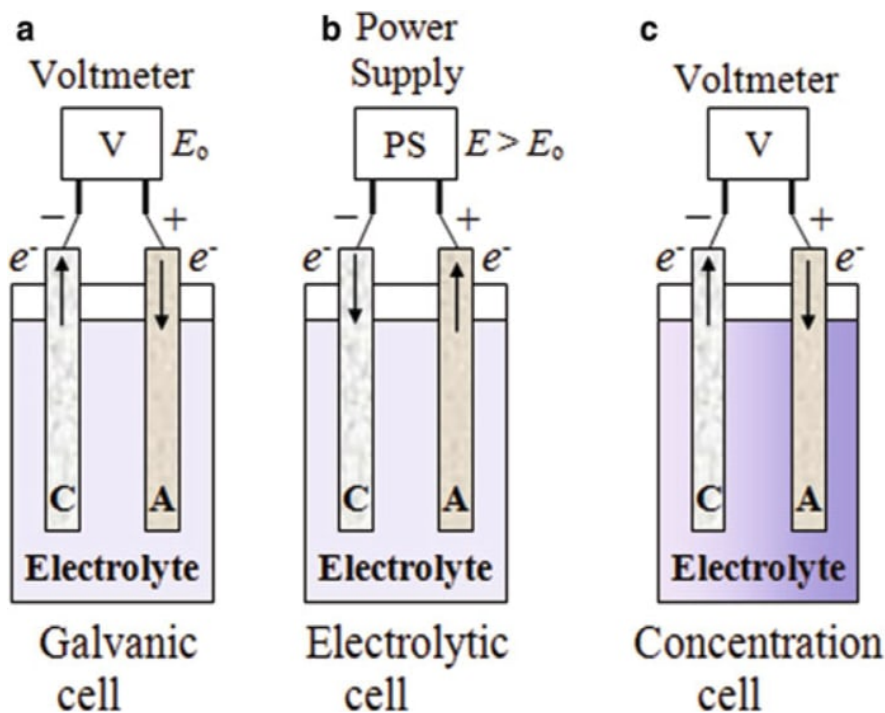
Figure 2.7: Electrochemical cells [6].

2.4.2   Nernst equation

The non-equilibrium electric potential (E) of an electrochemical cell can be calculated using the Nernst equation.

$$E = E_0 - \frac{RT}{zF} \ln Q \tag{2.6}$$

where:

E_0 = standard half-cell potential (V)
R = universal gas constant (8.314 J mol^{-1}K^{-1})
T = absolute temperature (K)
z = number of electrons transferred (-)
F = Faraday constant (96485 C mol^{-1})
Q = reaction quotient (-)

The Nernst equation presents the difference in open-circuit potential for a reversible galvanic cell, but excludes the effect of liquid junction potentials which are usually small in magnitude [6].

2.4.3 Pourbaix diagram

The Nernst equation can be used to construct thermodynamic diagrams that represent the phases of an aqueous electrochemical system. These potential-pH diagrams were founded by Marcel Pourbaix in 1938 and are therefore called Pourbaix diagrams [16]. For the analysis of corrosion in reinforced concrete, the Pourbaix diagram of a $Fe - H_2O$ system, as depicted in Figure 2.8, holds particular significance. The construction of this diagram is detailed in Appendix A. It's important to emphasise that the presented diagram is a simplified representation of reality.
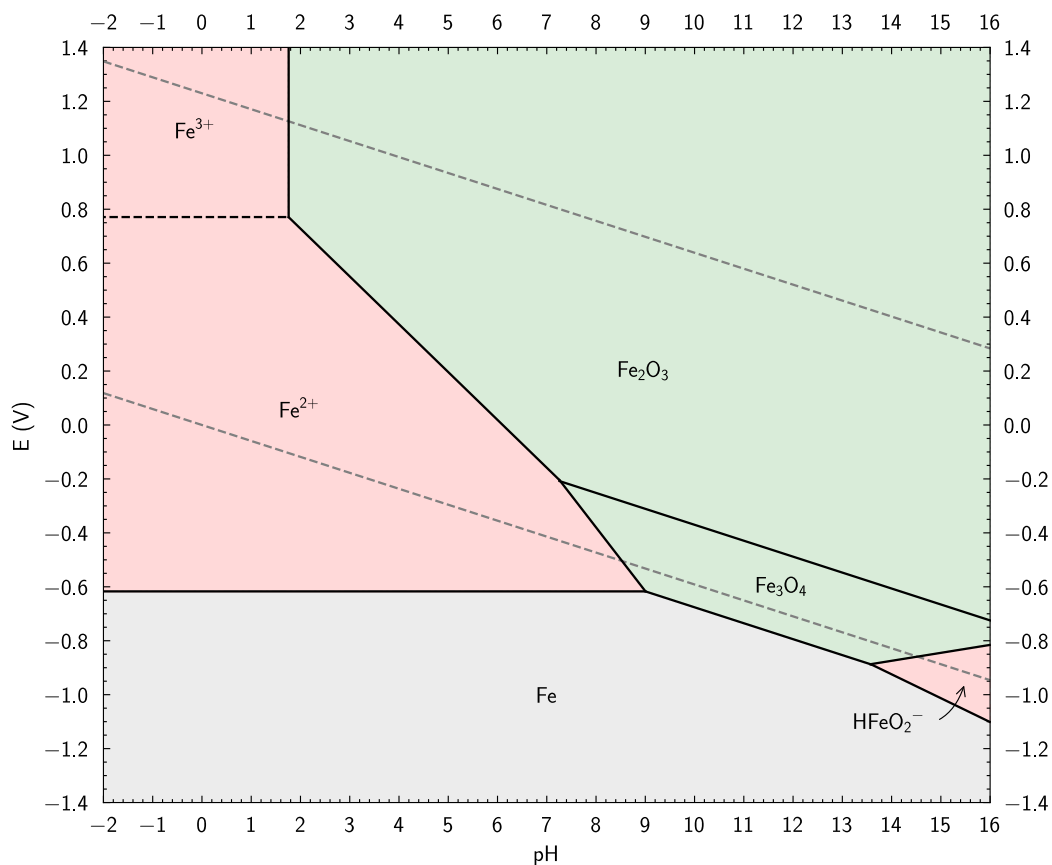
Figure 2.8: Pourbaix diagram for a $Fe - H_2O$ system ($T = 25°C$, $P = 1$ atm and all ionic concentrations 10^{-6} M).

The Pourbaix diagram in Figure 2.8 features three distinct zones: the red zone is indicative of active corrosion, the green zone representing passivity, and the grey zone denoting the immunity region. The area between the dotted lines, corresponding to water equilibrium lines, marks the zone where water is thermodynamically stable. For normal reinforced concrete the pH typically ranges somewhere between 12 and 14 [16]. The diagram does not convey information about the corrosion rate, which is a component of corrosion kinetics.

The Pourbaix diagram serves as a valuable tool for designing a cathodic protection system by aiming to lower the potential into the immunity region, particularly when the environmental conditions align with those depicted in the diagram.

2.5   Corrosion kinetics

2.5.1   Activation polarisation

Polarisation is a mechanism characterised by a kinetic deviation from the equilibrium potential when an electric current flows through an electrochemical cell. The term activation polarisation refers to an electrochemical process triggered by the application of an overpotential. When a positive overpotential is applied, oxidation reactions become prevalent, while a negative overpotential triggers reduction reactions [6]. The assessment of corrosion kinetics involves the determination of the corrosion potential (E_{corr}) and corrosion current density (i_{corr}). This corrosion current density can be used to determine the corrosion rate.

2.5.2   Polarisation diagram

Reaction rates are dictated by chemical kinetics, while corrosion rates are primarily governed by electrochemical kinetics. In order to characterize the kinetics of a corroding metal, the corrosion current density (i_{corr}) and the equilibrium potential, also known as corrosion potential (E_{corr}) can be determined. The corrosion behavior can then be visualised by a polarisation diagram.

The evaluation of corrosion behavior for a one-step reaction under steady-state conditions and without the effects of mass-transport, can be described by the Butler-Volmer equation.

$$i = i_o \left\{ \exp\left[\frac{\alpha_a z F \eta}{RT} \right] - \exp\left[-\frac{\alpha_c z F \eta}{RT} \right] \right\} \tag{2.7}$$

where:

i_o	= exchange current density (A/cm^2)
R	= universal gas constant (8.314 J mol^{-1}K^{-1})
T	= absolute temperature (K)
z	= number of electrons transferred (-)
F	= Faraday constant (96485 C mol^{-1})
η	= overpotential (V)
α_a	= anodic transfer coefficient (-)
α_c	= cathodic transfer coefficient (-)
$\alpha_a + \alpha_c = 1$	

The exchange current density (i_o) is the current density at which the oxidation and reduction rate are at equilibrium. The exact potential dependence is controlled by the unitless anodic and cathodic transfer coefficients [17]. In order to approximate the current density, the following inequality can be considered when the overpotential is large and anodic:

$$\exp\left[\frac{\alpha_a zF\eta}{RT}\right] \gg \exp\left[-\frac{\alpha_c zF\eta}{RT}\right] \tag{2.8}$$

Similarly when the overpotential is large and cathodic (η is therefore negative):

$$\exp\left[-\frac{\alpha_c zF\eta}{RT}\right] \gg \exp\left[\frac{\alpha_a zF\eta}{RT}\right] \tag{2.9}$$

By applying these inequalities to Equation 2.7 and solving for η the so called Tafel equation is obtained.

$$\eta = \pm\beta \log\left(\frac{i}{i_o}\right) \tag{2.10}$$

Equation 2.10 can be divided into an anodic and a cathodic part, resulting in Equations 2.11 and 2.12 respectively.

$$\eta_a = \beta_a \log\left(\frac{i_a}{i_o}\right) \tag{2.11}$$

$$\eta_c = -\beta_c \log\left(\frac{i_c}{i_o}\right) \tag{2.12}$$

Having β_a and β_b represent the anodic and cathodic Tafel slopes:

$$\beta_a = \frac{2.303RT}{\alpha_a zF} \tag{2.13}$$

$$\beta_c = \frac{2.303RT}{\alpha_c zF} \tag{2.14}$$

The corrosion current density (i_{corr}) can be determined by identifying the point of intersection between the anodic and cathodic Tafel slopes, as illustrated in Figure 2.9. The anodic and cathodic Tafel plots combined represent the so called *Evans diagram*. Note that in this figure, the lines are illustrated with similar slopes for clarity, but in reality, the slopes may differ due to variations in ionic concentrations and environmental factors.
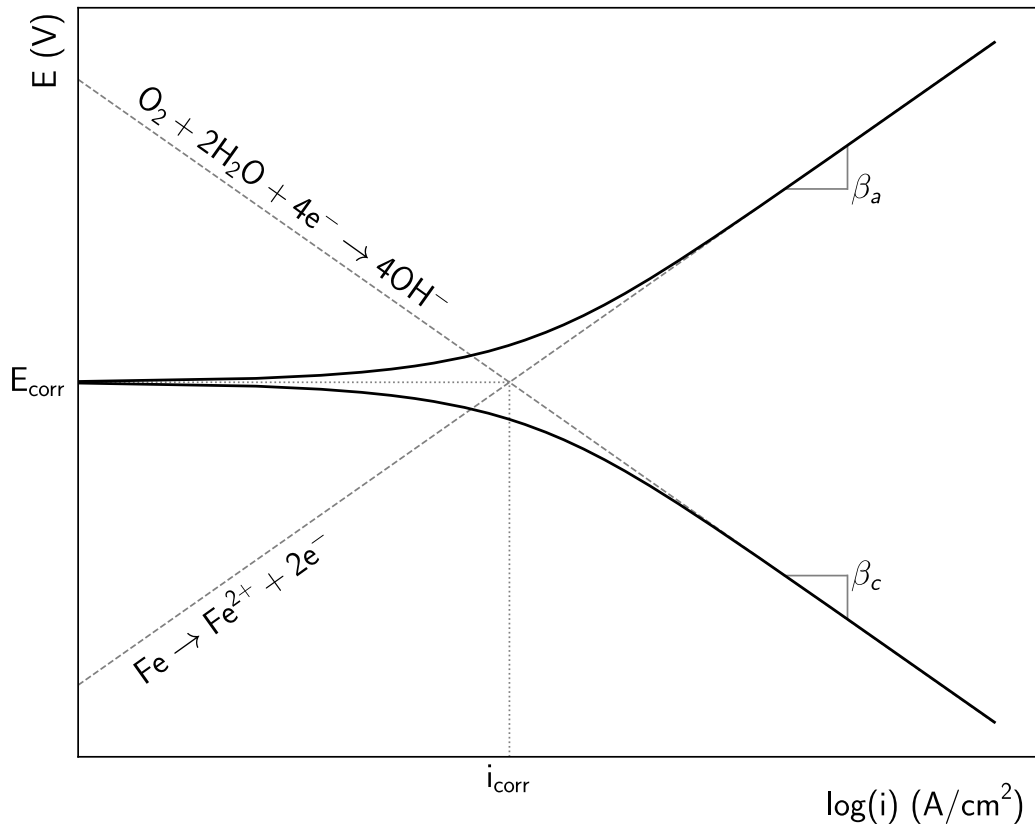
Figure 2.9: Schematic polarisation curve with Evans diagram.

An example of the anodic polarisation curve of steel at a pH of 6 is given in Figure 2.10. At potentials more negative than the equilibrium potential, steel remains immune to corrosion or dissolution. As the potential is progressively increased beyond this equilibrium potential, active corrosion initiates (A-B). At a critical point (B), the dissolution rate equals the rate of metal oxide formation. Beyond this point, the formation of a protective metal oxide layer predominates, resulting in a significant reduction of active corrosion, effectively rendering the steel passive (B-C). However, rapid dissolution starts if the metal's electrode potential becomes excessively positive, reaching the oxygen equilibrium line (C) from where oxygen will be generated. This marks the beginning of the transpassive region, where the metal's passive state breaks down, and rapid dissolution begins. The anodic polarisation curve varies with an increasing chloride content: passivity is lost at an increasingly lower potential. Consequently, the corrosion rate will increase [18].
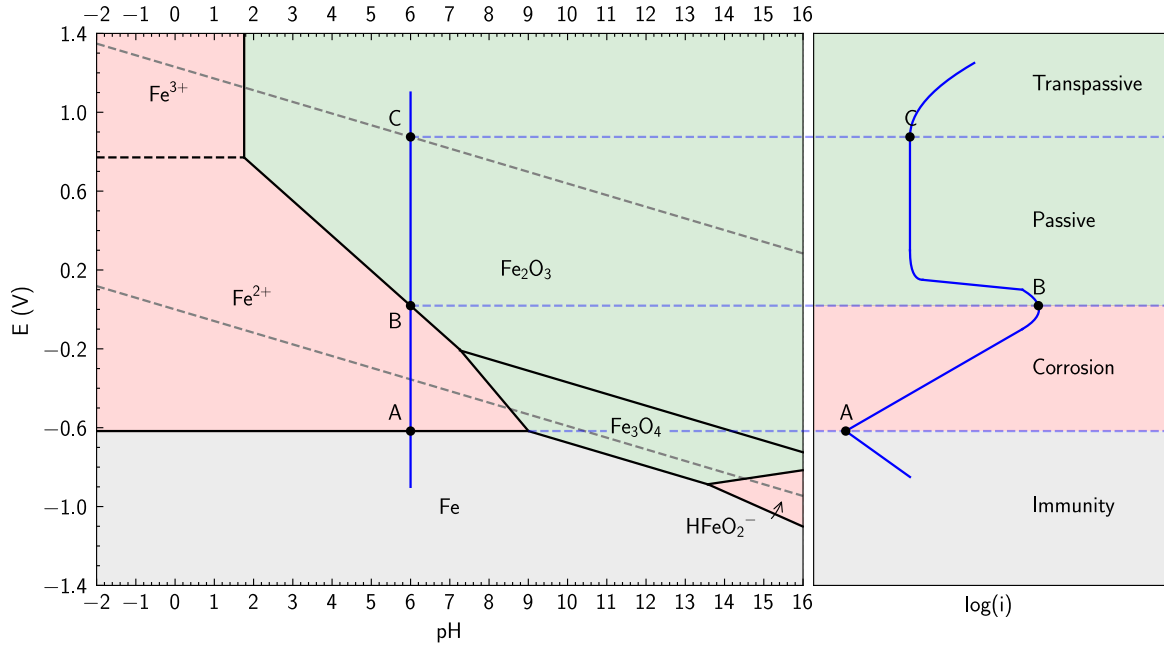
Figure 2.10: Anodic polarisation curve alongside the Pourbaix diagram at a pH of 6 (adapted from [6]).

2.5.3 Linear polarisation resistance

In 1957, M. Stern and A.L. Geary introduced a polarisation resistance (R_p) technique for determining the corrosion rate. When polarising the reinforcement with a small amount ($\pm 5 - 10$ mV), the polarisation resistance can be determined [16].

$$R_p = \frac{\Delta E}{\Delta i} = \frac{\eta}{\Delta i} \tag{2.15}$$

Equation 2.7 can be rewritten using the Tafel slopes:

$$i = i_{corr} \left\{ \exp\left[\frac{2.303\eta}{\beta_a}\right] - \exp\left[-\frac{2.303\eta}{\beta_c}\right] \right\} \tag{2.16}$$

The derivative of Equation 2.16 with respect to η can be subsequently applied to Equation 2.15:

$$\frac{1}{R_p} = 2.303 i_{corr} \left(\frac{1}{\beta_a} + \frac{1}{\beta_c}\right) \tag{2.17}$$

Rewriting this equation in terms of i_{corr} yields the *Stern-Geary equation* [19].

$$i_{corr} = \frac{\beta_a \beta_c}{2.303 R_p (\beta_a + \beta_c)} \tag{2.18}$$

In literature the Stern-Geary equation is often encountered in the following form:

$$i_{corr} = \frac{B}{R_p} \qquad (2.19)$$

where:

$B = \frac{\beta_a \beta_c}{2.303(\beta_a + \beta_c)}$ (V)

The Stern-Geary equation holds significant importance in determining the corrosion current density in reinforced concrete when using the modulated confinement method, as elaborated further in Section 2.7.8. The constant B has been identified as 52 mV for reinforcement in the passive state and 26 mV in the active or corroded state. However, 26 mV can be used in all cases, considering that a factor of 2 error in passive steel is negligible in the context of gravimetric losses [20]. It is also noteworthy that R_p is measured in $\Omega \cdot cm^2$ when the corrosion current density is expressed in A/cm^2.

2.5.4 Corrosion rate

When the corrosion current density is known, Faraday's laws of electrolysis can be used to calculate the corrosion rate for reinforcement.

$$CR = \frac{i_{corr} M_{Fe}}{zF\rho_{Fe}} \qquad (2.20)$$

where:

CR = corrosion rate (cm/s)
i_{corr} = corrosion current density (A/cm^2)
M_{Fe} = molar mass of iron (55.845 g/mol)
z = number of electrons transferred (-)
F = Faraday constant (96485 C mol^{-1})
ρ_{Fe} = density of iron (7.85 g/cm^3)

A relation between the electrochemical weight loss and gravimetric weight loss has been reported in [21]. It was found that the electrochemical weight loss determined by the modulated confinement method (Section 2.7.8) gives similar values to the gravimetric technique [22]. In cases of localised corrosion however, the corrosion current density may not be accurately represented by the measured average corrosion current density. As a result, the corrosion rate calculated based on this average may not accurately reflect the true corrosion rate, even after performing gravimetric tests.
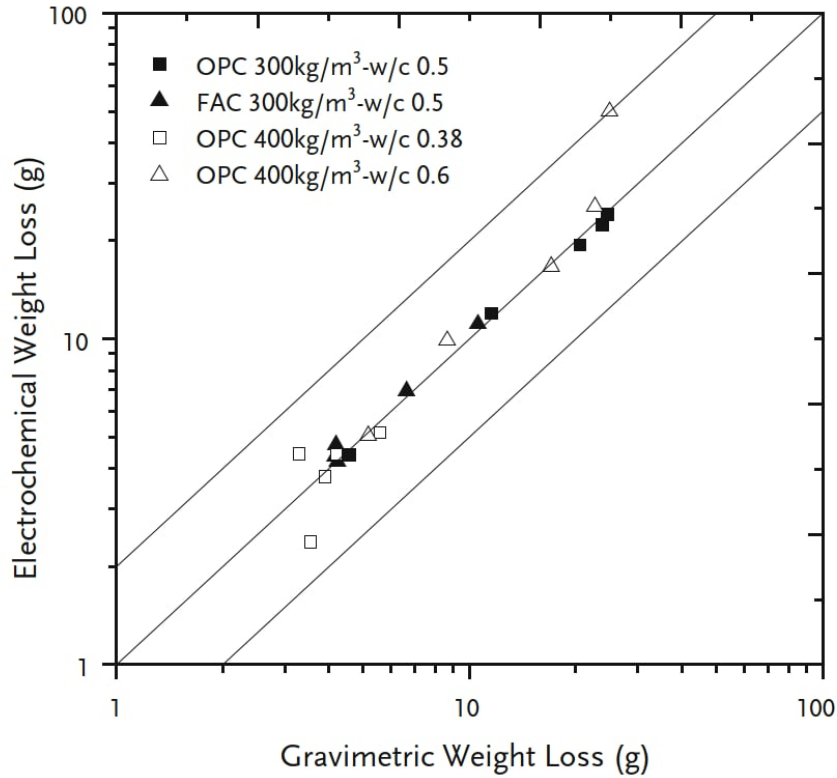
Figure 2.11: Gravimetric weight loss and electrochemical weight loss of concrete submerged in sea water for several years [21].

2.6 Mass transport

Chlorides penetrate through capillary pores and cracks in concrete. There are four mechanisms that describe the mass transport of chlorides through concrete: *diffusion*, *permeation*, *migration* and *capillary suction* [23].

2.6.1 Diffusion

Diffusion describes the mass transport under a concentration gradient. Chlorides always diffuse into areas with a smaller concentration. It is described in [23] as the predominant transportation mechanism for chlorides in concrete. The theory of diffusion is based on mathematical models created by Adolph Eugen Fick.

Fick's first law of diffusion
For a one-dimensional problem, the transport of chloride ions through an unit area of concrete per unit of time (flux J) is assumed to be proportional to the concentration gradient of the chloride ions:

$$J = -D\frac{\partial C}{\partial x} \tag{2.21}$$

where:

D $\;=$ diffusion coefficient (m^2/s)

$\frac{\partial C}{\partial x}$ $=$ concentration gradient (mol/m^4)

A negative sign is required because the diffusion of chloride ions takes place in the opposite direction to the increasing concentration of chloride ions.

Fick's second law of diffusion

Fick's second law of diffusion states that a change of concentration per unit time is equal to the change of flux per unit length (Equation 2.22). A derivation for this equation can be found in Appendix A.2.

$$\frac{\partial C}{\partial t} = -\frac{\partial J}{\partial x} \tag{2.22}$$

A solution can be found by considering a semi-infinite medium, using the boundary condition and initial condition specified in Equation 2.23 and 2.24 respectively.

$$C = C_s, \quad x = 0, \quad t > 0 \tag{2.23}$$

$$C = 0, \quad x > 0, \quad t = 0 \tag{2.24}$$

Solving this system results in Equation 2.25 of which the derivation can be found in [24].

$$C(x,t) = C_s \left[1 - \mathrm{erf}\left(\frac{x}{2\sqrt{Dt}} \right) \right] \tag{2.25}$$

The equation features the error function, denoted as Equation 2.26 with the corresponding plot presented in Figure 2.12.

$$\mathrm{erf}(x) = \frac{2}{\sqrt{\pi}} \int_0^x e^{-t^2} dt \tag{2.26}$$
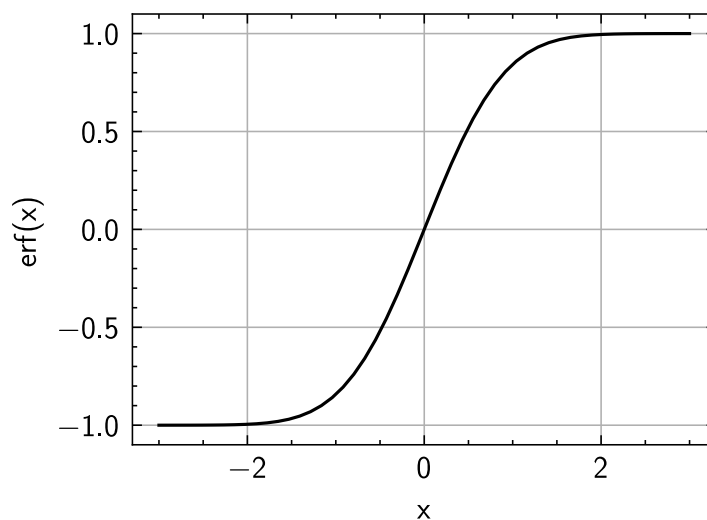
Figure 2.12: The error function.

The heterogeneous composition of concrete and its exposure to diverse environmental conditions result in a convection zone. This particular zone holds substantial influence over the precision of estimations founded on Fick's second law. The impact stemming from this convection zone is commonly referred to as the *skin effect*. The external layer of concrete often differs in composition from the internal structure due to factors like mold contact or aggregate segregation. Chloride ions must initially deposit onto the surface of concrete before penetrating its interior and the concentration of these deposited chloride ions is fundamental for setting the boundary conditions in models relying on Fick's second law [25].

2.6.2 Permeation

Permeation describes the transport of an incompressible fluid under influence of a pressure gradient. This process can be described by Darcy's Law:

$$\frac{dq}{dt} = \frac{kA\Delta P}{\mu L} \tag{2.27}$$

where:

$\frac{dq}{dt}$ = flow (m^3/s)
k = intrinsic permeability of concrete (m^2)
A = surface of the cross-section (m^2)
ΔP = pressure head (Pa)
μ = viscosity (Pa · s)
L = length of medium (m)

The intrinsic permeability of concrete is influenced by various factors, including porosity and pore inter-connectivity.

2.6.3 Migration

Migration occurs when chloride ions are transported in the presence of an electrical field, with chloride ions migrating towards zones exhibiting a lower electrical potential. The migration of chloride ions takes place exclusively through water-filled pores, making it dependent on the porosity and pore inter-connectivity of the material.

2.6.4 Capillary suction

Capillary suction manifests as a consequence of a difference in moisture content, causing water containing chloride to migrate from areas of higher to lower moisture content. This movement is driven by surface tension within the capillary pores. For a spherical pore, the Young-Laplace equation can be used to calculate the pore pressure.

$$P = \frac{2\gamma\cos(\theta)}{r} \tag{2.28}$$

where:

γ = surface tension (N/mm)
θ = contact angle ($\circ$)
r = pore radius (mm)

The effect of capillary suction is important in non-saturated concrete and has a high influence on the outermost layer.

2.7   Non-destructive testing

This section provides the background information on the NDTs applied during the evaluation of the Sluinerweg viaduct. It is important to note that numerous other NDTs are available. A comprehensive overview is presented in Appendix A.3 [2].

2.7.1   Visual inspection

Before conducting any tests on a concrete structure, it is always advisable to start with a visual inspection. In some cases, a visual inspection alone may suffice to identify the cause of damage. However, a drawback is that damage is often only visible when it has already started affecting the structure's service life. During a visual inspection, it is crucial to work systematically and document any anomalies using photos and notes. Additionally, there are several straightforward non-destructive tools that can be used during a visual inspection, including the *coin tap* and the *chain drag* methods.

Coin tap
By tapping a coin at the surface of concrete, one can identify localised delaminations, cracks or voids by detecting a change in frequency by ear. This is actually a simple form of impulse echo testing [26].

Chain drag
The chain drag method can be used to detect delaminations on uncovered bridge decks. A hollow sound is a sign of delamination. The accuracy of the method is therefore dependent on the hearing of the inspector and also on the severity of the delaminations. It can still be an useful method however for periodical inspections, especially in combination with other NDTs.

2.7.2   Ground penetrating radar (GPR)

A Ground Penetrating Radar (GPR) is a NDT widely used in civil engineering, geophysics, and archaeology. It uses the principles of radar technology to provide valuable insights into subsurface structures and materials. In reflection mode, it functions by emitting short electromagnetic pulses through a transmitter. These pulses reflect at the object that is under inspection and are then received by the receiver antenna [27].

For the investigation of concrete structures, the method is particularly suitable for measuring the cover thickness and locating cracks, reinforcement, tendons or tendon ducts. A great advantage of the method is the significant depth it can reach, especially with low frequency transmitters, although the accuracy will decrease at higher depths. The method

has also been used in different experiments to measure the extent of corrosion damage in the reinforcement. This is done by observing the change in reflected energy due to changes at the concrete-steel interface and in the material. However this proved to be challenging since the influence of other material parameters like moisture content on the GPR signal were not known [28].

Figure 2.13: Concrete testing block at Newa HQ and Screening Eagle's GP8000.

Data acquisition

In order to obtain accurate data from a GPR, it is important to use a consistent grid for the measurements. Once this grid is established, the type of measurement can be selected. A measurement consisting of a single radar trace in the longitudinal direction is called an A-scan. When measuring over a certain length with consecutive radar waveforms, this is referred to as a B-scan or Line scan. When creating a visualization over a horizontal surface, it is called a C-scan or Area scan.

One of the most critical parameters to configure is the value of the dielectric constant (ϵ_r), also known as the relative permittivity. This property is a measure of a material's ability to store electrical energy in an electric field. The speed of an electromagnetic wave through a dielectric medium can be calculated according to Equation 2.29.

$$v = \frac{c}{\sqrt{\epsilon_r}} \tag{2.29}$$

where:

v = speed of an electromagnetic wave (m/s)
c = speed of light in vacuum (m/s)
ϵ_r = dielectric constant (-)

Air has the lowest dielectric constant with a value close to 1, which is the value in vacuum. Water on the other hand has a dielectric constant of 80.1 at a temperature of 20°C [29]. Concrete is an inhomogeneous material influenced by many external factors, making it difficult to estimate its dielectric constant. In the context of concrete structures in the Netherlands, a value of 6 was personally recommended as a practical starting point by *Ivo Verheijen*, the owner of Newa, who has many years of experience in the field of non-destructive testing. However, the value can range from 5 to 10, according to ASTM D6432-19 [30]. Steel reinforcement has an exceptionally high relative permittivity, approaching infinity. Therefore the electromagnetic signal undergoes complete reflection at the interface with reinforcement. This distinctive behavior manifests in the GPR analysis as the characteristic parabolic shape. After running an analysis with a certain dielectric constant as input, it is possible with some devices to use parabola fitting in order to estimate the dielectric constant and check the initial assumption.

Influencing factors

Several external factors and concrete properties can influence the GPR signal. Table 2.1 provides an overview of these effects, indicating whether they tend to increase or decrease the amplitude of the signal. Determining the precise impact is challenging, as it depends on the specific device used and the combination of influencing factors.

Table 2.1: Effect of external factors and concrete properties on the GPR signal amplitude.

Increased factor	Effect on signal amplitude	References
Relative humidity	No effect	[31]
Moisture content	Decrease	[32, 33]
Temperature	Decrease	[31]
Porosity	Increase[a]	[34]
w/c ratio	Increase	[32]
Compressive strength	Slight increase	[34]
Chloride content	Decrease	[31, 33]
Carbonation depth	Decrease	[35]

[a] An increase of porosity in saturated concrete however will result in a decrease of the signal's velocity and amplitude.

Codes and guidelines

There are currently no existing European standards for the use of GPR in concrete structures. The American ASTM D6432-19: "Surface Ground Penetrating Radar Method for Subsurface Investigation" is not specifically written for applications in concrete structures, but provides a good overview of the method [30]. Additionally, two relevant standards

are the ASTM D6087-22: "Standard Test Method for Evaluating Asphalt-Covered Concrete Bridge Decks Using Ground Penetrating Radar" [36] and the AASHTO R 37-04: "Standard Practice for Application of Ground Penetrating Radar (GPR) to Highways" [37].

2.7.3 Ultrasonic pulse velocity (UPV)

The ultrasonic pulse velocity (UPV) technique uses a pulse of longitudinal vibrations produced by a transducer. The pulse is transmitted into the concrete using a coupling liquid. Both primary or longitudinal and secondary or shear waves are generated. The longitudinal waves have a faster travel time and are therefore the first to arrive at the receiving transducer. By dividing the distance between the transducers by the travel time, the longitudinal pulse velocity can be estimated.

$$V_P = \frac{L}{t} \tag{2.30}$$

where:
  L = path length (m)
  t = transition time (s)

The UPV method can be used to evaluate the uniformity of a concrete structure. An ultrasonic pulse will diffract around the periphery of a void in concrete resulting in a longer travel time. This effect is less pronounced with smaller voids. Low pulse velocities (< 3.0 km/s) therefore usually indicate a poor quality of the concrete structure [38]. The UPV method can also be used to estimate the compressive strength, modulus of elasticity and dynamic Poisson's ratio. Further details on the estimation of compressive strength are elaborated in Section 2.7.10.

Given that sound travels more than four times faster in water than in air, concrete saturation significantly impacts the readings. Moreover, when conducting measurements near reinforcement, the pulse velocity tends to be higher, depending upon factors such as the proximity to the reinforcement, the diameter of the rebars, and their orientation relative to the transmission path.

Data acquisition
There are three possibles transmission modes for the UPV method:

1. Direct transmission: placing the two transducers on the opposite faces.
2. Semi-direct transmission: placing the two transducers on adjacent faces.
3. Indirect transmission: placing the two transducers on the same face.
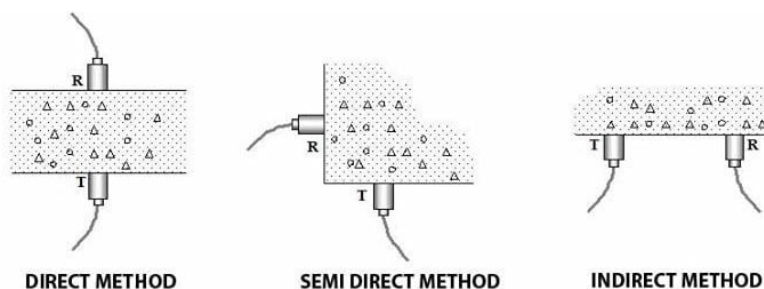
Figure 2.14: UPV transmission modes [38].

It is advisable to prioritise the use of the direct transmission mode whenever possible, as it ensures the maximum transfer of energy which leads to a more accurate estimation of the pulse velocity.

High transducer frequencies (>150 kHz) are used for short path lengths and are also more sensitive to small cracks, whereas low transducer frequencies are used for long path lengths. A commonly used transducer frequency for assessing concrete structures is 54 kHz.

Influencing factors

Several external factors and concrete properties can influence the measured transmission time. Table 2.2 provides an overview of these effects, indicating whether they tend to increase or decrease the transmission time. Determining the precise impact is challenging, as it depends on the specific device used and the combination of influencing factors.

Table 2.2: Effect of external factors and concrete properties on the ultrasonic pulse transmission time.

Increased factor	Effect on transmission time	References
Relative humidity	Increase	[39][a]
Moisture content	Increase	[34]
Temperature	Increase	[40]
Porosity	Decrease	[41]
w/c ratio	Increase	[41]
Compressive strength	Increase	[42]
Chloride content	No effect	[34]
Carbonation depth	Increase	[34]

[a] Observed for early age OPC mortars.

Codes and guidelines

The current applicable codes and guidelines for using UPV on concrete structures are detailed in Table 2.3.

Table 2.3: Codes and guidelines for UPV.

Standard	Description
ISO 1920-7	"Testing of concrete - Part 7: Non-destructive tests on hardened concrete (Chapter 4)"
EN 12504-4	"Testing concrete in structures - Part 4: Determination of ultrasonic pulse velocity"
ASTM C597	"Standard Test Method for Pulse Velocity Through Concrete"

2.7.4 Ultrasonic pulse echo (UPE)

Ultrasonic pulse echo is a technique where ultrasonic pulses are transmitted through the concrete, and the time taken for the waves to reflect back (echo) from the opposite surface or any internal flaws is measured. It can be effectively applied to concrete structures with one-sided access. In the UPE technique, shear waves are employed instead of longitudinal waves, as shear waves offer improved imaging characteristics [43]. The velocity of a single shear wave can be estimated using Equation 2.31.

$$V_S = \frac{2L}{t} \tag{2.31}$$

where:

L = path length (m)
t = transition time (s)

The S-wave velocity can be converted into P-wave velocity:

$$V_P = \sqrt{\frac{2V_S^2(\nu - 1)}{2\nu - 1}} \tag{2.32}$$

where:

V_P = P-wave velocity (m/s)
V_S = S-wave velocity (m/s)
ν = Poisson's ratio of concrete (-)

A pulse echo device is equipped with multiple rows of transducers, where during each scan, one transducer transmits a pulse, and the other transducers receive the signal. The cycling through transducers is a sequential process. The level of reflection is influenced by the acoustic impedance of the materials under inspection. For instance, a concrete-air interface typically results in nearly 100% reflection, while a concrete-steel interface may yield around 40-50% reflection [44]. This characteristic makes the pulse echo method well-suited for detecting voids or delamination but less ideal for reinforcement detection.

Data acquisition

With newer UPE devices such as the Proceq PD8050, it's possible to create 3D images of the object under inspection using AI-assisted positioning, while moving along a horizontal or vertical line. When measuring greater depths, controlling the time gain compensation allows amplification of echoes that traveled deeper. When the depth or thickness of an object is known, the scans can be corrected, if needed, by adjusting the global pulse velocity. It's crucial not only to examine a single scan at a location and focus on the absolute values, but also to compare with other scans in the same area.

In essence, GPR and UPE serve as complementary techniques, with GPR excelling in locating reinforcement and UPE being more adept at identifying defects. Properly combining these methods theoretically allows for the detection of grouting defects in tendon ducts. The initial step involves localising the reinforcement using GPR, followed by using UPE to search for grouting defects. UPE is particularly advantageous in this context as it can penetrate through thick layers of reinforcement. Fully grouted ducts result in partial reflection, whereas badly grouted ducts result in total reflection of the signal.

Figure 2.15: Proceq Pundit PD8050 UPE device used for inspecting tendon ducts after the localisation of the reinforcement with GPR.

Influencing factors

Limited information is available in the literature regarding this method, especially for the latest types of UPE devices introduced to the market. Nevertheless, since it remains an ultrasonic technique, it is reasonable to expect that similar effects of external factors and concrete properties apply as those listed in Table 2.2. An additional point worth noting is that in [43], it was observed that S-waves are less affected by moisture content.

Codes and guidelines

As of now, there are no currently active codes and guidelines designed specifically for modern UPE devices. However, information focused on ultrasonic pulse velocity (UPV) testing

found in standards such as EN 12504-2 [45] and EN 13791 [46] could also be applicable for UPE testing.

2.7.5 Rebound hammer

The rebound hammer, sometimes called Schmidt hammer or sclerometer is a device that can be used to determine the surface hardness of concrete. The principle behind this device is based on the conservation of energy. A plunger is pressed against the surface of the concrete, the mass then rebounds from the plunger and retracts against the force of the spring as illustrated in Figure 2.16. The rebound value, which is the distance traveled by the mass upon rebound, can then be determined. This value is directly proportional to the surface hardness of the concrete, which is a measure of its resistance to abrasion or scratching. The rebound value can be empirically correlated to the compressive strength of the concrete, providing a quick and simple means of estimating the strength of the structure (see also Section 2.7.10).
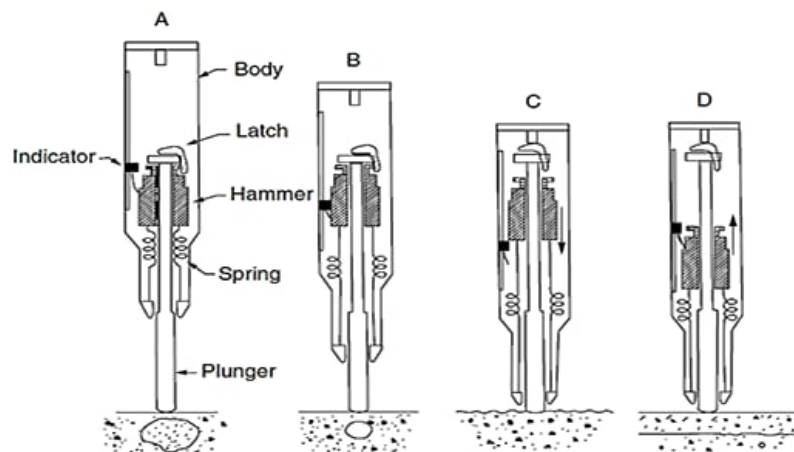
Figure 2.16: Principle of the rebound hammer [38].

There are two types of rebound numbers, depending on the hammer used, and it is important to highlight their differences. The older rebound hammers report the so-called R-value, which is the classic rebound number. These devices rely on the mechanical travel of the mallet on rebound, making them susceptible to friction losses, aging, and the direction of impact. In contrast, newer developments introduced the Q-value, measurable using an "optical" rebound hammer. The key distinction is that the optical rebound hammer records the velocity before and after impact. The Q-value is then the ratio between the rebound velocity and inbound velocity, mitigating the impact of friction losses. While an empirical relation between R- and Q-values has been identified for rock samples, a similar correlation has not yet been established for concrete [47]. A conversion factor of $\pm\,10$ units was found to be appropriate for all but the softest rock types with Q-values lower than 40.

Data acquisition
Measuring the rebound number in-situ is a straightforward process, and optimal results are achieved on a smooth surface. It's noteworthy that using a Q-type rebound hammer

eliminates concerns about the orientation of the hammer relative to the surface. Depending on the specific code or guideline, it is recommended to conduct 9 or 10 measurements per test region and subsequently calculate the median rebound number. This is crucial, as the intrinsic features of the rebound hammer can influence the test results. The limited area hit by the plunger increases the likelihood of encountering local irregularities [48].

Influencing factors

Several external factors and concrete properties can influence the measured rebound number. Table 2.4 provides an overview of these effects, indicating whether they tend to increase or decrease the rebound number. Determining the precise impact is challenging, as it depends on the specific device used and the combination of influencing factors.

Table 2.4: Effect of external factors and concrete properties on the rebound number.

Increased factor	Effect on rebound number	References
Relative humidity	Undocumented[a]	
Moisture content	Decrease	[49]
Temperature	No effect[b]	
Porosity	Decrease	[34]
w/c ratio	Decrease	[34, 49]
Compressive strength	Increase	[34, 49]
Chloride content	No effect	[34]
Carbonation depth	Increase	[34, 49]

[a] The effect of the relative humidity on the rebound number is not well documented in literature. When the relative humidity is around 50% the carbonation rate is the highest as presented in Figure 2.5. One could argue that in that case an increase of the rebound number is to be expected in the longer term.

[b] For daily temperature variations, there is no significant effect reported in the literature. However, at elevated temperatures exceeding 600°C, a notable decrease in rebound number is observed. This reduction can be correlated with a decrease in compressive strength [50].

It must also be noted that other factors such as the presence of surface coatings, orientation of the surface (in case of a R-type rebound hammer), type of aggregates, type of cement and age of concrete can influence the results [51].

Codes and guidelines
The current applicable codes and guidelines for using the rebound hammer on concrete structures are detailed in Table 2.5.

Table 2.5: Codes and guidelines for the rebound hammer.

Standard	Description
ISO 1920-7	"Testing of concrete - Part 7: Non-destructive tests on hardened concrete (Chapter 3)"
EN 12504-2	"Testing concrete in structures - Part 2: Determination of rebound number"
ASTM C805	"Standard Test Method for Rebound Number of Hardened Concrete"

2.7.6 Concrete resistivity

Resistivity provides an indication of the material's ability to transport electrical charges through the material. It is an intrinsic property and therefore independent of the geometry. The four-point probe, commonly known as the *Wenner probe*, is the most widely used tool for measuring electrical resistivity in concrete. A current is applied between the outer probes and the potential difference is measured between the inner electrodes (Figure 2.17). The resistance calculated from the four-point measurement can be converted to resistivity when the equal probe distance is known. The obtained resistivity is in reality an apparent resistivity which is an average of the resistivity distribution in the investigated concrete volume [27].

$$\rho_a = 2\pi aR \tag{2.33}$$

where:

ρ_a = apparent resistivity (Ω·m)
R = resistance (Ω)
a = probe distance (m)

By identifying areas of low resistivity, the Wenner probe helps pinpoint the most permeable spots within the concrete, indicating where corrosion may occur more rapidly. However, it's important to note that it cannot determine whether the reinforcement steel is active or passive. Areas with low resistivity indicate a higher corrosion rate, especially in regions where depassivation has occurred. Also, the preparation of the concrete surface for measurement is crucial. Extensive pre-wetting is not recommended as it can alter the bulk resistivity of the material. Instead, using wet sponges without allowing water film formation on the surface is preferred. Wetting the sponge frequently may be necessary as concrete can absorb water over time. An average decrease of resistance of 6% for three measurements was observed when using wet sponges [52].
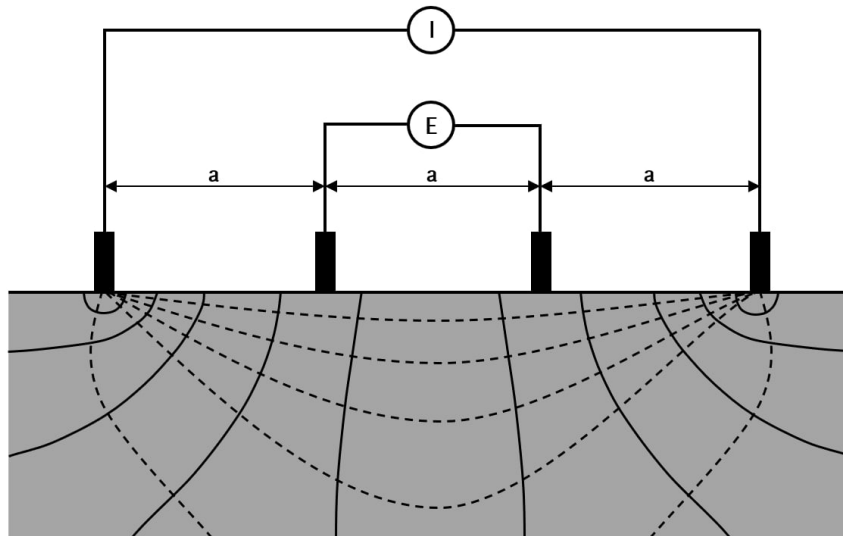
Figure 2.17: Wenner probe technique.

Data acquisition

To achieve accurate measurements with the Wenner probe, it is essential to position it as far from the reinforcement as possible, preferably within the reinforcement mesh at a diagonal angle (Figure 2.18). If this isn't possible, measuring perpendicularly over the reinforcement is the best alternative. It is suggested to take five readings and then determine the median from these measurements; this will serve as the representative resistivity for that location [53]. Additionally, it's recommended to avoid measuring near the edges of the structure, as resistivity values tend to be overestimated in those areas. A common sample spacing would be a 1 m square grid. In the case of a smaller structure, a grid spacing as small as 0.5 m can be employed, though there's usually no practical advantage in going any smaller than this. Starting with a coarse spacing first and subsequently performing a more in-depth survey of areas of concern is the most useful strategy [54].

For OPC concrete at a temperature of 20°C, widely accepted guidelines correlating resistivity with the likelihood of corrosion are presented in Table 2.6. Note that these values must be corrected for a different concrete composition and temperature.

Table 2.6: Probability of corrosion for different ranges of resistivity in OPC concrete at 20°C [53].

Resistivity ($\Omega \cdot$ m)	Concrete condition	Probability of corrosion
>1000	Dry	Negligible
>500 – 1000	Moderately dry	Low
100 – 500	Wet	Moderate
<100	Wet and a high porosity	High

Before comparing the results with the ranges in Table 2.6, it is crucial to adjust the measurements for the temperature influence. An empirical approach is necessary, and the simplest method involves applying a linear correction factor of 3% per degree Celsius. The temperature influence is more significant than the moisture related influences, as

temperature fluctuations occur more rapidly compared to changes in humidity over the same period of time [54].
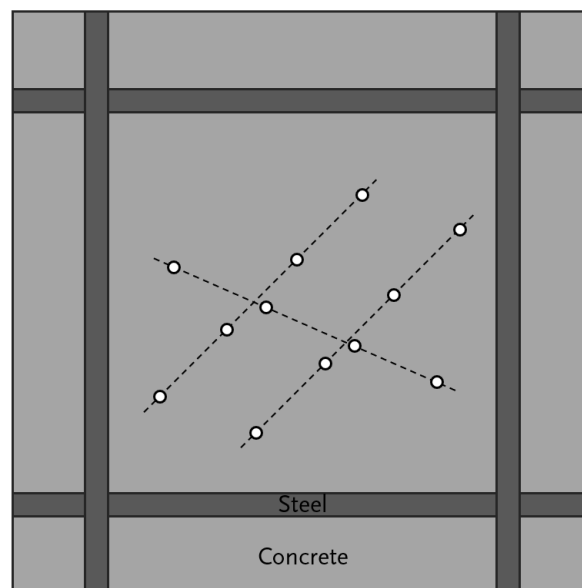
Figure 2.18: Preferred positioning of the Wenner probe.

Influencing factors

Localised effects on resistivity can be quite pronounced. When the concrete surface undergoes carbonation or drying out, it typically exhibits higher resistivity values. Conversely, after a period of rainfall, the surface resistivity may temporarily decrease compared to the bulk resistivity. Several external factors and concrete properties can influence the measured resistivity. Table 2.8 provides an overview of these effects, indicating whether they tend to increase or decrease the resistivity. Determining the precise impact is challenging, as it depends on the specific device used and the combination of influencing factors.

Codes and guidelines

The current applicable codes and guidelines for using the Wenner probe on concrete structures are detailed in Table 2.7.

Table 2.7: Codes and guidelines for resistivity measurements.

Standard	Description
RILEM TC 154-EMC	"Electrochemical techniques for measuring metallic corrosion in concrete: Test methods for on site measurements of resistivity of concrete"
AASHTO T 358	"Standard method of Test for Surface Resistivity Indication of Concrete's Ability to Resist Chloride Ion Penetration"

Table 2.8: Effects of external factors and concrete properties on concrete resistivity.

Increased factor	Effect on resistivity	References
Relative humidity	Decrease	[10, 27]
Moisture content	Decrease	[27, 34]
Temperature	Decrease[a]	[10, 27, 34, 53]
Porosity	Decrease[b]	[27, 53]
w/c ratio	Decrease	[10, 27, 34, 53, 55]
Compressive strength	Increase	[34, 55]
Chloride content	Decrease	[10, 34, 53]
Carbonation depth	Increase	[10, 27, 34, 53]

[a] It can be assumed that a change in resistivity of 3% in saturated concrete and 5% in dry concrete occurs for each one-degree Kelvin change in temperature. It is therefore recommended to refrain from conducting resistivity measurements during extremely hot or cold weather conditions [53].

[b] [34] reports an increase of resistivity with an increase of porosity, which is not in line with the other references.

2.7.7   Half-cell potential

In order to perform half-cell potential measurements, a reference electrode is connected to a high-impedance voltmeter, which, in turn, is linked to the reinforcement. In this way, potential differences can be obtained against the reference electrode which can be used to assess the risk of corrosion. Table 2.9 provides an overview of some common reference electrodes along with their potential against the standard hydrogen electrode (SHE). The saturated calomel electrode is not used anymore in-situ due to the presence of the poisonous mercury.

Table 2.9: Different reference electrodes for half-cell potential measurements [56].

Reference electrode	Name	Electrolyte	Potential vs. SHE
$Cu/CuSO_4$	Copper-copper sulfate	Saturated $Cu/CuSO_4$	+0.318 V
$Ag/AgCl$	Silver-silver chloride	1M KCl	+0.222 V
Hg/Hg_2Cl_2	Saturated calomel	Saturated KCl	+0.241 V

With macrocell or localised corrosion, a nuanced approach is necessary. In these cases, the measured potential does not represent the true corrosion potential due to the influence of an ohmic drop (IR-drop). Instead, it reflects a mixed value, dependent on the electrode's position and resistivity of concrete [57]. The most negative value always indicates the local anode.
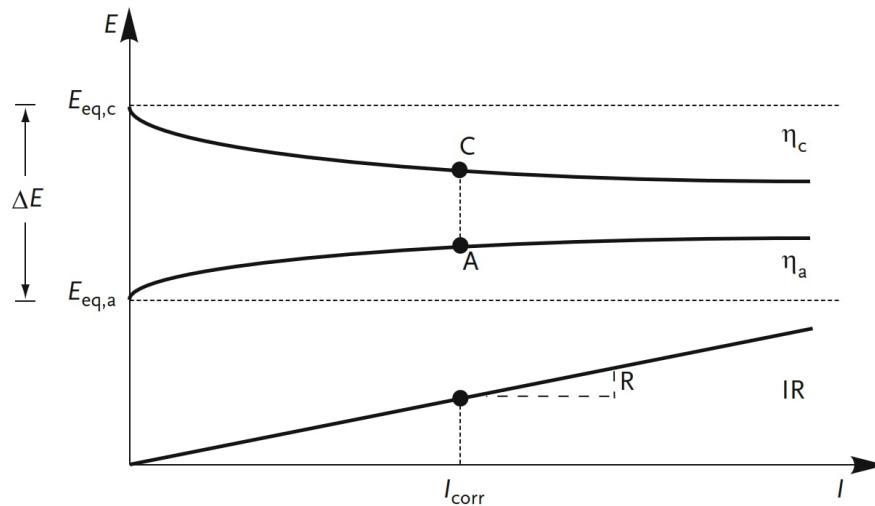
Figure 2.19: Effect of an ohmic drop in the electrolyte [57].

Practical experiences have provided valuable insights. For instance, concrete containing GGBFS concrete generally results in more negative potentials compared to OPC concrete [58]. Additionally, when dealing with buried concrete, potential values are typically low due to reduced oxygen presence. Therefore, it's important not to misinterpret adjacent rebars near buried or submerged ones as corroding rebars. In such cases, the cathodic current density may be too low to sustain the passive film, causing the steel to behave actively but with an exceedingly low current density.

Data acquisition
Before performing half-cell potential measurements, electrical continuity must be ensured (<1Ω excluding cable resistance). Depending on the volume to be inspected a choice can be made between point electrodes or wheel electrodes. Wheel electrodes are particularly effective in generating potential maps, but when measuring horizontal surfaces from the bottom, it's essential to guarantee a sufficient supply of electrolyte. Additionally, one must be cautious of the potential drift phenomenon associated with wheel electrodes, stemming from localized changes in moisture content due to water ingress into dry concrete. However, this effect can be disregarded if it stays below 20 mV/minute. Maintaining the sponge in a regularly wet and clean state is crucial, but overwetting should be prevented.

To assess the probability of corrosion, Table 2.10 can be a useful reference, although attention to environmental conditions is key. Ensuring a surrounding temperature exceeding +2°C is important for accurate readings. The temperature dependence of the electrodes is negligible and has no practical influence on the in-situ readings [58]. Interpreting data becomes particularly challenging with high-resistive surface layers. In such cases, it is advisable to focus on local minima and gradients rather than fixating on absolute values.

Table 2.10:   Probability of corrosion for different potential ranges vs.
Cu/CuSO$_4$ electrode in OPC concrete.

Potential vs. CSE (mV)	Probability of corrosion
>−200	Negligible / Low (<10%)
Between −200 and −350	Moderate
<−350	High (>90%)

It's important to note that these measurements are influenced by various factors such as moisture content, cover depth, resistivity, temperature, oxygen content and the presence of surface coatings. Concrete that has undergone carbonation tends to yield more positive potentials, and in the case of wet concrete, more negative potentials are obtained as illustrated in Figure 2.20. However, these changes in potential due to a changing moisture content do not necessarily affect potential gradients or the location of corroding spots in a structure [58].
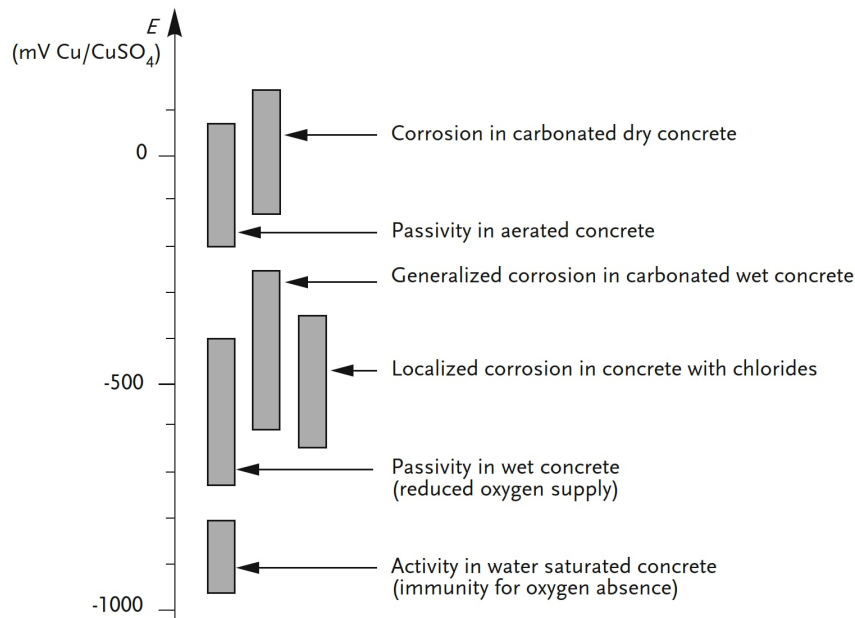
Figure 2.20: Typical potential ranges for reinforcement steel under different conditions [57].

Influencing factors

Several external factors and concrete properties can influence the measured potential. Table 2.11 provides an overview of these effects, indicating whether they tend to increase or decrease the potential. Determining the precise impact is challenging, as it depends on the specific device used and the combination of influencing factors.

Table 2.11: Effects of external factors and concrete properties on the measured potential.

Increased factor	Effect on potential	References
Relative humidity	Decrease	[59]
Moisture content	Decrease	[10, 58, 60]
Temperature	Decrease	[59]
Porosity	Undocumented[a]	
w/c ratio	Undocumented[a]	
Compressive strength	Increase	[60]
Chloride content	Decrease	[10, 59, 60]
Carbonation depth	Increase[b]	[10]

[a] The impact of porosity and w/c ratio on the potential is not well-documented, but a higher w/c ratio likely reduces potential due to increased water content. Increased porosity also lowers the potential in saturated concrete.

[b] Even though corrosion can be carbonation induced due to an increase in pH (refer to Section 2.3). Carbonation of the surface can increase the potential due to surface densification.

Codes and guidelines

The current applicable codes and guidelines for performing half-cell potential measurements on concrete structures are detailed in Table 2.12.

Table 2.12: Codes and guidelines for half-cell potential measurements.

Standard	Description
RILEM TC 154-EMC	"Electrochemical techniques for measuring metallic corrosion in concrete: Potential mapping on reinforced concrete structures"
ASTM C876	"Standard Test Method for Corrosion Potentials of Uncoated Reinforcing Steel in Concrete"

2.7.8 Corrosion current density

Section 2.5 presented an extensive examination of corrosion current density and the linear polarisation method. In the context of large structures, applying current to the reinforcement can result in a non-uniform distribution of this current. However, achieving a uniform current distribution is essential for the proper application of the linear polarisation method. To address this challenge, the *modulated confinement method* proves to be a viable solution. To counterbalance the electrical field, two reference electrodes are strategically positioned between the central counter electrode and the external guard ring. These electrodes play a crucial role in monitoring the external ring continuously, detecting current lines originating from the central counter electrode. This detection allows for real-time adjustments, ensuring that the current lines fall within the predetermined area. This precise confinement facilitates accurate calculations of the polarisation resistance. Additionally, the equipment is designed to automatically compensate for potential drops attributed to the electrical resistance of the concrete [61].
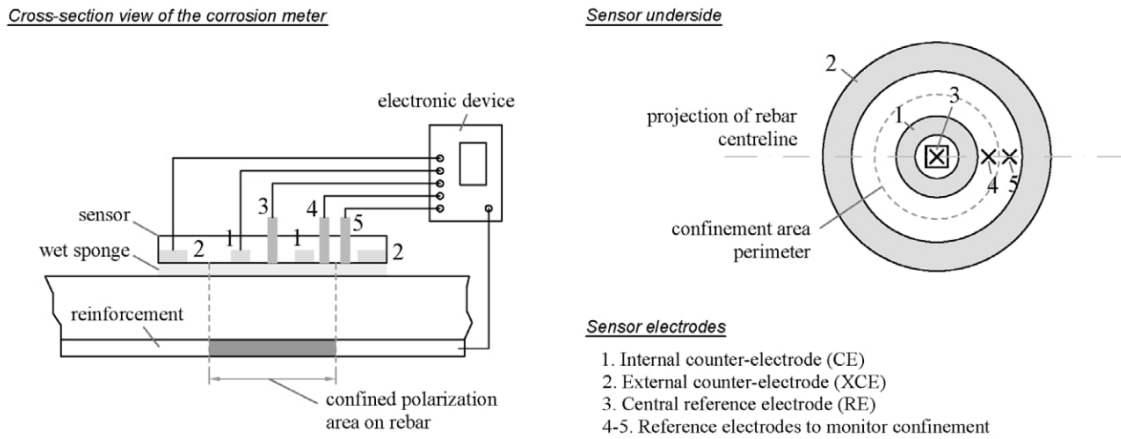
Figure 2.21: Schematic representation of the modulated confinement probe
[62].

Equation 2.19 must be modified in order to account for the area of the rebar that is being polarised.

$$i_{corr} = \frac{B}{R_p \cdot A} \tag{2.34}$$

The linear polarisation resistance and polarised area are determined by the device according to:

$$R_p = \frac{E_{max} - E_\Omega}{I_a} = \frac{E_{pol}}{I_a} \tag{2.35}$$

$$A = L_{pol} \cdot \pi \cdot \varnothing \tag{2.36}$$

Here the ohmic drop is related to the electrical resistance of concrete.

$$R_c = \frac{E_\Omega}{I_a} \tag{2.37}$$

where:

i_{corr} = corrosion current density (μA/cm^2)
B = Stern-Geary constant (mV)
R_p = linear polarisation resistance (kΩ)
A = polarised area (cm^2)
E_{max} = maximum polarisation (mV)
E_Ω = ohmic drop (mV)
E_{pol} = rebar polarisation (mV)
I_a = applied current (μA)
R_c = concrete electrical resistance (kΩ)

Data acquisition
When performing in-situ corrosion current density measurements with a modulated confinement probe, various factors must be considered. Firstly, knowledge of the diameter of the rebar under inspection is essential. It's crucial to wet the sponge adequately without overwetting it. The pulse duration selection is a sensitive parameter, with suggested values being 30 seconds for an active rebar and 100 seconds for a passive rebar [62]. Selecting an inappropriate pulse duration may result in an underestimation of the corrosion current density. This aspect can be challenging since the nature of the rebar (active or passive) is typically unknown beforehand, which is the primary reason for investigating the structure in the first place. The time-consuming aspect may make the in-situ use of a confinement probe undesirable. Chapter 4 therefore addresses a potential strategy to tackle these issues.

The values presented in Table 2.13 can be used as a guideline for estimating the probability of corrosion. It's important to reiterate that this kinetic parameter is the only way of gaining insights into the speed of corrosion process.

Table 2.13: Probability of corrosion for different ranges of corrosion current density in OPC concrete [61].

Corrosion current density (μA/cm^2)	Probability of corrosion
<0.1	Negligible
0.1 - 0.5	Low
0.5 - 1	Moderate
>1	High

Influencing factors
Several external factors and concrete properties can influence the measured corrosion current density. Determining the precise impact is challenging, as it depends on the specific device used and the combination of influencing factors. Since there are limited corrosion current density devices readily accessible for in-situ use, their documentation in the literature is not extensive. While the corrosion current density and half-cell potential measurements share influencing factors, there isn't a direct mathematical relationship between the two, as they are influenced in varying proportions. An increase of chloride content resulted in an increased corrosion current density, particularly when it reached the steel surface and led to depassivation [61]. Furthermore, based on the observations provided in

Appendix B, the corrosion current density sometimes doubled when measuring a concrete beam under dry conditions compared to wet conditions.

In the context of in-situ inspection with a corrosion current density device, the environment plays a key role. According to [63], measurements on a bridge in Spain suggested that, generally, an increase in temperature leads to higher corrosion current density. However, it was observed that values at the same location could be higher in winter than in summer due to moisture evaporation and concrete drying.

Codes and guidelines
As of now, the only existing guideline for the linear polarization method is provided by RILEM, specifically in RILEM TC 154-EMC: "Electrochemical techniques for measuring metallic corrosion in concrete: Test methods for on-site corrosion rate measurement of steel reinforcement in concrete by means of the polarization resistance method".

2.7.9   Handheld X-ray fluorescence (HXRF)

A handheld X-ray fluorescence device is a qualitative and semi-quantitative technique that uses the fluorescence properties of materials for the analysis of their chemical composition. For a detailed look on this method and its application, reference is made to the research of Laura Sofía Gómez Jaramillo [64]. Part of the measurements in her research were performed on the Sluinerweg viaduct.

2.7.10   SonReb models

For a more accurate assessment of compressive strength using NDTs, it is possible to combine the UPV and rebound hammer with compressive strength tests on core or cube samples. This approach is commonly referred to as the *Sonic Rebound* or *SonReb* method. The main goal is to minimize the requirement for drilling cores in-situ. There are numerous SonReb regression models described in the literature, many of which have been developed in controlled laboratory environments. Among the most prevalent model types are linear, polynomial, and power models. Table 2.14 gives an overview of some models found in literature. In general, the authors have concluded that the combination of UPV with the rebound hammer yields a better correlation with compressive strength than either method used alone.

Table 2.14: SonReb models.

Author	Year	Model $f_{ck,cube} =$	Ranges	No. of samples	Calibration method
RILEM [42]	1993	$9.27 \cdot 10^{-11} V^{2.6} R^{1.4}$	f_{cube}: - V: 3000 - 4800 m/s R: 16 - 49	-	Cubes
Kheder [65]	1999	$0.0158 V^{0.4254} R^{1.1171}$	f_{cube}: 12.9 - 52.1 MPa V: 2587 - 5212 m/s R: 18.5 - 44.1	103	Cubes[a]
Menditto et al. [66]	2004	$0.00004 V^{0.80840} R^{1.88148}$	f_{cube}: 2.3 - 107.3 MPa V: 2350 - 4850 m/s R: 12.2 - 61	1000	Cubes
Hobbs and Kebir [67]	2007	$-173.033 - 4.069 V^2 + 57.693V$ $+ 1.307R$	f_{cube}: 19.5 - 49.5 MPa V: 3.95 - 4.45 km/s R: 22.5 - 36.5	25	Cubes
Faella et al. [68]	2011	(a) $2.6199 \cdot 10^{-8} V^{2.2878} R^{0.5341}$ (b) $-34.51583 + 0.01385V + 0.26511R$	f_{core}: 6.97 - 39.8 MPa V_{mean}: 3243 m/s (std = 637) R_{mean}: 34.8 (std = 4.84)	-	Cores[b]
Shih et al. [69]	2015	$f_{cyl} = 0.0182V + 1.25733R - 65.387$	f_{cyl}: 24.2 - 33.6 MPa V: - R: -	95	Cylinders
Benyahia et al. [70]	2017	(a) $0.0806 V^{2.1547} R^{0.7496}$ (b) $0.0435 V^{1.5672} R^{1.1892}$ (c) $0.0634 V^{1.1202} R^{1.2392}$	f_{cube}: 10 - 45 MPa V: 3 - 5 km/s R: 20 - 40	204	Cubes
Abbaszadeh et al. [71]	2018	$f_{c,is} =$ (a) $-61.22V + 3.855V^2 + 1.7R-$ $0.06R^2 + 0.934RV + 91.24$ (b) $-28.72V + 6.65V^2 + 0.96Q+$ $0.016Q^2 - 0.45QV + 37.85$	f_{core}: 15 - 45 MPa V: 3.10 - 4.85 km/s R: 29 - 45 Q: 38 - 58	45	Cores[c]
Bingöl and Çavdar [72]	2018	$-34.21 + 0.009V + 0.952R$	f_{cube}: 27 - 51 MPa V: 4674 - 5106 m/s R: 20 - 36	101	Cubes
Chandak and Kumavat [73]	2020	$0.0841 R^{-0.572} V^{0.945}$	f_{cube}: 19.4 - 37.2 MPa V: 2220 - 4388 m/s R: 25.8 - 34.9	27	Cubes
Cristofaro et al. [74]	2020	(a) $-28.44 + 0.01174V + 0.370R$ (b) $41.59 - 0.02181V - 0.859R+$ $5.808 \cdot 10^{-6} V^2 + 0.01539R^2$ (c) $10^{-4.251} V^{1.281} R^{0.686}$ (d) $1.974 e^{0.000542V} e^{0.01605R}$ (e) $26.74 \ln(V) + 15.67 \ln(R) - 249.21$	f_{core}: 6.4 - 44.5 MPa V: 2208 - 4135 m/s R: 24.1 - 52.8	78	Cores[d]
Al-Neshawy et al. [75]	2023	$f_c =$ (a) $0.32035 V^{0.49282} R^{0.27346}$ (b) $0.0507 V^{0.6138} Q^{0.467}$	f_{core}: 39 - 49 MPa V: - R: - Q: -	12	Cores[e]

[a] Incorporates different densities.
[b] Converted to cube strength.
[c] In-situ compressive strength according to EN 13791, with cores drilled from a building.
[d] One of the few models that provides a clear description of the conversion procedure to cube strength.
[e] Equivalent compressive strength according to ACI-214, with cores drilled from a mockup wall.

Essentially, a SonReb model is a representation of a surface in 3D space. However, interpreting a 3D graph can be challenging, so it is practical to transform it into an isoquant map. This allows one to read compressive strength values within a 2D plot. In Figure 2.22, an example is provided for the model by Menditto et al. [66].
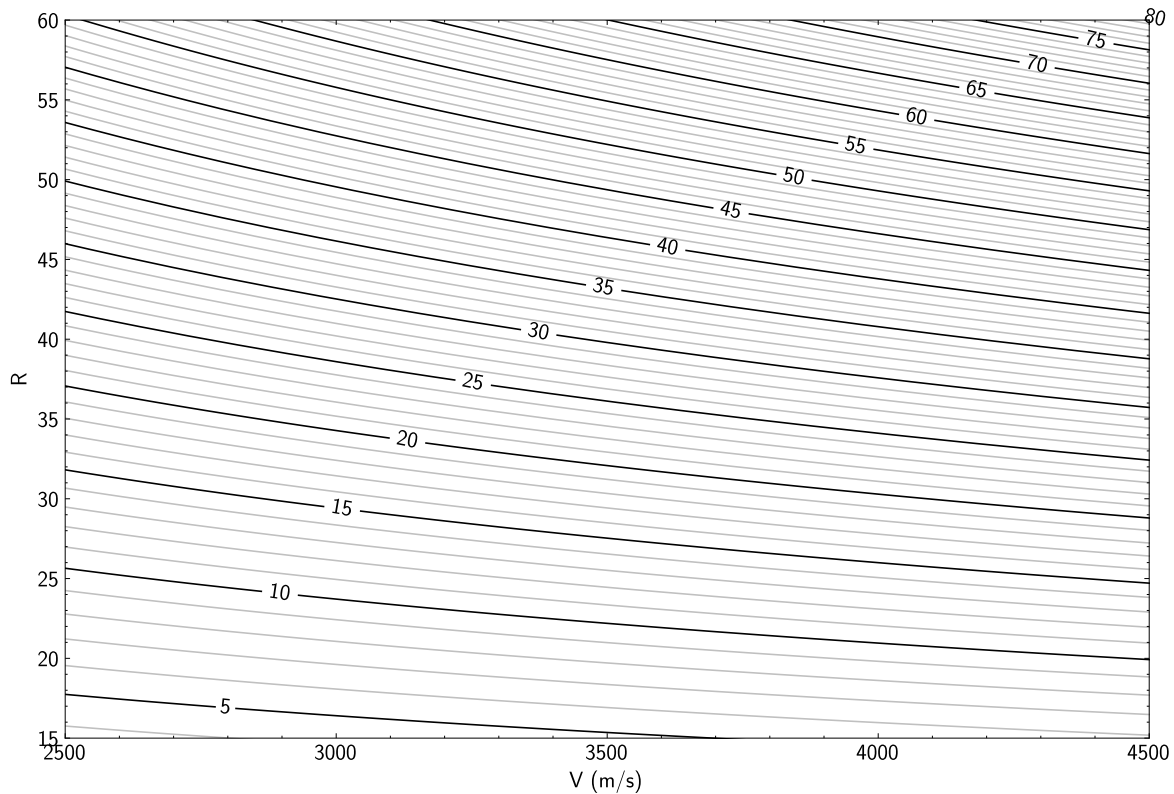
Figure 2.22: Example of an isoquant map of the SonReb model by Menditto
et al. [66].

The extensive literature review on SonReb models highlights several limitations:

- The majority of models rely on laboratory concrete, posing difficulties in comparing them to in-situ concrete. Additionally, the authors have conducted limited comparisons with real structures.
- Frequently, important details are absent, such as whether the rebound hammer used was R-type or Q-type, the sample type used, the number and age of samples, the mix design, humidity conditions, carbonation status, and specifics about the compressive strength test protocol.

None of the considered models contain all the necessary information, rendering the in-situ application of SonReb models impractical due to substantial uncertainty.

2.8   Coring

The most common type of destructive testing involves coring of a structure, with subsequent analysis of these cores in a laboratory to assess various properties. This research specifically emphasises the significance of evaluating compressive strength, carbonation depth, and chloride content.

2.8.1 General considerations

Before determining the number of cores and their locations, it's essential to consider certain factors. Core placements should be within zones that accurately represent the average conditions of the concrete, considering influences such as casting and aging effects. Breysse and Balayssac provide valuable coring recommendations, as outlined in their work [34].

- Take into account the various structural members and stress conditions.
- Ensure coring is performed at a safe distance from joints and corners to avoid compromising structural stability.
- Ensure cores don't contain reinforcement.
- Cold areas, construction joints or macro-cracked areas must be avoided.

An even more effective approach is *conditional coring*, where core locations are determined after using NDTs. This method not only minimises the number of cores required but also doesn't necessarily increase costs. However, it is important to ensure the reliability of the NDT measurements themselves.

2.8.2 Compressive strength

There exist different models to determine the in-situ compressive strength from a core such as the methods described in ACI-214 [76] and EN 13791 [46]. Rijkswaterstaat had their own method for assessing the in-situ compressive strength in the past. However, in the newest version of the RBK [77], reference is made to EN 13791.

ACI-214
The equivalent in-situ compressive strength can be calculated according to:

$$f_c = F_{l/d} F_{dia} F_{mc} F_d f_{core} \tag{2.38}$$

The overall standard deviation s_o is based on the sample standard deviation s_c and the standard deviation due to the applied strength correction factors s_a.

$$s_o = \sqrt{s_c{}^2 + s_a{}^2} \tag{2.39}$$

$$s_c = \sqrt{\frac{\sum_{i=1}^{n} \left(f_{ci} - \bar{f_c}\right)^2}{n-1}} \tag{2.40}$$

$$s_a = \bar{f_c} \sqrt{V_{l/d}^2 + V_{dia}^2 + V_{mc}^2 + V_d^2} \tag{2.41}$$

From the value of f_c it is possible to calculate the 10% fractile of the in-situ strength $f'_{c,\text{eq}}$. The strength correction factors and their coefficients of variation can be found in Appendix A.4.

EN 13791

Initially, the in-situ compressive strength is denoted as $f_{c,is}$. When the core has a length-to-diameter ratio of 1:1 and needs to be converted into a 2:1 core, the measured in-situ compressive strength must be multiplied by a core length factor (CLF). In the case of normal-weight concrete, the CLF is standardised at 0.82.

$$f_{c,is} = f_{c,core} \cdot CLF \tag{2.42}$$

Following this, the mean and standard deviation can be calculated.

$$f_{c,m(n)is} = \frac{\sum_{i=1}^{n} f_{c,is}}{n} \tag{2.43}$$

$$s_c = \sqrt{\frac{\sum_{i=1}^{n} \left(f_{c,is} - f_{c,m(n)is} \right)^2}{n-1}} \tag{2.44}$$

The guideline specifies that the sample standard deviation should be utilized only when it exceeds a threshold that yields a coefficient of variation of 8%.

$$s = \max\{s_c;\ 0.08 \cdot f_{c,m(n)is}\} \tag{2.45}$$

Finally, the characteristic compressive strength can be determined using Equation 2.46. The values for k_n and M can be found in Appendix A.4.

$$f_{ck,is} = \min\{f_{c,m(n)is} - k_n s;\ f_{c,is,lowest} + M\} \tag{2.46}$$

The Grubbs test can be used for testing outliers:

$$\frac{f_{c,is,highest} - f_{c,m(n)is}}{s} > G_p \tag{2.47a}$$

$$\frac{f_{c,m(n)is} - f_{c,is,lowest}}{s} > G_p \tag{2.47b}$$

2.8.3   Carbonation depth

The determination of carbonation depth can be carried out either in-situ or in the laboratory. The procedure for assessing carbonation depth in hardened concrete, using a phenolphthalein solution, is outlined in EN 14630 [78]. Further details on this method, particularly its application to the Sluinerweg viaduct, are provided in Chapter 4.

2.8.4   Chloride content

The rapid chloride ion penetration test (RCPT) is described in ASTM C1202 [79]. This test offers a quick estimation of the chloride ion penetrability by applying an electrical field. A

variation of this test, the rapid chloride migration test (RCM) can be used to determine the non-steady state chloride migration coefficient, which also takes into account the binding of chlorides to the cement phases. However, to accurately determine the actual chloride content in a core sample, titration is necessary, particularly the Volhard method. This method is explained in detail in Section 4.3.3 for the case of the Sluinerweg viaduct.

2.9 Cathodic protection

The principle of cathodic protection lies within suppressing the anodic reaction occurring at the reinforcement by applying an external current. The flow of current can be made by connecting the reinforcement to a negative terminal and an electrode to the positive terminal. The reinforcement is therefore made the cathode of the electrochemical cell. This principle is illustrated in Figure 2.23, where the potential is shifted from E_{corr} to a lower potential $E_{eq,a}$ by means of an external current i_{ext}.
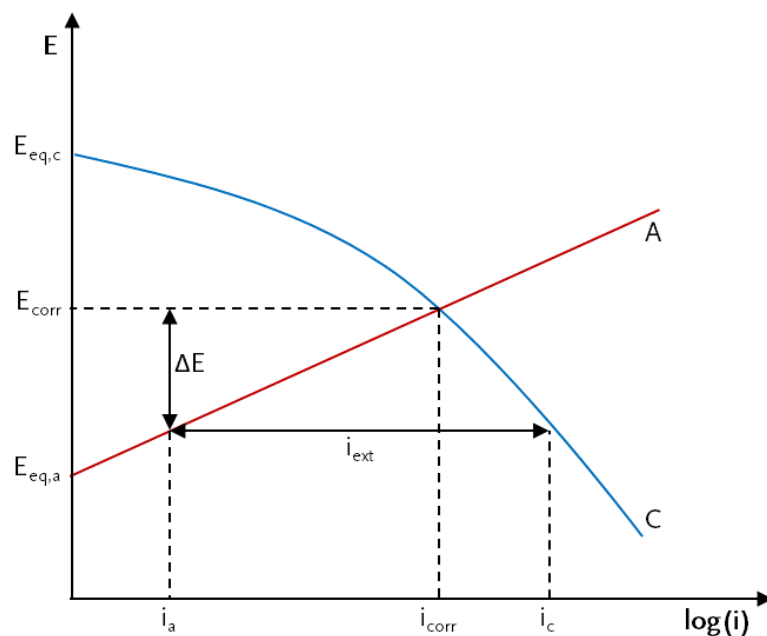
Figure 2.23: Schematic representation of the effect of cathodic protection (adapted from [18]).

Cathodic protection is widely used in underground pipelines and marine structures, but also in concrete bridges. Different situations require specific solutions. There are two main types of cathodic protection systems: galvanic anodes and impressed current.

2.9.1 Galvanic anodes cathodic protection (GACP)

Galvanic anodes cathodic protection relies on the installation of a more reactive metal, known as a galvanic anode or sacrificial anode, to protect the target metal structure from corrosion. The galvanic anode is typically made of a metal alloy with a more negative electrochemical potential than the metal it is protecting. The difference in natural potential

is therefore the driving force of a galvanic anodes cathodic protection system. In reinforce concrete structures, the reinforcement turns into a cathode and negatively charged hydroxyl ions are formed according to Equation 2.2 resulting in the passivation of the reinforcement. One of the main disadvantages of the galvanic anode system is the limited driving voltage. A zinc anode for example is limited to a maximum driving voltage of 0.7 V when coupled to reinforcement [80]. This type of cathodic protection is mainly used with marine structures or in the offshore industry.

2.9.2   Impressed current cathodic protection (ICCP)

Instead of relying on sacrificial anodes, impressed current cathodic protection systems rely on an external power source to generate an electrical current to protect the metal structure. A low-voltage direct current (typically 2V to 8V) is delivered to the negative pole (the reinforcement), while the positive pole is connected to an anode. Preferably, this is an inert anode that does not oxidise itself, such as platinum-coated titanium.

Impressed current and galvanic anode cathodic protection systems each have their own advantages and disadvantages, and the choice between them depends on the specific application. Table 2.15 provides an overview of these factors.

Table 2.15: Advantages and disadvantages of GACP and ICCP systems
(adapted from [57]).

	GACP	ICCP
Advantages		
	• Feeding power not required. • Current adjustment not required. • Easy and almost inexpensive installation. • No stray current arising. • No maintenance costs required. • Almost uniform current distribution. • Additional areas not required around facilities.	• Voltages and currents can vary. • High current output if necessary. • A single groundbed can protect large surface structure. • Suitable for high resistivity environments. • Effective for protecting bare or badly coated structures.
Disadvantages		
	• Low driving voltage. • Low current output. • Costly installation post-commissioning. • Bare or badly coated structures require many anodes. • Unsuitable in high resistivity environments.	• Stray current problems. • Subject to vandalism. • Maintenance necessary. • Need of feeding. • Operating cost. • Overprotection risks. • Cable and connection failure risks. • Additional areas required around facilities.

2.9.3   Anode systems

With every cathodic protection system, an even distribution of protection current is essential. A non-uniform distribution may result in over- or underprotection. There are various

types of anode systems for current distribution, with three of the most common being activated titanium, conductive coatings, and galvanic anodes.

Activated titanium

Activated titanium is typically titanium coated with noble metal oxides, known as Mixed Metal Oxides (MMO) [81]. It can be applied using either titanium mesh or titanium strips. The activated titanium meshes or strips are connected to primary anodes, which are typically strips or wires of plain titanium. An example of a connection between a titanium mesh with titanium strips as primary anodes is shown in Figure 2.24.

Figure 2.24: Connection between isolated copper cable, titanium mesh and plain titanium strip welded in-situ [81].

Conductive coatings

Conductive coatings consist of a binder filled with carbon particles, which provide conductivity and result in a black color. Another coating can be applied over the conductive coating to provide protection against wind, UV radiation, and to enhance aesthetic appeal. Primary anodes, typically made of copper or titanium wire coated with platinum, are embedded in the conductive coatings. An example of such a system is presented in Section 3.3.5, detailing its application on the Sluinerweg viaduct.

Galvanic anodes

Galvanic anodes for reinforced concrete structures are typically zinc-based, requiring an activator to remain active and prevent passivation [18]. Zinc anodes can be applied in various forms, including foil with a hydrogel adhesive for attachment to concrete surfaces. They can also be sprayed onto the concrete or installed as zinc rods or meshes.

2.9.4   Control measurements

To monitor the cathodic protection system, various reference electrodes are often installed. There are two types: true reference electrodes and decay probes. True reference electrodes have a stable potential and can monitor the potential of the reinforcement and prestressing, but they are relatively expensive. Decay probes are suitable only for depolarisation measurements over a maximum of 24 hours, and they are relatively inexpensive. The depolarisation is measured from the instantaneous off potential, which refers to the immediate measurement of the electrode potential when the cathodic protection system is turned off as illustrated in Figure 2.25. All reference electrodes should be installed at corroding and non-corroding locations to provide the most representative data.
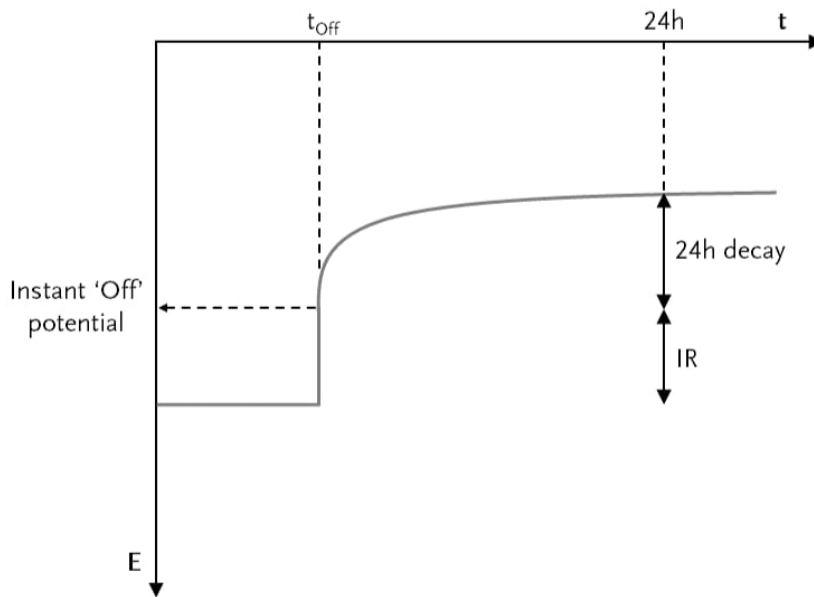
Figure 2.25: Idealised instantaneous off potential plot.

ISO 12696 [82] presents three criteria for assessing the performance of the cathodic protection system, only one criteria has to be met:

1. An instantaneous off potential more negative than -720 mV with respect to Ag/AgCl in 0.5M KCl.
2. A potential decay over a maximum of 24 h of at least 100 mV from instantaneous off.
3. A potential decay over an extended period (typically 24 hours or longer) of at least 150 mV from instantaneous off subject to continuing decay and the use of reference electrodes (not potential decay probes) for the measurement extended beyond 24 hours.

Furthermore, it is recommended that the potential should not drop below -900 mV to prevent hydrogen embrittlement of the prestressing steel. However, if the prestressing steel is already corroded, it may not have a safe potential limit, making cathodic protection impractical.

2.10 Summary of literature findings

Chloride-induced corrosion, primarily caused by the extensive use of de-icing salts and the presence of leaking joints, poses a significant risk to reinforced concrete structures in the Netherlands. This can lead to pitting corrosion, which can rapidly reduce the cross-section of reinforcement locally without causing visible cracking or spalling of the concrete, making detection challenging through visual inspection alone. Moreover, when chloride-contaminated concrete is also carbonated, the corrosion process can intensify.

GPR is a valuable tool for detecting reinforcement and prestressing in structures, capable of reaching significant depths. The dielectric constant, indicating a material's ability to store electrical energy in an electrical field, serves as an important parameter. In the Netherlands, a dielectric constant of 6 is recommended as an initial setting for reinforced concrete structures. A high moisture content can decrease the signal amplitude. While GPR shows potential for detecting corrosion, further research is needed in this area. Currently, there are no European standards for GPR, with American standards mainly focusing on subsurface investigations and asphalt-covered bridge decks.

UPV can be used to assess the quality of concrete and provide an indication of compressive strength. Direct transmission, achieved by transmitting ultrasonic pulses through the concrete using two transmitters and coupling gel, is the most accurate method. However, moisture content significantly impacts the measurements, as the speed of sound travels approximately four times faster in water than in air. The prevailing European standard for the use of UPV is EN 12404-4 [83].

UPE provides an advantage for structures with one-side access. It uses S-waves, which ares less affected by moisture content. The acoustic impedance of air causes S-waves to be reflected nearly 100%, making UPE less suitable for detecting reinforcement but effective for inspecting behind reinforcement. UPE complements GPR and together they are suitable for tendon duct inspections. Currently, there are no established codes or guidelines for this method in Europe.

The rebound hammer, measuring surface hardness, provides an indication of compressive strength. Q-type hammers measure the velocity of inbound and rebound, minimising the impact of friction losses. However, there is no conversion between R- and Q-values for concrete, unlike for rock samples. The rebound hammer readings are mainly influenced by local surface irregularities. The current standard in Europe for rebound hammer testing is EN 12504-2 [45].

Three crucial parameters for corrosion assessment in concrete structures include resistivity measured using a Wenner probe, half-cell potential, and corrosion current density. All these parameters are influenced by the moisture content. Areas prone to corrosion typically exhibit low resistivity values, low half-cell potentials, and high corrosion currents. For measuring corrosion current density using the guard ring method, a pulse duration of 30 seconds for active and 100 seconds for passive reinforcement is recommended. The most prominent guideline for these methods is RILEM TC 154-EMC [53, 58, 61].

SonReb models integrating UPV and rebound hammer data in laboratory settings, demonstrate improved estimations of compressive strength. Nevertheless, direct comparisons with in-situ concrete are challenging due to the absence of important model parameters in many existing models.

Conditional coring involves taking cores at specific locations after using NDTs. This method does not necessarily raise costs, provided the NDT results are reliable.

Chapter 3

Sluinerweg viaduct

3.1 Project liggerkoppen

In 2002, inspections conducted around the Dutch city of Apeldoorn revealed damages in several viaducts constructed using prefabricated post-tensioned T-beams. More specifically, this damage was primarily to the beam heads, referred to as 'liggerkoppen' in Dutch, which later became the project's namesake. The main cause of damage was determined to be the accelerated ingress of chlorides due to leaking joints. Considering the role of the beams and the potential consequences if the beams were to fail locally, an inventory was conducted at that time to identify other structures in the Apeldoorn district where this could also be a concern. Ultimately, Rijkswaterstaat took action on 38 structures built between 1965 and 1976 [1]. A strategy was developed for the maintenance of these beam heads and it was later decided to place cathodic protection if there existed a risk of prestressing function loss. Three rules were established for the placement of the CP system:

1. In case of immediate or long-term loss of prestressing function, initiate repairs and implement cathodic protection.
2. Include adjacent beam heads on both sides of a damaged beam head into the CP system.
3. If over half of the beam heads on a support qualify for CP, ensure that all beam heads on that support receive cathodic protection.

Between 2012 and 2014, CP was implemented on almost 1500 beam heads across the 38 different structures. A 20-year contract for the monitoring, repair, and maintenance was awarded to the consortium Mourik-Salverda.

3.2 Damage levels

Within the Liggerkoppen project, the damage to beam heads and cones of the viaducts are both categorized into five levels. These damage levels were determined by means of visual inspections using mirrors to look at the back of the beam heads. No other non-destructive or destructive tests were performed. Table 3.1 shows the five damage levels associated with the cracking and spalling of the beam heads, with level 5 representing the most severe damage. Table 3.2 shows the five damage levels associated with the cones surrounding the prestressing anchors.

Table 3.1: Damage levels for the assessment of damage to the beam heads.

Damage levels for beam heads
1 Cracks in the corners.
2 Spalling of (parts of) the corners.
3 Cracks in the corners and vertical cracks in the beam web.
4 Spalling of (parts of) the corners and beam web.
5 Spalling and or cracks beyond the support.

Table 3.2: Damage levels for the assessment of damage to the cones.

Damage levels for cones
1 Cone has cracks.
2 Cone is loose or pushed out.
3 Cone is (partially) missing.
4 Cone with corrosion damage.
5 Cone with corrosion damage and a visible tendon.

Figure 3.1: Example of a cone with corrosion damage (C4).

Based on these damage levels a risk class can be assigned. Three risk classes are distinguished for the loss of function of the prestressing as detailed in Table 3.3.

Table 3.3: Risk classes.

Risk of prestressing function loss.
R1 Long term function loss to be expected (within 10 years).
R2 Short term function loss to be expected (within 5 years).
R3 Immediate function loss to be expected (within 1 year).

3.3 Design

3.3.1 Overview

One of the viaducts within the Liggerkoppen project is the *Sluinerweg viaduct*. It is located in the Sluinerweg over the A1 highway, to the east of the city of Apeldoorn as illustrated by Figure 3.2. A side view of the viaduct captured from the *Blankenhuisweg* is presented in Figure 3.3.
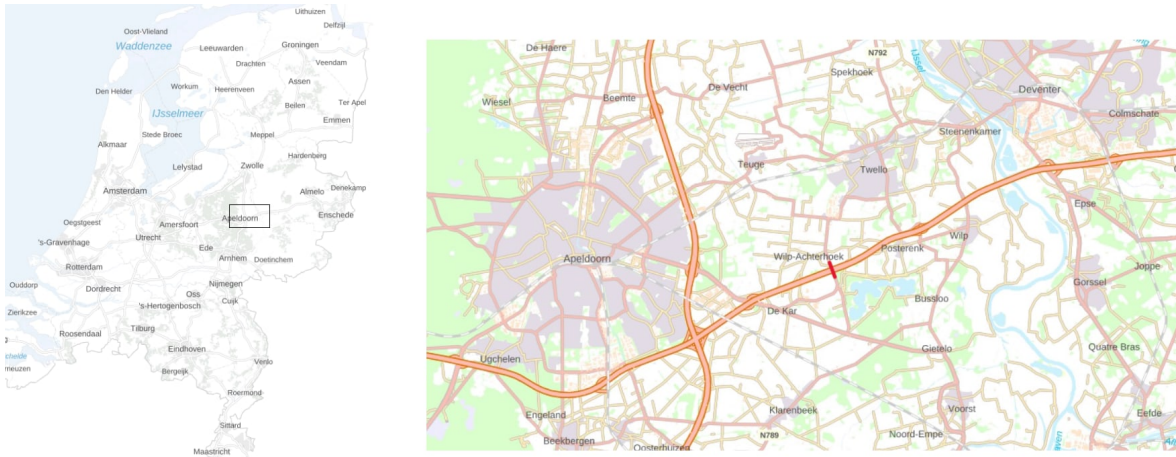
Figure 3.2: Location of the Sluinerweg viaduct over the A1 highway.

Figure 3.3: Sluinerweg viaduct as seen from the Blankenhuisweg.

The Sluinerweg viaduct was constructed in 1970 and consists of 4 spans with 5 supports (two abutments and three intermediate supports). Each span has a length of 18.95 m and contains 23 prefabricated T-beams. Additional characteristics are listed in Table 3.4. Noteworthy is the use of a KCG-layer, an abbreviation for the Dutch term *Kristal Cement Graniet* (Crystal Cement Granite). This coating was commonly applied to various structures across the Netherlands during the construction period of the Sluinerweg viaduct. It consists of a cement-based adhesive layer sprayed with granite granules. Its primary purpose is surface finishing, providing both functional and aesthetic benefits.

Table 3.4: Sluinerweg viaduct specifications.

Overview of Sluinerweg viaduct characteristics	
Year of construction	1970
Width	14.95 m
Length	76 m
Spans	4
T-beams per span	23
Reinforcement steel	FeB400
Prestressing	5 bars per beam, $4\varnothing32$ and $1\varnothing26$
	System: Dywidag
Finishing	KCG-layer

3.3.2   Structural design

The beams are post-tensioned using five bar tendons placed inside steel-sheeted tendon ducts. Each prestressing tendon has one blind end anchorage and one regular anchorage at the opposite end of the beam. The blind end anchorage is completely embedded in the concrete, at some distance from the end of the beam. The other anchorage is secured and sealed after tensioning. The sealing compound, usually mortar, forms a cone to protect the anchorage from corrosion. According to the documentation and drawings, the anchor ducts were injected after tensioning the bars. The transverse prestressing is carried out using Dywidag bar tendons as well, spaced at 400 mm centers. The anchorages of the transverse prestressing bars are located behind the edge elements.
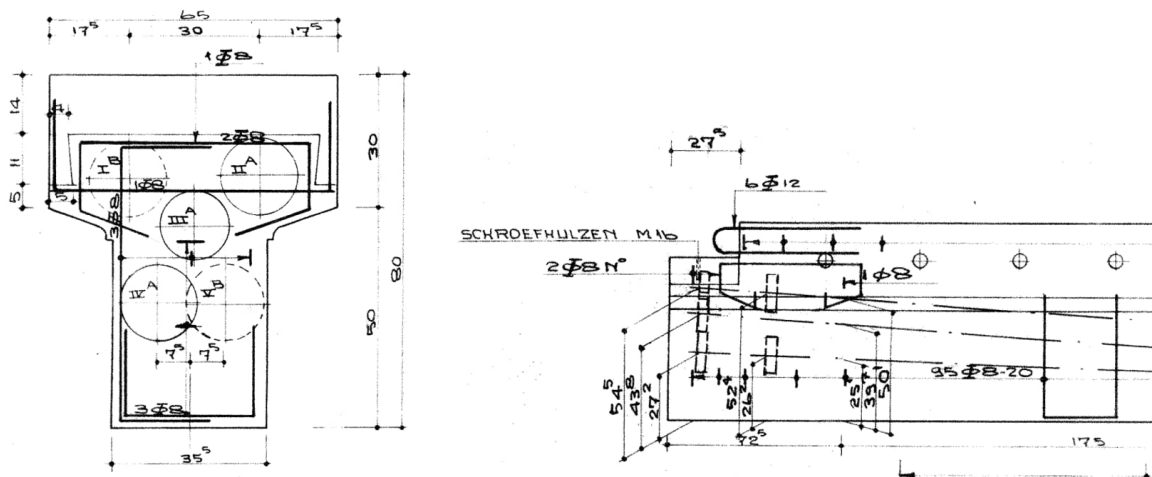
Figure 3.4: Technical drawing of the T-beams.

In 2010, Royal Haskoning conducted recalculations for two viaducts as part of the Liggerkoppen project, with a focus on structural safety. Their assessment included examining the loss of steel reinforcement and a prestressing bar tendon, with the recalculated findings then applied to similar structures. The viaduct T-beams were primarily designed with full prestressing, rendering normal reinforcement unnecessary for load-bearing. This was reaffirmed by the recalculation: reinforcement steel could theoretically corrode entirely, albeit leading to concrete cracking and spalling. The analysis demonstrated that the loss

of one prestressing bar per beam in most structures does not pose a safety risk, except for structures with three or four prestressing bars, which could potentially face unacceptable risks to the structural integrity. The most likely failure mechanism was determined to be the failure of a bar resulting from corrosion initiated by failure of the anchorage (*klokverankering*), followed by corrosion of the nut. Limited corrosion of the anchorage was deemed acceptable, considering the anchorages were over-dimensioned. Corrosion of the steel-sheeted tendon ducts was neither observed nor considered likely. The part of the tendon bar behind the nut is stress-free, although sometimes lacking sufficient concrete cover, permitting corrosion. In the so called *buigslappe voegen* (joints made of reinforced concrete), chloride exposure was assessed to be generally low making damage unlikely.

3.3.3 Dilatation joints

For the Sluinerweg viaduct, ACME joints were used, specifically ACME type 30D, which belongs to the family of nosing joints. This type of joint was frequently used in the 1960s and 1970s. The ACME joint profile is made of extruded EPDM rubber designed to withstand UV exposure, gasoline, oil, de-icing salts, and weather conditions. This type of joint consists furthermore of lane gratings anchored in the construction with clamped joint profiles.
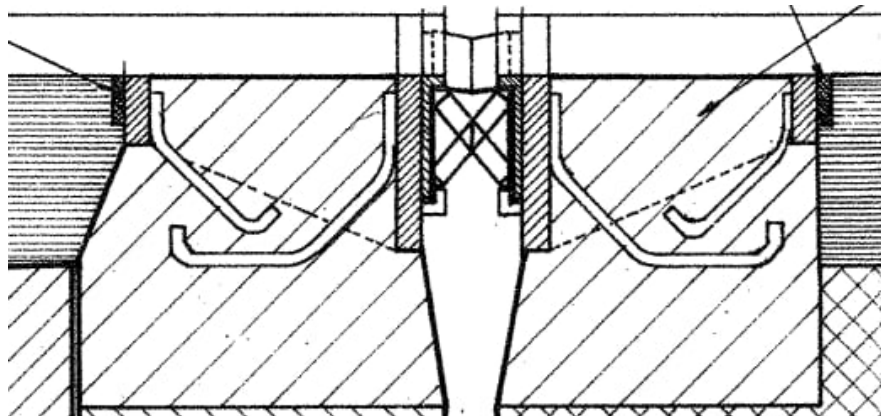
Figure 3.5: ACME type dilatation joint used for the Sluinerweg viaduct.

The ACME joint has a good water resistance when the rubber is correctly bonded and the steel profiles are adequately welded [84]. According to old documentation, in 2000, the joints were replaced due to persistent leaks, and a new TENSA-GRIP dilatation joint was installed.

3.3.4 Concrete mix design

Information about the concrete mix design for the prefabricated T-beams were retrieved from the specification *BR/5506* written in 1970, with an overview provided in Table 3.5. Information about the w/c ratio was not given in the specification. No specifications were provided for the other structural parts of the viaduct.

Table 3.5: Concrete mix design for the T-beams.

Concrete mix design specifications	
$f_{ck,cube}$ after 28 days	400 kg/cm^2
Cement	360 kg/m^3
Fine aggregate	River sand
Coarse aggregate	River gravel
Environmental class	XC4, XD3 and XF2

According to current standards, for construction class S4, a cover depth of 40 mm is required for normal reinforcement and 45 mm for prestressing, based on the specified environmental classes.

3.3.5   Cathodic protection system

Three rules were set for applying cathodic protection in the Liggerkoppen project:

1. If immediate or long-term function loss of prestressing is suspected then the damage should be repaired and cathodic protection should be applied.
2. Adjacent beam heads on either side of a damaged beam head should be included in the cathodic protection system.
3. If more than 50% of the beam heads on a support are eligible for cathodic protection then all beam heads of that support should be provided with cathodic protection.

The applied cathodic protection system is a so called cast^{3+} composite anode system which is shown in Figure 3.6. This system was chosen because of the long-time experience with the material in similar conditions, the durability of the conductive coating in relation to the requested lifetime of 20 years, good practical experience, and the advantages of a conductive coating with regard to the application in the restricted work space between the beam heads [1].
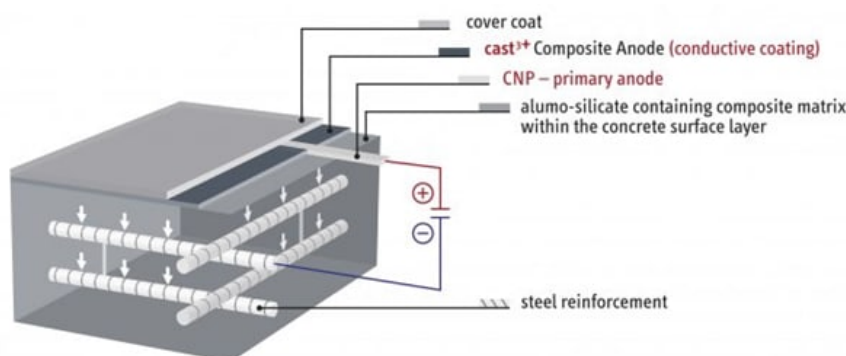
Figure 3.6: The cast^{3+} composite anode system [85].

The system consists of a primary current-carrying anode made of CuNbPt wire, with the cast^{3+} system serving as a secondary anode. Additionally, two types of reference electrodes were installed on the protected beam heads. A Ag/AgCl chloride true reference electrode was positioned near the prestressing to monitor the instantaneous off value

(approximately 25 years lifespan). Activated titanium electrodes, which are not stable over time due to factors like temperature, polarisation, or chloride content, were used to monitor the depolarisation value (approximately 75 years lifespan). A constant voltage of 5-6 volts was applied to the system.

Figure 3.7: The cast^{3+} composite anode system applied to beams 12, 13 and 14 of STP01 on the Sluinerweg viaduct.

3.4 Inspections

3.4.1 Early inspections

The earliest recorded inspections date back to 2002. Visual inspections revealed minimal damage; however, stalactites caused by efflorescence between the contact surfaces of the flanges were observed at various locations. Additionally, it was noted that the dilatation joints were filled with dirt, the wearing layer over the expansion joints had completely deteriorated, and corrosion was present on various areas of the steel. The ACME expansion joints were later replaced, as discussed in Section 3.3.3.

In 2011, a visual inspection of all beam heads was conducted using mirrors, and damages were classified according to the damage classes outlined in Tables 3.1 and 3.2. The most significant damage was observed on beam 13 at STP01 (Figure 3.9), classified as class 5 damage to the beam head and class 2 damage to the cone. These damages are shown in Figure 3.8. This beam head received cathodic protection in 2014. No leakages were observed during the inspection.

(a)   (b)

Figure 3.8: Damage to beam head (a) and cone (b) of beam 13 in 2011.

Additional inspections were performed during the period 2017-2018; however, specific details regarding these inspections are not available.

3.4.2   Inspection 2020

An inspection was performed in March 2020. During this inspection two NDTs were performed: cover depth measurements with a standard cover meter and half-cell potential measurements. Cores were also taken for carbonation and chloride profile determination. The scope of this investigation concentrated on the outermost supports, labeled STP01 and STP05 as illustrated in Figure 3.9. Looking at Figure 3.10, it is evident that the beam heads themselves were not included in this part of the inspection; they were only part of the visual inspection. Conclusions were drawn regarding the condition of the T-beams based on the assessment of the support beam. This research method may therefore raise potential questions.
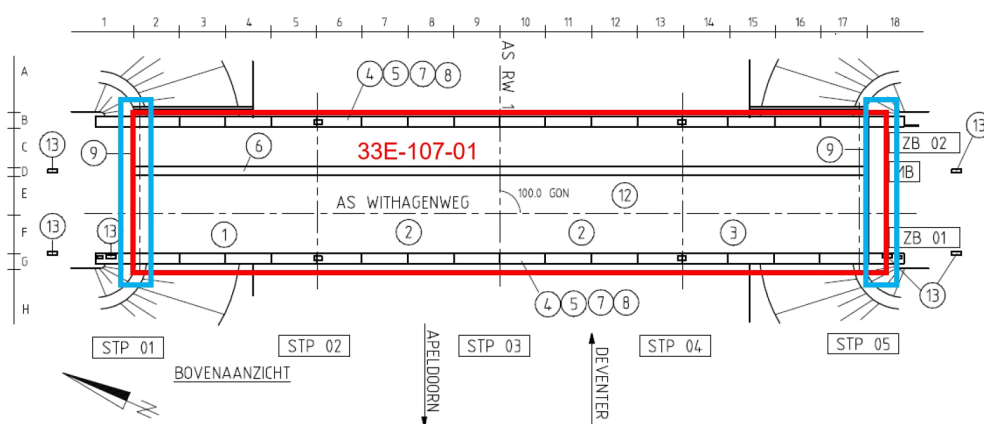
Figure 3.9: Location of STP01 and STP05 [86].
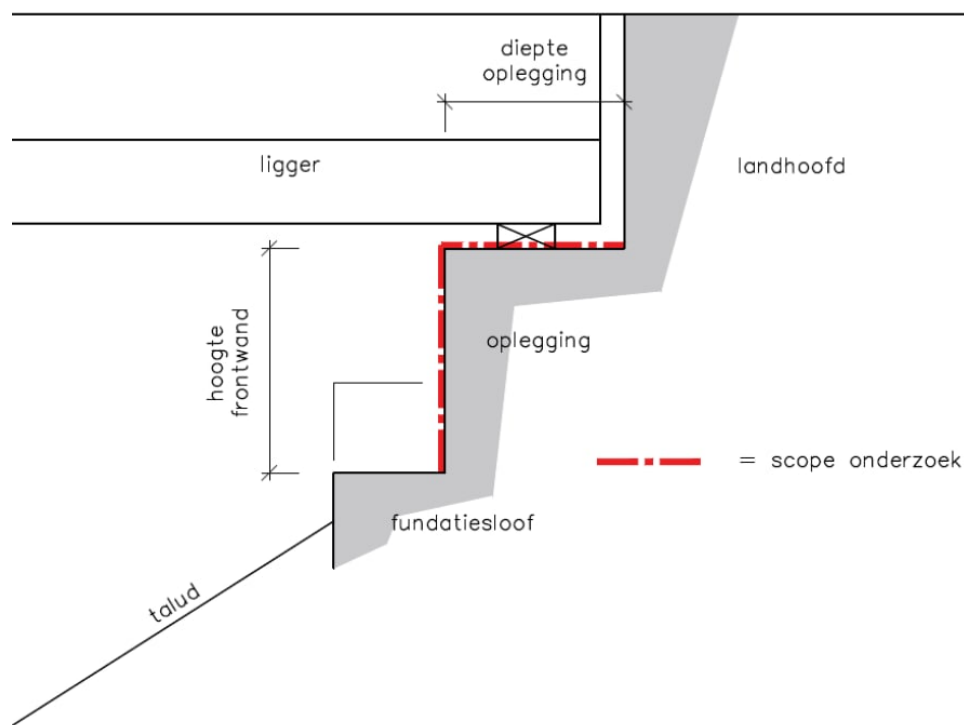
Figure 3.10: Scope of the inspection in 2020 [86].

The measured cover depths are listed in Table 3.6, for the measurements locations reference is made to Appendix C. Here, it can be observed that the cover depth varies significantly along the length of the support beams, with an insufficient cover depth at location 2 on STP01.

Table 3.6: Support beam cover depth measured in 2020 in mm.

Support	Location	$x_{c,required}$	$x_{c,min}$	$x_{c,mean}$
STP01	1	40	33	40
STP01	2	40	23	32
STP01	3	40	45	53
STP05	1	40	54	65
STP05	2	40	48	53
STP05	3	40	44	56

Half-cell potential measurements were performed on STP01 and STP05 on the 4th of March 2020 using $Cu/CuSO_4$ reference electrodes. The results are presented in Figure 3.11. The top row represents the measurements taken on the horizontal face of the support beam in between the T-beams. Based on these figures, it can be concluded that the probability of corrosion is likely low, particularly for STP01, as none of the values fall below -200 mV. Additionally, no significant potential jumps are observed, except for some minor ones on STP05.
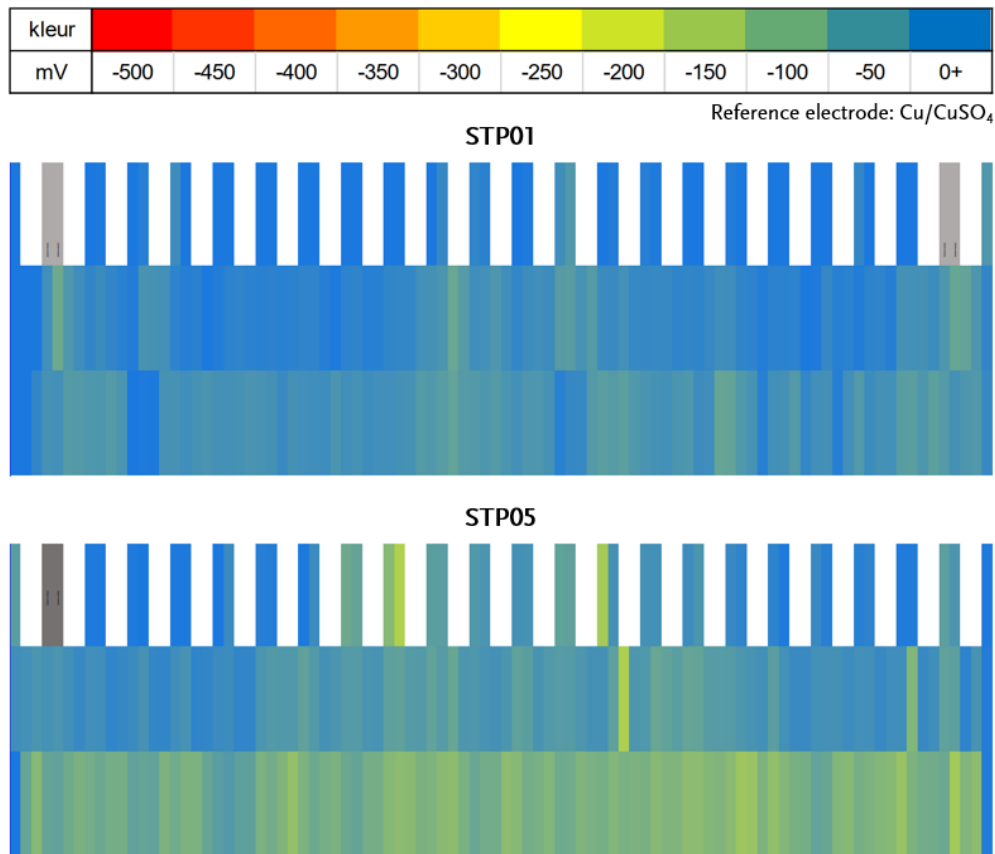
Figure 3.11: Potential maps for STP01 and STP05 [86].

The recorded carbonation depths found in the support beam are presented in Table 3.7. For the measurement locations, reference is made again to Appendix C.

Table 3.7: Support beam maximum carbonation depth measured in 2020 in mm.

Support	Location	$x(t)_{max}$
STP01	1	3
STP01	2	5
STP01	3	5
STP05	1	3
STP05	2	2
STP05	3	2

In Appendix A.3, the results of the chloride content determination in the support beams are presented. The method employed was Rapid Chloride Titration (RCT), with a constant assumption of 14wt% for the cement content during chloride content determination. At all locations, an elevated chloride content was found at the surface (depth 0 to 20 mm). At locations 1, 2, and 3, the values are 0.32%, 0.25%, and 0.34%, respectively relative to the cement weight, which is below the critical threshold of 0.5% defined in CUR Aanbeveling 121. At one of the three locations, an elevated chloride content was found at the reinforcement level (depth 20 to 40 mm), namely 0.26% relative to the cement weight, well below

the critical threshold. Chloride-induced reinforcement corrosion is not expected at these locations. At one of the two locations, a slight increase in chloride content was found at 20 mm below the horizontal plane, at a depth of 40 to 100 mm relative to the vertical plane, measuring 0.33% relative to the cement weight. Chloride-induced reinforcement corrosion is not expected at this location [86].

3.4.3 Inspection 2022

The most recent inspection was performed in November 2022. This was primarily a visual inspection with the main goal to evaluate the state of the beam heads using the the criteria mentioned in Table 3.1 and 3.2. The results are reported in Figure 3.12.

Support	Date of inspection	Joint	Tendons		1	2	3	4	5	6	7	8	9	10	11	12	13	14	15	16	17	18	19	20	21	22	23
STP01(2)	19 January 2022	Joint	5	Beam head												CP	CP	CP									
				Cone												CP	CP	CP									
				Risk class																							
STP02(1)	8 March 2022	Bituminous	5	Beam head																							
				Cone																							
				Risk class																							
STP02(3)	8 March 2022	Bituminous	5	Beam head																							
				Cone																							
				Risk class																							
STP03(2)	16 May 2022	Bituminous	5	Beam head	4	4	4									4	4										
				Cone																							
				Risk class	R1	R1	R1									R1	R1										
STP03(4)	16 May 2022	Bituminous	5	Beam head	4	4	4																				
				Cone								C2	C2	C1										C2			C5
				Risk class	R1	R1	R1					R1	R1	R1										R1			R2
STP04(3)	10 May 2022	Bituminous	5	Beam head																							
				Cone																							
				Risk class																							
STP04(5)	10 May 2022	Bituminous	5	Beam head																							
				Cone			C2																				
				Risk class			R1																				
STP05(4)	23 June 2022	Joint	5	Beam head																							
				Cone													C2					C2					
				Risk class													R1					R1					

Figure 3.12: Observed damage to beam heads during the inspection of 2022 [87].

From this figure, the most notable is the damage observed on STP03, the middle support. Multiple beams are labeled with a risk level R1 meaning that function loss is to be expected within 10 years. Beam 23 was labeled with a risk level R2, meaning that function loss is to be expected within 5 years. Based on this inspection, an advice was given to install cathodic protection for the middle support on the side of STP04. However, this system was never installed due to the planned demolition of the Sluinerweg viaduct in early 2024.

Chapter 4

Sluinerweg viaduct measurements

The measurements performed on the Sluinerweg viaduct spanned three consecutive days, from Monday to Wednesday, November 13-15, 2023. The assessment started with GPR, UPE, rebound hammer and UPV measurements on Monday. Subsequently, corrosion-related measurements were conducted on Tuesday, followed by the majority of coring activities on Wednesday.

4.1 Measurement plan

A comprehensive measurement plan was developed based on tests with the NDTs (see also Appendix B), analysis of prior inspections of the Sluinerweg viaduct and the literature reviewed in this research. It proved challenging to estimate the time required for each measurement, due to the novel approach of conducting numerous NDTs simultaneously. Ultimately, a plan was formulated covering STP01 and one side of STP02 accessible using the *Blankenhuisweg*. Although STP03 exhibited the most damage, its location in the middle of the highway, with lanes going in opposite directions on either side, made an inspection logistically complex and costly. The finalised measurement plan is detailed in Appendix D.

4.1.1 Safety measures

Ensuring safety during inspections is vital. A comprehensive safety plan is essential, and it's important for everyone to wear appropriate Personal Protective Equipment (PPE) during in-situ work. Specific safety measures have been implemented for the Sluinerweg viaduct to ensure safety during the inspection, particularly because the bridge remained in use throughout the process. This underscores the importance of considering safety measures as an integral part of in-situ measurements.

- **Safety plan**. A safety plan was created, which involved assessing risks and identifying necessary measures, including the requirement for Personal Protective Equipment (PPE).

- **VCA and GPI certificates**. For this project it was mandatory to have the Dutch VCA and GPI certificates which are proof that one has the necessary knowledge and skills to work safely. To obtain these certificates, one must successfully pass an exam. VCA covers a broad range of topics, while GPI is more specific to the type of work being undertaken.

- **PPE**. Wearing safety shoes, a pair of orange work trousers, an orange jacket, and a helmet were mandatory. Additionally, ear and eye protection were required during coring activities. In situations where a significant amount of dust is released, a mask of FFP3 level was also required.

- **Aerial work platform**. For the inspection of the tendon ducts and initially for the inspection of STP02, an aerial work platform was required, as illustrated in Figure 4.1a. A certified operator handled this platform, and fall protection was worn as an additional safety measure.

- **Walkway platform**. A walkway platform was required for access to STP01 to ensure a safe work environment, as illustrated in Figure 4.1b. This platform made it possible to stand and pause after taking measurements, preventing the need to crawl each time and reducing the risk of falling. The platform could be accessed using a staircase.

- **Road closure**. Although the *Blankenhuisweg* underneath the Sluinerweg viaduct next to the A1 highway is not a busy road, a road closure was still in place to prevent access for cars; however, cyclists could still pass through, so caution was required.

(a)   (b)

Figure 4.1: Measurement site (a) and walkway platform (b).

4.1.2   NDTs

Table 4.1 offers a summary of the NDT equipment used, along with their main applications.

Table 4.1: NDT equipment used for the inspection of the Sluinerweg viaduct.

NDT	Equipment used	Main application
GPR	Proceq GP8800	Localising reinforcement and prestressing.
UPE	Pundit PD8050	Localising and inspecting tendon ducts.
UPV	Pundit 200	Assessing compressive strength.
Rebound hammer	Silver Schmidt OS8200	Assessing compressive strength.
Concrete resistivity	1. Proceq Resipod 2. Gecor 10	Assessing corrosion probability.
Half-cell potential	1. Profometer PM8500 2. Gecor 10	Assessing corrosion probability.
Corrosion current density	Gecor 10	Assessing corrosion probability.
Handheld XRF[a]	Bruker S1 TITAN	Investigating surface chemical composition.

[a] For measurements on the Sluinerweg viaduct using this device reference is made to [64].

Tendon duct inspection strategy
An inspection of the tendon duct grouting can be conducted by combining GPR with UPE.

1. Localise the tendon using GPR or with a combination of GPR and UPE in case of a dense reinforcement mesh.
2. Use UPE on the side of the T-beams to detect suspicious areas along the tendon profile, areas with high reflections or loss of signal.
3. Make a small borehole with a 12 mm drill in order to inspect the tendon duct with an endoscope. An important consideration when assessing with endoscopy is its effectiveness in detecting large voids. However, evaluating small voids or cracks within boreholes can be challenging. For this purpose, more extensive destructive testing is required, such as core drilling or high-pressure water jetting.

Gecor 10 measuring strategy
A strategy for assessing the probability of corrosion for the Sluinerweg viaduct was developed based on the test measurements in Appendix B and the literature review.

1. Check electrical continuity along the rebar.

2. Perform half-cell potential measurements (sensor B) with the metal clamp connected to the rebar.
3. Perfom resistivity ρ measurements on moist concrete, but not overly wet concrete using the Wenner probe (sensor C).
4. Based on the measured half-cell potential and resistivity, a good estimate can be made for the required pulse duration for the confinement probe (sensor A). If the measured resistivity and half-cell potential show that the corrosion risk at a certain location is *negligible* or *low*, a current pulse duration of at least 60 seconds, but preferably even 100 seconds has to be set for a reliable CR measurement. If the measured resistivity and half-cell potential show that the corrosion risk of the reinforcement is *moderate* or *high*, a current pulse duration of 30 seconds should be set.

4.1.3   Coring

A coring plan was developed following the recommendations provided in EN 13791 [46] and *CUR Aanbeveling 72*. The coring plan underwent many changes over the course of the preparation of the inspection. The safety risks associated with coring the slender T-beams required careful discussion with a structural engineer. In the end, it was decided to take a total of 56 cores, with 28 on STP01 and 28 on STP02 as illustrated in Table 4.2.

Table 4.2: Number of cores according to the coring plan.

Construction part	Parameters	STP01	STP02(1)
Support beam	Compressive strength	4	4
	Carbonation	6	6
	Chloride content	3	3
Beam heads	Carbonation	2	2
1, 7, 13, 18, 23	Chloride content	1	1
		28	**28**

4.1.4   Changes to the measurement plan

A challenge arose as the aerial platform couldn't reach STP02 due to the excessively wet ground. To address this, steel roadway plates were necessary, but they only arrived at the end of the day on Monday. The plan was therefore overly ambitious and it was decided to shift the main focus to STP01. The aerial platform was then used for some tendon inspections and for evaluating the chemical composition of the concrete surface using hXRF. In the end, the total number of cores amounted to 28.

4.2   Measurements per construction part

The NDTs were conducted over a span of two days. On Monday, the 13th of November, the weather featured precipitation accompanied by a cold eastern wind with a force of 4-5, and temperatures ranging between 10-12 degrees Celsius. The following day, Tuesday the

14th of November, there was reduced rainfall, and the wind direction shifted to the west, maintaining a force of 4-5, with temperatures ranging between 10-12 degrees Celsius. As per the measurement plan, the inspection primarily targeted the support beam and T-beams 1, 7, 13, 18, and 23. An overview of the test regions at STP01 is presented in Figure 4.2.
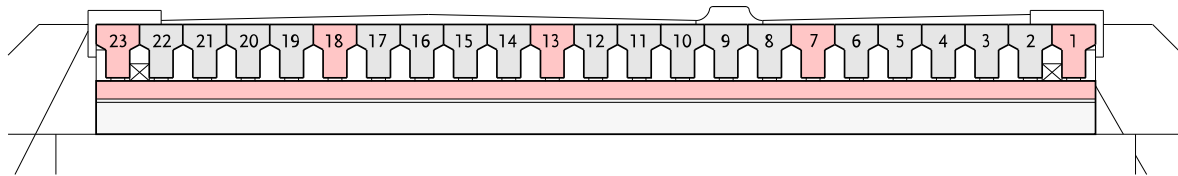

Figure 4.2: Overview of test regions at STP01.

4.2.1   Support beam

First GPR measurements were performed using the Proceq GP8800 in two directions, allowing for the identification of both longitudinal and shear reinforcement in the beam. The rough KCG-layer posed no challenge for the GPR device. Yellow chalk was used to pinpoint the locations for compressive strength cores and to expose the reinforcement for potential and corrosion current density measurements (Figure 4.3). The initial dielectric constant was consistently set to 6 for all GPR measurements conducted on the support beam, as indicated in paragraph 2.7.2.

Figure 4.3: Using GPR to locate the reinforcement in the support beam.

Four test locations were selected on the support beam for conducting rebound hammer and UPV measurements, followed by extracting cores from these designated locations, all conducted in accordance with EN 13791 [46]. Test location S1 is situated between beams 19 and 20, S2 between beams 14 and 15, S3 between beams 9 and 10, and S4 between beams 4 and 5, as illustrated in Figures 4.4 and 4.8. The UPV measurements were

carried out in semi-direct transmission mode by transmitting the pulse from the top face
to the vertical face of the support beam. This procedure was performed at three points
along a horizontal centerline, ensuring a consistent distance of 15 cm between this cen-
terline and the top of the support beam each time, as demonstrated in Figure 4.6. No
significant issues were found with the rebound hammer and UPV measurements on the
KCG-layer, except for the requirement of additional coupling gel for the UPV transducers.
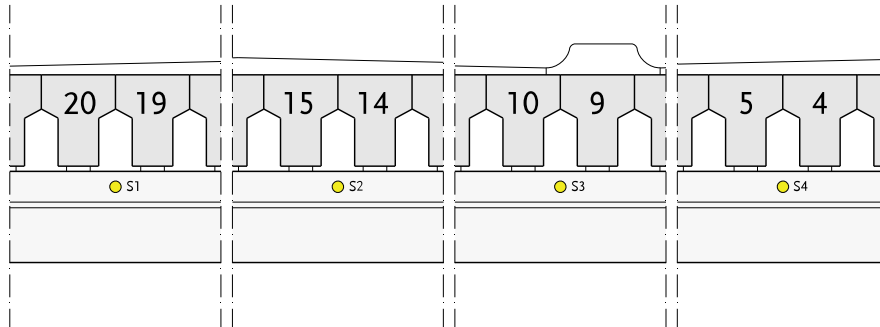

Figure 4.4: Test locations S1 through S4.

(a) Test location S1.

(b) Test location S2.

(c) Test location S3.

(d) Test location S4.

Figure 4.5: Test locations S1 through S4 in-situ.

Figure 4.6: Distance of 15 cm from the UPV centerline to the top of the support beam.

At four locations, the top rebar was exposed for conducting corrosion measurements. Due to the absence of drawings of the support beam, there was uncertainty regarding the location of the reinforcement. Upon inspection, it was found that the rebar had a diameter of 28 mm, with cover depths exceeding 80 mm as illustrated in Figure 4.7. This depth was significantly greater than initially anticipated based on previous inspections using a standard cover meter reliant on eddy currents. No notable corrosion was observed at the exposed locations.

(a) Rebar location 1.

(b) Rebar location 2.

(c) Rebar location 3.

(d) Rebar location 4.

(e) Close-up.

Figure 4.7: Exposed top rebar in the support beam.

After verifying the continuity of the top rebar, corrosion measurements were conducted. Initially, measurements with the Profometer PM8500 were carried out. Subsequently, for measurements with the Gecor 10, the strategy discussed in Section 4.1.2 was implemented. A pulse duration of 100 seconds was applied for each CR measurement due to the expected passivity. Figure 4.8d shows the author attempting to record the measurements on a notepad in windy conditions

(a) Water supply.

(b) Half-cell potential with a point electrode.

(c) Half-cell potential with a wheel electrode.

(d) Corrosion current density.

Figure 4.8: Corrosion measurements on the support beam.

4.2.2 T-beams

GPR was used to map the reinforcement within the beam heads, and in conjunction with UPE, an inspection of the tendon ducts was conducted to identify potential grouting defects, as shown in Figure 4.11. Following this, an assessment involving the rebound hammer and UPV with direct transmission was undertaken. Corrosion measurements were subsequently performed on the beam heads, using the previously exposed reinforcement. Prior to this, electrical continuity was established. Beam 13 has been previously equipped with cathodic protection as described in Section 3.3.5.

The reinforcement was exposed at the bottom of the T-beams at the level of the walkway platform, as shown in Figure 4.9. All identified rebars have a diameter of 8 mm and an average concrete cover of 35 mm.

(a) Beam 1.

(b) Beam 7.

(c) Beam 13.

(d) Beam 18.

(e) Beam 23.

Figure 4.9: Exposed bottom reinforcement in the T-beams.

(a)   (b)

Figure 4.10: Using GPR on the outer face of beam 1 (a) and measuring the corrosion current density on beam 13 using the Gecor-10 (b).

(a)   (b)

(c)

Figure 4.11: Performing endoscopy on a tendon duct at midspan on beam 2 (a), UPE testing (b) and drilling a 12 mm borehole (c).

4.3   Coring and lab testing

The majority of the cores were drilled on the 15th of November. A total of 28 cores were extracted from STP01, comprising 13 cores from the support beam and 15 cores in total from the five investigated T-beams, with three cores obtained from each beam. The locations of these cores are illustrated in Figures 4.12 and 4.13, along with corresponding in-situ images provided in Figures 4.14 and 4.15. Further details can be found in Appendix E.
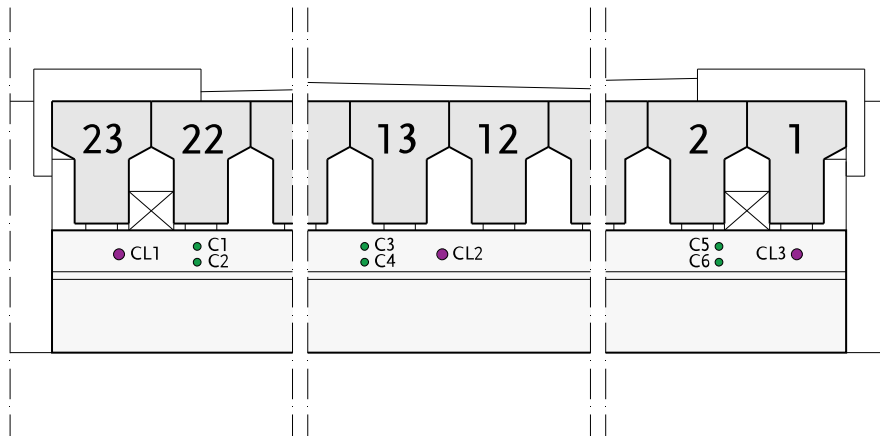
Figure 4.12: Location of the cores for carbonation (green) and chloride content (purple) analysis on the support beam.
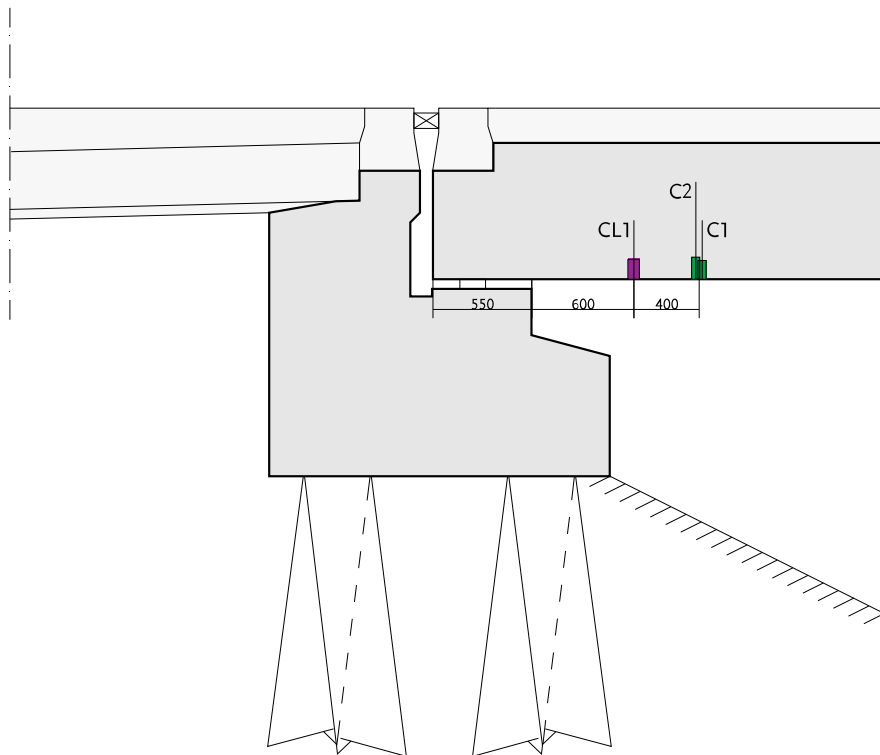
Figure 4.13: Locations of the cores for carbonation (green) and chloride content (purple) analysis on the T-beams.

(a) Beam 1.

(b) Beam 7.

(c) Beam 13.

(d) Beam 18.

(e) Beam 23.

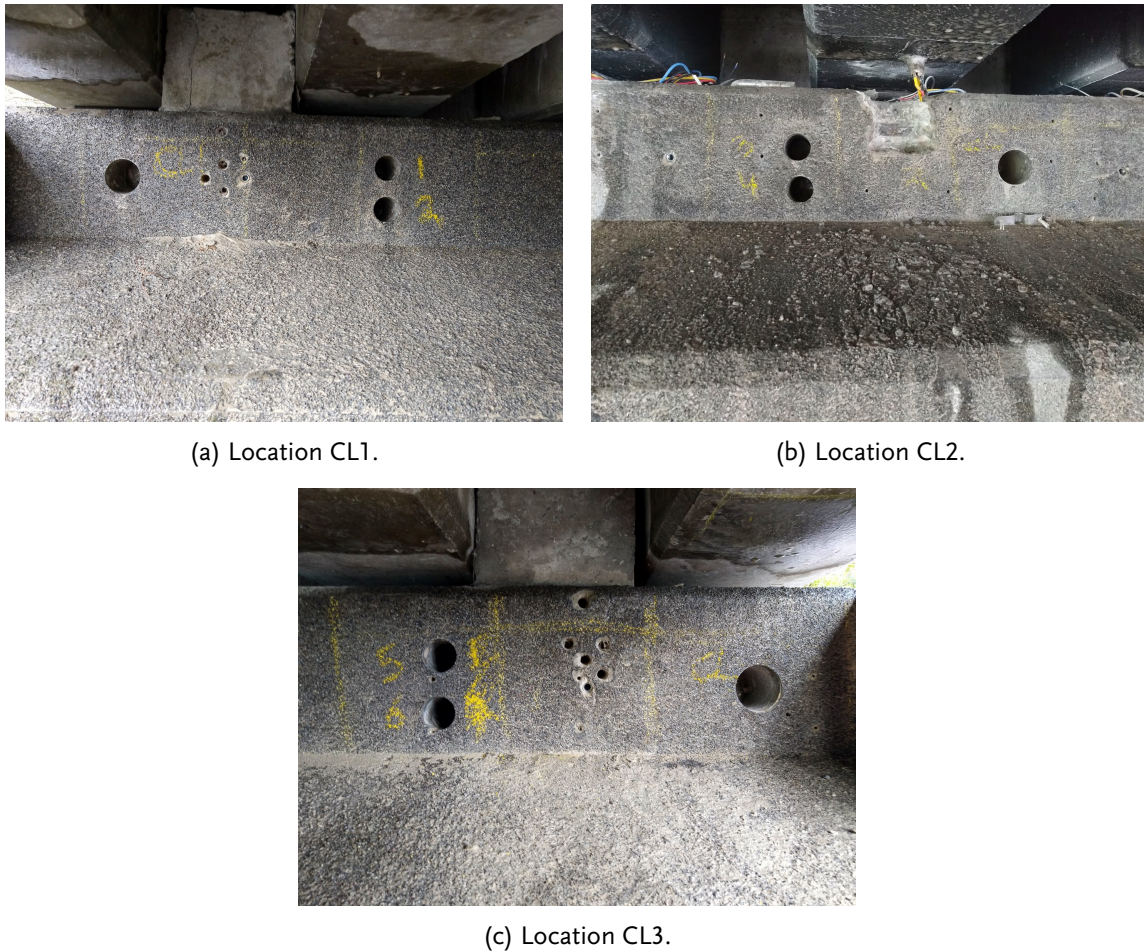Figure 4.14: Location of the cores taken from the T-beams.

(a) Location CL1.

(b) Location CL2.

(c) Location CL3.

Figure 4.15: Locations of the cores taken from the support beam.

4.3.1 Compressive strength

After the cores are extracted, it's important to ensure that there is no reinforcement present in them, and GPR is invaluable for this purpose. The cores were stored in a sealed container until they were ready to be trimmed to length, following the guidelines outlined in EN 12504-1 [88]. Grinding the ends is recommended as the most precise method for preparing them. Testing the compressive strength of the prepared samples was in accordance with EN 12390-3 [89].

4.3.2 Carbonation

Cores for carbonation depth measurements were taken in pairs, following the recommendations outlined in *CUR Aanbeveling 72*. Subsequently, carbonation measurements were conducted according to the procedure specified in EN 14630 [78]. The cores were split along their longitudinal axis by creating a notch with a saw and then using a hammer and chisel. The resulting surfaces were cleaned of dust and sprayed with a phenolphthalein solution. Images captured immediately after spraying are included in Appendix E.2.

4.3.3 Chloride content

Three cores were extracted from the support beam, while one core each was taken from T-beams 1, 7, 13, 18, and 23 (refer to Appendix E for details). The cores were obtained in proximity to the support as can be illustrated in Figure 4.14, with the limitation being the length of the drilling machine.

The chloride profiles were determined using argentometry, specifically the Volhard method. The method involves precipitating chloride in an acidic environment with an excess of silver nitrate solution. The excess is titrated back with an ammoniumthiocyanate solution using ammonium iron(III) sulfate solution as an indicator. To prevent the formation of silver thiocyanate by consumption of silver chloride, the silver chloride is removed by filtration after adding the excess silver nitrate. The original amount of chloride can be calculated based on the difference between the added and titrated amounts of silver ions.

Determination of the cement content

1. The cores are cut into six discs from 10 mm according to CUR recommendation 72. A disc is crushed into smaller pieces using the sample crushing device depicted in Figures 4.16c and 4.16d. Around 30 grams of concrete from a 10 mm core disc are placed in a 400 mL beaker.

(a) Core after sawing.

(b) Concrete disc.

(c) Filling the crushing device.

(d) Crushing the concrete.

Figure 4.16: Preparation of the sample.

2. In the fume hood, 100 mL of 4M nitric acid is added using a graduated cylinder to the beaker containing the concrete sample. The beaker is covered with a watch glass, placed on a heating plate, and brought to a boil. Subsequently, it is boiled for 5 minutes with occasional stirring using a stirring rod.

Figure 4.17: Boiling the sample in 4M nitric acid.

3. The heated solution is filtered through a large Büchner funnel using a 1000 mL filter flask and a membrane vacuum pump. Glass microfiber filter paper with a diameter of 110 mm is employed. The undissolved material is rinsed and quantitatively transferred with a small amount of deionized water. The residue on the filter is washed with four portions of 10 mL 1M nitric acid.

(a)   (b)

Figure 4.18: Filtering the heated solution using a Büchner funnel (a) and the resulting filter with residue (b).

4. The filter with residue is quantitatively transferred into a pre-weighed Petri dish and placed in the drying oven at 105°C. After drying in the oven overnight, the cement content in the sample can be determined.
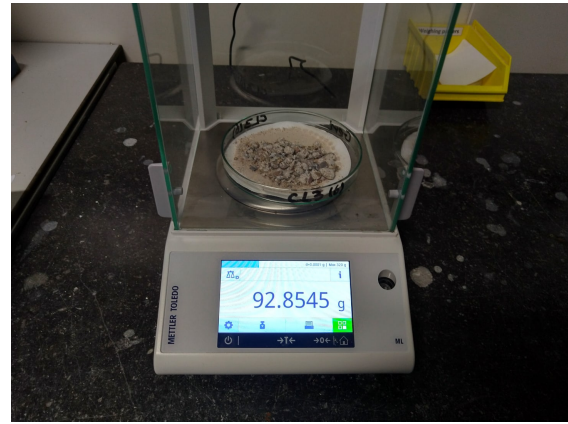

| (a) | (b) |

Figure 4.19: Drying the filter with residue at 105°C (a) and weighing after drying (b).

Determination of the chloride content

1. The filtrate is quantitatively transferred into a 500 mL volumetric flask. Using a volumetric pipette, 100 mL is pipetted into an Erlenmeyer flask. A magnetic stir bar is added, and 10 mL of 0.1M silver nitrate is slowly introduced with continuous stirring.
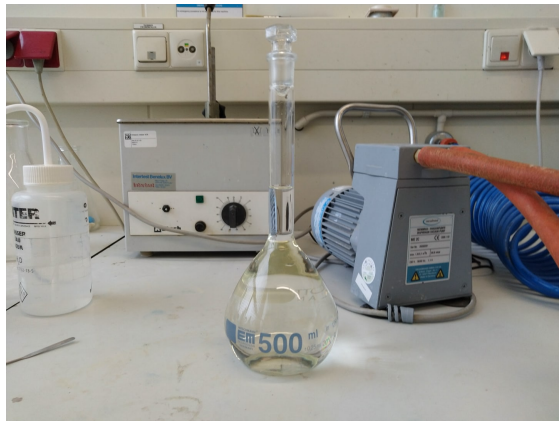
| (a) | (b) |

Figure 4.20: Volumetric flask containing the filtrate (a) and adding 0.1 M silver nitrate solution (b).

2. The Erlenmeyer flask is placed on a heating plate in the fume hood, covered with a splash head, and boiled for 2 minutes, inducing the coagulation of AgCl. Subsequently, the solution is allowed to cool completely.

3. The solution is filtered through a Büchner funnel into a 500 mL filter flask using a membrane vacuum pump. The precipitate on the filter is washed with four portions of 10 mL 0.5M nitric acid.
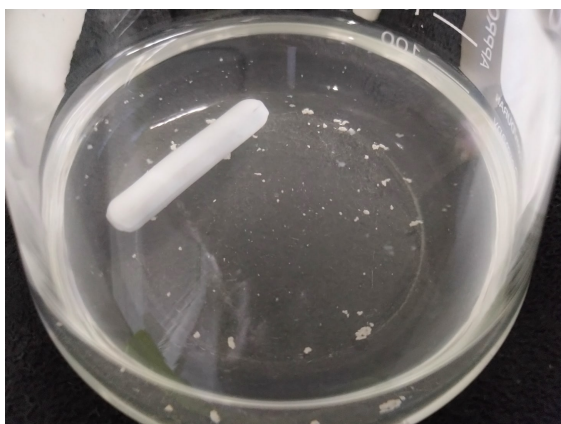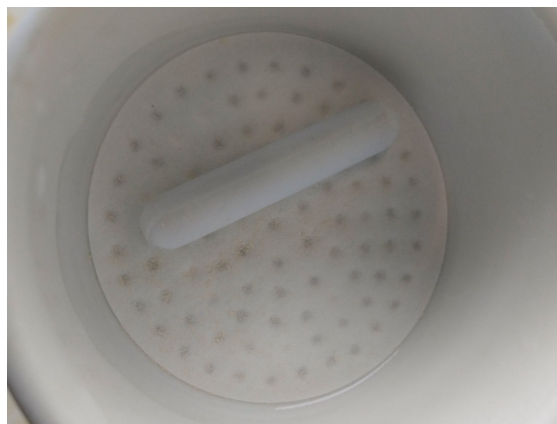
(a)   (b)

Figure 4.21: Coagulation of AgCl (a) and AgCl residue after filtering (b).

4. To the filtrate, 10 mL of a 20% w/w iron(III) ammonium sulfate solution is added. A piston burette is filled with a 0.1M ammonium thiocyanate solution, and the titration is carried out until a color change occurs from white to orange.

(a)   (b)

Figure 4.22: Iron(III) ammonium sulfate solution (a) and titration setup (b).

5. Every titration is performed in duplicate.

In addition to the above procedure, it is necessary to perform a blank titration to verify the accuracy of the concentrations of the chemicals used.

4.4 Summary of practical findings

Several practical findings were made during the inspection of the Sluinerweg viaduct, some of which may seem obvious but are still important for future inspections using these NDTs:

- Make sure that the ground is not too soggy so that the aerial platform can stand stable. This aspect was overlooked during the planning of the inspection of the Sluinerweg viaduct.
- It is advisable to bring towels to the inspection when the structure is wet, as even using chalk can prove difficult for writing on a wet concrete surface.
- Measuring through the KCG layer proved to be no problem for most NDTs. However, the UPV method required the use of extra coupling gel due to the roughness of the surface. Performing measurements with the hXRF on this surface is not feasible and requires the removal of this surface coating [64].
- A dielectric constant of 6 is a great starting point for GPR measurements for this type of structure.
- Carefully plan the order of tests and accurately document the quantity of water applied to the structure. It's essential to recognise that not all tests are equally sensitive to moisture content, and this consideration should be integrated into the planning of the inspection.

Chapter 5

Data analysis

5.1 Visual inspection

During the visual inspection, no significant issues were identified apart from minor corrosion damage, minor cracking, and some efflorescence. A summary of these damages is provided in Appendix F.1. Additionally, black crusts were observed on the T-beams, which were found to have a high sulfur content using hXRF [64]. A visual inspection for damage to the concrete cones using mirrors was not conducted as it had already been carried out in 2022.

5.2 Non-destructive testing

5.2.1 Localisation of reinforcement and prestressing with GPR

GPR was used to localise reinforcement and prestressing in-situ. Figure 5.6a shows radargrams of individual line scans conducted on the KCG-coated support beam, using a fitted dielectric constant of 6.1. Analysis of this figure indicates that the scans were carried out vertically, progressing from bottom to top. This observation is based on the positioning of the primary longitudinal rebar at the top of the support beam. Had the scans been conducted horizontally, stirrups would have appeared in a continuous line scan. Figure 5.6b provides a migrated heatmap obtained through the application of a Hilbert transform, which can make it easier to interpret the results. However, it's important to be cautious in this specific case, as the presentation might be misleading. It appears as a single continuous scan, which doesn't accurately represent the data in this figure. A cover depth of approximately 9.7 cm can be observed, which closely aligns with the true values depicted in Figure 4.7. It's worth noting that these observed values are also more precise than those obtained using a standard cover meter, as indicated in Table 3.6. The scans, however, do not provide any information on the rebar diameter.

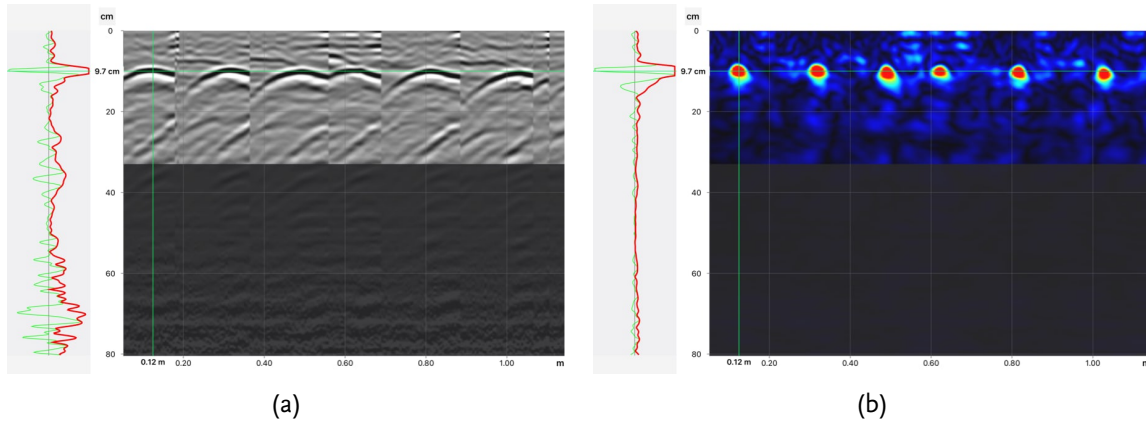(a)   (b)

Figure 5.1: Radargrams (a) and migrated heatmap (b) depicting a section of
the vertical face of the supporting beam.

Area scans were conducted for the beam heads of the T-beams. Figure 5.2 shows various views of a 1.6-meter scan conducted on the west face of beam head 7. The settings used for generating these figures with the Proceq GPR app are detailed in Table 5.1. In Figure 5.2a, the area scan up to a depth of 19 centimeters is shown, revealing the presence of two prestressing bars. This distinction has been accentuated by adjusting the color scale in the 3D scan presented in Figure 5.2b. The same information is evident when examining the radargram and migrated heatmaps depicted in Figures 5.2c and 5.2d, respectively, which represent vertical scan 16 in the area scan. Here, three distinct peaks are observed, corresponding to the longitudinal reinforcement and the two prestressing bars. Additionally, it should be noted that the rightmost bottom peak in Figure 5.2c appears considerably wider, potentially indicating an inclination of the prestressing bar relative to the GPR measurement, a finding that is further confirmed by Figures 5.2a and 5.2b.

Table 5.1: Beam 7 west face GPR scan settings.

Settings	Area scan 3D scan Migrated heatmap	Radargram
Linear gain (dB)	8	29
Time gain compensation (dB/ns)	4	5.8
Noise cancellation	On	On
Background removal depth (ns)	2.5	2.5
Dielectric constant (-)	6.7	6.7

A significant reflection is observed approximately 30 centimeters from the start of the area scan. Comparing this to the original drawings of the beam in Figure 5.3, it can be deduced that this corresponds to the position of the anchorage.
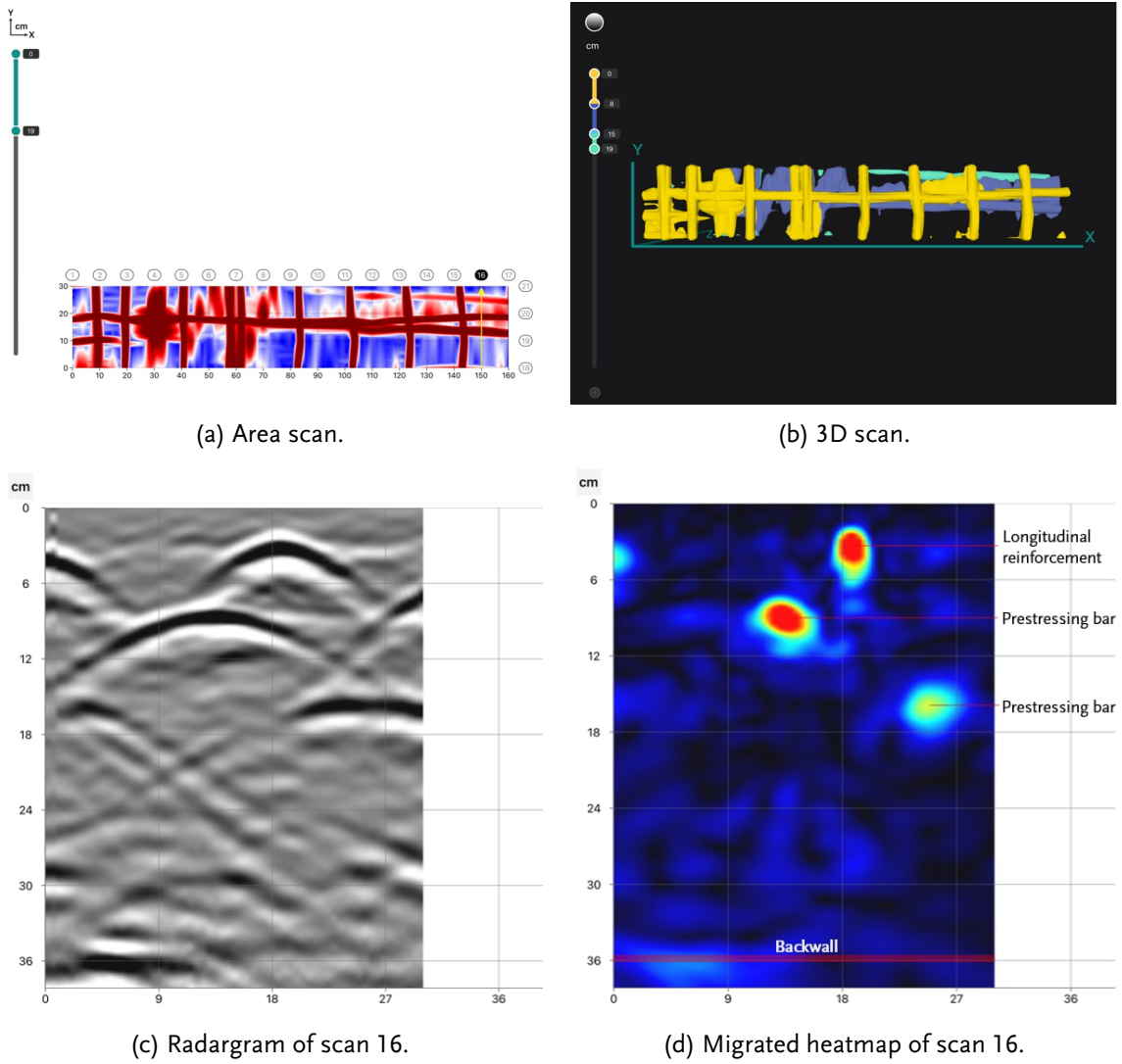
(a) Area scan.

(b) 3D scan.

(c) Radargram of scan 16.

(d) Migrated heatmap of scan 16.

Figure 5.2: GPR scan of beam 7 west face.
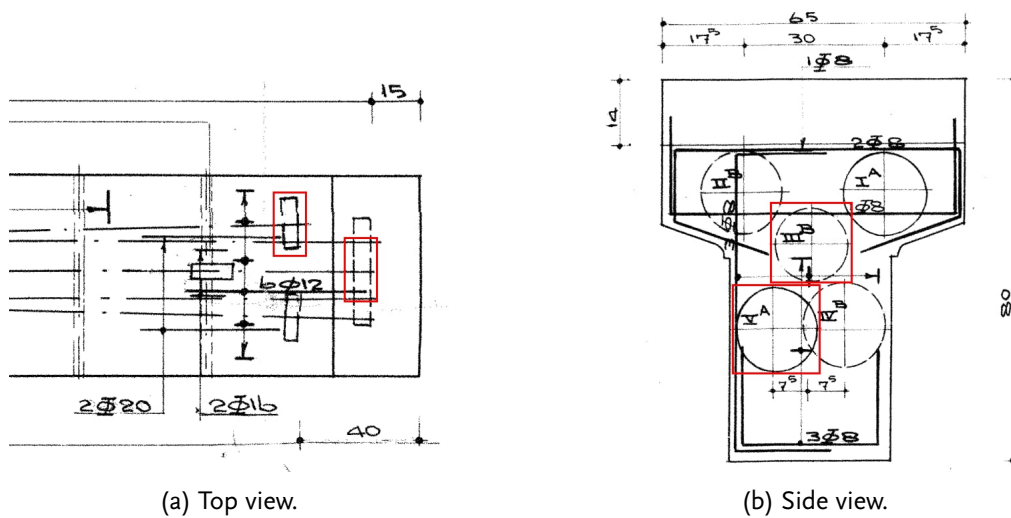

(a) Top view.

(b) Side view.

Figure 5.3: Location of the prestressing bars in beam 7 west face according to the original drawings.

Beam 13 cathodic protection

It was discovered that measuring through the cathodic protection system was impossible. This outcome was not unexpected, given the conductive nature of the coating. Figure 5.4 clearly indicates the boundary where the coating ends.
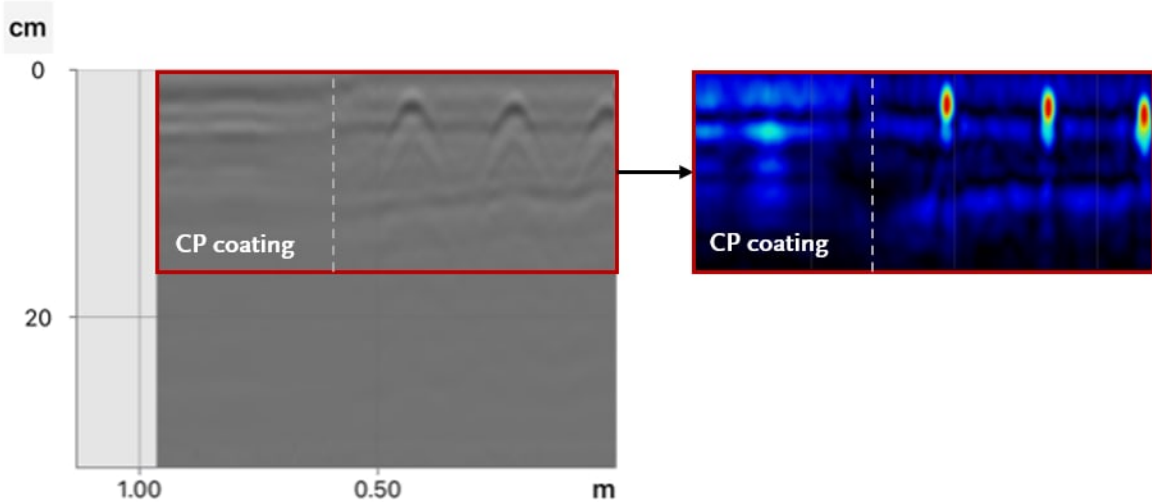
Figure 5.4: GPR scan of beam 13 west face demonstrating the effect of measuring on the CP coating.

The analysis of all other GPR scans was conducted in a similar manner, with no particularities found. Additional scans can be found in Appendix F. For access to the complete dataset, interested parties may contact the author.

5.2.2 Inspection of tendon ducts with UPE

With UPE a so called *stripe scan* can be performed. The Pundit PD8050 employs AI positioning to execute such a scan, from which a 3D image of the inspected object can be generated (Figure 5.5c). Once again, the back-wall is observed at 0.36 m, as shown in Figure 5.5b. The presence of two large reflections possibly indicates two tendon ducts, although this identification is not straightforward. Nevertheless, the scan can be compared with a GPR scan from the same beam, as shown in Figure 5.6. It's worth noting that the axis configurations in the two figures are different.

Table 5.2: Beam 18 west face UPE scan settings.

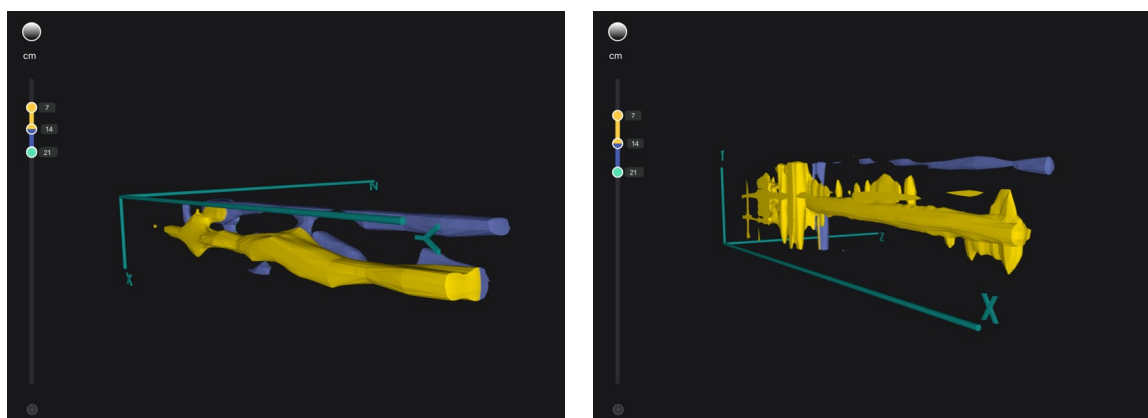| Settings	Heatmap 3D scan
Linear gain (dB)	-1
Digital time gain compensation (dB)	-1.3
Global pulse velocity (m/s)	1900
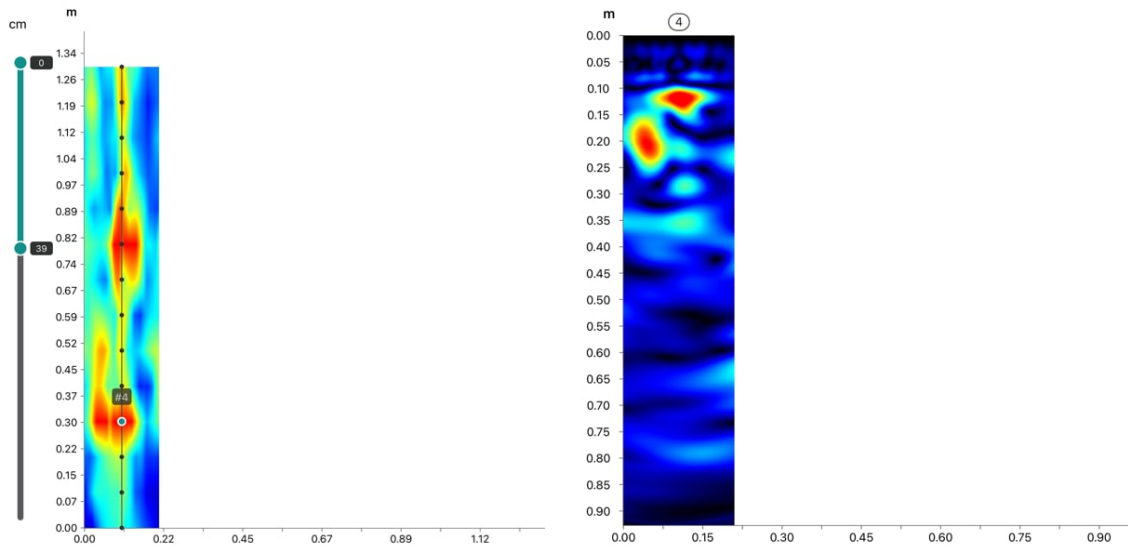
(a) Stripe scan.

(b) Heatmap of scan 4.
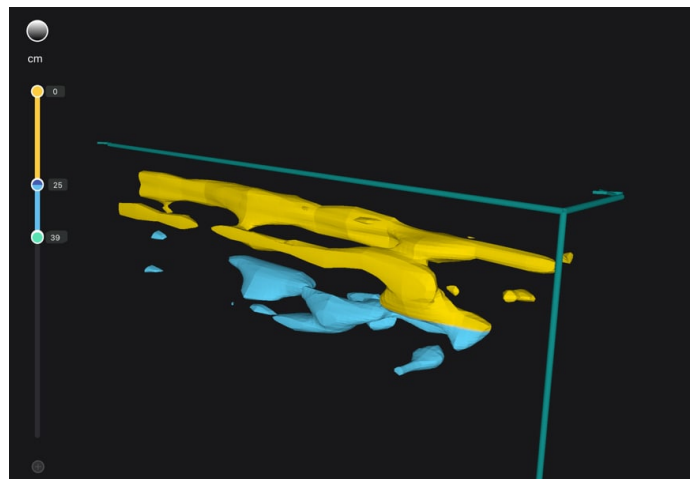
(c) 3D scan.

Figure 5.5: UPE scan of beam 18 west face.

(a)

(b)

Figure 5.6: UPE (a) and GPR (b) scan of beam 18 west face starting at a depth of 7 centimeter.

Interpreting UPE data poses challenges, as unlike GPR signals where a signal strongly reflects on a steel surface, an ultrasonic pulse partially passes through. However, ultrasonic waves quickly attenuate when encountering air voids. Consequently, these methods can be viewed as complementary. When UPE is combined with GPR, one can explore deeper behind the reinforcement and theoretically identify potential grouting defects. Figure 5.7 shows the UPE scan conducted at the midspan of beam 1's west face, where the tendons are at their lowest depth. In each scan, two tendon ducts are clearly visible. By comparing individual scans, suspicious areas can be identified—these are characterised by either very strong reflections or absence of a back-wall reflection. A photograph is included showing a 12 mm hole drilled at a non-suspicious location.

In total, 11 similar investigations were conducted across 6 different T-beams at various positions. In none of the examined cases were grouting defects found. Additional scans can be found in Appendix F. For access to the complete dataset, interested parties may contact the author.
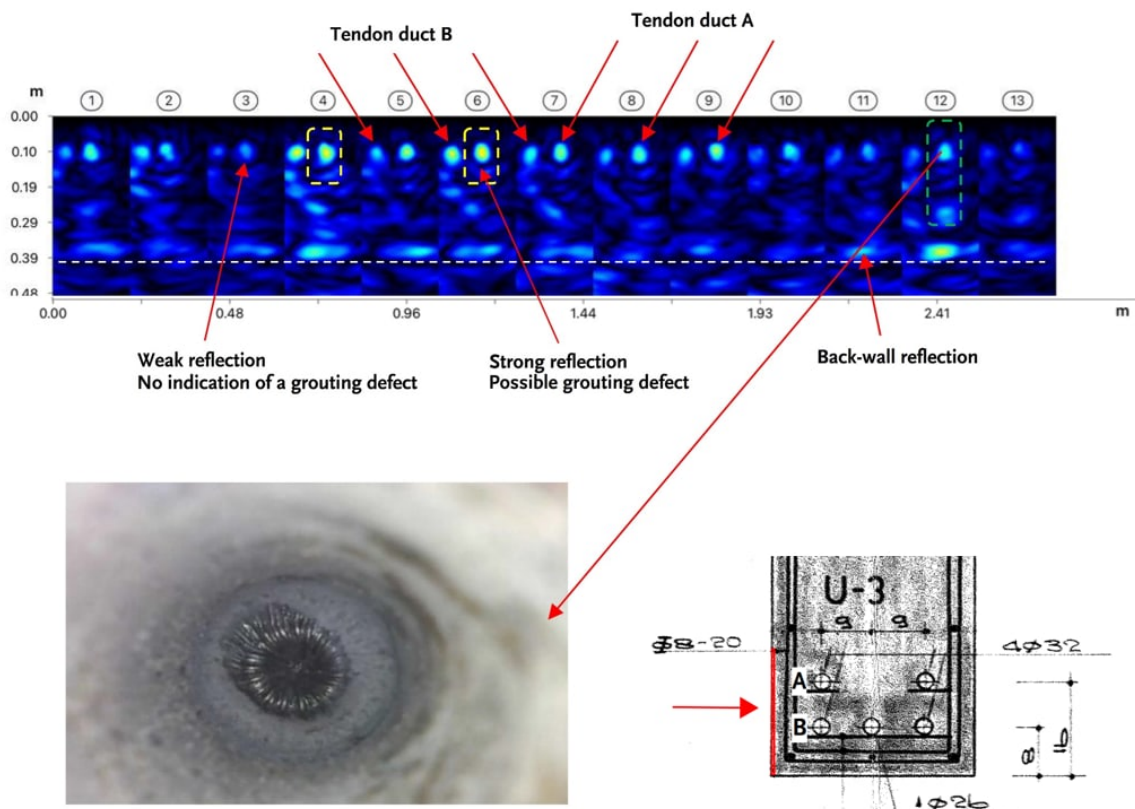
Figure 5.7: UPE analysis of beam 1 west face at midspan position [90].

Beam 13 cathodic protection

Figure 5.8 shows an UPE measurement on the west face of beam 13, the presence of the coating is not visible. It should also be noted that scan 17 in the same figure shows signs of a possible grouting defect.
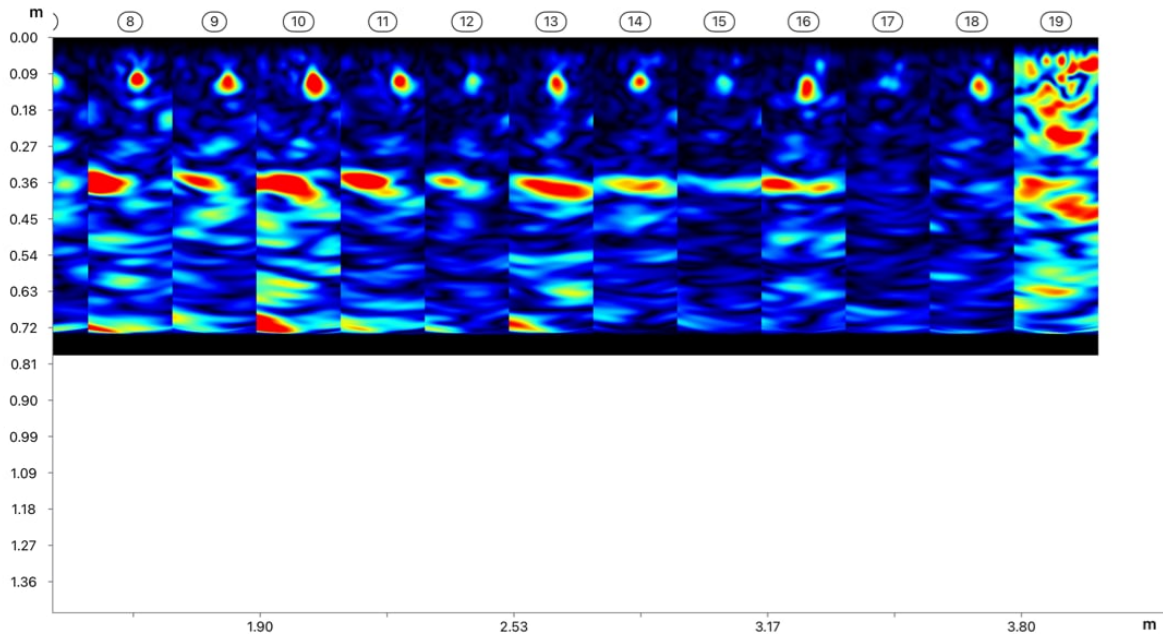
Figure 5.8: UPE measurement on the west face of beam 13.

5.2.3 Compressive strength assessment with rebound hammer and UPV

Appendix F presents the rebound hammer and UPV data. Starting with the rebound hammer data, it is recommended in EN 12504-2 [45] to use the median of the data at a specific test location. Boxplots are used to visualize the dataset, as shown in Figure 5.9. Corresponding statistical values, including quartiles[1], interquartile range, and median, are detailed in Table 5.3. Analysis of these results reveals that, on average, the spread in Q-values is higher for the support beam compared to the T-beams. This is likely influenced, at least in part, by the rough surface of the support beam attributed to the presence of the KCG-layer. Notably, beam 13 shows the widest Q-value variation among the five beams. However, it remains inconclusive solely from this dataset whether this variability can be attributed to the cathodic protection system.
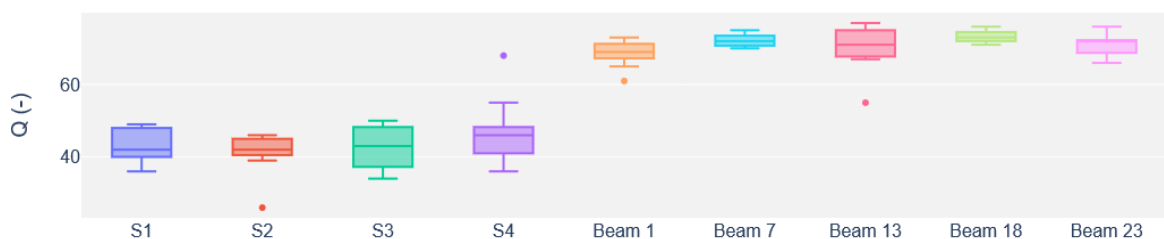
Figure 5.9: Boxplots for the rebound hammer measurements.

---

[1]Note that the values might vary slightly from those in Excel, as the Python Plotly package uses a different calculation method.

Table 5.3: Statistical data of rebound numbers.

Test location	Quartile 1	Quartile 3	IQR	Median
S1	40	48	8	42
S2	40.5	45	4.5	42
S3	37.25	48.25	11	43
S4	41	48.25	7.25	46
Beam 1	67.25	71.25	4	69
Beam 7	70.75	73.5	2.75	72
Beam 13	67.75	75	7.25	71
Beam 18	72	74.5	2.5	73
Beam 23	68.75	72.25	3.5	72

A similar analysis can be made for the UPV data. It is recommended in EN 12504-4 [83] to use the mean of the data at a specific test location. The UPV dataset is too small to show data with boxplots effectively. Instead, Table 5.4 lists the mean UPV alongside the median of the rebound numbers. A notable distinction between the support beam and T-beams can be observed in terms of concrete quality, evident in both ultrasonic pulse velocities and Q-values. The values for the T-beams suggest high-strength concrete. Interestingly, an increase in rebound number doesn't consistently correlate with an increase in UPV. For instance, location S4 on the support beam exhibits the highest median Q-value but the lowest mean UPV. Similarly, beam 18 displays the highest median Q-value yet the lowest mean UPV. This observation diverges from findings in the literature; nevertheless, the overall trend persists and it's essential to consider several nuances:

- Given the relatively small size of the dataset, local variations can exert a significant influence on the measurements.
- Moisture content affects UPV measurements to a much greater extent than rebound hammer measurements.
- The Q-values were measured at the bottom of the T-beams, while the UPV measurements were taken from the sides.

Table 5.4: Mean ultrasonic pulse velocities and median of the rebound numbers.

Test location	UPV Transmission mode	UPV (m/s)	Rebound number Q (-)
S1	Semi-direct	3792	42
S2	Semi-direct	3532	42
S3	Semi-direct	3798	43
S4	Semi-direct	3477	46
Beam 1	Direct	4370	69
Beam 7	Direct	4486	72
Beam 13	Direct	4383	71
Beam 18	Direct	4286	73
Beam 23	Direct	4333	72

SonReb

A direct comparison with SonReb models from existing literature proves challenging due to their predominant use of R-values rather than Q-values, as explained in Section 2.7.5. While it's tempting to assume the R-value to be 10 units lower than the Q-values, as indicated by findings for pyroxene-granulite rock surfaces in [47], this introduces additional uncertainty and is thus not pursued. Instead, it's crucial for manufacturers to provide well-established conversions between devices available in the market.

The use of ultrasonic pulse velocity is limited in this context; it simply indicates that the T-beams exhibit high-strength concrete in contrast to the support beam's normal strength. Relying solely on UPV data for compressive strength conversion is not recommended mainly due to its susceptibility to moisture content. Models derived from wet-cured specimens in laboratory environments tend to yield significantly higher pulse velocities. An assessment for the compressive strength is therefore based on the measured Q-values only.

In Figure 5.10, two conversion curves are presented. The curve depicted to the left was constructed in 2023 using cubes of various compressive strength ranges, all cured for 28 days [91]. The rightmost curve in Figure 5.10 represents a large dataset from CEN/TR 17086 [92], with its 5th percentile exponential curve serving as the foundational background for Annex B of EN 13791 [46]. Additional Q-value conversion models for this extensive range of Q-values are nearly nonexistent at this point, or if available, they exhibit poor correlation.
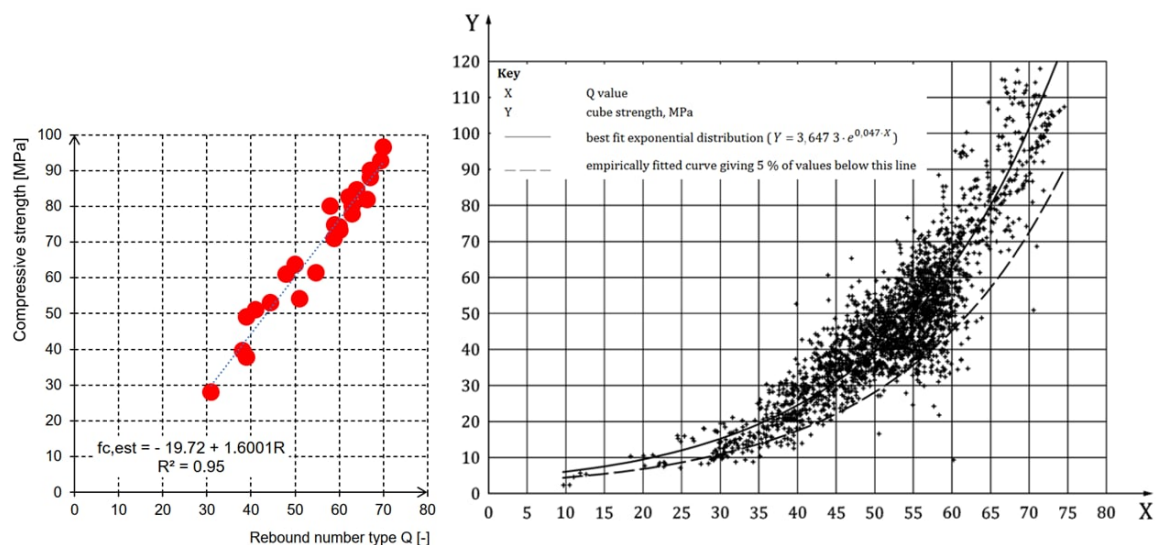
Figure 5.10: Rebound number Q vs cube compressive strength according to Nedeljkovic et al. [91] (left) and CEN/TR 17086 [92] (right).

The models have been applied to the rebound hammer measurements of the Sluinerweg viaduct of which the results can be found in Table 5.5. Here, it can be observed that the models are not in agreement with each other. For the higher strength T-beams, the average differs by approximately 10 MPa, but the spread is much greater in the CEN/TR 17086 model. For the support beam, the predicted strengths differ by more than 20 MPa, yet the spreads are nearly equal.

Table 5.5: Cube compressive strengths based on two rebound number Q
conversion models.

Test location	Q (-)	$f_{c,cube}$ (MPa) [91]	$f_{c,cube}$ (MPa) [92]
S1	42	47.5	26.3
S2	42	47.5	26.3
S3	43	49.1	27.5
S4	46	53.9	31.7
	Mean	**49.5**	**28.0**
	Std	**3.0**	**2.6**
Beam 1	69	90.7	93.4
Beam 7	72	95.5	107.6
Beam 13	71	93.9	102.6
Beam 18	73	97.1	112.7
Beam 23	72	95.5	107.6
	Mean	**94.5**	**104.8**
	Std	**2.4**	**7.3**

5.2.4   Corrosion assessment

Half-cell potential

As described in Section 4.2, half-cell potential measurements were performed using the Gecor-10 point electrode and the Profometer PM8500 wheel electrode, both using a Cu/CuSO$_4$ reference electrode. The readings obtained with the Gecor-10 had to be manually recorded and stored in Excel, whereas those from the Profometer could be directly visualized in-situ. Figure 5.12 illustrates the measurements carried out on the support beam using the Profometer. In this representation, values exceeding 0 mV are colored in green, those below -100 mV in red, and those falling between 0 and -100 mV in yellow. The Gecor-10 measurements were conducted along a horizontal line over the middle of the support beam, corresponding to lane 2 in Figure 5.12, and are presented in Figure 5.11.
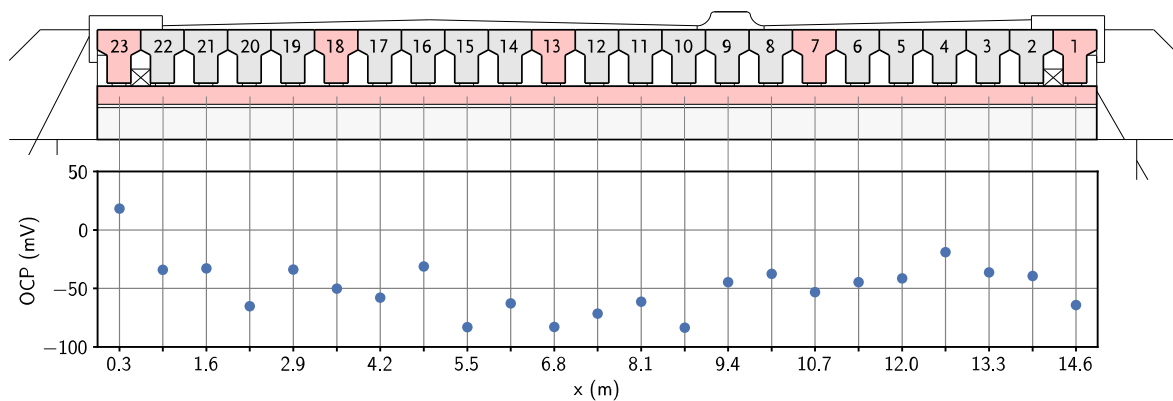
Figure 5.11:   Distribution of Gecor-10 half-cell potential measurements
across the length of the support beam.
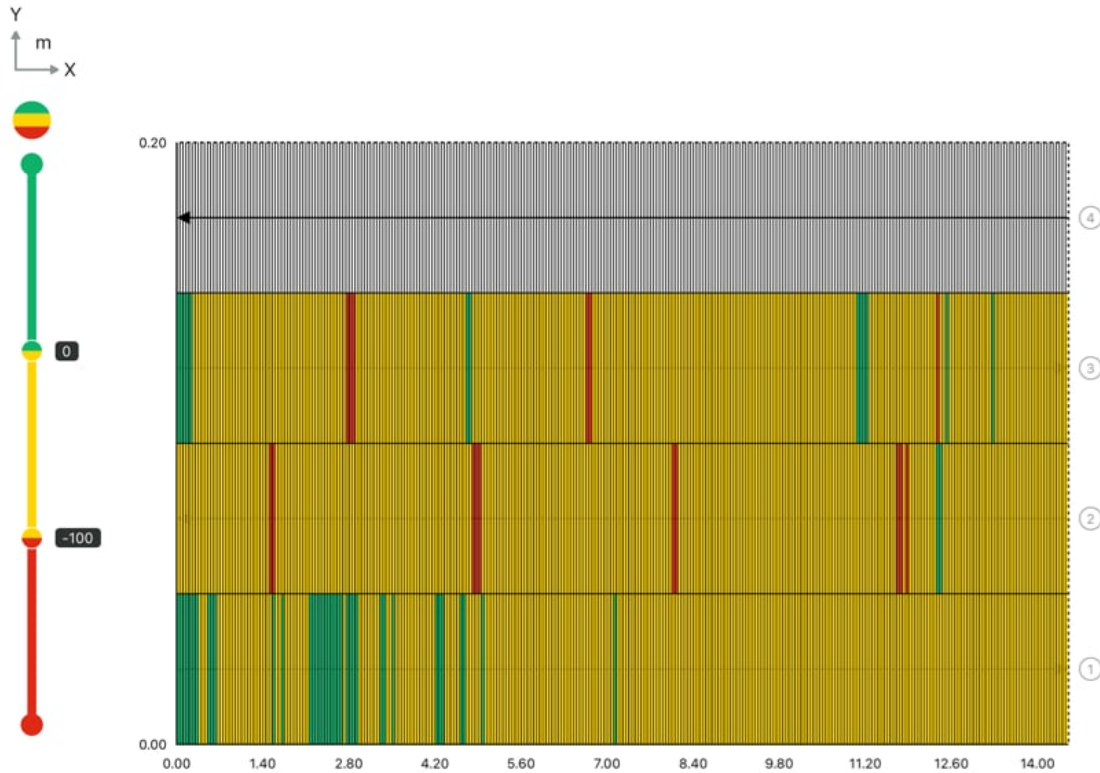
Figure 5.12: Half-cell potential measured on the support beam using the
Profometer PM8500 Cu/CuSO$_4$ wheel electrode.

The measurements are presented in a boxplot in Figure 5.13, with Table 5.6 providing
the corresponding statistical values. Analysis of this table reveals that both devices are in
agreement, showing similar data spreads. However, the Profometer displays more local
minima and maxima, which is not surprising given its significantly larger number of data
points, exceeding that of the Gecor-10 by more than 12 times.

Figure 5.13: Boxplots of the half-cell potentials measured on the support
beam using the Gecor-10 and Profometer PM8500.

Table 5.6: Statistical data of half-cell potentials in mV.

Device	N	Quartile 1	Quartile 3	IQR	Median	Mean	Std
Gecor-10	23	-64.1	-34.1	30.0	-44.5	-48.3	23.2
Profometer PM8500	290	-53.0	-31.0	22.0	-39.5	-45.0	24.1

The half-cell potential maps for the T-beams measured with the Profometer can be found in Appendix F.3, here the majority shows positive potentials, in some areas exceeding 200 mV, indicating dense concrete or potentially high surface carbonation. The half-cell potential measurements performed on the T-beams using the Gecor-10 can be observed in Figure 5.16. In conclusion, the following observations can be made:

- Both the Gecor-10 point electrode and Profometer PM8500 wheel electrode (both $Cu/CuSO_4$) show good agreement with each other.
- The potentials measured on the support beam generally show negative values, typically up to around -100 mV. In contrast, the high-strength T-beams predominantly display positive potentials, with some areas exceeding 200 mV. Although the support beam exhibits seven local areas with potentials below -100 mV, none of them drop below -200 mV. Based on the half-cell potential measurements, the probability of corrosion is therefore considered low for both the support beam and the T-beams.

Resistivity

Resistivity measurements were mainly performed on the support beam conform the procedure described in Section 2.7.6 using the Proceq Resipod and Gecor-10 Wenner probe (Sensor C). A third approach was subsequently introduced, involving an estimation of the resistivity derived from the concrete resistance calculated using the guard ring (Sensor A). This method is described in the Gecor-10 manual, represented by Equation 5.1. For the Gecor-10, with a counter electrode diameter of 3 centimeters, this results in $0.06R_c$.

$$\rho = 2 \cdot D \cdot R_c \tag{5.1}$$

where:

D = diameter of the counter electrode (m)
R_c = concrete electrical resistance (kΩ)

Resistivity measurements on the T-beams were only conducted using the Resipod due to time constraints. The corresponding results are presented in Table 5.7. The beams demonstrate significantly high resistivity values, with the outer and most exposed beams 1 and 23 showing the lowest resistivity. Nonetheless, these findings suggest that the probability of corrosion is negligible.

Table 5.7: Mean resistivity measured at the underside of the beam heads using the Resipod.

	Mean resistivity (k$\Omega \cdot$ m)
Beam 1	3.36
Beam 7	4.49
Beam 13	4.46
Beam 18	3.89
Beam 23	3.63

The measurements performed on the support beam are presented in Figure 5.14 and summarised in a boxplot in Figure 5.15, with Table 5.8 providing the corresponding statistical values.
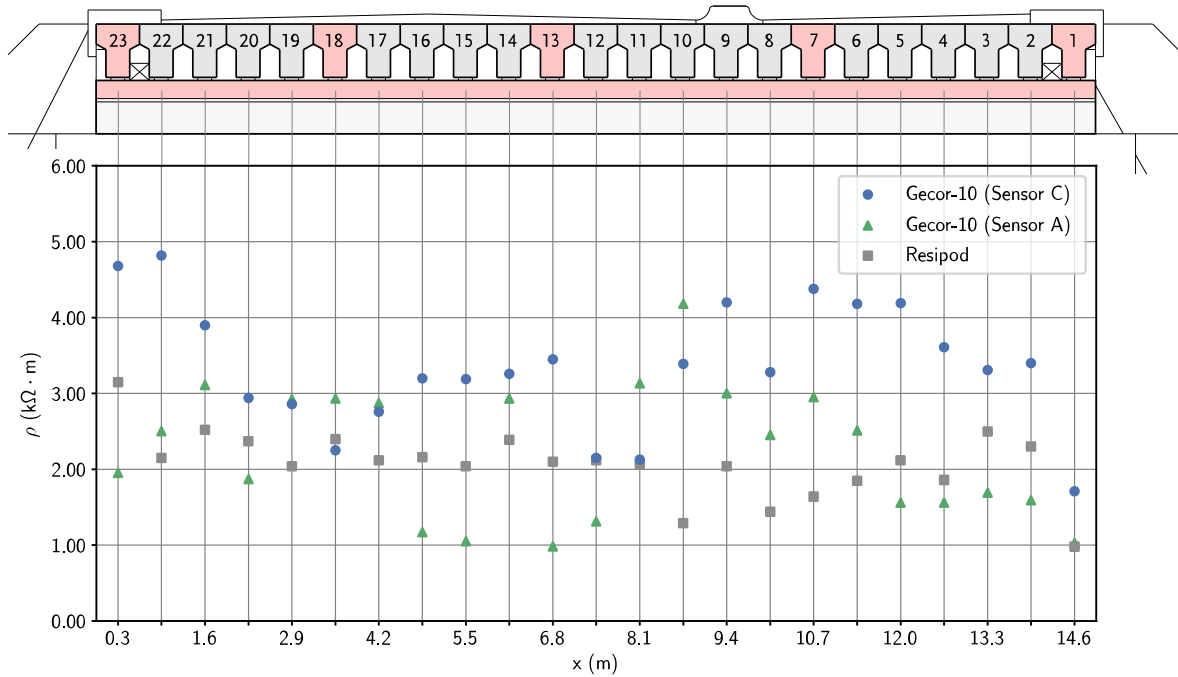
Figure 5.14: Distribution of the resistivity values across the middle of the support beam.

Figure 5.15: Boxplots of the resistivity measured on the support beam using the Gecor-10 and Resipod.

Table 5.8: Statistical data of resistivity measurements in $k\Omega \cdot m$.

Device	N	Quartile 1	Quartile 3	IQR	Median	Mean	Std
Gecor-10 (C)	23	2.88	4.11	1.23	3.31	3.36	0.83
Gecor-10 (A)	23	1.56	2.93	1.37	2.45	2.23	0.87
Resipod	23	1.91	2.35	0.44	2.12	2.07	0.45

Two observations can be made from this data analysis:

- The data spread for the Gecor-10 is almost twice as large as that for the Resipod.

- Both the mean and median values obtained with the Gecor-10 Wenner probe are more than 1 k$\Omega \cdot$ m higher than those obtained with the Resipod. However, the method based on the guard ring yields values closer to those obtained with the Resipod.

Figure 5.14 illustrates that the Gecor-10 (Sensor C) and the Resipod, both Wenner probes, follow a trend to a certain degree, whereas the method employing the guard ring (Sensor A) shows more random fluctuations. Although all measured values for resistivity are high, indicating a negligible probability of corrosion, the differences between the two Wenner probes call for further investigation. Consequently, additional analysis was carried out in the laboratory, which is outlined in Appendix G. It is worth noting that the method using the guard ring was not further evaluated due to its time-consuming nature. The following conclusions can be drawn based on the in-situ measurements and the laboratory test described in Appendix G:

- The Resipod consistently reports lower resistivities than the Gecor-10, with nearly a factor of 2 difference observed in the laboratory for the non-corroded rebar, as well as in-situ. For the corroded rebar, the discrepancies between the measurements obtained by the two devices are smaller. Nevertheless, the differences are too significant to conclude that both devices fall within the same range of error for assessing the probability of corrosion.
- In the laboratory, both devices exhibit a similar trend where an increase or decrease in measurements from one point to another is well reflected by the other device. However, this trend is less pronounced in-situ.
- Unlike the Resipod, the Gecor-10 displays the applied current on the outer electrodes and the measured potential on the middle electrodes.
- Wetting the support beam in-situ did not appear to be the cause of the problem, as the substantial difference in measurements persisted in the laboratory under controlled conditions.
- No correction factors are applied for geometry, as both devices have similar probe spacing—38 mm for the Resipod and 35 mm for the Gecor-10. However, the contact area for both devices differs.
- This data alone is insufficient to conclude whether a device is functioning inadequately. However, the Resipod provides more stable measurements, can be used on rougher surfaces (due to its spring electrodes), and tends to be more conservative compared to the Gecor-10.

Corrosion current density

The corrosion current density was evaluated at the same locations where the half-cell potential and resistivity measurements were conducted. Combining all earlier results, it is evident that the probability of corrosion in the assessed locations is negligible to low, as presented in Figures 5.16 and 5.17. The green zone in these figures indicates a low risk of corrosion, while the orange zone signifies a moderate risk of corrosion. The red zone represents a high risk of corrosion. Any data points in the white zones are inconclusive, and those within the grey zones are considered inconsistent. Figure 5.18 presents the previously shown distribution of potential and resistivity values for the support beam, along with the measured current densities obtained with the Gecor-10. With the exception of some outliers, a clear trend can be observed where decreasing potential and resistivity values coincide with an increase in current density.
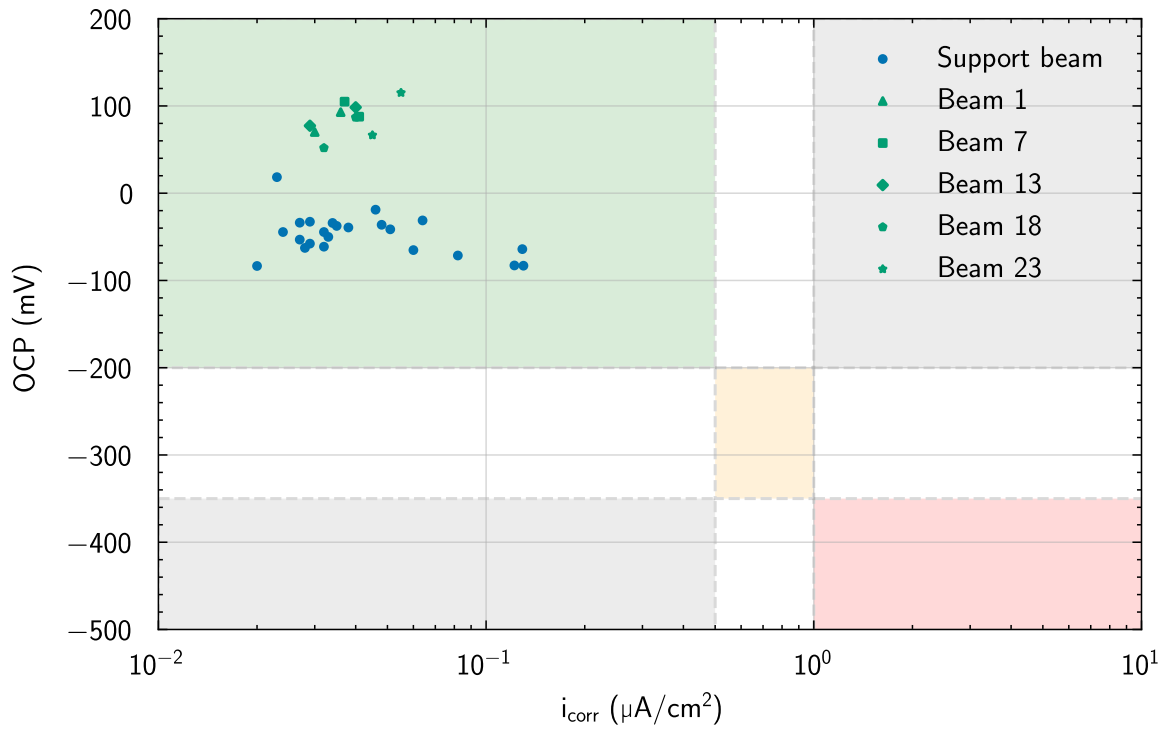
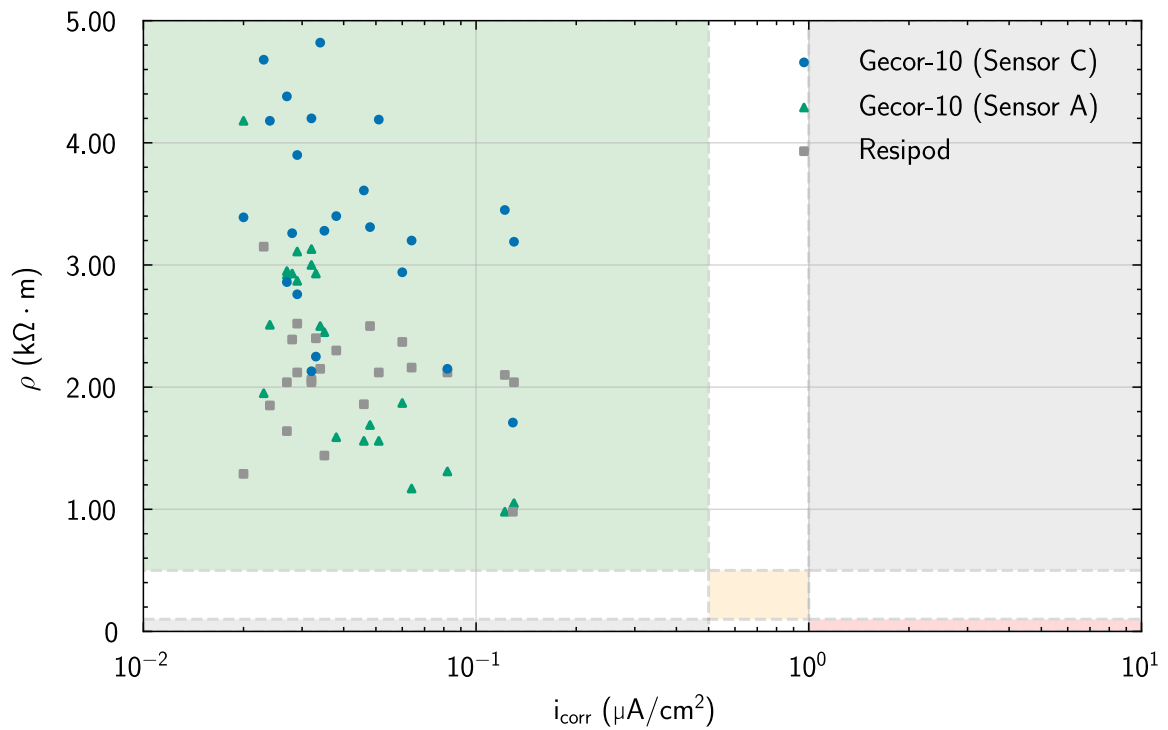Figure 5.16: Corrosion current density vs OCP for the support beam and T-beams.

Figure 5.17: Corrosion current density vs resistivity for the support beam.
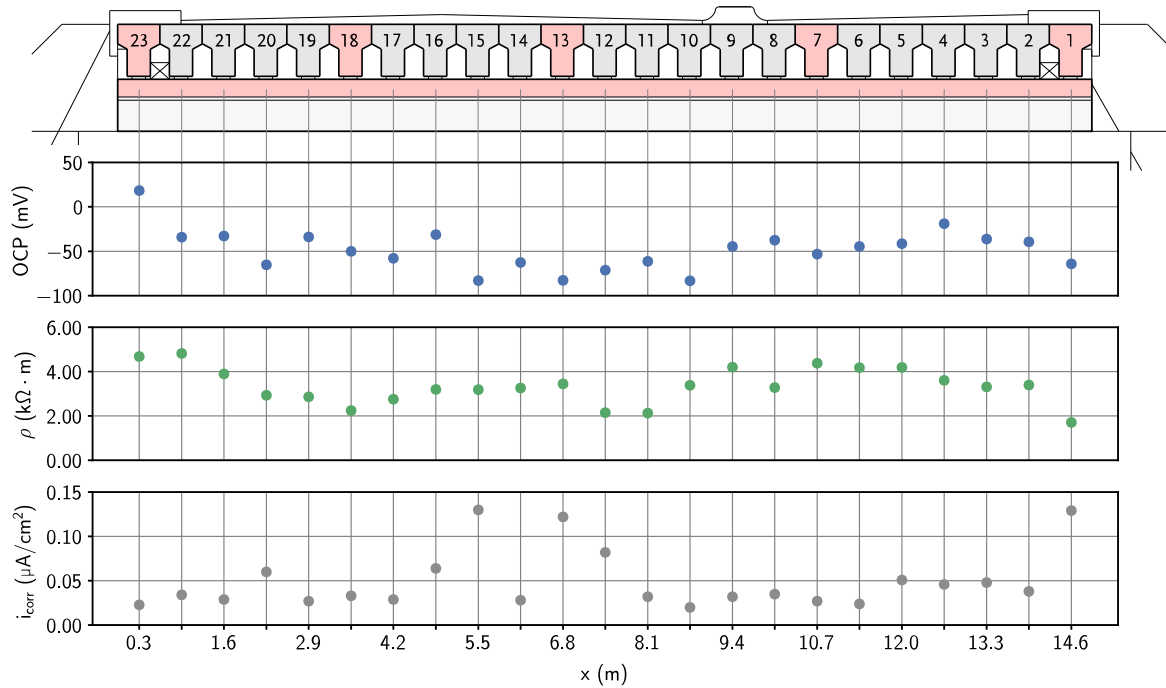
Figure 5.18: Corrosion assessment of the support beam with the Gecor-10.

5.3   Destructive verification

5.3.1   Compressive strength

The results for the compressive strength tests on the support beam are shown in Table 5.9

Table 5.9: Compressive strength test results for the support beam.

	S1	S2	S3	S4
Force (kN)	533.8	391.1	299.8	363.3
Area (mm^2)		7854.0		
$f_{c,cyl,1:1}$ (MPa)	70.5	49.8	38.2	46.3

Unfortunately the result for Core S1 proved unusable, attributed to an excessively high loading speed employed during compression. The mean and standard deviation for the remaining three cores are 44.8 MPa and 6.0 MPa, respectively, as per Equation 2.43 and 2.44. According to EN 13791 [46], the support beam can be accounted for as a small test region since the volume is less then 15 m^3 and the strengths lie within the 15% interval from the mean. The mean can therefore be regarded as the characteristic in-situ compressive strength.

$$38.1 \leq f_{c,is} \leq 51.5 \text{ MPa} \tag{5.2}$$

Right before the demolition of the Sluinerweg viaduct, a possibility arose to take cores from some of the beams. The cores were grinded and stored for 48 hours in a wet chamber and loaded with a loading speed of 0.6 MPa/s according to EN12504-1 [88].

Table 5.10: Compressive strength test results for the T-beams.

	B4	B6	B7	B8	B16	B18
Force (kN)	648.9	576.7	546.9	639.2	502.4	507.3
Area (mm^2)			6939.8			
$f_{c,cyl,1:1}$ (MPa)	**93.5**	**83.1**	**78.8**	**92.1**	**72.4**	**73.1**

When considering the beams as one test region, the procedure described in 2.8 can be applied to this dataset. With a mean of 82.2 MPa and a standard deviation of 9.1 MPa, the Grubbs test results in:

$$\frac{f_{c,is,highest} - f_{c,m(n)is}}{s} = \frac{93.5 - 82.2}{9.1} = 1.241 < 1.973 \tag{5.3}$$

$$\frac{f_{c,m(n)is} - f_{c,is,lowest}}{s} = \frac{82.2 - 72.4}{9.1} = 1.077 < 1.973 \tag{5.4}$$

Therefore, according to the Grubbs test, the minimum and maximum compressive strength values are not considered outliers. Additionally, all values lie within 15% of the mean.

$$69.9 \leq f_{c,is} \leq 94.5 \text{ MPa} \tag{5.5}$$

The values for the 1:1 cylinders can be considered equivalent to cubes with sides measuring 150 x 150 mm according to EN 12504-1 [88]. It is observed that both Q-value conversion models presented in Section 5.2.3 overestimate the compressive strength, but the model of CEN/TR 17086 shows the poorest fit.

Table 5.11: Comparison of rebound number Q conversion models with measured cube compressive strength in MPa.

Test location	f$_{c,cube}$ [91]	f$_{c,cube}$ [92]	f$_{c,is,mean}$
Support beam	49.5	28.0	44.8
T-beams	94.5	104.8	82.2

5.3.2 Carbonation

Table E.1 presents the average carbonation depth for the 16 cores, rounded to the nearest 0.5 mm. In instances of a distinct carbonation 'pit', the maximum value is provided and is excluded from the overall calculation. An overview of the splitted cores with the marked carbonation front can be found in Appendix E.2.

Table 5.12: Carbonation depths in mm.

Supporting beam		T-beams	
Core	$x(t)_m$	**Core**	$x(t)_m$
C1	1.5 (max = 9.5)	**C1-1**	0.5
C2	1.5	**C2-1**	10.5 (max = 18)
C3	2.5	**C1-7**	0.5
C4	5	**C2-7**	1.5
C5	5	**C1-13**	6 (max = 14)
C6	5	**C2-13**	1.5 (max = 10)
		C1-18	0.5
		C2-18	2.5
		C1-23	0.5 (max = 6.5)
		C2-23	0.5

What is noteworthy is that the difference in carbonation depth between two cores taken around the same location can be quite significant, as particularly shown in the case of C1-1 and C2-1, this underscores why the *CUR Aanbeveling 72* advises consistently taking a pair of cores for carbonation analysis. Furthermore, the carbonation depths observed in the T-beams may not be notably deep, indicating that carbonation alone may not be the primary factor contributing to the high measured potentials.

Compared to previous carbonation measurements conducted on the Sluinerweg (Table 3.7), the carbonation depths observed on the east side of the support beam appear similar, both measuring 5 mm. However, there is a notable difference on the west side, where measurements showed 3 mm in 2020 and 1.5 mm in 2023. This variation is striking as one would expect a stable carbonation depth or an increase over this period of time. This difference could be attributed in part to variations in measurement methods and their respective accuracies. The carbonation depth was directly measured in-situ in 2020.

5.3.3   Chloride content

The results of the Volhard titrations are shown in Figure 5.19, with a comprehensive overview of all recorded values provided in Appendix E.3. Given the low chloride content measured and the time-consuming nature of the test, it was decided to analyse only the first two discs of every core. However, for the core with the highest initial chloride content (CL3), the entire profile was determined. A good fit with Fick's 2nd law was obtained for this chloride profile as illustrated in Figure 5.20.
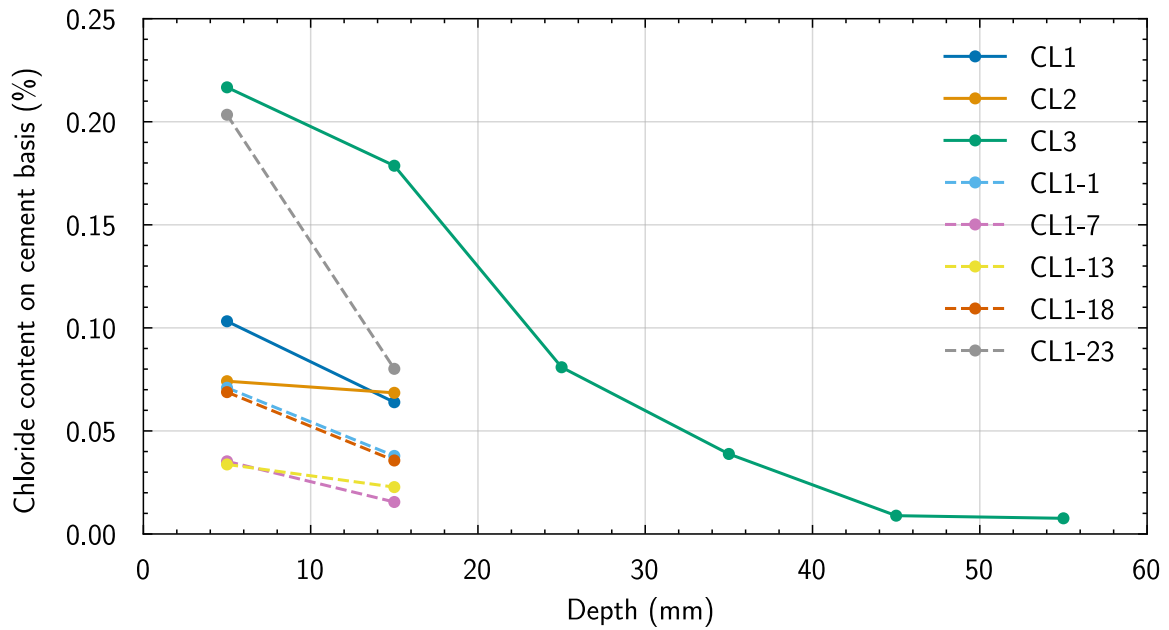
Figure 5.19: Chloride profiles.

$$C_x = 0.273 - 0.273 \times \mathrm{erf}\left(\frac{x}{35.570}\right)$$
$$R^2 = 0.97$$
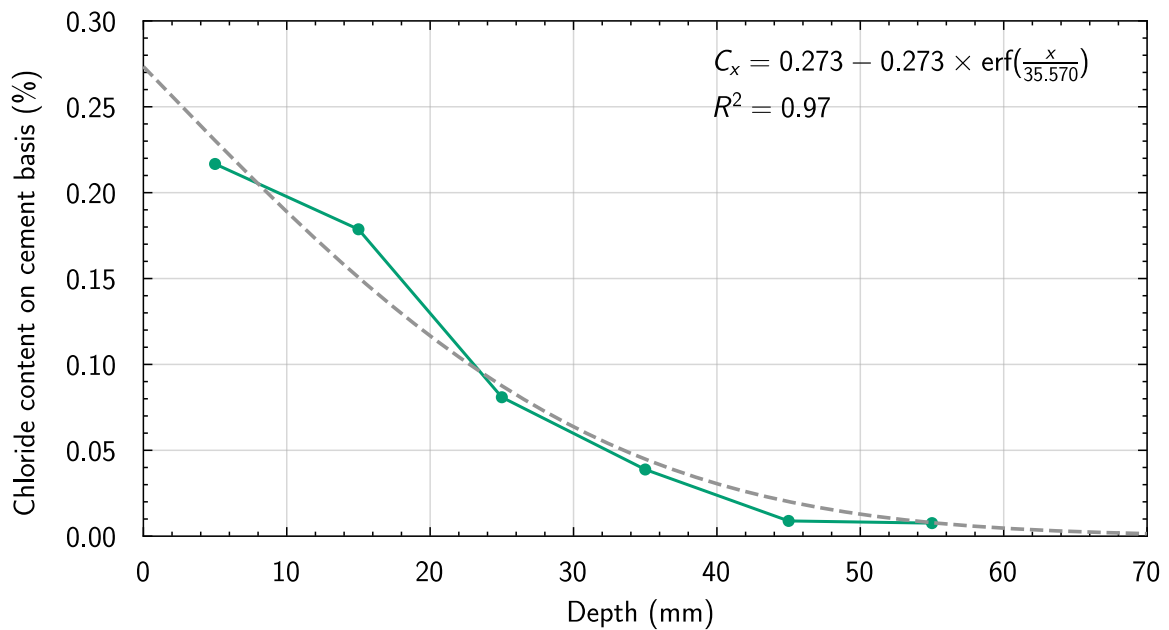
Figure 5.20: Fick's 2nd law fitted to the chloride profile of core CL3.

It should be emphasised that the cores were extracted from the underside of the T-beams at a distance of 1.15 m from the end of the beams, as indicated in Figure 4.13. Additionally, wet cutting of the cores was the only feasible option in the laboratory. Taking these factors into account, the following conclusion can be drawn:

- Bubbling and foaming when introducing HNO_3 to the crushed concrete samples were most pronounced in samples characterised by the highest carbonation depth.
- All recorded chloride content values are notably low. None of the measurements exceeds the critical chloride content of 0.5%, as specified in *CUR aanbeveling 121*.

This demonstrates that the corrosion assessment using NDTs has provided a reliable indication.

- The T-beams typically demonstrate a lower chloride content compared to the supporting beam.
- Core CL3-01 exhibits the highest chloride content and highest carbonation depth within the supporting beam. Additionally, at this position it demonstrates the highest corrosion current density at 0.129 $\mu A/cm^2$.
- Among the T-beams, Beam 23 exhibits the highest chloride content and the highest corrosion current density at 0.055 $\mu A/cm^2$, but lowest carbonation depth among all measured T-beams. This can be explained by examining the placement of the drainage system, as illustrated in Figure 5.21, which is situated between beam 22 and 23.
- Overall, it can be concluded that the leakage of the joints in the past did not have a significant impact on the durability of the measured sections of the Sluinerweg viaduct.
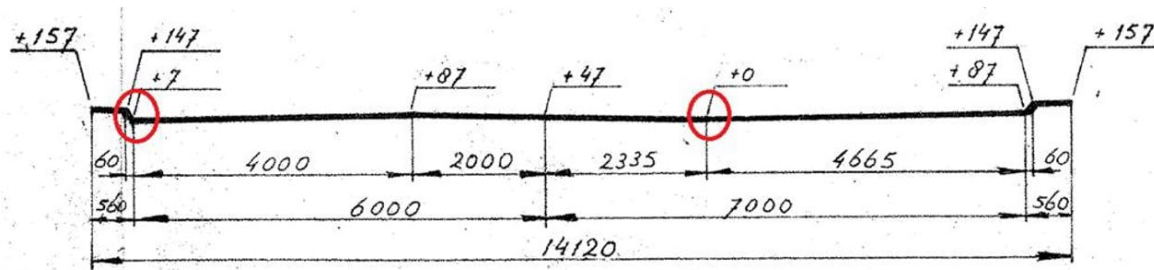
Figure 5.21: Location of the drainage system.

The observation that the T-beams generally have lower chloride contents than the support beam, despite being the first to come into contact with chlorides, suggests that the concrete structure may be dense. This observation aligns with the results obtained for compressive strength, both through destructive and non-destructive testing. Figure 5.22 displays an epoxy-impregnated polished section under ultraviolet light of a core from one of the T-beams, confirming a seemingly dense pore structure. Unfortunately, no polished section analysis was conducted for the support beam.

(a)   (b)
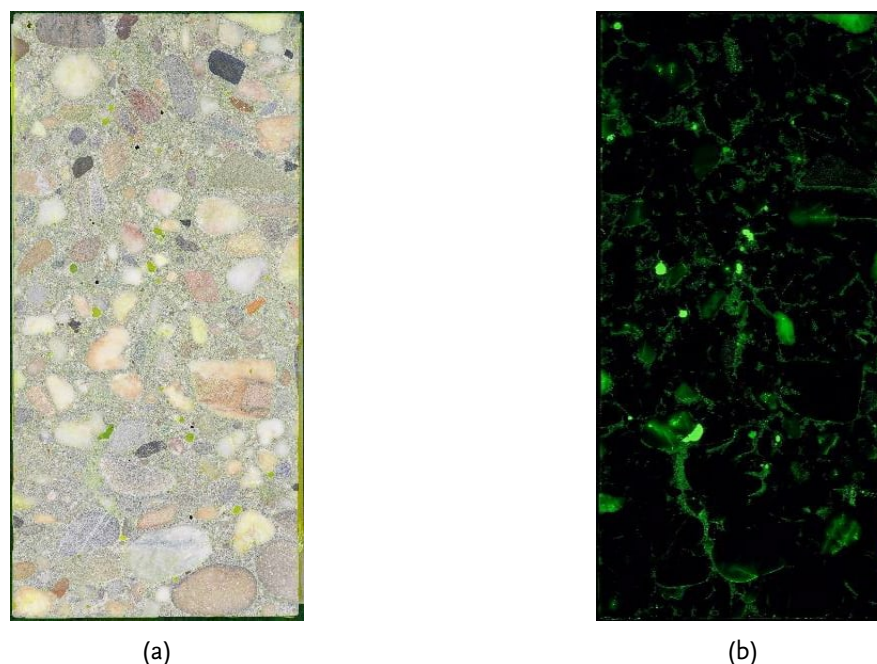
Figure 5.22: Epoxy-impregnated polished section of a core from a beam head
under normal lighting conditions (a) and ultraviolet light (b) [93].

Comparison with 2020 inspection
The measured chloride content can be compared with that measured in 2020, as presented
in Appendix C. Figure 5.23 shows the locations where the chloride cores were extracted in
2020 relative to those extracted in 2023. The core at location 1 can be compared to CL1,
while the core at location 2 corresponds to CL3. However, the core at location 2 cannot be
compared with CL2 due to the significant distance between the two locations; moreover,
location 2 is much closer to the drainage system. Table 5.13 presents an overview of the
measured chloride contents on a cement basis.

Table 5.13: A comparison of the chloride content measured on a cement
basis in the support beam in 2020 and 2023.

Location	Depth (mm)	Chloride content 2020 (%)	Depth (mm)	Chloride content 2023 (%)
1 / CL1	0 - 20	0.32	0 - 10	0.10
			10 - 20	0.065
3 / CL3	0 - 20	0.34	0 - 10	0.22
			10 - 20	0.18
	20 - 40	0.05	20 - 30	0.08
			30 - 40	0.035
	40 - 60	0.004	40 - 50	0.01
			50 - 60	0.01
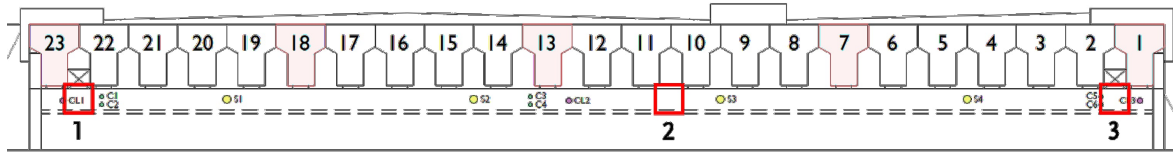
Figure 5.23: Location of the chloride cores extracted in 2020 relative to the cores extracted in 2023.

In the first 20 mm, the chloride content measured in 2020 exceeds that of 2023, albeit with non-alarming differences. A slightly higher chloride content is observed in the 2023 measurements for CL3 at depths beyond 20 mm. The 2020 measurements were conducted using RCT with an estimated cement content of 14wt%, a less precise method compared to the Volhard titration employed in this research, which provides an exact calculation of the cement content. The cement weight varied between the samples, ranging from 11.5wt% to 22.4wt%.

Chapter 6

Discussion

The following discussion draws upon the findings of this research to address three fundamental aspects concerning the non-destructive material evaluation of concrete viaducts which are directly related to the sub-questions outlined in Section 1.4:

- Distrust in applying NDTs in-situ.
- Effectiveness of NDTs in-situ.
- Reflection on previous inspection regimes for the Sluinerweg viaduct.

The second point addresses the sub-questions concerning the effective use of different NDTs and their correlation with destructive measurements for evaluating the material status of a reinforced concrete viaduct, as well as the practical challenges encountered during in-situ implementation of these tests. The final point corresponds with the sub-question regarding the effectiveness of the earlier employed inspection methodology. All of these factors should be taken into account when formulating a practical methodology.

6.1   Distrust in applying NDTs in-situ

As mentioned in Chapter 1, there is a certain degree of distrust regarding the in-situ application of NDTs in the Netherlands[1]. The fact that many of these techniques are relatively old, their usefulness has been proven frequently, yet they are still applied relatively infrequently, underscores this skepticism. The distrust can be attributed to a lack of experience with these techniques, a lack of codes or guidelines, and conflicting results observed when employing them in-situ. However, this distrust is often unfounded. For example, as demonstrated by this research, with the appropriate application of NDTs, the installation of cathodic protection would have been unnecessary for the Sluinerweg viaduct.

With the increasing number of concrete structures requiring maintenance and in line with Rijkswaterstaat's VenR policy, the use of NDTs becomes increasingly important for conducting efficient inspections and reducing the need for core sampling. This was also the primary motivation behind initiating the Sluinerweg pilot project. This research provided valuable insights into the effectiveness of NDTs and their accompanying software, with the objective of enhancing confidence in these methods among industry professionals by demonstrating their challenges and advantages. Ultimately, the aspiration is that this research will play a role in encouraging the increased use of NDTs in the future. The next steps will involve conducting additional inspections similar to the one outlined in this research, while also considering structures in conditions more severe than those of

---

[1]It is worth noting, however, that some common NDTs such as the cover meter and half-cell potential are occasionally used in practice.

the Sluinerweg viaduct. By consolidating all the data, recommendations can be formulated and integrated into codes, guidelines, and training programs. This will enable Rijkswaterstaat to require its subcontractors to implement these tests in-situ.

6.2 Effectiveness of NDTs in-situ

6.2.1 GPR and UPE

The GPR proved to be a highly valuable tool for locating reinforcement and tendon ducts, primarily due to advancements in software and the compactness of modern devices. Results obtained with GPR were also found to be more accurate than those obtained with the standard cover meter, and it can penetrate to greater depths. For structures lacking drawings, GPR can be particularly beneficial in mapping out reinforcement. However, it is important to consider that anything metallic can interfere with the device; for instance, it was impossible to measure through the conductive CP coating. Looking behind a thick reinforcement mesh with GPR is therefore also difficult, and that's where UPE can come in handy.

The combination of GPR and UPE, along with a semi-destructive borehole and an endoscope, can be a great tool for investigating possible grouting defects in a tendon duct. However, the boreholes of 12 mm used in this research were on the small side, making judgment rather difficult. As some suspicious areas were found with this method, but no grouting defects were found, the question arises about the effectiveness of the method in detecting real grouting defects. This method should therefore be further investigated to determine its true effectiveness.

6.2.2 Rebound hammer and UPV

The rebound hammer is a straightforward and time-efficient method for estimating the compressive strength of concrete. However, its effectiveness relies heavily on the quality of the conversion models. Newer Q-value rebound hammers demonstrate improved performance and applicability across a broader range of compressive strengths, as detailed in Section 2.7.5. Nonetheless, only a limited number of conversion models with significant correlations are available in the literature. The UPV method faces similar challenges, albeit slightly less time-efficient and significantly influenced by concrete moisture content compared to the rebound hammer. This poses a significant challenge in establishing reliable conversion models. Literature has consistently shown that combining rebound hammer and UPV data enhances model correlations. Despite this, the utility of such SonReb models remains debatable, as evidenced by this research. Nevertheless, one could argue that UPV still holds value in estimating concrete quality by employing empirically determined limits; for instance, values below 3 km/s may indicate poor concrete quality. Additionally, UPV can assist in detecting concrete defects, although achieving accuracy requires calibration specific to the structure under investigation. Currently, the most effective in-situ application would involve using UPV as a complementary method to the rebound hammer, particularly in instances of uncertainty or when the rebound hammer cannot be applied.

6.2.3 Probability of corrosion

In this research, the probability of corrosion was assessed using three different techniques: half-cell potential, resistivity, and corrosion current density measurements. No active corrosion sites were found, except for some minor corrosion damage. This makes evaluating the methods challenging, but valuable lessons were still learned. For all three techniques, the empirically established limits for determining the probability of corrosion can be subject to discussion. These limits depend on various concrete properties and external factors. It would be beneficial to further investigate these limits and compile an overview with different limits for different types of structures and concrete compositions.

Half-cell potential
Half-cell potential measurements are reliable when conducted by an experienced operator. Both the wheel electrode and point electrode yielded similar results, although the wheel electrode allows for recording a larger number of values in a shorter amount of time. However, in narrow spaces, a point electrode may be more practical. The Profometer Corrosion software enables quick on-site assessment of the probability of corrosion.

Resistivity
Concrete resistivity measurements conducted in-situ yielded questionable results when comparing the Gecor-10 Wenner probe with the Proceq Resipod. Despite similar probe spacing, the Resipod consistently records lower resistivity values compared to the Gecor-10, prompting further laboratory investigation. Although this investigation ruled out moisture content as the cause, it did not identify the underlying reason for the differences. It can be said however that the Resipod demonstrated greater stability and is more conservative than the Gecor-10. While resistivity measurements should not be solely relied upon, they should not be disregarded either. Among all corrosion assessment methods, resistivity measurement remains the fastest.

Corrosion current density
Corrosion current density measurement proved to be valuable and in good agreement with other corrosion measurements. As the only technique capable of providing information about the rate of corrosion, it serves an important role in corrosion assessment. However, measurement time can be lengthy, and sufficient expertise is required to interpret the results in situ. Additionally, there are currently limited options available on the market for this specific purpose. The Gecor-10 offers a three-in-one solution, providing reliable results in the lab and decent performance in situ, although the accuracy of the resistivity measurements may be questionable. Data processing is analog, which can be time-consuming and prone to errors.

6.2.4 Costs of NDTs

This research does not delve into the specific costs associated with the NDT methods themselves, focusing more on highlighting their benefits. Conducting a detailed cost-benefit analysis would therefore undoubtedly be valuable. With the insights gained from this research however, it is possible to provide a qualitative assessment. This is presented in Table 6.1, where three key categories—expenses, expertise, and in-situ effectiveness—are rated as either low, medium, or high. To determine these ratings, the NDT methods

are compared to one another based on their specific application, such as compressive strength assessment.

Table 6.1: Qualitative assessment of expenses, expertise and effectiveness of NDTs in-situ based on the inspection of the Sluinerweg viaduct.

NDT	Expenses	Expertise	Effectiveness in-situ
Rebound hammer	Low	Low	High
UPV	Medium	Medium	Low
GPR	High	Medium	High
UPE	High	High	Medium
Half-cell potential	Low	Medium	High
Resistivity	Low	Low	Medium
Corrosion current density	Medium	High	Medium

The rebound hammer turned out to be the most effective method for the in-situ assessment of compressive strength. Not only is it cost-effective, but it also demands less expertise compared to UPV. Furthermore, for concrete quality assessment, UPE demonstrated superior performance over UPV. While GPR is an expensive method and requires a certain level of expertise, recent advancements in software have significantly simplified interpretation. UPE is also an expensive method and is less adept at detecting reinforcement and prestressing compared to GPR, although it shows promise in identifying grouting defects. Half-cell potential measurements, while inexpensive and requiring moderate expertise, have proven highly effective. Conversely, resistivity is a cost-effective method requiring minimal expertise. However, its effectiveness is debatable, as evidenced by the discrepancies between the Resipod and Gecor-10 Wenner probes. Corrosion current density measurement demands a higher level of expertise compared to the other corrosion assessment methods, yet it stands out as the sole test capable of estimating corrosion rates. However, its effectiveness in assessing pitting mechanisms is uncertain, and the prolonged waiting time reduces its effectiveness.

6.3   Reflection on previous inspection regimes

The inspection regime previously employed for the Sluinerweg viaduct, as described in Chapter 3, is also used for similar structures within the Liggerkoppen project. Based on the results of this research, one could argue that the application of cathodic protection on the Sluinerweg viaduct may not have been necessary, which could have potentially saved costs.

In prior inspection regimes, the chloride content in the supporting beam at specific locations was assessed, and conclusions regarding the T-beams were drawn from these findings. However, the results of this research suggest that reconsideration of this inspection regime may be necessary. Firstly, the mix design of the support beam and T-beams differs, with the T-beams exhibiting a much higher strength. Additionally, as highlighted in Section 5.3.3, the location of the highest chloride content in the support beam does not necessarily align with the location of the highest chloride content in the T-beams. It is essential to note, however, that the chosen locations for the chloride cores in the T-beams

were suboptimal due to physical limitations of the coring device. Coring closer to the support (and consequently, to the joint) was not possible. Additionally, coring from the top of the deck was not feasible due to ongoing traffic. However, even if it had been possible, it is unlikely to have made a significant difference due to the presence of a thick asphalt layer.

An argument can be made that a high chloride content identified in the support beam could potentially serve as an upper limit for what is present in the beam heads, as water accumulates on the support beam. This research serves as evidence of that, with the chloride content in the support beam being higher than that of the T-beams, except for beam 23, which is closest to the drainage system. Practical considerations regarding structural safety must also be taken into account, particularly given the precision required when drilling into slender prestressed beams. Therefore, while the inspection regime employed in the past may not be optimal, it is certainly reasonable given these challenges.

Chapter 7

Conclusions and recommendations

The inspection of the Sluinerweg viaduct posed significant challenges and provided valuable lessons. Reference to the CASE model from Chapter 1 can be insightful in this context. Coring in the T-beams was deemed **unsafe** due to the presence of prestressing, alongside the ongoing use of both the viaduct and the highway underneath at the time of inspection. Ultimately, after careful consultation with a structural engineer, it was decided to extract only small cores from the T-beams. Certain areas, such as the back of the beam heads, proved **inaccessible** to certain NDT methods. Additionally, accessing the more damaged middle support proved impractical due to its location between highway lanes, which would have required a **time-consuming and costly** operation. Measurements were conducted by **experienced** NDT professionals to ensure safety and accuracy. The original inspection plan had to be adjusted as some NDT measurement took longer than anticipated, highlighting the non-standard nature of inspections involving a diverse range of NDT methods.

7.1 Conclusions

The following two main conclusions can be formulated:

- The inspection of the Sluinerweg viaduct demonstrated the effectiveness of several NDTs in-situ, with good correlation observed with destructive verification. These findings should help to build trust in the reliability of these methods for future inspections.
- The previous inspection regimes used within the Liggerkoppen project can be regarded to be suboptimal in some respects. The inspection of the Sluinerweg viaduct revealed no signs of active corrosion. Therefore, the application of a cathodic protection system could potentially have been avoided. The previous inspection regime, however, is reasonable given the complexity of the project in terms of safety and accessibility.

Additionally, more specific conclusions can be drawn regarding the NDTs used:

- GPR should be preferred over a standard cover meter due to its proven accuracy, compactness, and ability to provide comprehensive information about the reinforcement and prestressing layout. However, estimating rebar diameters with GPR can be challenging. The consistency of the data with the provided drawings is encouraging, especially since drawings are often unavailable.

- The combination of GPR, UPE, and an endoscope shows promise for inspecting tendon ducts. However, the use of 12 mm boreholes poses challenges for accurate judgment. While suspicious areas were identified, no grouting defects were detected, raising questions about the method's effectiveness.
- Measuring through the conductive CP-coating is impossible with GPR, but it does not pose any problems with UPE. Therefore, a tendon duct inspection using a combination of GPR and UPE should be conducted preferably *before* the application of any CP system.
- The KCG-layer, previously applied to numerous structures in the Netherlands, did not pose any issues for the GPR, UPE, rebound hammer, resistivity, half-cell potential, and current density measurements. However, when using UPV, additional coupling gel is required due to the roughness of the surface.
- The use of existing SonReb models for in-situ estimations of compressive strength should be avoided. While it's possible to calibrate the models specifically for the structure under inspection, this approach may defeat the purpose of using them in the first place.
- At present, there are few Q-value to compressive strength conversion models with a strong correlation, and those presented in this research tend to overestimate the compressive strength. Nevertheless, it should still be acceptable to use the conversion table for Q-values to compressive strength in EN 13791 [46], as it is based on a 5th percentile curve.
- UPV should only be used as a complementary method to the rebound hammer for estimating the quality of the concrete. When used to identify defects within the concrete, it should be specifically calibrated for the structure under inspection.
- The Proceq Resipod consistently records lower resistivity values compared to the Gecor-10 Wenner probe. This difference could not be attributed to the moisture content. Fortunately, the discrepancy is less noticeable when testing corroded reinforcement in laboratory conditions. The Resipod offers more stable measurements and tends to yield more conservative results.
- The limit values for estimating the probability of corrosion, as outlined in old RILEM guidelines, are tailored to specific conditions (e.g., OPC concrete at 20°C). However, the significance of these limits cannot be overstated, as they determine whether a structure is deemed to be corroding or not. The validity of these limits in-situ is not investigated in this research.

7.2   Practical methodology

Based on the research findings, a practical methodology for conducting a non-destructive material evaluation of a reinforced concrete viaduct has been developed, as detailed in **Appendix H**. This, along with the other conclusions, directly addresses the primary research question: What is a practically feasible non-destructive inspection methodology for evaluating the material status of a reinforced concrete viaduct? It's important to recognise that this methodology offers a simplified representation of reality, and various choices during the inspection process can significantly influence its course, as illustrated by the CASE model. The methodology is not based on any quantitative cost data but does consider the qualitative assessment provided in Table 6.1. When referring to the accompanying flowchart, the following practical considerations should be taken into account:

- Inspections should be conducted by trained and professional personnel. Ideally, official training programs should be available for mastering the various non-destructive techniques, as expertise plays a crucial role in ensuring the quality of the results.
- When using an aerial platform, ensure that the ground is not too soggy to maintain stability.
- For GPR measurements, it is recommended to start with a dielectric constant setting of 6-7.
- UPE should preferably be used in conjunction with GPR rather than in isolation, as these two methods complement each other effectively.
- By interpreting half-cell potential measurements in-situ, it becomes possible to decide whether to investigate suspicious areas using resistivity measurements, corrosion current density measurements, or both. Depending on the initial assessment of active or passive reinforcement, the pulse duration for the corrosion current density device should be chosen accordingly. For now, it is advised to use a pulse duration of 30 seconds for active reinforcement and 100 seconds for passive reinforcement.
- Over-wetting the surfaces before conducting corrosion measurements should be avoided. It is recommended to perform measurements closely together in time and to keep track of the amount of water added during wetting to maintain consistency in the testing conditions.

7.3 Recommendations for future research

The following recommendations are suggested for future research into the non-destructive material evaluation of reinforced concrete structures:

- Perform similar large-scale inspections to improve the proposed methodology, build trust and gain experience. Such efforts could also enhance the efficiency and inform decision-making regarding the implementation of cathodic protection.
- Conduct a comprehensive cost-benefit analysis to clearly illustrate the economic feasibility and practical benefits of integrating NDTs into concrete assessment practices, thereby encouraging wider adoption within the industry.
- Establish a reliable correlation between R-value and Q-value rebound hammers for reinforced concrete, preferably in collaboration with the device manufacturers.
- Investigate the possibility to estimate the probability of corrosion using GPR technology.
- Test the Giatec iCOR device, as presented in Appendix A.3, in-situ to validate its manufacturer's claim that it can estimate the probability of corrosion without direct contact with the reinforcement.
- Investigate further the resistivity parameter, including laboratory testing on core samples and in a more corrosive environment. This is crucial given that resistivity is a fundamental parameter, and other parameters are derived from it.
- Investigate in more depth the influence of pulse duration on corrosion current density measurements to determine the optimal duration for inspections.
- Investigate the validity of the limit values specified in RILEM guidelines for assessing the probability of corrosion under non-standard in-situ conditions.
- Investigate the possibility and challenges of applying NDTs on *natte kunstwerken* (hydraulic structures).

Appendix A

Literature review background

A.1   Construction of the Pourbaix diagram

The Pourbaix diagram in Figure 2.8 consists of eleven equilibrium lines. These lines are labeled in Figure A.1 with their respective equations listed in Table A.1.
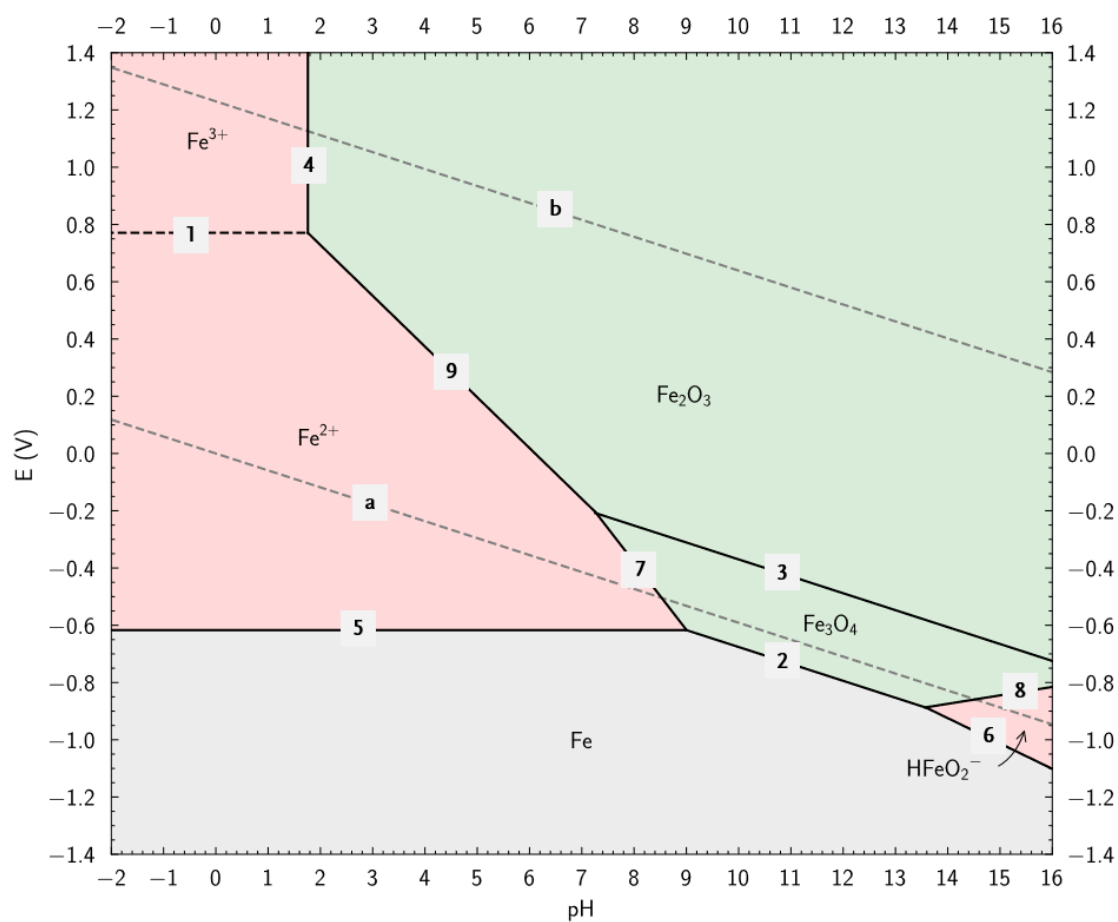
Figure A.1: Construction of the Pourbaix diagram.

Table A.1: Reactions and equilibrium formulas

	Chemical reaction	Equilibrium formula
a)	$2\,H^+ + 2\,e^- \rightleftharpoons H_2$	$E = -0.0592\,pH$
b)	$O_2 + 4\,H^+ + 4\,e^- \rightleftharpoons 2H_2O$	$E = 1.23 - 0.0592\,pH$

	Two dissolved substances	
1)	$Fe^{2+} \rightleftharpoons Fe^{3+} + e^-$	$E = 0.771 + 0.0592\log\frac{[Fe^{3+}]}{[Fe^{2+}]}$

	Two solid substances	
2)	$3\,Fe + 4\,H_2O \rightleftharpoons Fe_3O_4 + 8\,H^+ + 8\,e^-$	$E = -0.085 - 0.0592\,pH$
3)	$2\,Fe_3O_4 + H_2O \rightleftharpoons 3Fe_2O_3 + 2\,H^+ + 2\,e^-$	$E = 0.221 - 0.0592\,pH$

	One solid substance and one dissolved substance	
4)	$2\,Fe^{3+} + 3\,H_2O \rightleftharpoons Fe_2O_3 + 6\,H^+$	$\log(Fe^{3+}) = -0.72 - 3pH$
5)	$Fe \rightleftharpoons Fe^{2+} + 2\,e^-$	$E = -0.440 + 0.296\log(Fe^{2+})$
6)	$Fe + 2\,H_2O \rightleftharpoons HFeO_2^- + 3\,H^+ + 2\,e^-$	$E = 0.493 - 0.0886\,pH + 0.0296\log(HFeO_2^-)$
7)	$3\,Fe^{2+} + 4\,H_2O \rightleftharpoons Fe_3O_4 + 8\,H^+ + 2\,e^-$	$E = 0.980 - 0.236\,pH - 0.0886\log(Fe^{2+})$
8)	$3\,HFeO_2^- + H^+ \rightleftharpoons Fe_3O_4 + 2\,H_2O + 2\,e^-$	$E = -1.819 + 0.0295\,pH - 0.0886\log(HFeO_2^-)$
9)	$2\,Fe^{2+} + 3\,H_2O \rightleftharpoons Fe_3O_4 + 6\,H^+ + 2\,e^-$	$E = 0.728 - 0.177\,pH - 0.0592\log(Fe^{2+})$

Example: hydrogen evolution

An example calculation is provided using the Nernst equation for the hydrogen evolution line (line a in Figure A.1). All ionic concentrations are considered as 10^{-6} M, and water activity is assumed to be unity. The thermodynamic data was obtained from [29].

$$2\,H^+ + 2\,e^- \rightleftharpoons H_2 \tag{A.1}$$

$$Q = \frac{[H_2]}{[H^+]^2} \tag{A.2}$$

$$\log Q = \log[H_2] - 2\log[H^+] \tag{A.3}$$

Equaion A.3 can be rewritten and inserted into the Nernst equation:

$$E_{H_2} = E^0_{H^+/H_2} - 2.303\frac{RT}{zF}\left(\log([H_2]) + 2pH\right) \tag{A.4}$$

where:

$E^0_{H^+/H_2} = 0$ (V)

$R \quad\quad = 8.314$ (J mol^{-1}K^{-1})

$T \quad\quad = 298$ (K)

$z \quad\quad = 2$ (-)

$F \quad\quad = 96485$ (C mol^{-1})

$P \quad\quad = 1$ (atm)

This results in the formula listed in Table A.1:

$$E_{H_2} = -0.0592 \text{pH} \tag{A.5}$$

A.2   Derivation of Fick's second law of diffusion

$$\Delta C = \frac{\Delta N}{A \cdot \Delta x} \tag{A.6}$$

$$\Delta N = N_{in} - N_{out} = J(x) \cdot A \cdot \Delta t - J(x + \Delta x) \cdot A \cdot \Delta t \tag{A.7}$$

$$\frac{\Delta C}{\Delta t} = \frac{J(x) - J(x + \Delta x)}{\Delta x} \tag{A.8}$$

$$\frac{\partial C}{\partial t} = -\frac{\partial J}{\partial x} \tag{A.9}$$

Input of Fick's first law of diffusion:

$$\frac{\partial C}{\partial t} = -\frac{\partial}{\partial x}\left(-D\frac{\partial C}{\partial x}\right) \tag{A.10}$$

If D is a constant:

$$\frac{\partial C}{\partial t} = D\frac{\partial^2 C}{\partial x^2} \tag{A.11}$$

A.3   Overview of non-destructive tests

The overview, adapted from the author's internship literature review, is presented starting from the next page [2].

In-situ tests				
Testing method	Usage	Advantages	Disadvantages	Examples of devices
Acoustic emission	▪ Characterise failures as they are occurring. ▪ Crack propagation.	▪ Continuous monitoring. ▪ Detect failures at a very early stage.	▪ High equipment costs, since the sensors need to be very sensitive. ▪ Skills and experience needed. ▪ Background noise problems. ▪ Kaiser effect*.	▪ Physical Acoustics Corporation Pocket AE-2
Chain drag	▪ Can be used during visual inspection to detect surface delaminations.	▪ Easy to use; no cables needed. ▪ Inexpensive.	▪ Accuracy depends on the hearing of the user. ▪ Accuracy depends on the severity of the delaminations. ▪ Localised measurements.	N/A
Coin tap	▪ Can be used during visual inspection to detect surface delaminations.	▪ Easy to use; no cables needed. ▪ Inexpensive. ▪ Measure over a large area.	▪ Accuracy depends on the hearing of the user. ▪ Accuracy depends on the severity of the delaminations.	N/A
Cover meter	▪ Determine the cover depth.	▪ Easy to use. ▪ Quick.	▪ No accuracy guaranteed after 10 cm. ▪ Not suitable in areas where rebars are closely spaced.	▪ Elcometer 331 Cover Meter ▪ Proceq Profoscope
Concrete radar	▪ Determine the location and diameter of reinforcement.	▪ Portable. ▪ More advanced capabilities than a cover meter.	▪ No accuracy guaranteed after 20 cm. ▪ Not suitable in areas where rebars are closely spaced. ▪ Destructive verification advised.	▪ Hilti PS 1000
Hallf-cell potential	▪ Assessment of the corrosion risk (probability).	▪ Quick results. ▪ Can be used irrespective of the cover depth (although >75 mm can result in a loss to discriminate variation in relative corrosion activity according to ASTM C876-15).	▪ Experience required. ▪ Results influenced by carbonation, temperature and relative humidity. ▪ Contact with the rebar required.	▪ Giatec XCell ▪ Proceq Profometer PM8500

Electrical resistivity	• Resistivity is related to the moisture content. • Assessment of the corrosion risk (probability).	• Low equipment costs. • Low expertise required. • Take many measurements in a short amount of time.	• Temperature corrections needed (3~5% per degree). • Not reliable when the moisture content is high. • The w/c ratio has a large influence on the results; careful calibration is needed. • Not accurate around the edges of a structure. • Can not be used when coatings, epoxies, tendon duct sheathings, asphalt wearing surfaces/waterproofing or FRC are applied.	• Giatec RCON (laboratory) • Proceq Resipod
Endoscope and fibre optic sensors	• Evaluate the condition of concrete. • Detection of voids. • Measure ASR expansions (embedded sensors). • Evaluate the effectiveness of repairs.	• Fiber optic sensors can be embedded into new structures. • Real-time results.	• Drillholes are required (semi-destructive). • Skills and experience needed. • Limited access and view.	• Bosch GIC 120C Pro
Gamma radiography	• Localisation of rebars. • Determine the rebar diameter. • Localisation of cracks and voids.	• Simple to operate. • Results easy to interpret.	• Serious health and safety risks. • Licensed personnel required. • Time-consuming setup. • Limited penetration depth (up to 300 mm). • Both sides of the structure need to be accessible.	• Sentinel 880
Ground penetrating radar	• Road surface degradation. • Locating rebars, tendons, tendon ducts, anchors and dowels. • Localisation of cracks and voids. • Evaluating frost-thaw damage. • Measuring chloride content (difficult and only in experimental setups).	• Fast method for large areas. • 3D radar surveys possible. • Significant depths can be reached (1-2 [m]), however accuracy decreases with an increase in depth.	• Expensive. • Experience required. • Moisture content influences the accuracy. • Less suitable for smaller areas.	• Radiodetection LMX200 • GSSI Flex NX • Proceq GP8800

Method	Applications	Advantages	Limitations	Commercial examples
Impact echo	▪ Determine the thickness and crack depth. ▪ Localisation of voids and delaminations. ▪ Estimate the extent of ASR damage.	▪ Only one side of the concrete needs to be accessible. ▪ Can be automated. ▪ Can detect flaw location and depth.	▪ The effectiveness of FFT for this method is questionable. ▪ Experience required. ▪ Rough surfaces will distort the impacts.	▪ James Instruments Vu-Con ▪ FPrimeC Impact-Echo (uses AI in its core)
Impulse response	▪ Investigate the extent of freeze-thaw damage. ▪ Localisation of delaminations and honeycombing. ▪ Detect subgrade voids. ▪ Determine the E-modulus, thickness and density of concrete. ▪ Usually used for deep foundations.	▪ Robust. ▪ Fast output.	▪ Not often tested on superstructures. ▪ Experience required.	▪ Olson Instruments Slab Impulse Response System
Infrared thermography	▪ Investigate the extent of freeze-thaw damage. ▪ Localisation of delaminations. ▪ Insight in heat loss and moisture movement (leakage). ▪ Crack detection is also possible, but surface preparation is needed.	▪ Portable; wireless. ▪ No surface contact needed.	▪ High equipment costs. ▪ Reference standards needed. ▪ Mostly surface measurements; limited sub-surface measurements only with active thermography. ▪ Heat sources may interfere.	▪ Fluke TiX580 ▪ FLIR A6701sc
Magnetic flux leakage (MFL)	▪ Detect defects in rebars and tendons.	▪ Relatively fast method.	▪ Strict preparation and precise positioning are required. ▪ Closely spaced rebars or tendons are not reliably detected. ▪ Not many option available on the market.	▪ N/A

Maturity method	• Determine the strength of new concrete based on the temperature development.	• Some sensors can be embedded.	• Calibration needed. • Expertise required for interpretation.	N/A
Microwave moisture measurement	• Determine the moisture content.	• Inexpensive. • Good penetration in concrete. • Only one side of the concrete needs to be accessible.	• Expertise required. • Data influenced by the presence of rebars.	• Trotec T610
Permeability test (adapted Figg test)	• Determine the air and water permeability of concrete.	• Easy to use • Inexpensive.	• Semi-destructive. • The Figg number gives an indirect relation to the permeability.	• Matest C375-10KIT
Permeability test (Permea-TORR AC)	• Determine the air permeability of concrete.	• Easy to use • The newer models require less calibration. • Can also be battery powered.	• Only for determining the air permeability. • Smooth surface required.	• Permea-TORR AC
Pull-off test	• Determine the tensile strength of concrete. • The compressive strength of concrete can be empirically correlated to the tensile strength.	• Easy to use.	• Semi-destructive method. • Surface preparation needed. • Hardening of the adhesive can take a day. • The size and type of aggregates influence the results, therefore calibration tests are advised.	• Hydrajaws M2000 Pro

Rebound hammer	• Determine the surface hardness (related to the concrete compressive strength).	• Easy to use. • Inexpensive.	• Local measurements. • The measurements are influenced by surface carbonation, presence of coatings and moisture content. • Smooth surface required.	• Proceq Original Schmidt • Proceq Silver Schmidt OS8200 (this is an optical rebound hammer with a higher rebound number range and lower dispersion)
Relative humidity test	• Determine the relative humidity.	• Easy to use. • Inexpensive.	• Semi-destructive test. • Long waiting time, according to the procedure in ASTM F2170).	• Gilson Concrete Humidity Measurement Kit with Tec RH Meter • Tramex ME5
Ultrasonic pulse echo	• Thickness estimation. • Detect delaminations, debonding, voids, cracks, honeycombing and grouting defects.	• Access to only one side of the structure is required. • Portable. • High penetration depth. • Automated testing possible.	• Close spacing of points to test. • High level of expertise required. • Calibration required.	• Proceq Pundit PD8050
Ultrasonic pulse velocity	• Evaluate the overall quality and uniformity of concrete. • Detect delaminations, debonding, voids, cracks, honeycombing and grouting defects.	• Easy and fast method. • Detect shallow cracks. • High penetration depth.	• Close spacing of points to test. • Both sides of the structure need to be accessible. • Sensor coupling can be difficult on rough surfaces. • Results influenced by moisture content and surface preparation. • Calibration required.	• Proceq Pundit 200
Penetration probe (Windsor probe)	• Measure the penetration depth which can be indirectly related to the compressive strength.	• Fast method. • Low expertise required. • No influence of moisture content, temperature and surface preparation.	• Minor surface damage. • The degree of carbonation and hardness of the aggregates influences the accuracy. • Calibration is necessary.	• James Instruments Windsor Probe

Wireless corrosion detection (iCOR)	• Measure electrical resistivity. • Determine the corrosion rate. • Determine the corrosion potential (connection to the reinforcement required).	• Portable. • Wireless detection of the corrosion rate. • Comes with interactive software.	• Only the first rebar layer can be detected (maximum cover depth is 90 mm). • Can not be used when coatings, epoxies, tendon duct sheathings, asphalt wearing surfaces/waterproofing or FRC are applied. • Large voids or cracks may influence the readings.	• Giatec iCOR
Gecor-10	• Measure electrical resistivity. • Determine the corrosion rate (wired). • Determine the corrosion potential (wired).	• Portable. • Uses the guard ring method for current density measurements. • Control over pulse duration. • Insight in all parameters related to the linear polarisation method. • Reliable results on a KCG-layer.	• Not wireless. • No interactive software. • Large voids or cracks may influence the readings.	N/A

*Kaiser Effect: In materials that display an initial seismic response when subjected to a certain load, the Kaiser effect denotes the lack of acoustic emission until that load is surpassed.

A.4 Statistics

Correction factors ACI-214

Table A.2: Magnitude and accuracy of strength correction factors according to ACI-214 [76].

Factor	Mean value	Coefficient of variation (%)
$F_{l/d}$: l/d ratio		
As-recieved	$1 - \{0.130 - \alpha f_{core}\}\left(2 - \frac{l}{d}\right)^2$	$2.5\left(2 - \frac{l}{d}\right)^2$
Soaked 48h	$1 - \{0.117 - \alpha f_{core}\}\left(2 - \frac{l}{d}\right)^2$	$2.5\left(2 - \frac{l}{d}\right)^2$
Air dried	$1 - \{0.144 - \alpha f_{core}\}\left(2 - \frac{l}{d}\right)^2$	$2.5\left(2 - \frac{l}{d}\right)^2$
F_{dia}: core diameter		
50 mm	1.06	11.8
100 mm	1.00	0.0
150 mm	0.98	1.8
F_{mc}: core moisture content		
As-received	1.00	2.5
Soaked 48h	1.09	2.5
Air dried	0.96	2.5
F_d: damage due to drilling	1.06	2.5

Tables for EN 13791 approach

Table A.3: Values of k_n for the 5% characteristic value according to EN 13791 [46].

n	8	10	12	16	20	30	∞
k_n	2	1.92	1.87	1.81	1.76	1.73	1.64

Table A.4: Value of margin M according to EN 13791 [46].

Value of $f_{c,is,lowest}$ (MPa)	Margin (MPa)
≥ 20	4
$\geq 16 < 20$	3
$\geq 12 < 16$	2
< 12	1

Table A.5: Critical values for testing outliers using the Grubbs test at a significance level of 1%.

n_t	G_p
4	1.496
5	1.764
6	1.973
7	2.139
8	2.274
9	2.387
10	2.482
11	2.564
12	2.636
13	2.699
14	2.755
15	2.806
16	2.852
17	2.894
18	2.932
19	2.968
20	3.001
25	3.135
30	3.236
35	3.316
40	3.381
50	3.482
60	3.560
70	3.621
80	3.673
90	3.716
100	3.754
120	3.817
140	3.867
160	3.910
180	3.946
200	3.978
250	4.042

Appendix B

Gecor 10 case study

Some preliminary measurements were conducted to gain practical experience, identify potential issues, and gather initial insights into the Gecor-10's response to moisture and the effect of pulse duration on current density measurements. While these datasets are limited in size, they offer valuable insights into the device's functionality and potential challenges for future testing.

The measurements were carried out on a concrete column that was once part of a parking garage. Five measurement points were placed at half-meter intervals along the face of the column to assess the two primary rebars with a diameter of 22 mm, which will be referred to as the *Top* and *Bottom* rebars hereafter which are in electrical contact. The top rebar is the one shown in Figure B.1b. For each of these points, half-cell potential and current density measurements were performed. Additionally, the resistivity was measured in between the measurement points, where little to no reinforcement was present. The half-cell potential measurements were conducted using Gecor-10's Sensor B with $Cu/CuSO_4$ electrodes until a stable OCP was recorded. Resistivity measurements were carried out with Gecor-10's Wenner probe (Sensor C). Weather conditions on the day of the measurements were variably cloudy with some rain in the morning prior to the experiment. The measurements were divided in two parts. The first part, referred to as the 'dry' phase, took place around 11 a.m., during which no water was added to the surface of the column or was kept to a minimum, just enough to ensure sensor functionality. The second part, designated as the 'surface wet' phase, was performed at 2 p.m. on the same day, involving thoroughly wetting the surface of the column and waiting around 10 minutes before starting the measurements.

(a)   (b)

Figure B.1: Parking garage column (a) and rebar clamp (b).

The data obtained from the measurements are presented in Table B.1 and B.2. For an explanation of the parameters, reference is made to Chapter 2.

Table B.1: Dry measurements.

	i_{corr} ($\mu A/cm^2$)	E_{corr} (mV)	R_c (kΩ)	E_{pol} (mV)	OCP (mV)	ρ (k$\Omega \cdot$ m)
Top						
1	0.078	-49.5	12.18	37.1	-47.0	1.68
2	0.048	-5.9	26.72	60.6	-10.2	1.35
3	0.072	35.4	21.13	39.9	17.4	1.28
4	0.108	45.6	11.76	26.8	56.0	5.67
5	0.200	-40.3	8.34	23.1	-26.0	0.852
Bottom						
1	0.047	-46.1	19.80	60.8	-79.8	1.68
2	0.035	-35.8	34.96	81.2	17.5	1.35
3	0.083	-9.2	18.64	41.8	-38.1	1.28
4	0.102	20.5	23.80	28.2	-35.6	5.67
5	0.118	-12.6	21.15	34.1	-41.5	0.852

Table B.2: Surface wet measurements.

	i_{corr} ($\mu A/cm^2$)	E_{corr} (mV)	R_c (kΩ)	E_{pol} (mV)	OCP (mV)	ρ (k$\Omega \cdot$ m)
Top						
1	0.173	-64.3	6.98	23.3	-72.2	1.54
2	0.179	-18.2	7.86	28.9	-29.3	0.973
3	0.152	15.5	11.25	30.4	-6.2	1.63
4	0.416	31.3	5.19	8.3	18.4	1.60
5	0.359	-54.9	4.70	22.4	41.8	0.815
Bottom						
1	0.087	-30.8	10.43	39.9	-27.2	1.54
2	0.051	-36.4	31.40	57.1	-32.4	0.973
3	0.281	-27.9	5.79	22.6	-40.4	1.63
4	0.195	-4.4	9.73	29.6	-26.6	1.60
5	0.202	-31.5	6.53	37.1	-47.8	0.815

By applying the criteria from Tables 2.6, 2.10 and 2.13 to the data from Tables B.1 and B.2, relevant plots can be made to assess the risk of corrosion. Figure B.2 presents the relation between the open circuit potential and the corrosion current density, while Figure B.3 presents the relation between concrete resistivity and corrosion current density. The green zone in these figures indicates a low risk of corrosion, while the orange zone signifies

a moderate risk of corrosion. The red zone represents a high risk of corrosion. Any data points in the white zones are inconclusive, and those within the grey zones are considered inconsistent. It is important to recognize that the datasets are relatively small and over-polarisation was prominent. However, despite these limitations, the following conclusions can still be drawn:

- The values for E_{corr} measured with the confinement probe are, in most cases, comparable to the OCP measured with Sensor B. However, Measurement 5 for the top rebar differs by 96.7 mV, which could indicate an unstable initial state or stray polarisation.
- Overall, upon reviewing Figures B.2 and B.3, all data points fall within the green zone, indicative of a negligible to low probability of corrosion.
- Wetting the surface affects the resistivity, typically causing a decrease, although this effect is not consistent across all measurements. Similarly, the current density generally experiences a strong increase after wetting. The potential shows a slight decrease, although this change is less pronounced compared to the variations observed in resistivity and current density. Since the exact amount of water added was not recorded in this experiment, no comments can be made regarding the quantification of its effects.
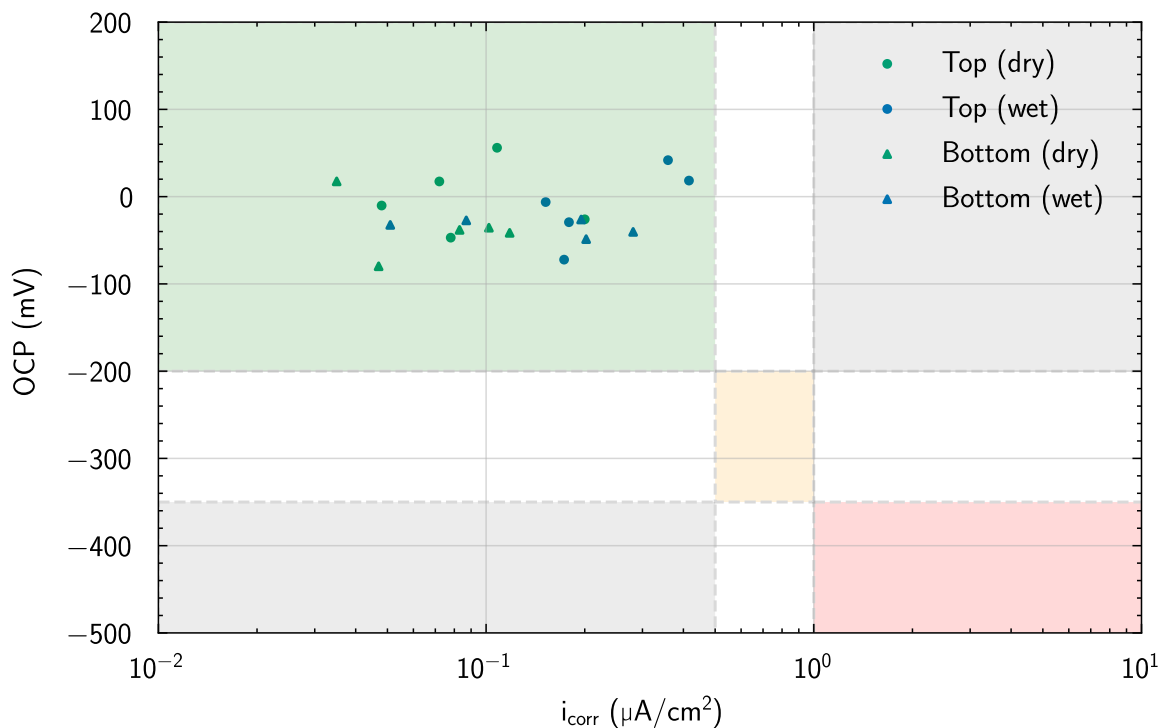
Figure B.2: Corrosion potential (Cu/CuSO$_4$) vs corrosion current density.
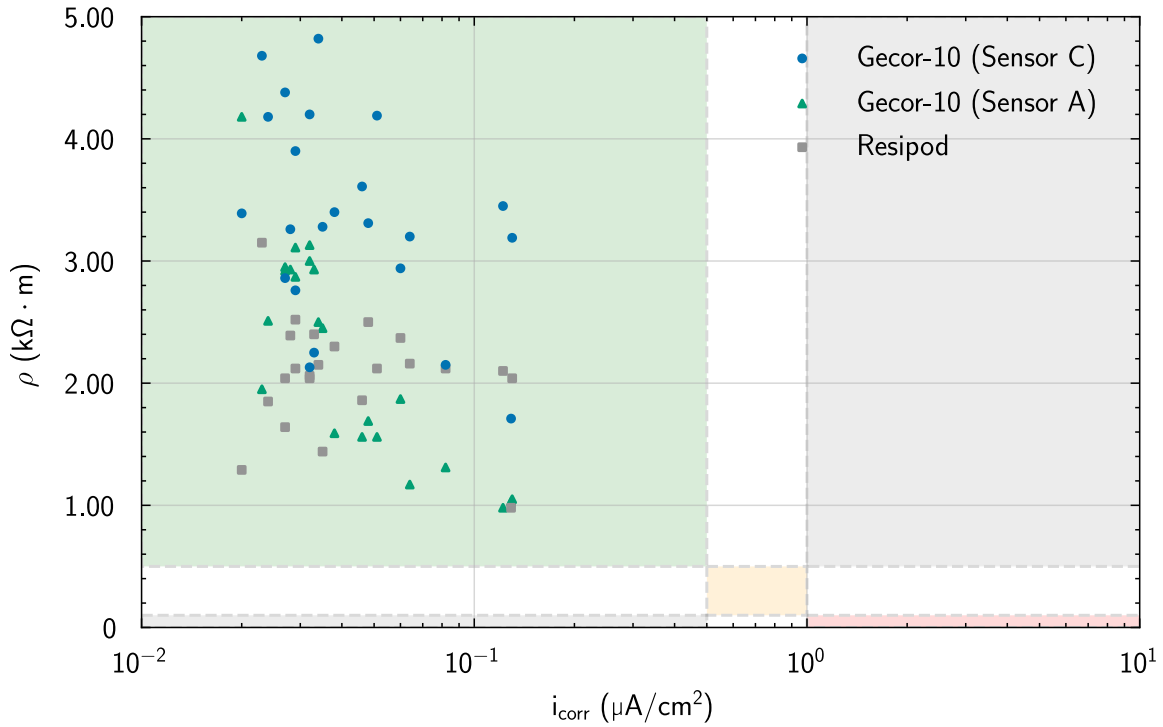
Figure B.3: Concrete resistivity vs corrosion current density.

The calculated value for i_{corr} is strongly dependent on the coefficient B from the Stern-Geary equation (Equation 2.19). However, it is worth noting that the Gecor-10 manual does not explicitly specify this coefficient. As discussed in Section 2.5, a value of 26 mV can be assumed for active steel and 52 mV for passive steel; however, using a single value of 26 mV for all measurements is deemed acceptable. To confirm whether the Gecor-10 indeed uses this value, the coefficient can be back-calculated using the applied current, which is displayed on the device before the measurement results. For instance, considering point 1 of the top rebar from the wet measurements, the applied current was 7.0 μA.

$$R_p = \frac{E_{pol}}{I_{ap}} \tag{B.1}$$

$$i_{corr} = \frac{B}{A_{eff} \cdot R_p} \tag{B.2}$$

The part of the rebar that is being polarized can be determined by multiplying the rebar circumference with the confined length which is 6.5 cm for the Gecor-10:

$$A_{eff} = \pi \cdot \emptyset \cdot l_{pol} = \pi \cdot 2.2 \cdot 6.5 = 44.9 \text{ cm}^2 \tag{B.3}$$

$$B = 0.173 \cdot 44.9 \cdot \frac{23.3}{7.0} \approx 26 \text{ mV} \tag{B.4}$$

Effect of current pulse duration

The impact of the current pulse duration was examined for durations of 30 seconds and 60 seconds.

Table B.3: Corrosion current density for a pulse duration of 30s and 60s.

	Top					Bottom			
	t = 30s	t = 60s	Δ	%		t = 30s	t = 60s	Δ	%
1	0.173	0.207	0.034	+19.7	**1**	0.087	0.053	0.133	-39.1
2	0.179	0.074	0.105	-58.7	**2**	0.051	0.184	0.021	+260.8
3	0.152	0.318	0.166	+109.2	**3**	0.281	0.302	0.023	+7.5
4	0.416	0.119	0.297	-71.4	**4**	0.195	0.172	0.108	-11.8
5	0.359	0.665	0.306	+85.2	**5**	0.202	0.310	0.034	+53.5

$$R_c = 1.31 \times i_{corr}^{-1.04}$$
$$R^2 = 0.89$$
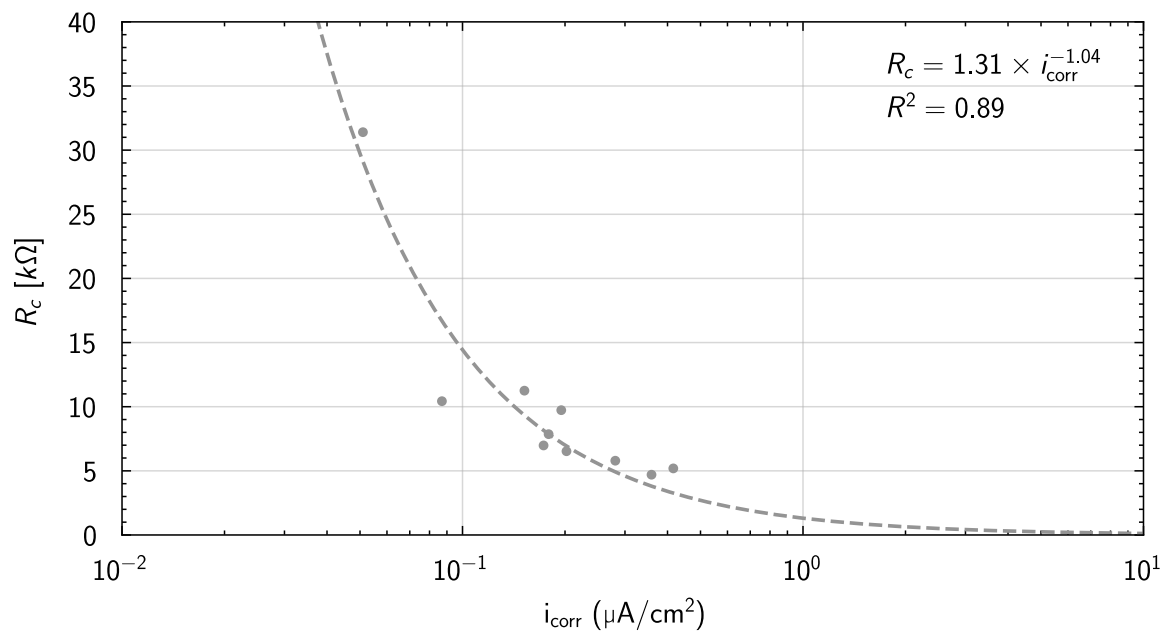
Figure B.4: Concrete electrical resistance vs corrosion current density for a pulse duration of 30s
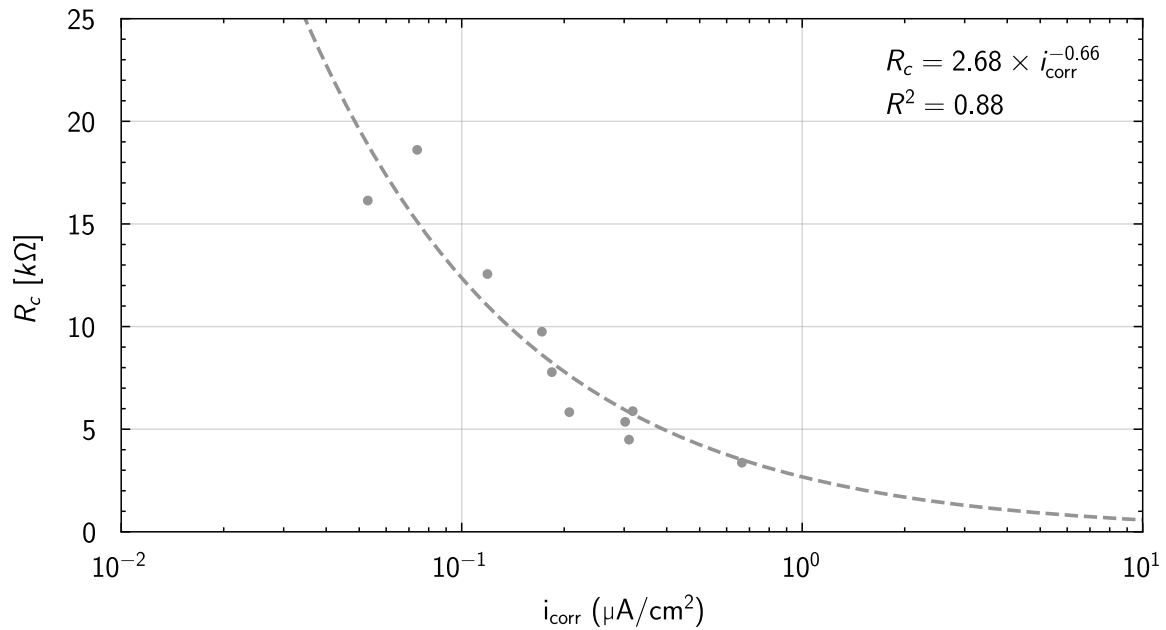
Figure B.5: Concrete electrical resistance vs corrosion current density for a
pulse duration of 60s

- A correlation exists between the concrete electrical resistance and corrosion current density. As expected, a lower concrete resistance corresponds to a higher corrosion current. A power function seems to be the best fit (Figure B.4 and B.5).
- From Table B.3 large percentage differences can be observed for the corrosion current density measured at 30 s and 60 s. The general trend observed is that a longer pulse duration leads to a higher corrosion current for the passivated reinforcement. Once again, measurement points 4 and 5 on the top rebar stand out the most with a difference of 0.3 $\mu A/cm^2$.
- Only one of the measurements indicated a corrosion current higher than 0.5 $\mu A/cm^2$ and none higher than 1 $\mu A/cm^2$.

Appendix C

Sluinerweg inspection 2020
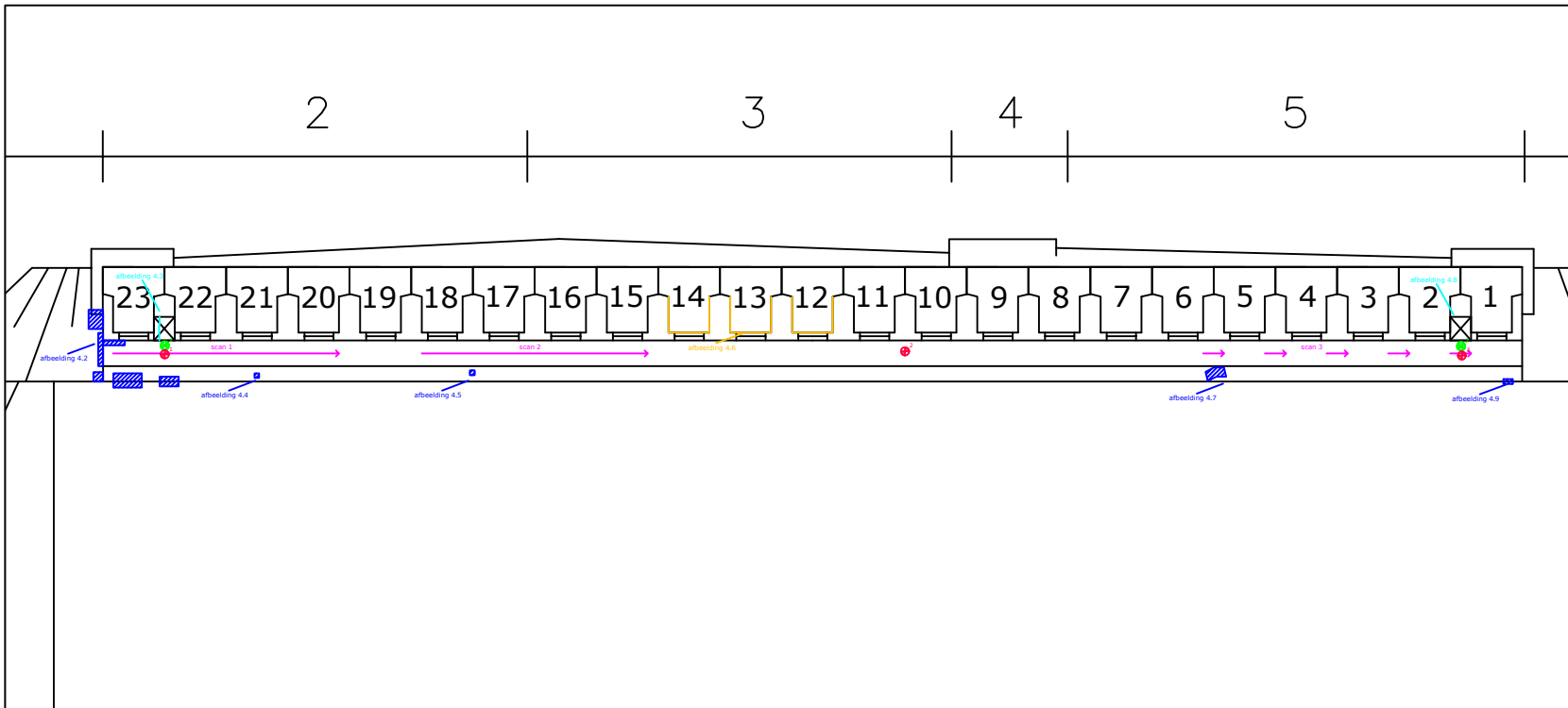
AANZICHT STP 01
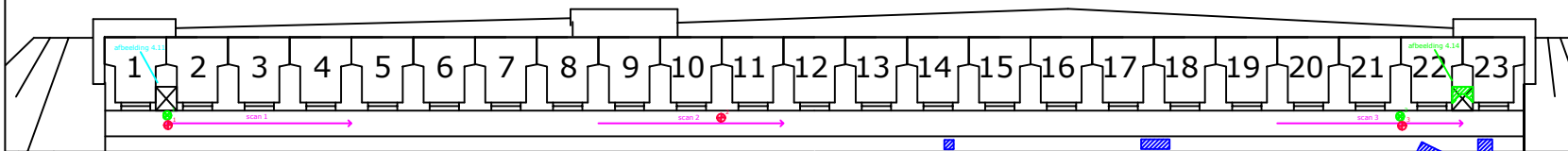
AANZICHT STP 05

Legenda

～～～	Scheurvorming
▨	Holklinkende delen bij afkloppen
▨	Bestaande reparatie
▨	Afgedrukte betondekking
▨	Roestende of blootliggende wapening
▨	Losse/ontbrekende KCG laag
⊗ˣ	Boorstofmonster 40-100 mm
⊕ˣ	Boorstofmonsters en carbonatatiemeting
ΛΛΛΛ	Dekkingsmeting
▢	KB-systeem op liggers

solid services
engineering

Opdrachtgever:	
Rijkswaterstaat Dienst Oost-Nederland	
Project:	
MJO Liggerkoppen	
Betreft:	
33E-107-01; STP01 en STP05	
Getekend door:	
KvD	
Tekeningnummer:	
19PV0188-32.01	

Datum:	Revisie:	Schaal:	Tekening:
5-3-2020			1/1

Project:	*Sluinerweg*		
Uitvoerder:	*Giovanni van Steveninck*	**Rapportnummer:**	*1.0*
Datum:	*vrijdag 13 maart 2020*		

R A P I D C H L O R I D E T E S T

IJkwaarden:			Voor	Na
mV	Chloridegehalte	Indicator	mV	mV
93,75	0,005%	Helder	95,5	92
76,3	0,020%	Paars	79	73,6
54,8	0,050%	Groen	57,1	52,5
-2,1	0,500%	Roze	-0,3	-3,9

RESULTATEN

Meetlocatie	Diepte (mm)	Meetwaarden				Opmerkingen
		mV	Bet. Cl-%	Cem. Cl-%		
STP 1 - 1	0-20 mm	57,2 mV	0,0451%	0,3224%		
STP 1 - 1	20-40 mm	91,2 mV	0,0061%	0,0437%		
STP 1 - 1	40-60mm	122,9 mV	0,0005%	0,0035%		
STP 1 - 1	40-100 mm	105,2 mV	0,0020%	0,0144%		
STP 1 - 2	0-20 mm	63,4 mV	0,0347%	0,2476%		
STP 1 - 2	20-40 mm	62,5 mV	0,0360%	0,2572%		
STP 1 - 2	40-60mm	78,8 mV	0,0164%	0,1171%		
STP 1 - 2	40-100 mm	57,0 mV	0,0455%	0,3252%		
STP 1 - 3	0-20 mm	56,1 mV	0,0473%	0,3379%		
STP 1 - 3	20-40 mm	90,6 mV	0,0064%	0,0459%		
STP 1 - 3	40-60mm	122,4 mV	0,0005%	0,0037%		
STP 5 - 1	0-20 mm	86,4 mV	0,0090%	0,0640%		
STP 5 - 1	20-40 mm	107,4 mV	0,0017%	0,0121%		
STP 5 - 1	40-60mm	129,8 mV	0,0003%	0,0020%		
STP 5 - 1	40-100 mm	83,5 mV	0,0113%	0,0806%		
STP 5 - 2	0-20 mm	85,5 mV	0,0096%	0,0688%		
STP 5 - 2	20-40 mm	122,8 mV	0,0005%	0,0036%		
STP 5 - 2	40-60mm	130,7 mV	0,0003%	0,0019%		
STP 5 - 2	40-100 mm	122,5 mV	0,0005%	0,0036%		
STP 5 - 3	0-20 mm	68,1 mV	0,0284%	0,2026%		
STP 5 - 3	20-40 mm	109,2 mV	0,0015%	0,0105%		
STP 5 - 3	40-60mm	130,3 mV	0,0003%	0,0020%		

Kleurcodering:

Weinig chloride   Veel chloride

Appendix D

Measurement plan Sluinerweg 13-15 November 2023

Measurement plan Sluinerweg viaduct
13 – 15 November 2023

Monday 13 November

Time	Activities	Who?	Notes
08:00	Register at Heijmans depot.	Everyone who is going to perform measurements on-site.	-
08:30	Arrival Sluinerweg: ▪ General instruction. ▪ Short visual inspection. ▪ Check weather situation. ▪ Clean the spaces in between the beams. ▪ Temporary removal of the barbed wire. ▪ Removal of the CP wiring.	Everyone Barbed wire and CP removal: Dikkerboom	-
09:00	Start GPR measurements at STP01: 1. Supporting beam. 2. Spaces in between the beams. 3. Beam heads*.	Markus, Rosaly, Ivo, Penny, Bryan and Gert	Marking of the reinforcement on the structure.
	Mark locations for 4 compressive strength cores on the supporting beam.	Gert	The locations of these cores should correspond to the UPV/RH measurement locations.
	Start UPV measurements at STP01: 1. Supporting beam using the spaces in between the beams (semi-direct transmission). 2. Beam heads* (direct transmission).	Markus, Rosaly, Ivo, Penny, Bryan and Gert Tendon ducts: Remco	-

	At the same time: inspection of the tendon ducts of one or more beams using the aerial work platform.		
	Start UPE measurements at **STP01**: 1. Supporting beam. 2. Spaces in between the beams. 3. Beam heads*. At the same time: inspection of the tendon ducts of one or more beams using the aerial work platform.	Markus, Rosaly, Ivo, Penny, Bryan and Gert Tendon ducts: Remco	-
	Start RH measurements at **STP01**: use the same locations as with the UPV measurements. At the same time: inspection of the tendon ducts of one or more beams using the aerial work platform.	Markus, Rosaly, Ivo, Penny, Bryan and Gert Tendon ducts: Remco	For the RH measurements, take at least 9 measurements per test location. The spaces in between the beams do not necessarily have to be included. If they are, note this clearly.
	STP01: ▪ Expose the reinforcement in ~3-4 places in the supporting beam. ▪ Expose the reinforcement in beam heads 1, 7, 13, 18 and 23. ▪ Take the cores for the compressive strength.	Dikkerboom	-
12:30	Break		
13:00	Start GPR measurements at **STP02**: 1. Supporting beam. 2. Spaces in between the beams. 3. Beam heads*.	Markus, Rosaly, Ivo, Penny, Bryan and Gert	-
	Start UPV measurements at **STP02**:	Markus, Rosaly, Ivo, Penny, Bryan and Gert	Grid 0.65mx0.5m, refer to drawing.

	1. Supporting beam using the spaces in between the beams (semi-direct transmission). 2. Beam heads* (direct transmission).		
	Start UPE measurements at STP02: 1. Supporting beam. 2. Spaces in between the beams. 3. Beam heads*.	Markus, Rosaly, Ivo, Penny, Bryan and Gert	-
	Start RH measurements at STP02: use the same locations as with the UPV measurements.	Markus, Rosaly, Ivo, Penny, Bryan and Gert	Grid 0.65mx0.5m, refer to drawing. For the RH measurements, take at least 9 measurements per test location. The spaces in between the beams do not necessarily have to be included. If they are, note this clearly.
16:00	Continuity measurement on the reinforcement at STP01.	Gert	-
16:30	Finishing	Everyone	-
*<u>At least</u> beams 1, 7, 13, 18 and 23. Performing measurements on the columns only if there is enough time to do so!			

Tuesday 14 November

Time	Activities	Who?	Notes
08:00	Arrival Sluinerweg: - General instruction.	Everyone	Erik Schlangen will visit the project today.
	STP02: ▪ Expose the reinforcement in ~3-4 places in the supporting beam. ▪ Expose the reinforcement in beam heads 1, 7, 13, 18 and 23. ▪ Take the cores for the compressive strength.	Dikkerboom	-
	Perform all corrosion measurements at **STP01** (supporting beam – spaces in between the beams – beam heads). Start with Resipod and Profometer Corrosion then the Gecor-10. hXRF at **STP01** (start from other side)	Markus, Rosaly, Ivo, Penny, John and Gert hXRF: Marija	Important for *resistivity* measurements: measure diagonally between the reinforcement in accordance with RILEM 154. Keep sponges constantly moist.
	Coring for carbonation and chloride profiles at **STP01**.	Dikkerboom	Coring activities at **STP01** can only start after all NDTs are performed there.
	Perform all corrosion measurements at **STP01** (supporting beam – spaces in between the beams – beam heads). Start with Resipod and Profometer Corrosion then the Gecor-10.	Markus, Rosaly, Ivo, Penny, John and Gert	-
12:30	Break		
13:00	Continuation of the measurements at STP02.	Markus, Rosaly, Ivo, Penny, John and Gert	-
16:30	Finishing	Everyone	-

Wednesday 15 november

Time	Activities	Who?	Notes
08:00	Coring for carbonation and chloride profiles at STP02.	Dikkerboom Bryan and Gert	-

Appendix E

Analysis of concrete cores

E.1   Overview of cores

C1-01

Date of coring: 15-11-2023
Part of structure: Support beam
Diameter: 44 mm
Minimum length: 115 mm
Notes: -

Figure E.1: Core C1-01.

C2-01

Date of coring: 15-11-2023
Part of structure: Support beam
Diameter: 44 mm
Minimum length: 132 mm
Notes: -

Figure E.2: Core C2-01.

C3-01

Date of coring: 15-11-2023
Part of structure: Support beam
Diameter: 44 mm
Minimum length: 108 mm
Notes: -

Figure E.3: Core C3-01.

C4-01

Date of coring:	15-11-2023
Part of structure:	Support beam
Diameter:	44 mm
Minimum length:	115 mm
Notes:	Cracked 55 mm from the surface.

Figure E.4: Core C4-01.

C5-01

Date of coring:	15-11-2023
Part of structure:	Support beam
Diameter:	44 mm
Minimum length:	116 mm
Notes:	-
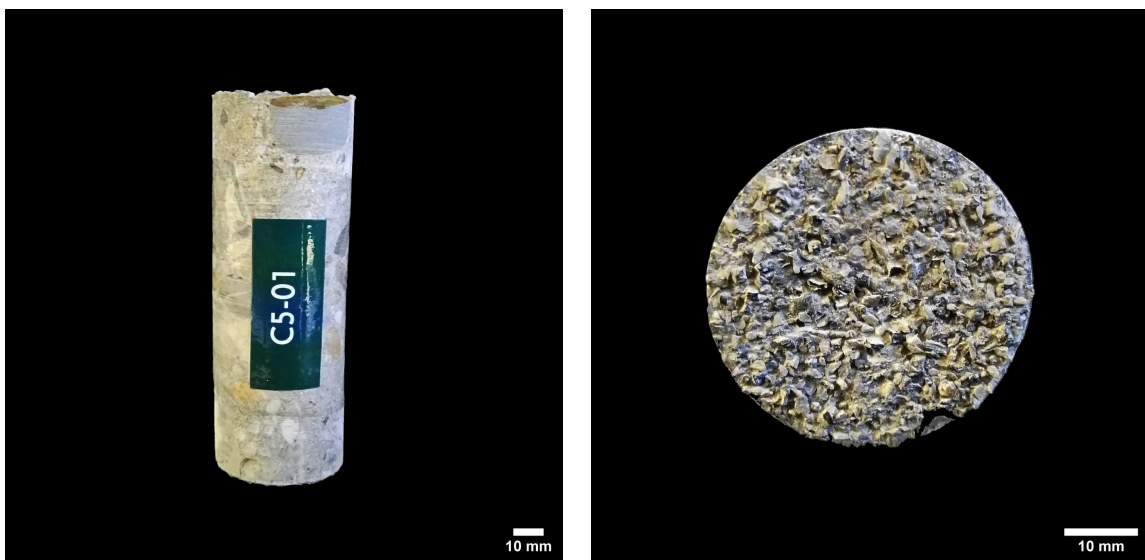
Figure E.5: Core C5-01.

C6-01

Date of coring:	15-11-2023
Part of structure:	Support beam
Diameter:	44 mm
Minimum length:	105 mm
Notes:	-

Figure E.6: Core C6-01.

C1-1-01

Date of coring:	14-11-2023
Part of structure:	T-beam
Diameter:	44 mm
Minimum length:	98 mm
Notes:	Cracked 35 mm from the surface. Contains part of a rebar.
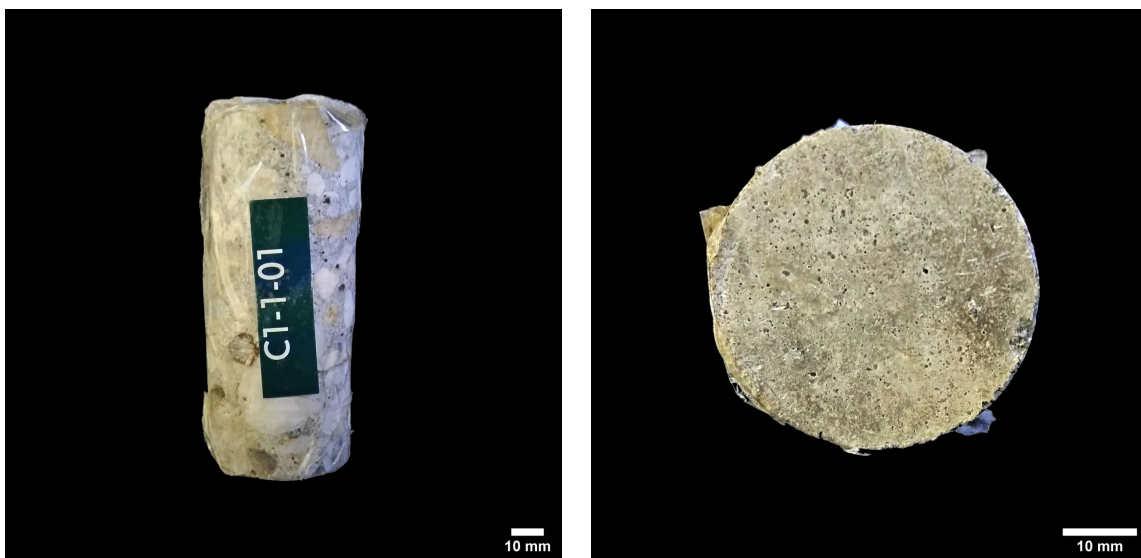
Figure E.7: Core C1-1-01.

C2-1-01

Date of coring: 14-11-2023
Part of structure: T-beam
Diameter: 44 mm
Minimum length: 61 mm
Notes: -
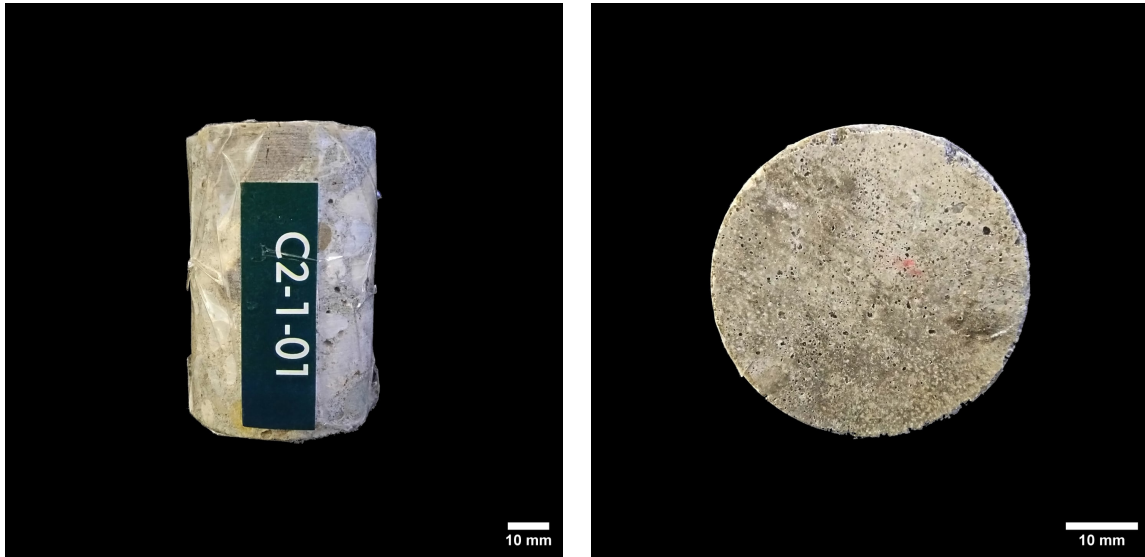
Figure E.8: Core C2-1-01.

C1-7-01

Date of coring: 15-11-2023
Part of structure: T-beam
Diameter: 44 mm
Minimum length: 94 mm
Notes: -

Figure E.9: Core C1-7-01.

C2-7-01

Date of coring: 15-11-2023
Part of structure: T-beam
Diameter: 44 mm
Minimum length: 112 mm
Notes: -

Figure E.10: Core C2-7-01.

C1-13-01

Date of coring: 15-11-2023
Part of structure: T-beam
Diameter: 44 mm
Minimum length: 110 mm
Notes: -

Figure E.11: Core C1-13-01.

C2-13-01

Date of coring:	15-11-2023
Part of structure:	T-beam
Diameter:	44 mm
Minimum length:	110 mm
Notes:	-

Figure E.12: Core C2-13-01.

C1-18-01

Date of coring:	15-11-2023
Part of structure:	T-beam
Diameter:	44 mm
Minimum length:	113 mm
Notes:	-

Figure E.13: Core C1-18-01.

C2-18-01

Date of coring:	15-11-2023
Part of structure:	T-beam
Diameter:	44 mm
Minimum length:	90 mm
Notes:	-

Figure E.14: Core C2-18-01.

C1-23-01

Date of coring:	15-11-2023
Part of structure:	T-beam
Diameter:	44 mm
Minimum length:	100 mm
Notes:	Cracked 55 mm from the surface.

Figure E.15: Core C1-23-01.

C2-23-01

Date of coring: 15-11-2023
Part of structure: T-beam
Diameter: 44 mm
Minimum length: 96 mm
Notes: -

Figure E.16: Core C2-23-01.

CL1-01

Date of coring: 15-11-2023
Part of structure: Support beam
Diameter: 64 mm
Minimum length: 121 mm
Notes: -

Figure E.17: Core CL1-01.

CL2-01

Date of coring: 15-11-2023
Part of structure: Support beam
Diameter: 64 mm
Minimum length: 113 mm
Notes: -

Figure E.18: Core CL2-01.

CL3-01

Date of coring: 15-11-2023
Part of structure: Support beam
Diameter: 64 mm
Minimum length: 131 mm
Notes: -

Figure E.19: Core CL3-01.

CL1-1-01

Date of coring: 14-11-2023
Part of structure: T-beam
Diameter: 64 mm
Minimum length: 87 mm
Notes: -

Figure E.20: Core CL1-1-01.

CL1-7-01

Date of coring: 15-11-2023
Part of structure: T-beam
Diameter: 64 mm
Minimum length: 100 mm
Notes: -

Figure E.21: Core CL1-7-01.

CL1-13-01

Date of coring: 15-11-2023
Part of structure: T-beam
Diameter: 64 mm
Minimum length: 93 mm
Notes: -

Figure E.22: Core CL1-13-01.

CL1-18-01

Date of coring: 15-11-2023
Part of structure: T-beam
Diameter: 64 mm
Minimum length: 91 mm
Notes: -

Figure E.23: Core CL1-18-01.

CL1-23-01

Date of coring:	15-11-2023
Part of structure:	T-beam
Diameter:	64 mm
Minimum length:	94 mm
Notes:	-

Figure E.24: Core CL1-23-01.

S1-01

Date of coring:	14-11-2023
Part of structure:	Support beam
Diameter:	100 mm
Minimum length:	130 mm
Notes:	-
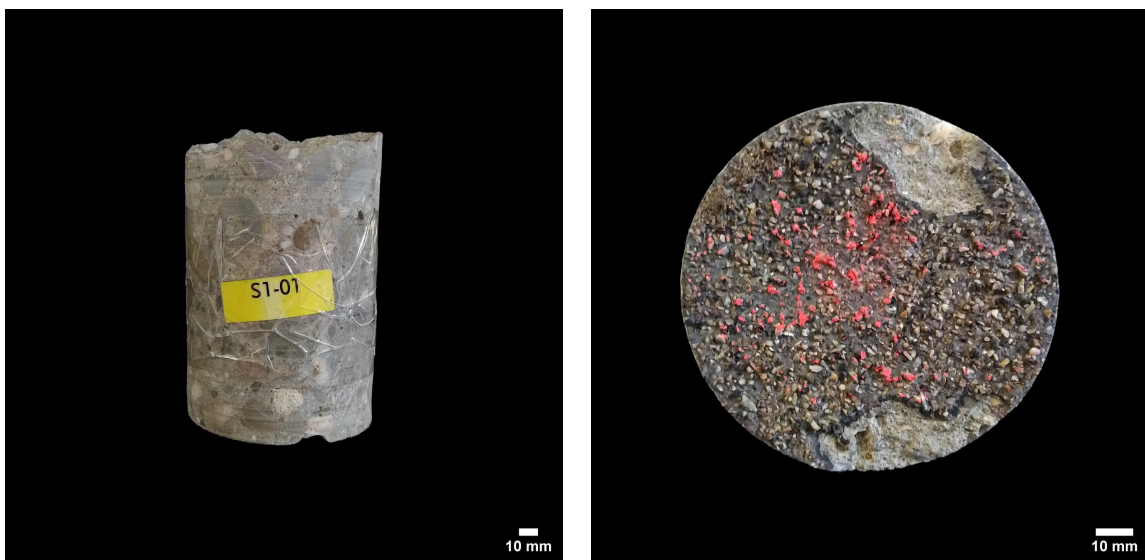
Figure E.25: Core S1-01.

S2-01

Date of coring:	14-11-2023
Part of structure:	Support beam
Diameter:	100 mm
Minimum length:	138 mm
Notes:	-

Figure E.26: Core S2-01.

S3-01

Date of coring:	14-11-2023
Part of structure:	Support beam
Diameter:	100 mm
Minimum length:	146 mm
Notes:	-
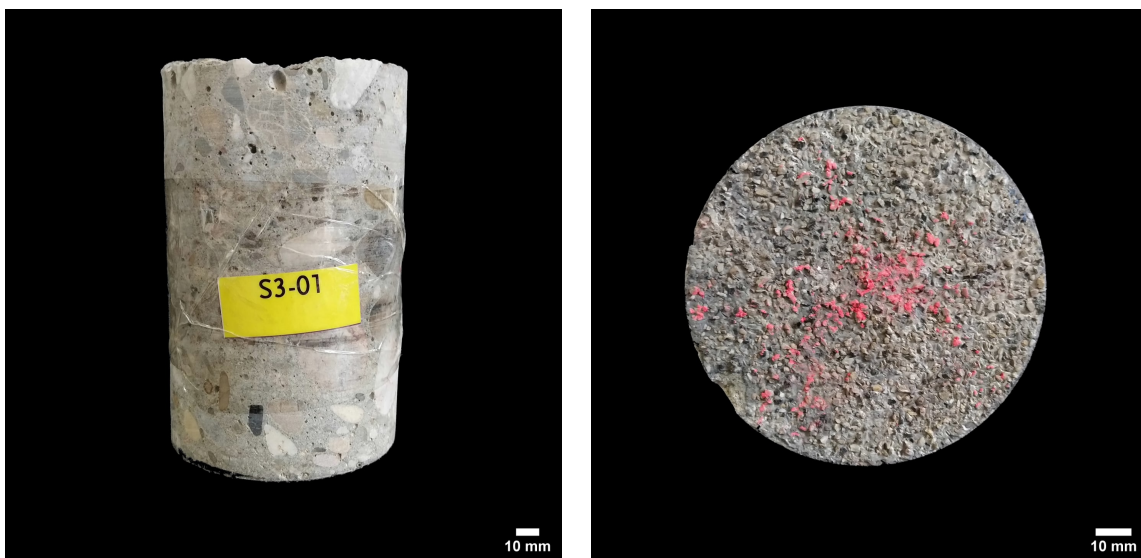
Figure E.27: Core S3-01.

S4-01

Date of coring: 14-11-2023
Part of structure: Support beam
Diameter: 100 mm
Minimum length: 150 mm
Notes: -

Figure E.28: Core S4-01.

E.2　Carbonation

Table E.1: Mean carbonation depths

Core	$x(t)_{left}$ (mm)	$x(t)_{right}$ (mm)
C1	1.5	1
	(max = 9.5)	(max = 9.5)
C2	1.5	1
C3	2.5	2
C4	4.5	5
C5	5	5
C6	5	4.5
C1-1	0.5	0.5
C2-1	11	10
	(max = 18)	(max = 14.5)
C1-7	0.5	0.5
C2-7	1.5	1.5
C1-13	6.5	5.5
	(max = 14)	(max = 16)
C2-13	1.5	1.5
	(max = 8)	(max = 10)
C1-18	0.5	0.5
C2-18	2.5	2
C1-23	0	0
	(max = 6.5)	
C2-23	0.5	0.5

Figure E.29: Carbonation front C1.

Figure E.30: Carbonation front C2.

Figure E.31: Carbonation front C3.

Figure E.32: Carbonation front C4.

Figure E.33: Carbonation front C5.

Figure E.34: Carbonation front C6.

Figure E.35: Carbonation front C1-1.

Figure E.36: Carbonation front C2-1.

Figure E.37: Carbonation front C1-7.

Figure E.38: Carbonation front C2-7.

Figure E.39: Carbonation front C1-13.

Figure E.40: Carbonation front C2-13.

Figure E.41: Carbonation front C1-18.

Figure E.42: Carbonation front C2-18.

Figure E.43: Carbonation front C1-23.

Figure E.44: Carbonation front C2-23.

E.3 Chloride content

Beam 1

Date	Name	Sample (g)	Empty Petri dish (g)	Filter (g)	Dry sample + dish and filter (g)	Cement (g)	Cement content (wt%)	Pipetted from solution (mL)	0.1M AgNO$_3$ (mL)	0.1M NH$_4$SCN (mL)	Chloride content (%)
22-12-2023	Blank							100.00	10.00	9.92	
22-12-2023	CL1-01-1 (1)	31.96	70.32	0.52	98.68	4.12	12.9	100.00	10.00	9.76	0.07
22-12-2023	*Duplo*	31.96	70.32	0.52	98.68	4.12	12.9	100.00	10.00	9.75	0.07
22-12-2023	CL1-01-1 (2)	31.90	63.46	0.52	91.90	3.98	12.5	100.00	10.00	9.84	0.04
22-12-2023	*Duplo*	31.90	63.46	0.52	91.90	3.98	12.5	100.00	10.00	9.83	0.04

Beam 7

Date	Name	Sample (g)	Empty Petri dish (g)	Filter (g)	Dry sample + dish and filter (g)	Cement (g)	Cement content (wt%)	Pipetted from solution (mL)	0.1M AgNO$_3$ (mL)	0.1M NH$_4$SCN (mL)	Chloride content (%)
3-1-2024	Blank							100.00	10.00	9.91	
3-1-2023	CL1-7-01 (1)	31.48	66.68	0.49	94.63	4.02	12.8	100.00	10.00	9.84	0.03
3-1-2023	*Duplo*	31.48	66.68	0.49	94.63	4.02	12.8	100.00	10.00	9.82	0.04
3-1-2023	CL1-7-01 (2)	31.56	63.45	0.50	91.52	4.00	12.7	100.00	10.00	9.89	0.01
3-1-2023	*Duplo*	31.56	63.45	0.50	91.52	4.00	12.7	100.00	10.00	9.86	0.02

Beam 13

Date	Name	Sample (g)	Empty Petri dish (g)	Filter (g)	Dry sample + dish and filter (g)	Cement (g)	Cement content (wt%)	Pipetted from solution (mL)	0.1M AgNO$_3$ (mL)	0.1M NH$_4$SCN (mL)	Chloride content (%)
22-12-2023	Blank							100.00	10.00	9.92	
27-12-2023	CL1-13-01 (1)	31.67	63.44	0.53	90.38	5.25	16.6	100.00	10.00	9.82	0.03
27-12-2023	*Duplo*	31.67	63.44	0.53	90.38	5.25	16.6	100.00	10.00	9.82	0.03
28-12-2023	CL1-13-01 (2)	31.65	70.32	0.53	98.60	3.90	12.3	100.00	10.00	9.88	0.02
28-12-2023	*Duplo*	31.65	70.32	0.53	98.60	3.90	12.3	100.00	10.00	9.86	0.03

Beam 18

Date	Name	Sample (g)	Empty Petri dish (g)	Filter (g)	Dry sample + dish and filter (g)	Cement (g)	Cement content (wt%)	Pipetted from solution (mL)	0.1M AgNO$_3$ (mL)	0.1M NH$_4$SCN (mL)	Chloride content (%)
22-12-2023	Blank							100.00	10.00	9.92	
28-12-2023	CL1-18-01 (1)	31.75	72.77	0.52	100.02	5.02	15.8	100.00	10.00	9.73	0.07
29-12-2023	Duplo	31.75	72.77	0.52	100.02	5.02	15.8	100.00	10.00	9.72	0.07
29-12-2023	CL1-18-01 (2)	32.48	63.45	0.52	92.73	3.73	11.5	100.00	10.00	9.84	0.04
29-12-2023	Duplo	32.48	63.45	0.52	92.73	3.73	11.5	100.00	10.00	9.85	0.03

Beam 23

Date	Name	Sample (g)	Empty Petri dish (g)	Filter (g)	Dry sample + dish and filter (g)	Cement (g)	Cement content (wt%)	Pipetted from solution (mL)	0.1M AgNO$_3$ (mL)	0.1M NH$_4$SCN (mL)	Chloride content (%)
3-1-2024	Blank							100.00	10.00	9.91	
3-1-2024	CL1-23-01 (1)	31.90	66.68	0.50	94.58	4.49	14.1	100.00	10.00	9.41	0.20
3-1-2024	Duplo	31.90	66.68	0.50	94.58	4.49	14.1	100.00	10.00	9.38	0.21
4-1-2024	CL1-23-01 (2)	31.91	72.77	0.49	99.54	5.64	17.7	100.00	10.00	9.68	0.07
4-1-2024	Duplo	31.91	72.77	0.49	99.54	5.64	17.7	100.00	10.00	9.63	0.09

Support beam CL1

Date	Name	Sample (g)	Empty Petri dish (g)	Filter (g)	Dry sample + dish and filter (g)	Cement (g)	Cement content (wt%)	Pipetted from solution (mL)	0.1M AgNO$_3$ (mL)	0.1M NH$_4$SCN (mL)	Chloride content (%)
22-12-2023	Blank							100.00	10.00	9.92	
29-12-2023	CL1-01 (1)	32.59	70.32	0.52	96.14	7.30	22.4	100.00	10.00	9.50	0.10
29-12-2023	Duplo	32.59	70.32	0.52	96.14	7.30	22.4	100.00	10.00	9.49	0.10
29-12-2023	CL1-01 (2)	32.97	72.77	0.50	101.25	4.99	15.1	100.00	10.00	9.72	0.07
29-12-2023	Duplo	32.97	72.77	0.50	101.25	4.99	15.1	100.00	10.00	9.76	0.06

Support beam CL2

Date	Name	Sample (g)	Empty Petri dish (g)	Filter (g)	Dry sample + dish and filter (g)	Cement (g)	Cement content (wt%)	Pipetted from solution (mL)	0.1M AgNO$_3$ (mL)	0.1M NH$_4$SCN (mL)	Chloride content (%)
22-12-2023	Blank							100.00	10.00	9.92	
28-12-2023	CL2-01 (1)	32.07	70.32	0.52	96.22	6.69	20.9	100.00	10.00	9.62	0.08
28-12-2023	Duplo	32.07	70.32	0.52	96.22	6.69	20.9	100.00	10.00	9.66	0.07
28-12-2023	CL2-01 (2)	31.81	63.45	0.53	90.62	5.18	16.3	100.00	10.00	9.76	0.05
28-12-2023	Duplo	31.81	63.45	0.53	90.62	5.18	16.3	100.00	10.00	9.68	0.08

Support beam CL3

Date	Name	Sample (g)	Empty Petri dish (g)	Filter (g)	Dry sample + dish and filter (g)	Cement (g)	Cement content (wt%)	Pipetted from solution (mL)	0.1M AgNO$_3$ (mL)	0.1M NH$_4$SCN (mL)	Chloride content (%)
22-12-2023	Blank							100.00	10.00	9.92	
22-12-2023	CL3-01 (1)	31.26	72.78	0.53	97.65	6.91	22.1	100.00	10.00	9.07	0.22
22-12-2023	Duplo	31.26	72.78	0.53	97.65	6.91	22.1	100.00	10.00	9.08	0.22
27-12-2023	CL3-01 (2)	32.08	66.72	0.52	93.22	6.10	19.0	100.00	10.00	9.38	0.16
27-12-2023	Duplo	32.08	66.72	0.52	93.22	6.10	19.0	100.00	10.00	9.23	0.20
3-1-2024	Blank							100.00	10.00	9.91	
4-1-2023	CL3-01 (3)	32.18	70.32	0.50	96.42	6.57	20.4	100.00	10.00	9.62	0.08
4-1-2023	Duplo	32.18	70.32	0.50	96.42	6.57	20.4	100.00	10.00	9.60	0.08
4-1-2023	CL3-01 (4)	31.96	63.46	0.49	89.97	5.94	18.6	100.00	10.00	9.80	0.03
5-1-2023	Duplo	31.96	63.46	0.49	89.97	5.94	18.6	100.00	10.00	9.76	0.04
5-1-2023	CL3-01 (5)	32.08	72.77	0.49	99.36	5.99	18.7	100.00	10.00	9.89	0.01
5-1-2023	Duplo	32.08	72.77	0.49	99.36	5.99	18.7	100.00	10.00	9.87	0.01
5-1-2023	CL3-01 (6)	32.66	66.69	0.50	92.85	6.99	21.4	100.00	10.00	9.88	0.01
5-1-2023	Duplo	32.66	66.69	0.50	92.85	6.99	21.4	100.00	10.00	9.88	0.01

Appendix F

Data non-destructive testing

F.1   Visual inspection

(a) Beam 5 bottom face.

(b) Beam 6 bottom face.
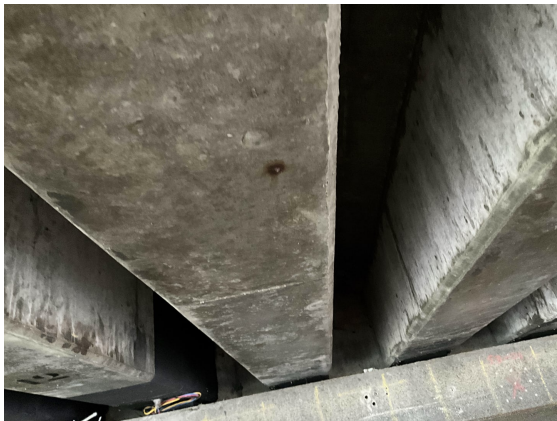
(c) Beam 11 bottom face.

(d) Beam 12 east face.

(e) Beam 14 bottom face.

(f) Beam 17 bottom face.

(g) Beam 18 east face.

(h) Beam 18 west face.

Figure F.1: Minor corrosion damage observed on several beams possibly
due to a ferrous aggregate or a loose tie wire.

F.2   Additional GPR and UPE scans

Support beam
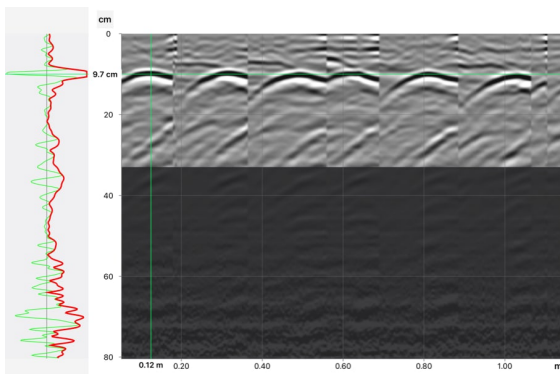
(a)
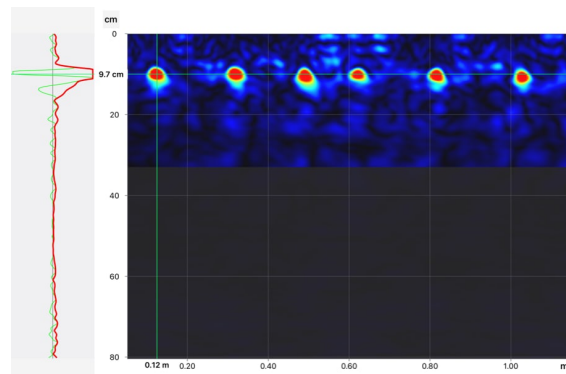
(b)

Figure F.2: Radargrams (a) and migrated heatmap (b) depicting a section of
the vertical face of the supporting beam.

Beam 1

(a)

(b)
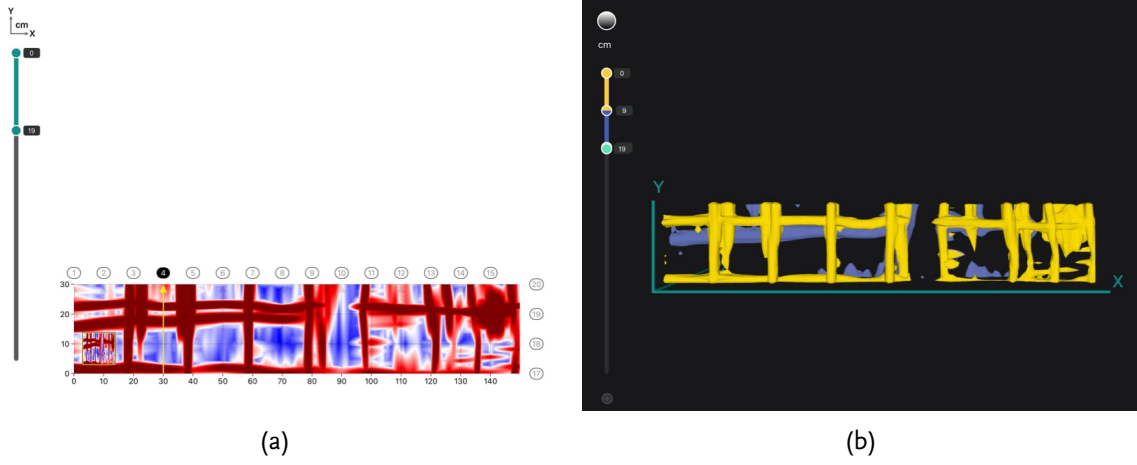
Figure F.3: Area scan (a) and 3D scan (b) of beam 1 east face.

(a)

(b)

(c)
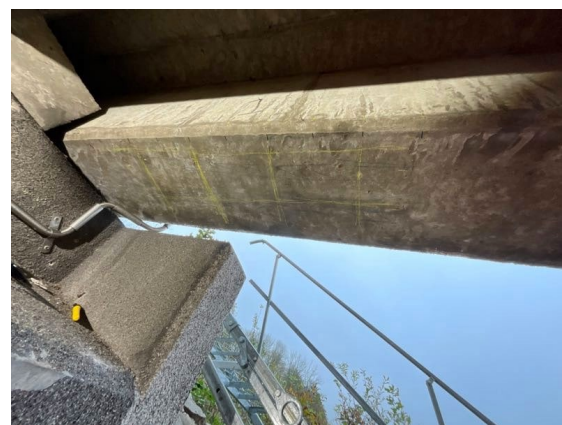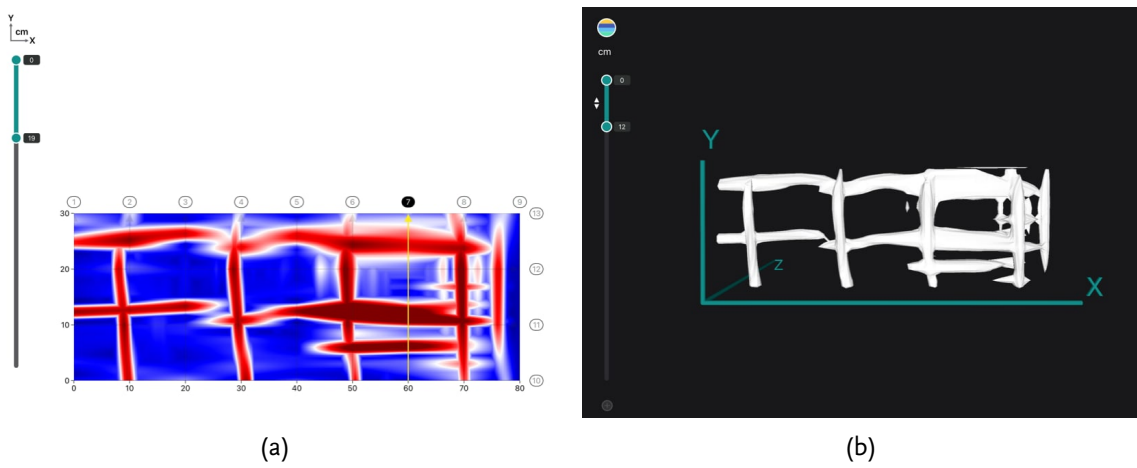
Figure F.4: Area scan (a), 3D scan (b) and GPR grid (c) of beam 1 bottom face.

(a)

(b)

(c)
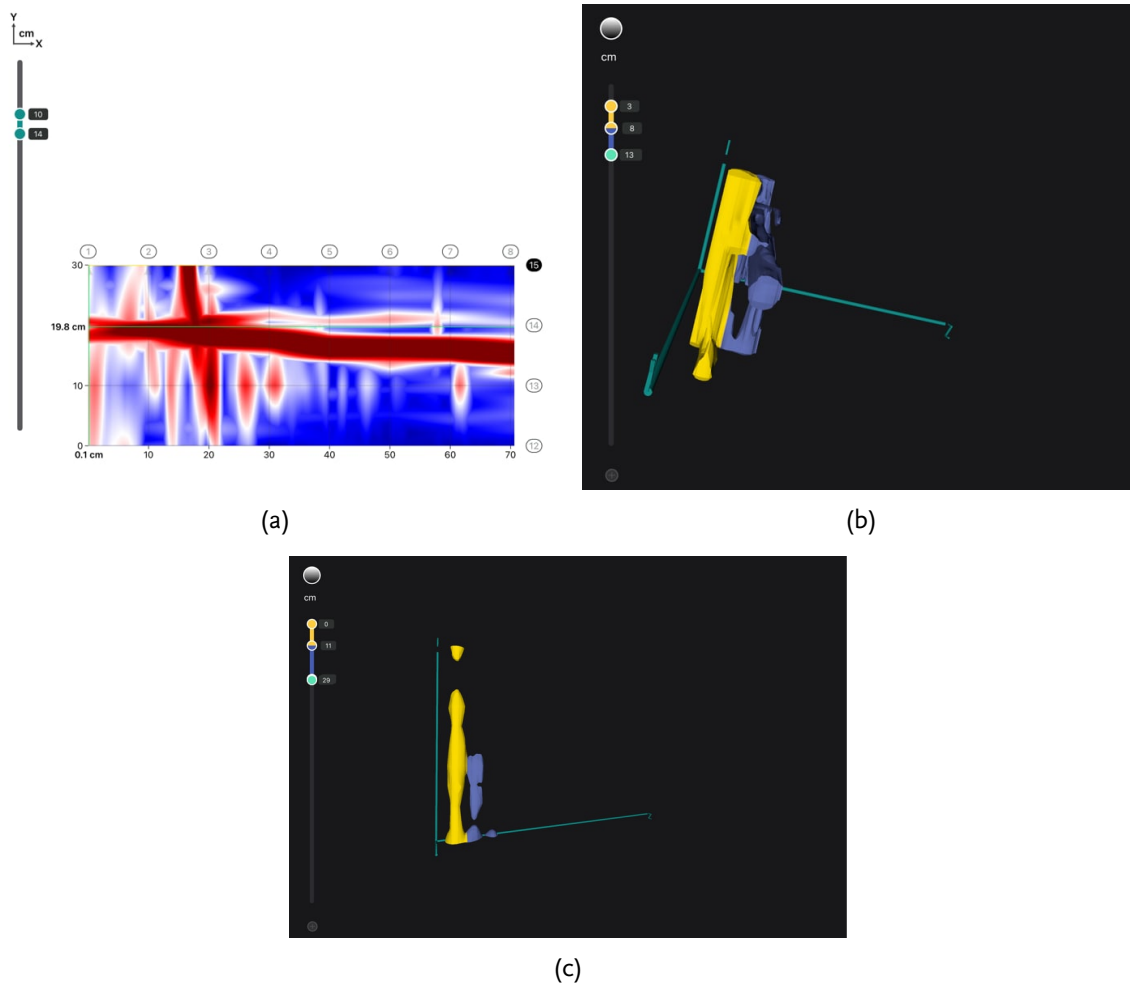
Figure F.5: Area scan (a), 3D scan (b) and UPE scan (c) of beam 1 west face.

Beam 7

(a)

(b)
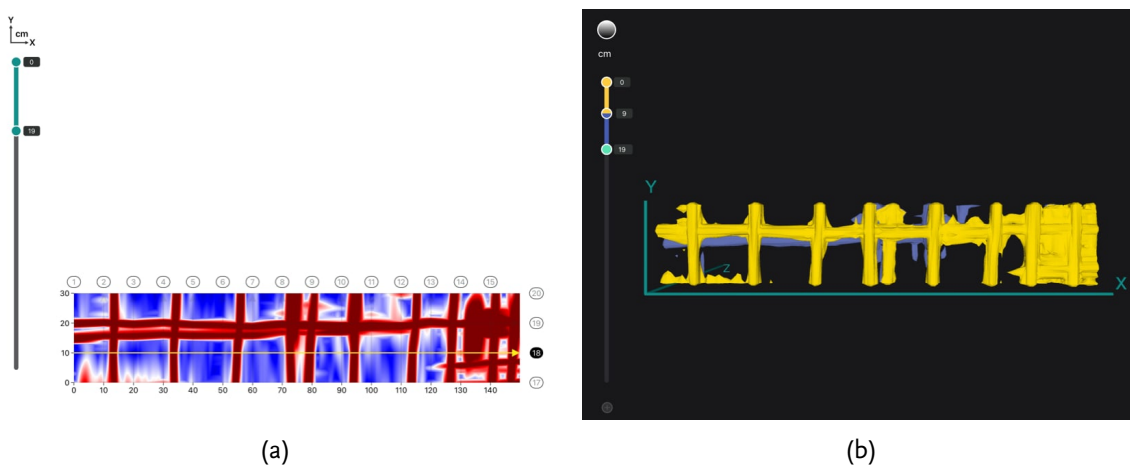
Figure F.6: Area scan (a) and 3D scan (b) of beam 7 east face.

Beam 13: Using GPR on the CP-coating is not possible, and unfortunately, UPE scans were lost in the process except for Figure 5.8.

(a)

(b)

(c)
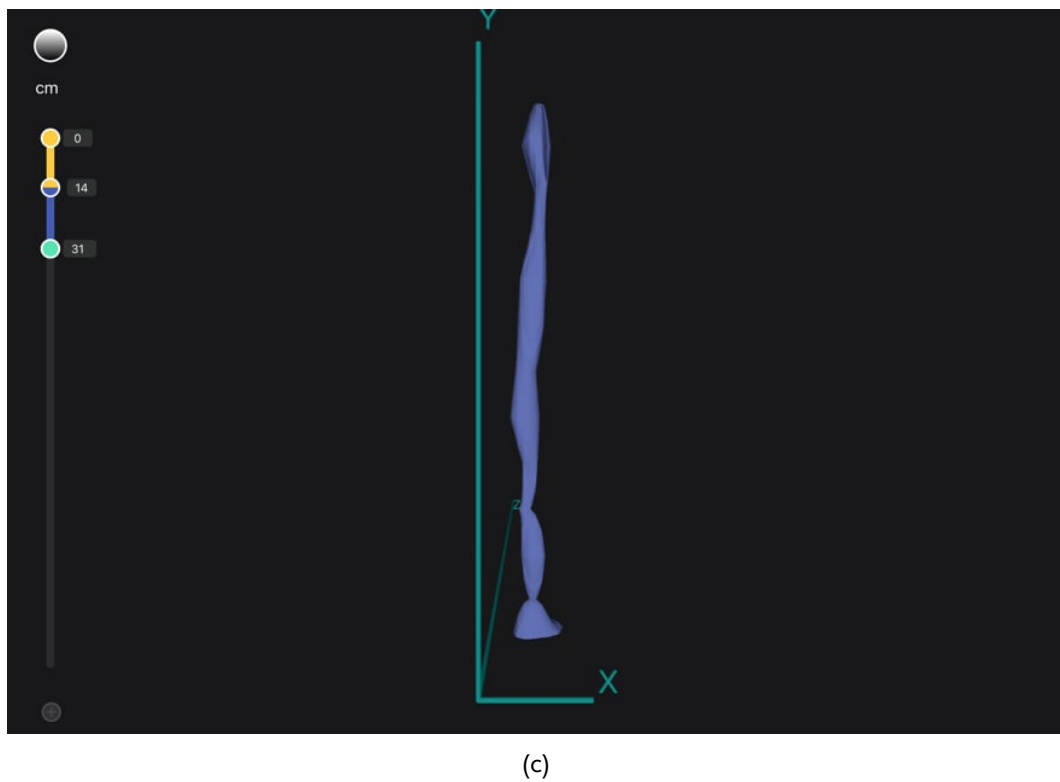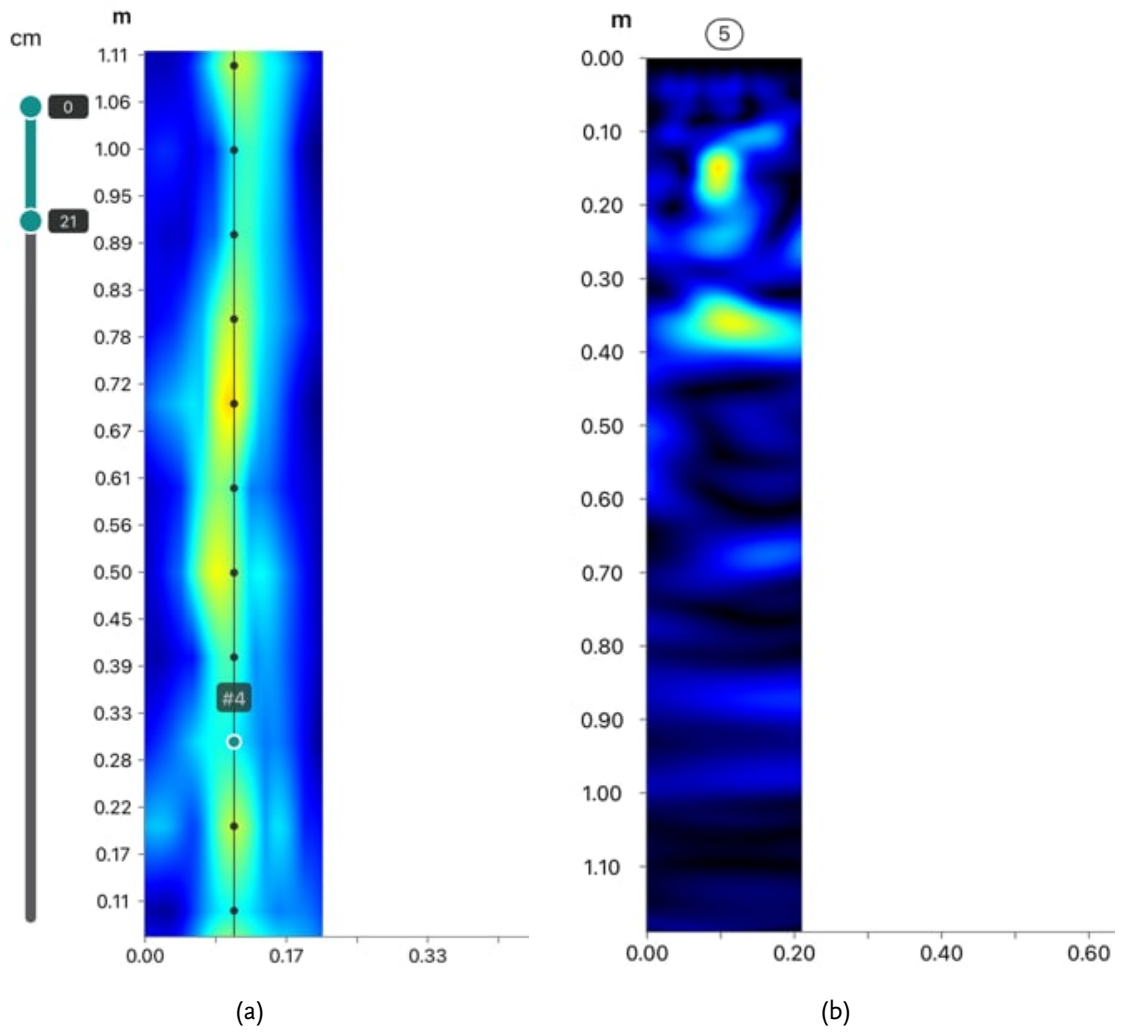
Figure F.7: UPE stripe scan (a), heatmap of scan 5 (b) and 3D scan (c) of beam 7 west face.

Beam 18

(a)

(b)
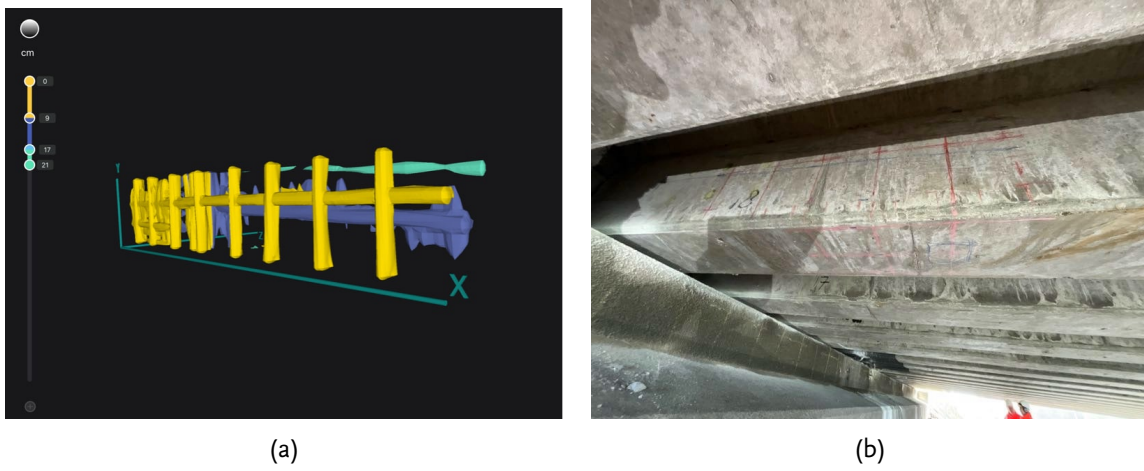
Figure F.8: 3D scan (a) and GPR grid (b) of beam 18 west face.

Beam 23
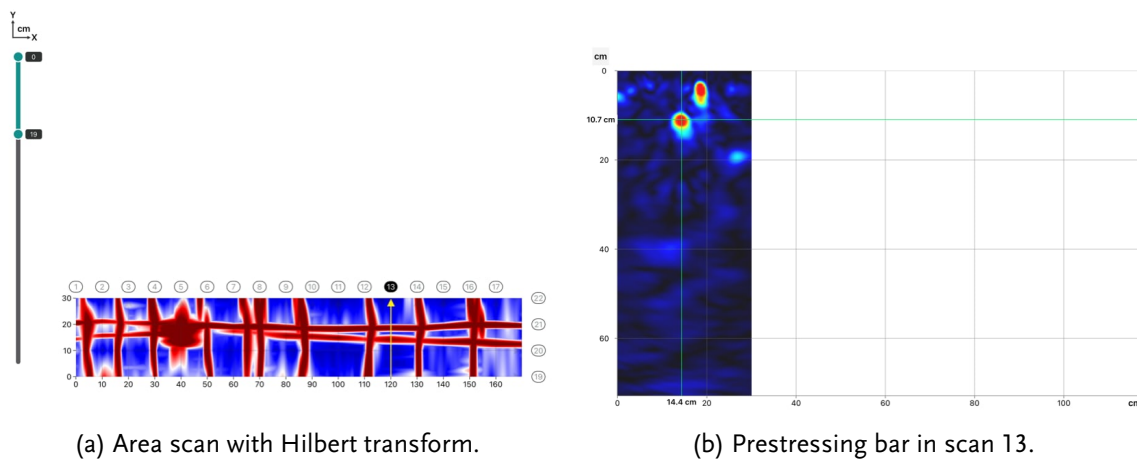
(a) Area scan with Hilbert transform.

(b) Prestressing bar in scan 13.
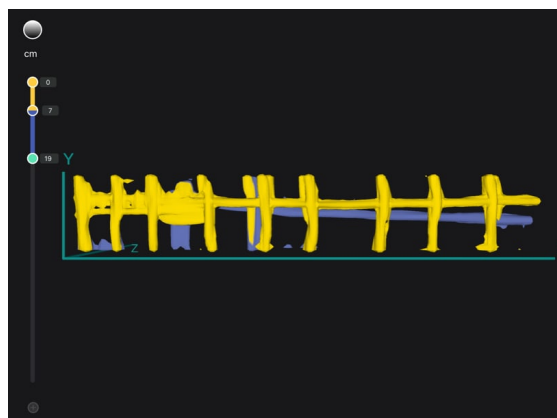
(c) 3D view of the scan.

Figure F.9: GPR area scan of the west face of beam head 23, showing a clear distinction between the prestressing and regular reinforcement.

(a)

(b)

(c)
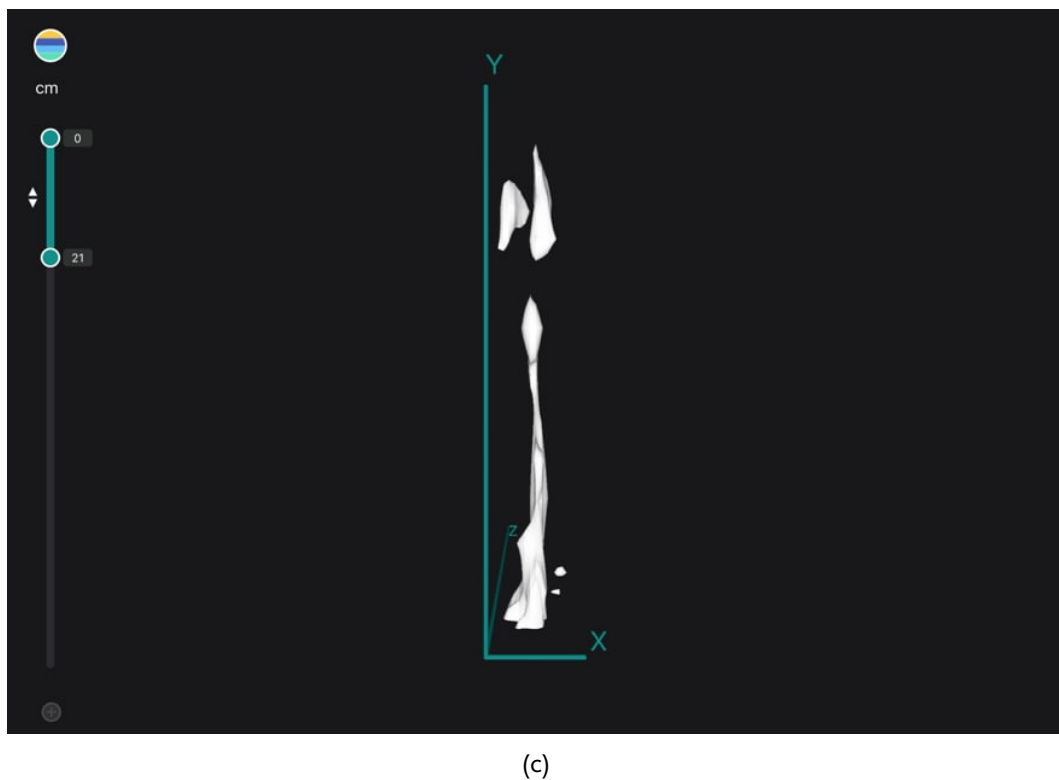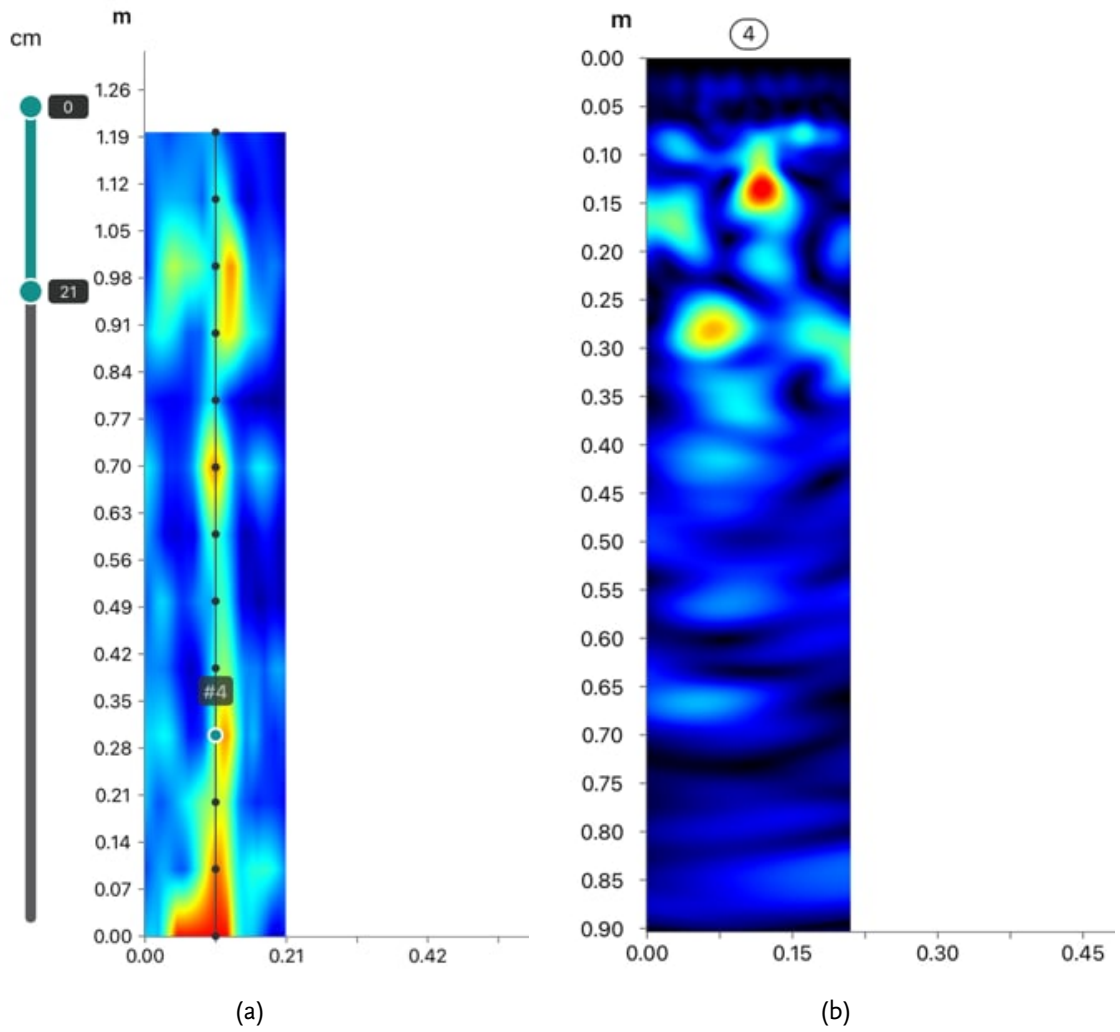
Figure F.10: UPE stripe scan (a), heatmap of scan 4 (b) and 3D scan (c) of beam 7 west face.

3.3 Onderzoekslocaties

In totaal is ter plaatse van zes liggers ultrasoononderzoek uitgevoerd. Op twee locaties in het midden van de overspanning en op vier locatie ter hoogte van steunpunt 01. Zie ook onderstaande tabel en figuren.

Ligger – voorspankanaal	Locatie	Lengte doorgemeten voorspankanaal
1-A	Midden overspanning 01-02	2,7 m
1-B	Midden overspanning 01-02	2,7 m
1-C	Midden overspanning 01-02	2,7 m
2-A	Midden overspanning 01-02	4,0 m
2-B	Midden overspanning 01-02	4,0 m
2-C	Midden overspanning 01-02	4,0 m
2-D	Midden overspanning 01-02	4,0 m
12-D	Ter hoogte van steunpunt 01	3,8 m
13-D	Ter hoogte van steunpunt 01	4,0 m
21-A	Ter hoogte van steunpunt 01	4,0 m
23-A	Ter hoogte van steunpunt 01	2,3 m

Tabel 3.1: Overzicht onderzoekslocaties.
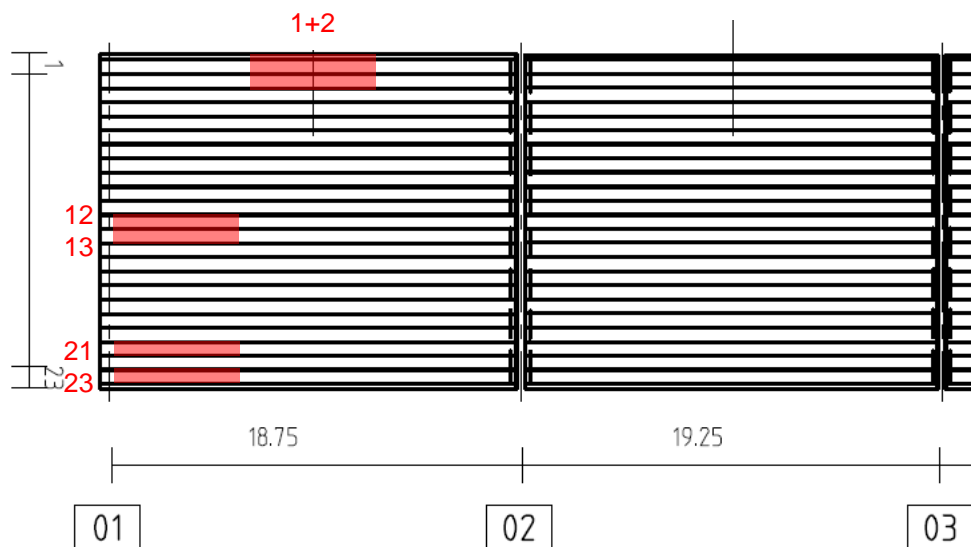
Figuur 3.7: Inspectietekening onderaanzicht brugdek, met ingetekende onderzoekslocaties.
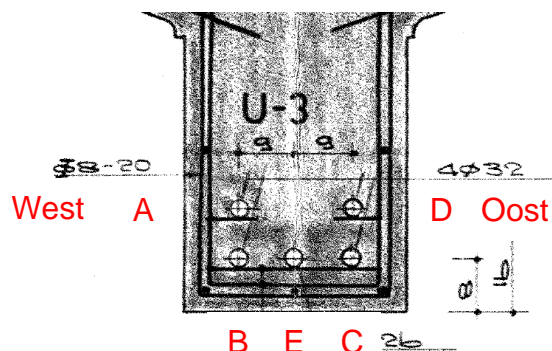
Figuur 3.8: Principe aanduiding voorspankanalen in doorsnede.

Meting 1-B
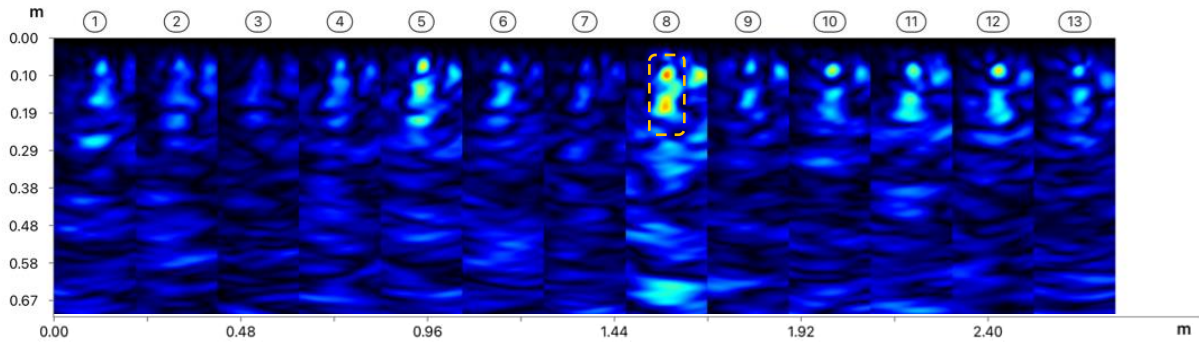
Figuur 4.3: Kijkgat locatie 1-B meetpunt 8.

Bevindingen onderzoekslocatie 1-B:

- Voorspankanaal zichtbaar in elke individuele meting.
- De amplitude van de reflectie van voorspankanaal B varieert in de meting. Ter plaatse van meting 8 is de reflectie het grootst. Indicatie op holte.
- Ter verificatie van een verdachte meting is een kijkgat gemaakt bij meetpunt 8. Geen holte aangetroffen.

Meting 1-C
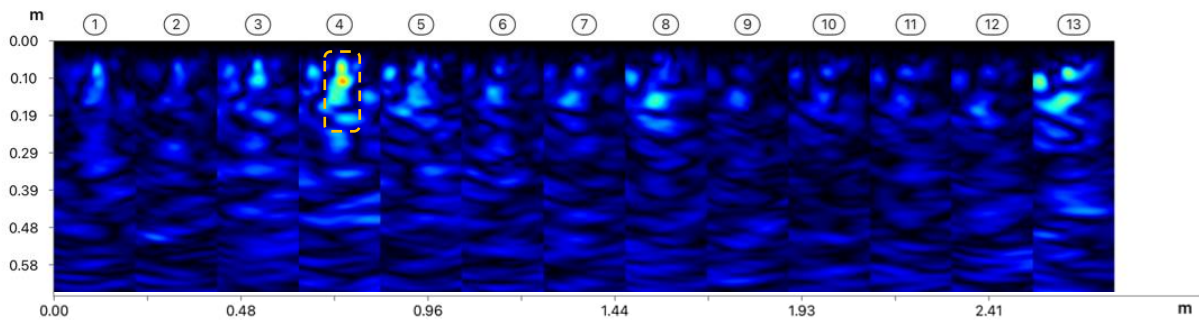
Figuur 4.4: Kijkgat locatie 1-C meetpunt 4.

Bevindingen onderzoekslocatie 1-C:

- Voorspankanaal zichtbaar in elke individuele meting.
- De amplitude van de reflectie van voorspankanaal C varieert in de meting. Ter plaatse van meting 4 is de reflectie het grootst. Indicatie op holte.
- Ter verificatie van een verdachte meting is een kijkgat gemaakt bij meetpunt 4. Geen holte aangetroffen.

Meting 2-A
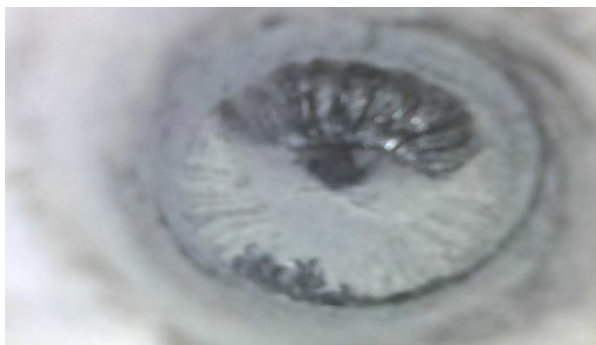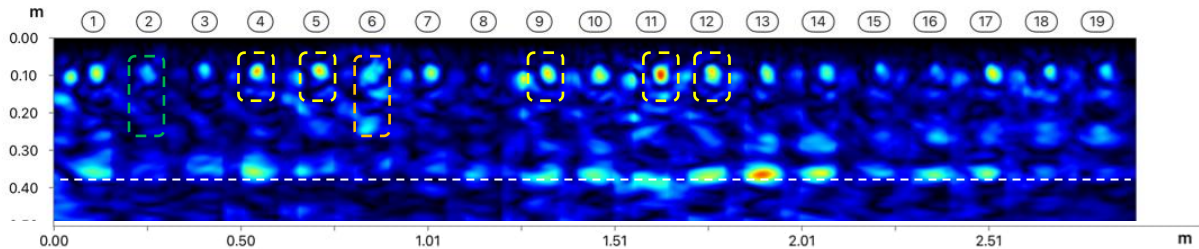
Figuur 4.5: Kijkgat locatie 2-A meetpunt 2.
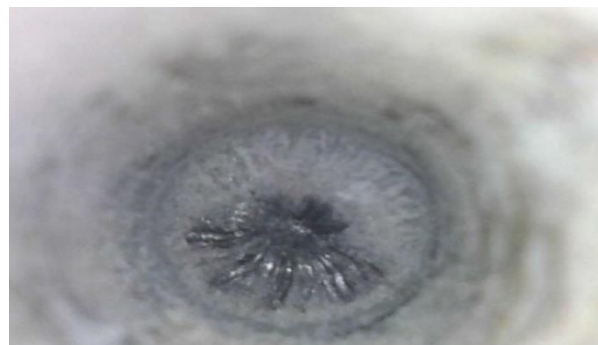
Figuur 4.6: Kijkgat locatie 2-A meetpunt 6.

Bevindingen onderzoekslocatie 2-A:

- Voorspankanaal zichtbaar in elke individuele meting.
- Goede reflectie tegen de achterzijde van de doorsnede in de gehele meting.
- De amplitude van de reflectie van voorspankanaal A varieert in de meting. Op meerdere locaties een sterkere reflectie (geel omkaderd). Indicatie op holte.
- Ter verificatie van een verdachte meting is een kijkgat gemaakt bij meetpunt 6. Geen holte aangetroffen. Deze meting is beperkt verdacht door de extra dieper gelegen verstoring. Bij nader inzien is dit vermoedelijk voorspankanaal D aan de andere zijde van de doorsnede.
- Ter verificatie van een niet verdachte meting is een kijkgat gemaakt bij meetpunt 2. Geen holte aangetroffen.

Meting 2-B
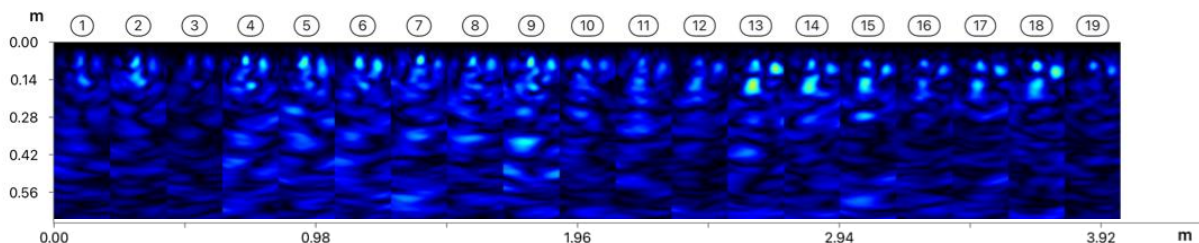
Bevindingen onderzoekslocatie 2-B:

- Voorspankanaal zichtbaar in elke individuele meting.
- Geen indicaties.

Meting 2-C
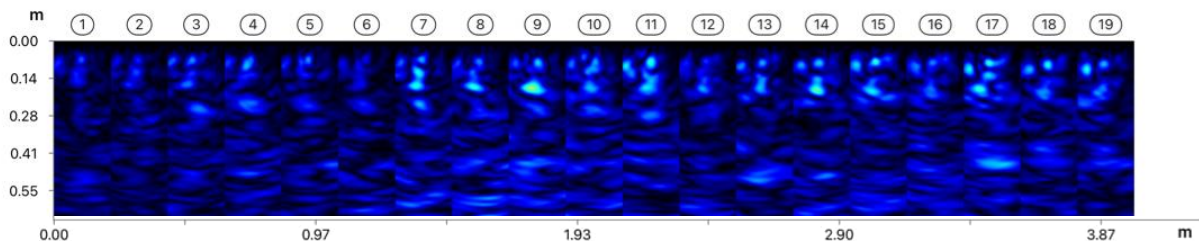
Bevindingen onderzoekslocatie 2-C:

- Voorspankanaal zichtbaar in elke individuele meting.
- Geen indicaties.

Meting 2-D
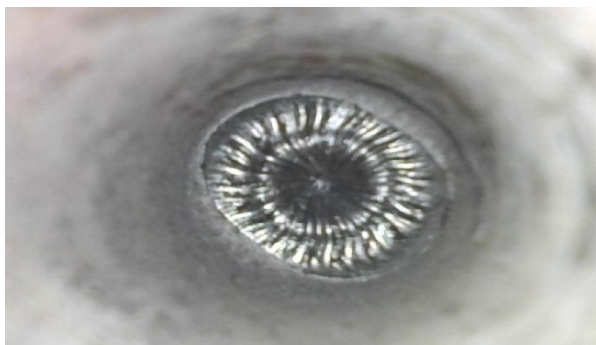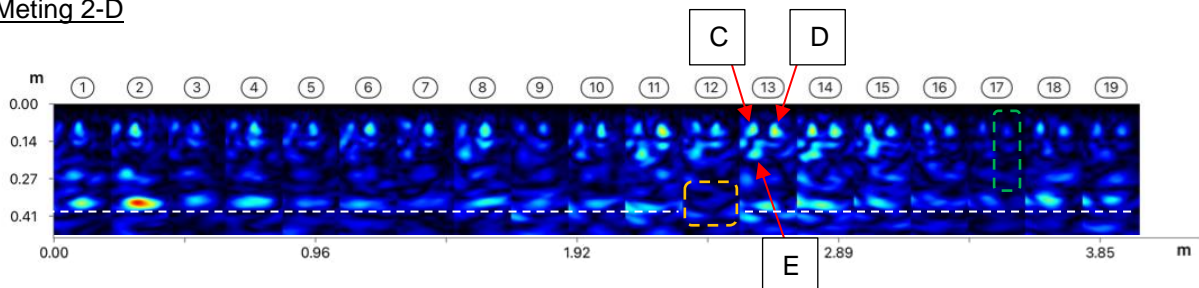
Figuur 4.7: Kijkgat locatie 2-D meetpunt 12.   Figuur 4.8: Kijkgat locatie 2-D meetpunt 17.

Bevindingen onderzoekslocatie 2-D:

- Goede reflectie tegen de achterzijde van de doorsnede in nagenoeg de gehele meting.
- Voorspankanaal zichtbaar in elke individuele meting. Op diverse metingen zijn drie voorspankanalen zichtbaar. Deze zijn met rode pijlen aangeduid op meetpunt 13.
- De amplitude van de reflectie van voorspankanaal D varieert nauwelijks. Geen indicatie op holte.
- Indicatie meetpunt 12 gebaseerd op wegvallen reflectie tegen achterzijde. Geen holtes aangetroffen in kijkgat.
- Kijkgat meetpunt 17 betreft referentiemeting niet verdachte locatie.

Meting 12-D
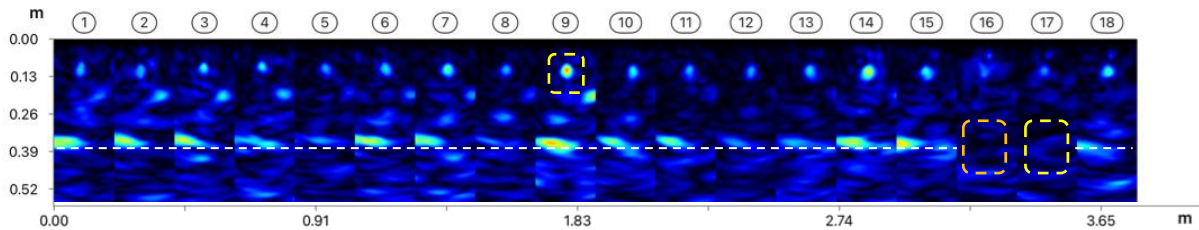
Figuur 4.9: Kijkgat locatie 12-D meetpunt 16.

Bevindingen onderzoekslocatie 12-D:

- Goede reflectie tegen de achterzijde van de doorsnede in nagenoeg de gehele meting.
- Voorspankanaal zichtbaar in elke individuele meting.
- De amplitude van de reflectie van voorspankanaal D varieert in de meting. Ter plaatse van meting 9 is de reflectie het grootst. Indicatie op holte.
- Indicatie meetpunt 16 en 17 gebaseerd op wegvallen reflectie tegen achterzijde. Geen holtes aangetroffen in kijkgat.
- Ter verificatie van een verdachte meting is een kijkgat gemaakt bij meetpunt 16. Geen holte aangetroffen.

Meting 13-D
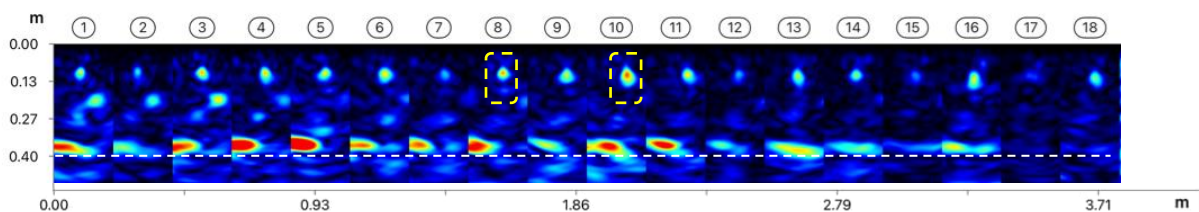
Bevindingen onderzoekslocatie 13-D:

- Goede reflectie tegen de achterzijde van de doorsnede in de gehele meting.
- Voorspankanaal zichtbaar in elke individuele meting.
- De amplitude van de reflectie van voorspankanaal D varieert in de meting. Ter plaatse van meting 9 is de reflectie het grootst. Indicatie op holte.

Meting 21-A
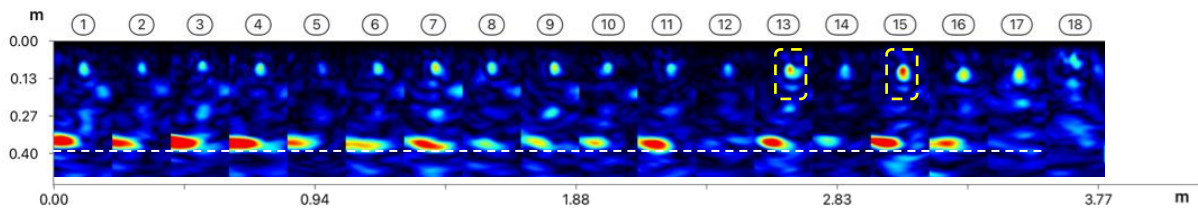
Bevindingen onderzoekslocatie 21-A:

- Goede reflectie tegen de achterzijde van de doorsnede in de gehele meting.
- Voorspankanaal zichtbaar in elke individuele meting, met uitzondering van meetpunt 18. Deze meting is voorbij de verankering uitgevoerd. Hier is geen voorspankanaal meer aanwezig in de doorsnede.
- De amplitude van de reflectie van voorspankanaal A varieert in de meting. Ter plaatse van meting 13 en 15 is de reflectie het grootst. Indicatie op holte.

Meting 23-A
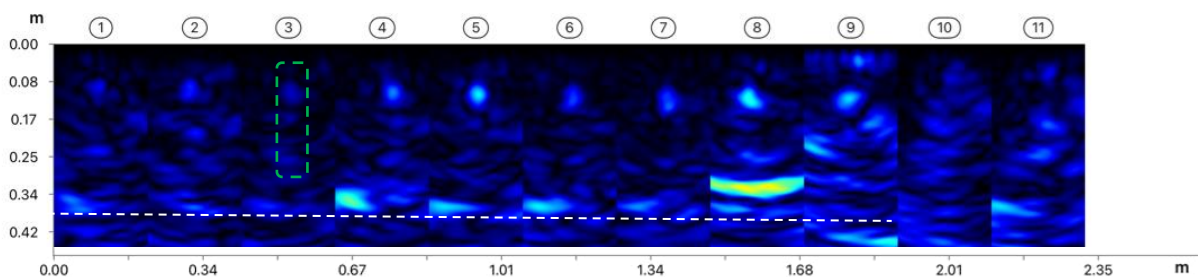
Figuur 4.10: Kijkgat locatie 23-A meetpunt 3.

Bevindingen onderzoekslocatie 23-A:

- Goede reflectie tegen de achterzijde van de doorsnede in de gehele meting.
- Voorspankanaal zichtbaar in elke individuele meting, met uitzondering van meetpunt 10 en 11. Deze meting is voorbij de verankering uitgevoerd. Hier is geen voorspankanaal meer aanwezig in de doorsnede.
- Geen indicaties.
- Ter verificatie van een niet verdachte meting is een kijkgat gemaakt bij meetpunt 3. Geen holte aangetroffen.

F.3   Half-cell potential maps
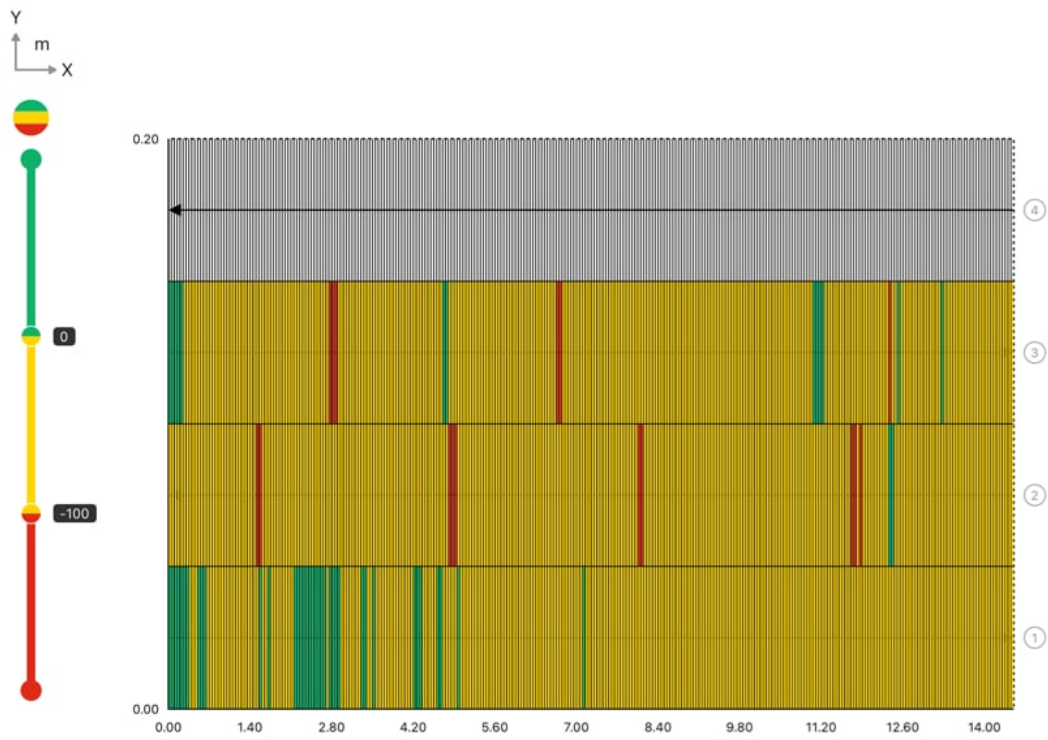
Figure F.11: Support beam half-cell potential map (1).

Figure F.12: Support beam half-cell potential map (2).
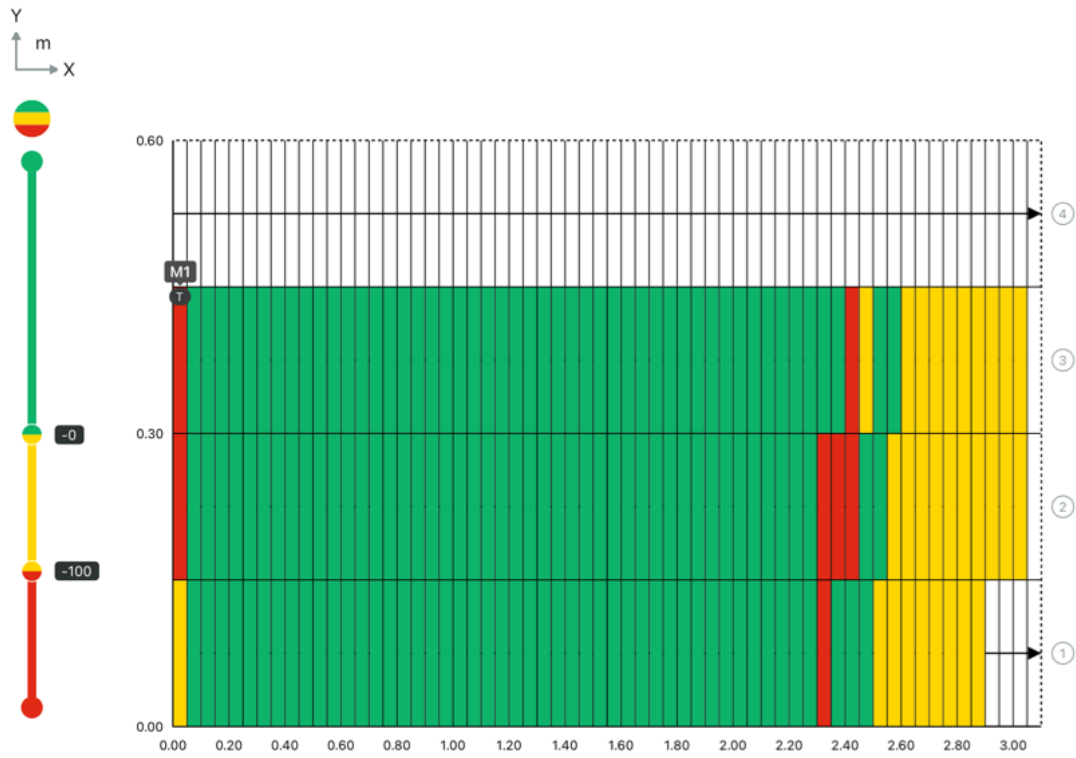
Figure F.13: Beam 1 east face half-cell potential map (1).

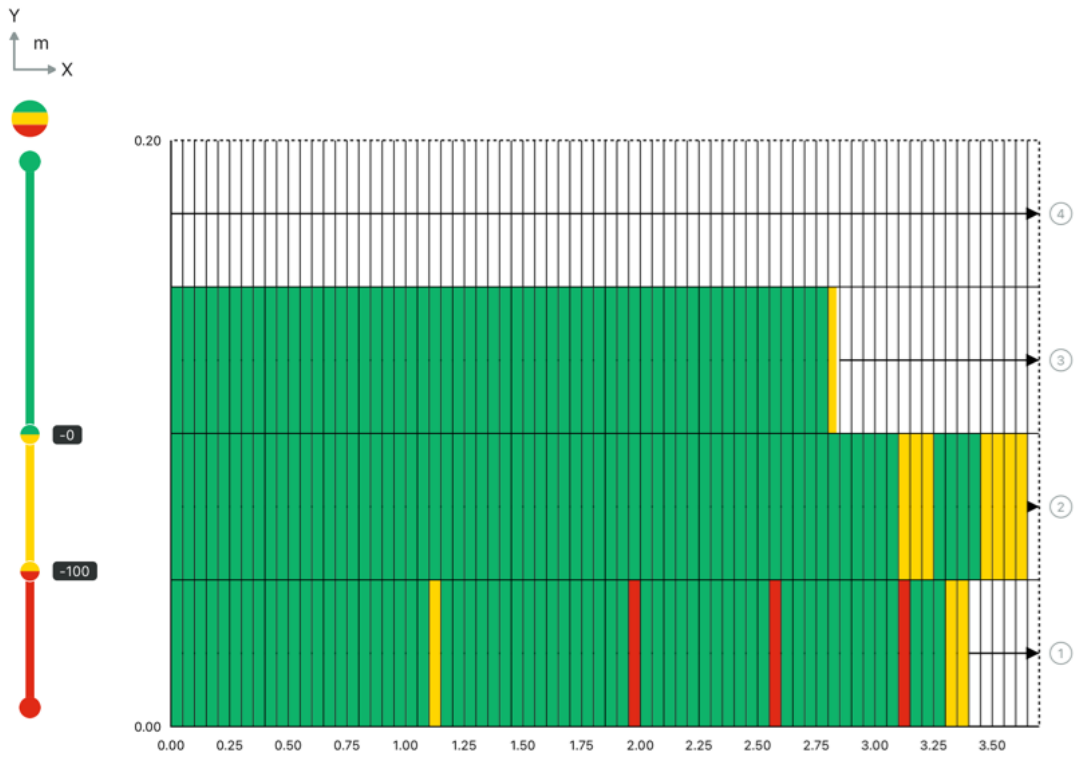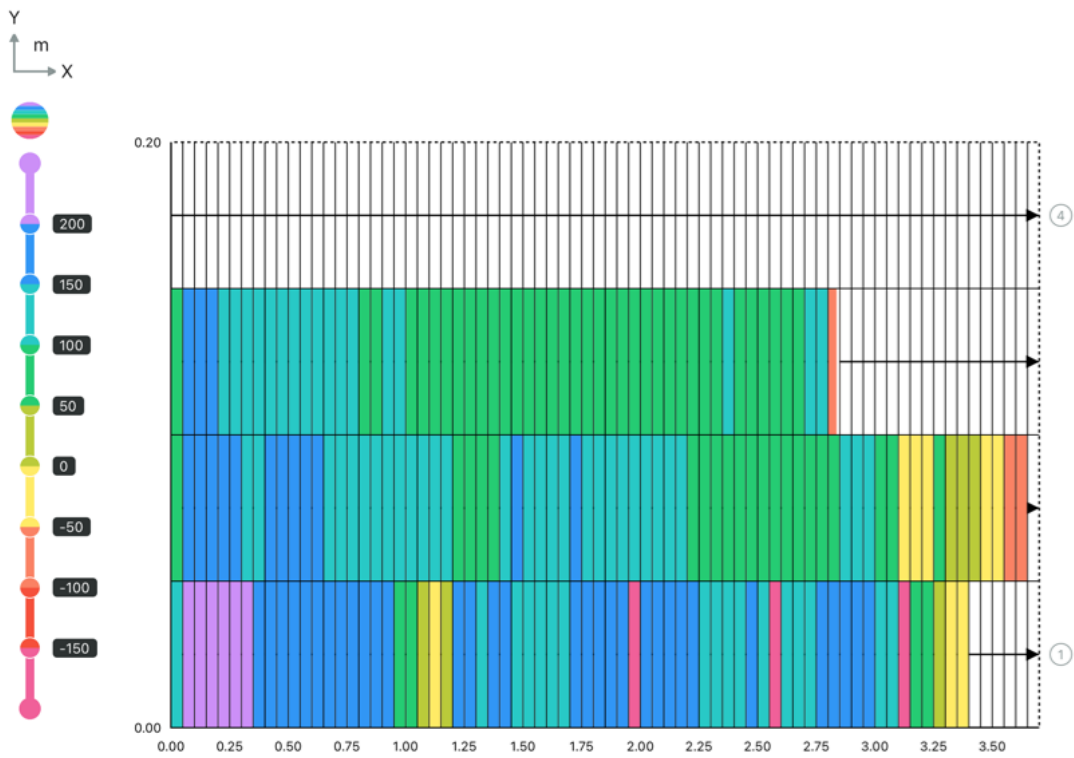Figure F.14: Beam 1 east face half-cell potential map (2).
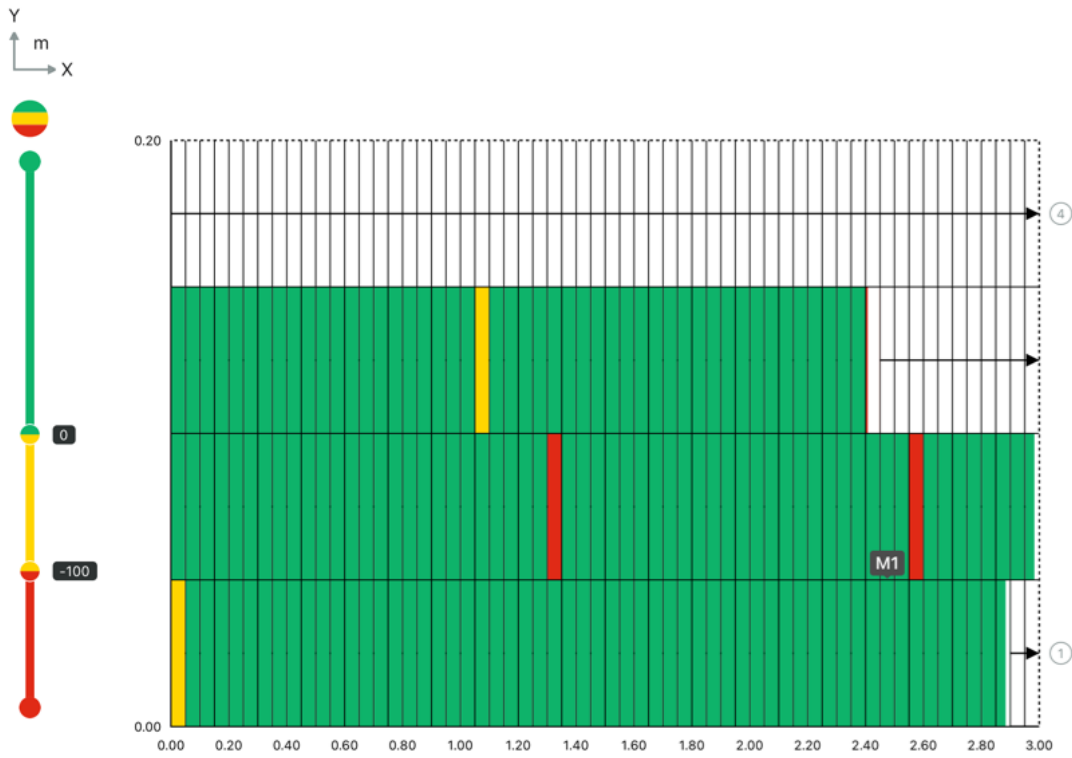
Figure F.15: Beam 1 west face half-cell potential map (1).
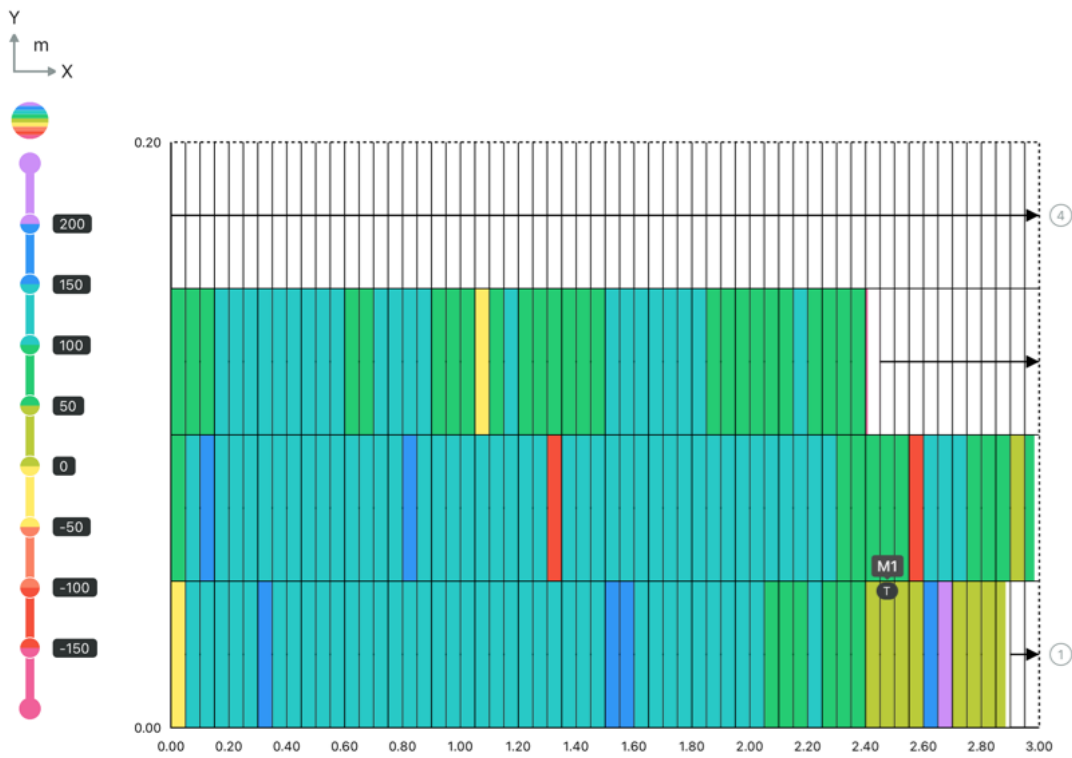
Figure F.16: Beam 1 west face half-cell potential map (2).
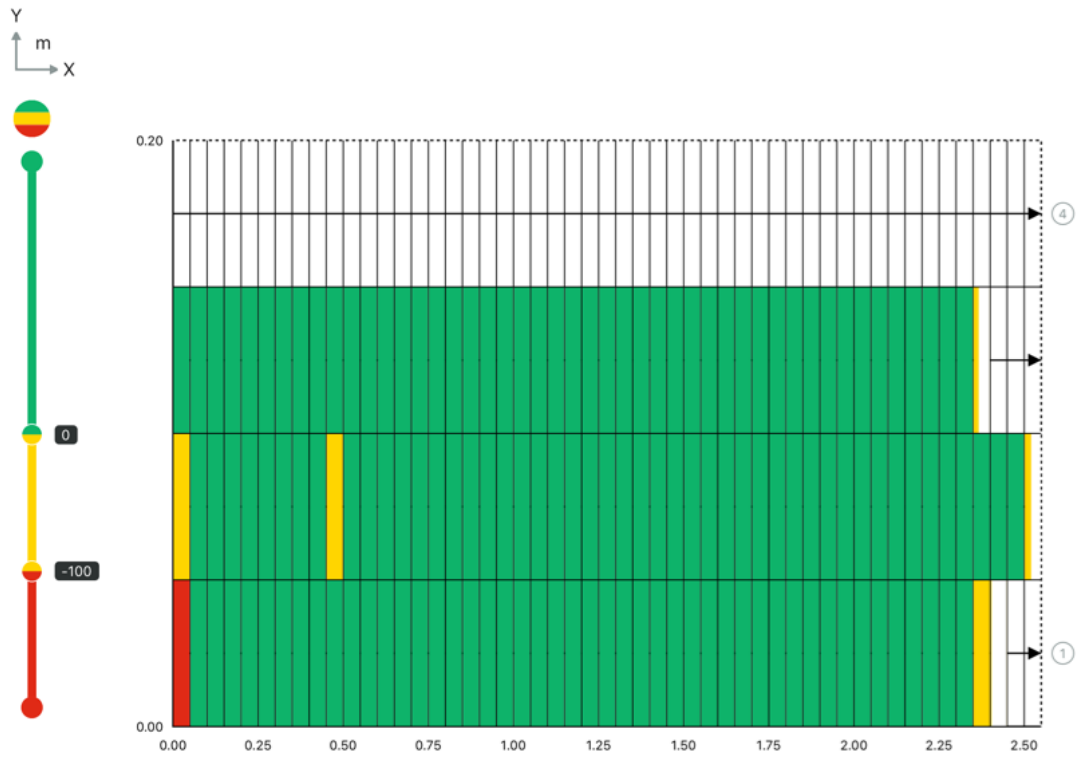
Figure F.17: Beam 1 bottom half-cell potential map (1).
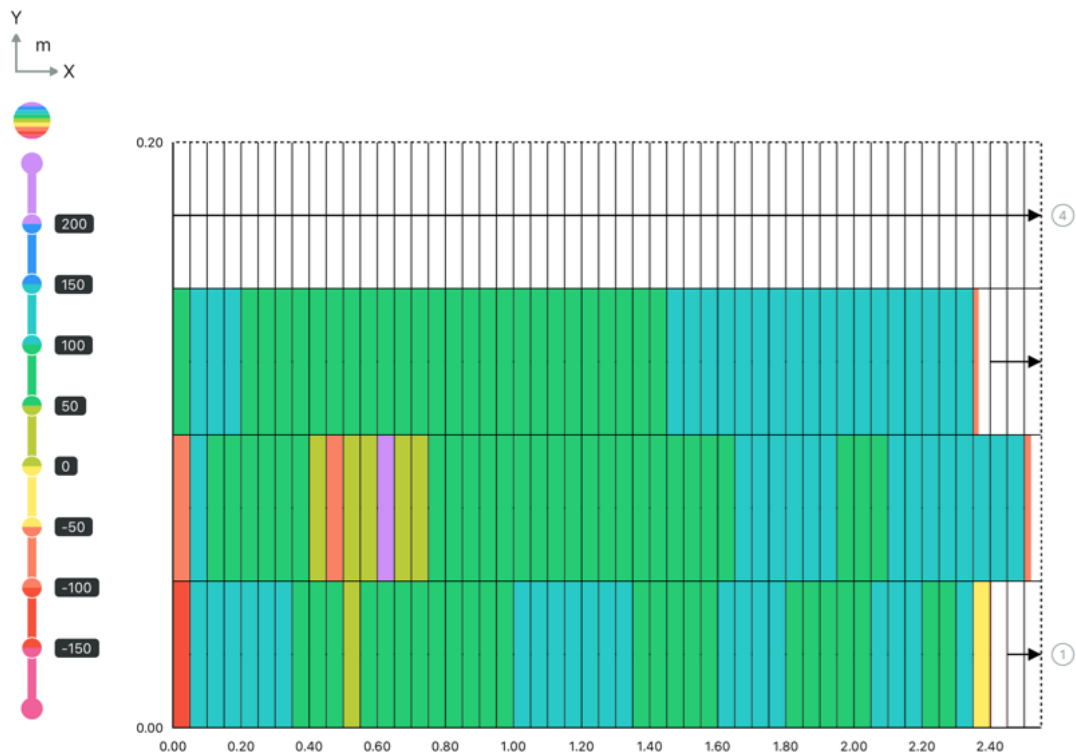
Figure F.18: Beam 1 bottom half-cell potential map (2).
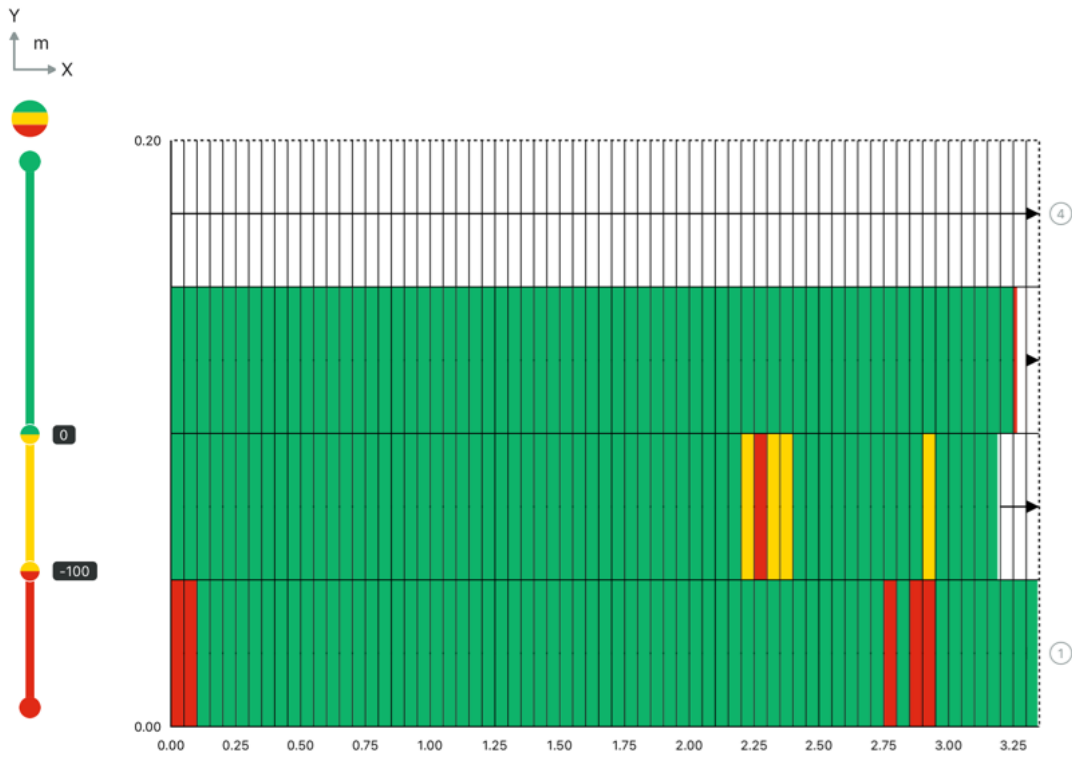
Figure F.19: Beam 7 east face half-cell potential map (1).
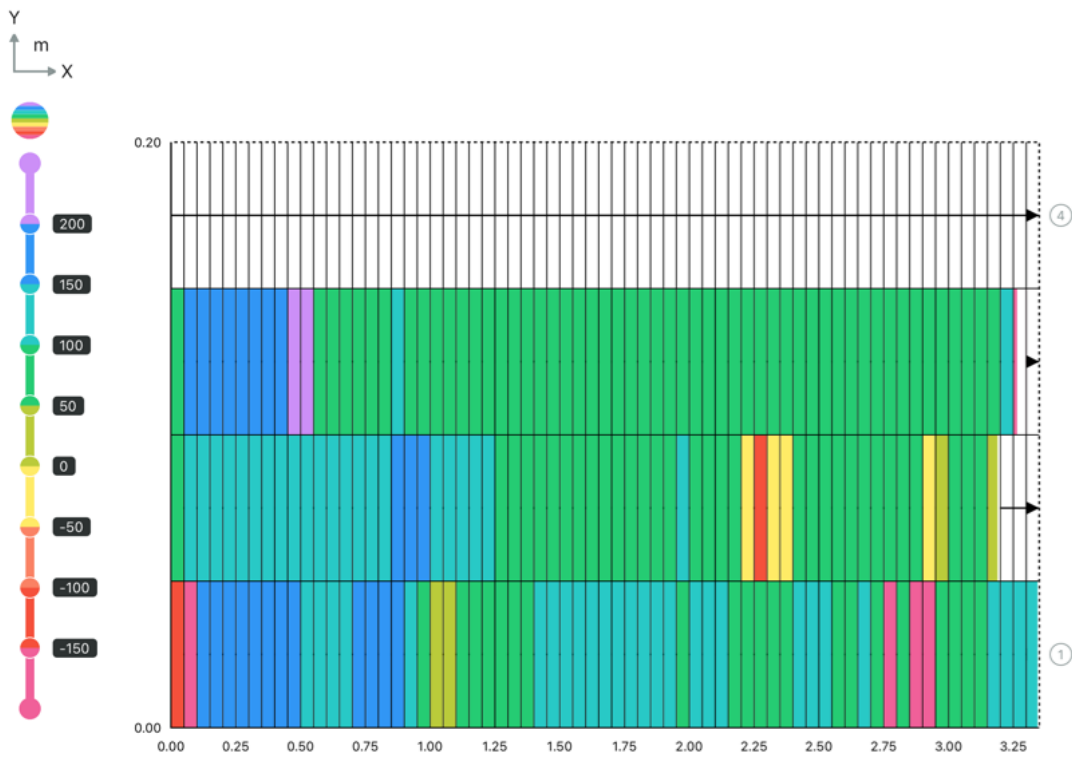
Figure F.20: Beam 7 east face half-cell potential map (2).
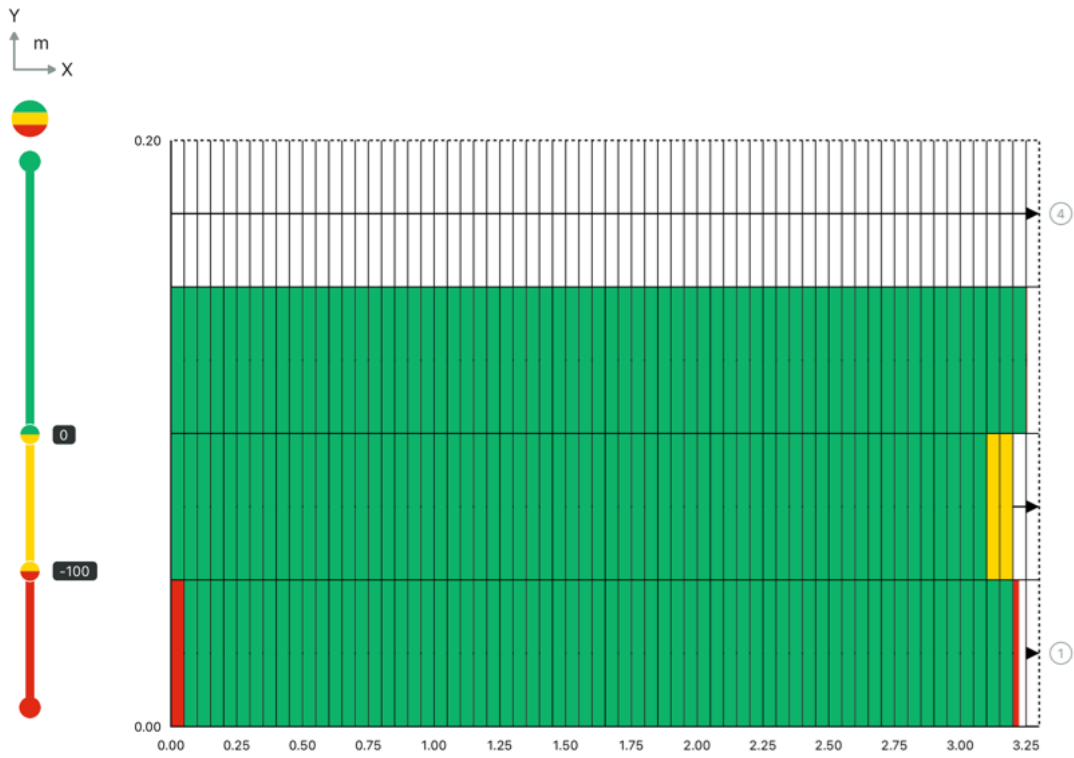
Figure F.21: Beam 7 west face half-cell potential map (1).
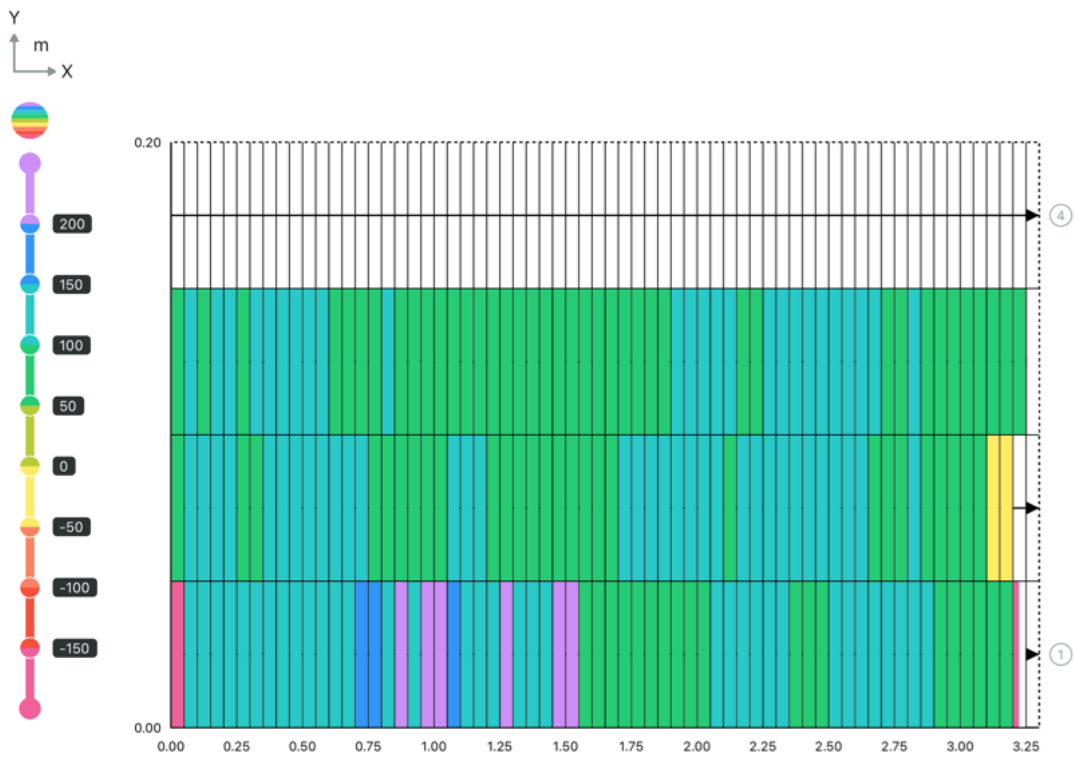
Figure F.22: Beam 7 west face half-cell potential map (2).
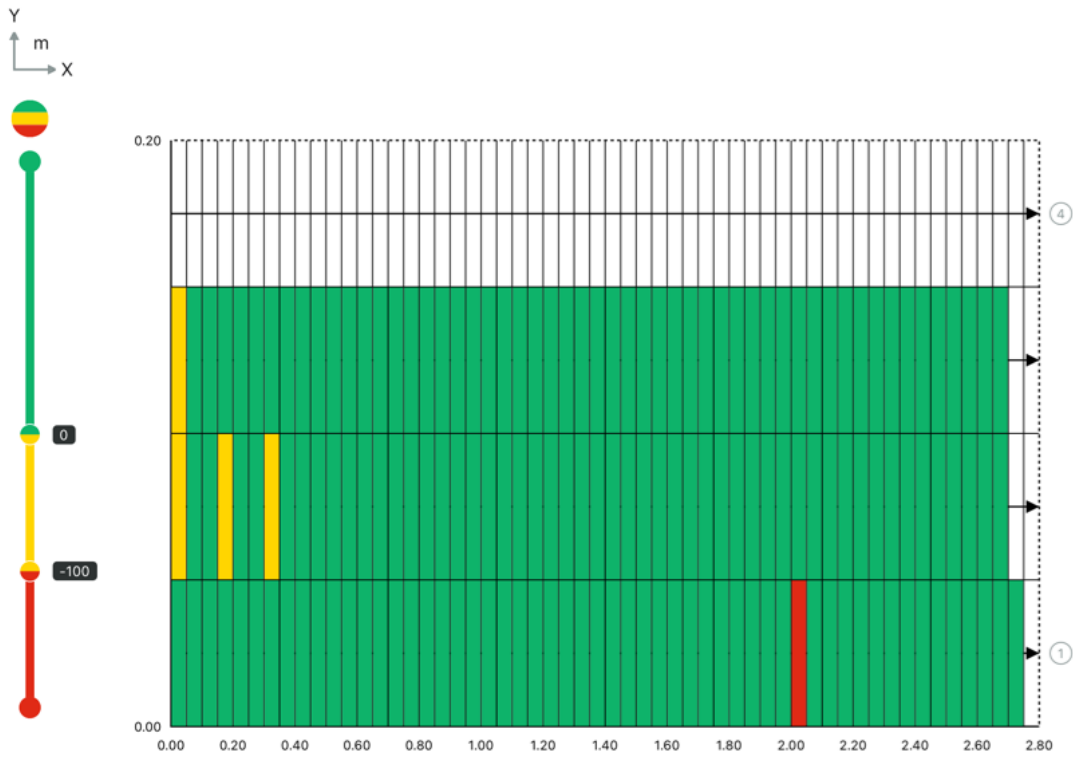
Figure F.23: Beam 7 bottom half-cell potential map (1).
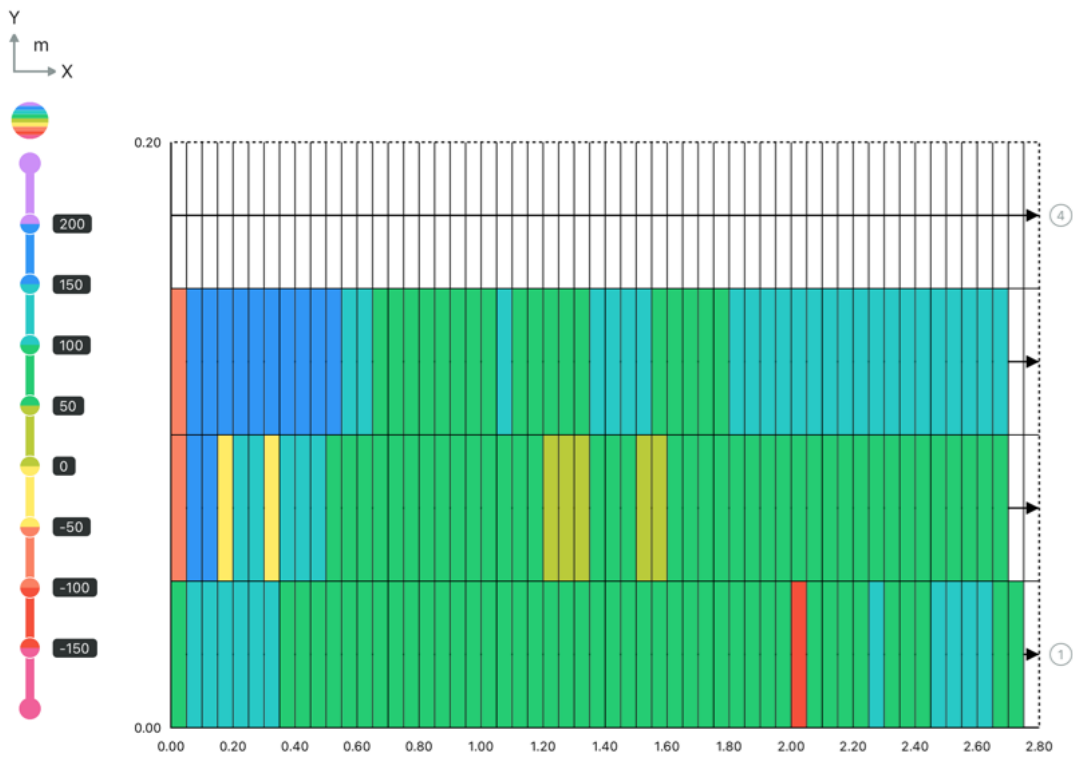
Figure F.24: Beam 7 bottom half-cell potential map (2).
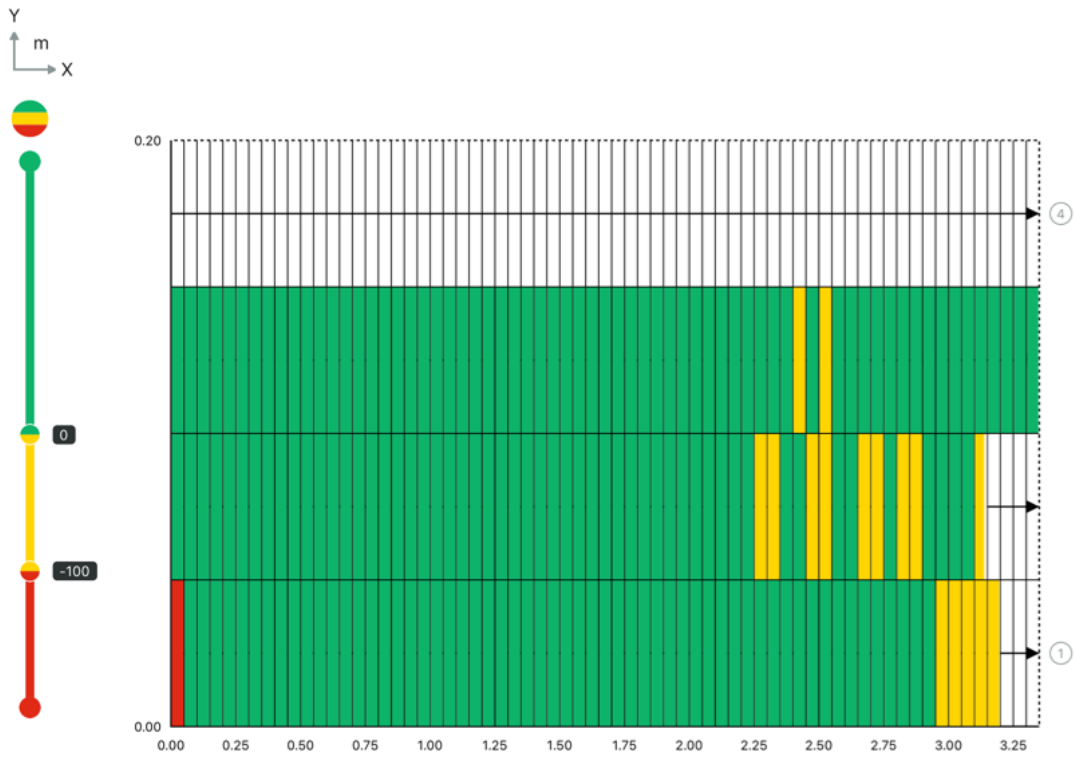
Figure F.25: Beam 13 east face half-cell potential map (1).
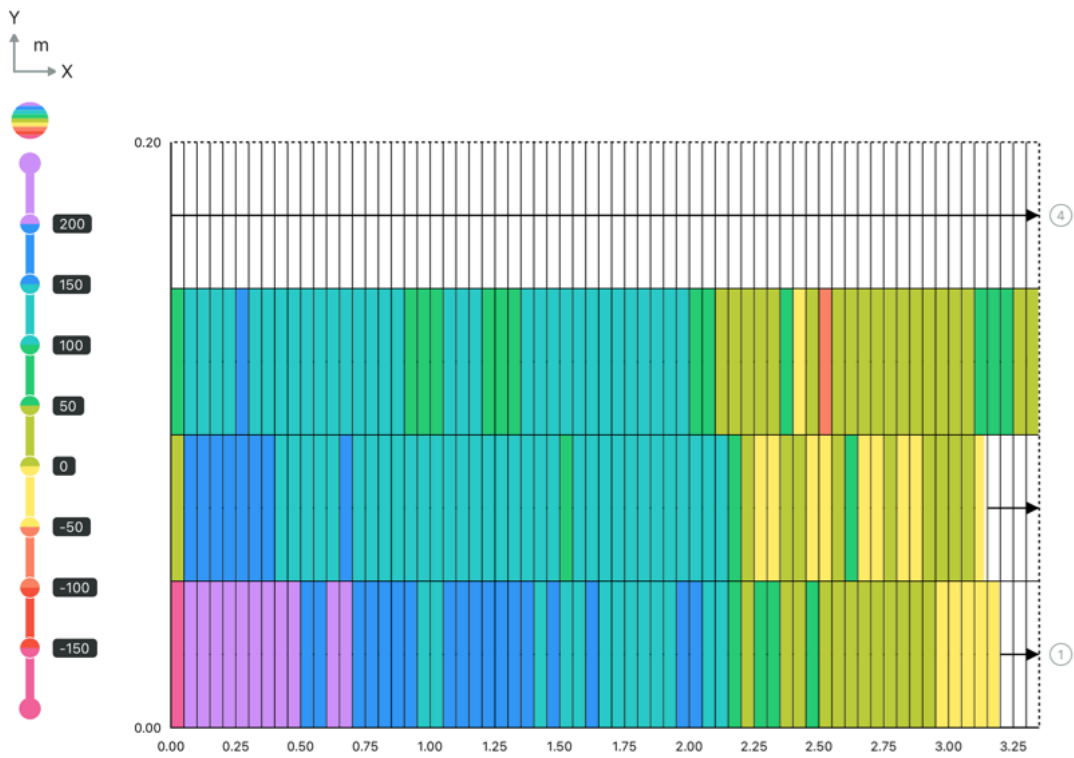
Figure F.26: Beam 13 east face half-cell potential map (2).
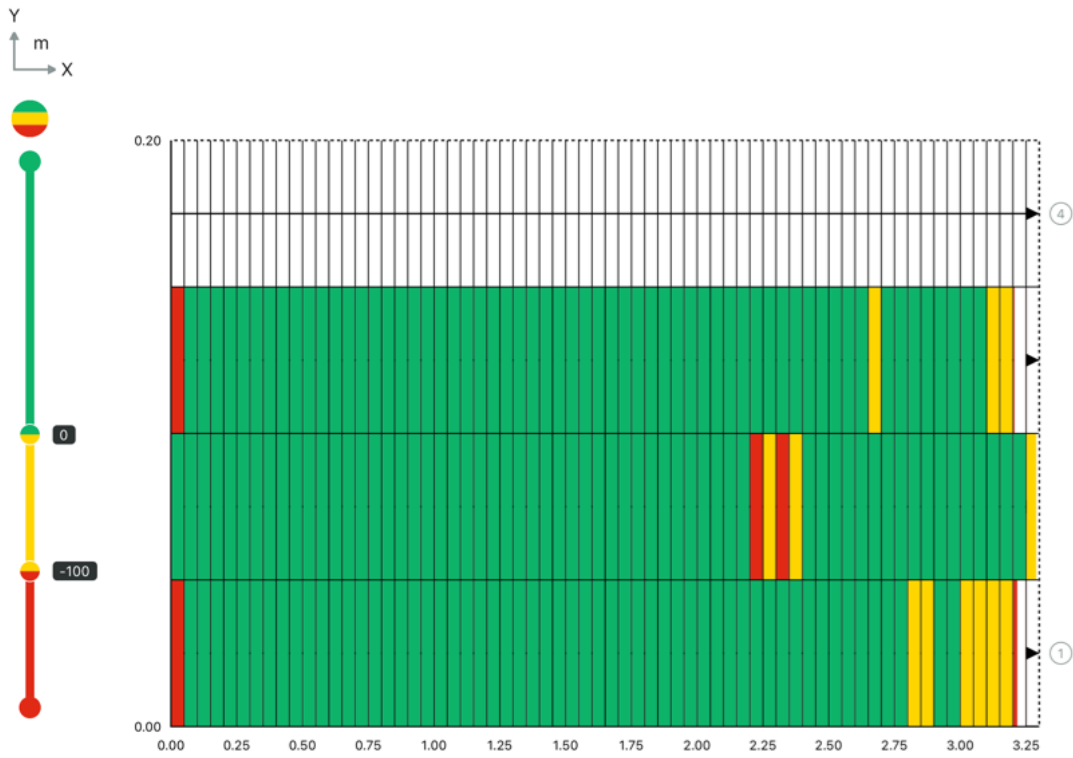
Figure F.27: Beam 13 west face half-cell potential map (1).
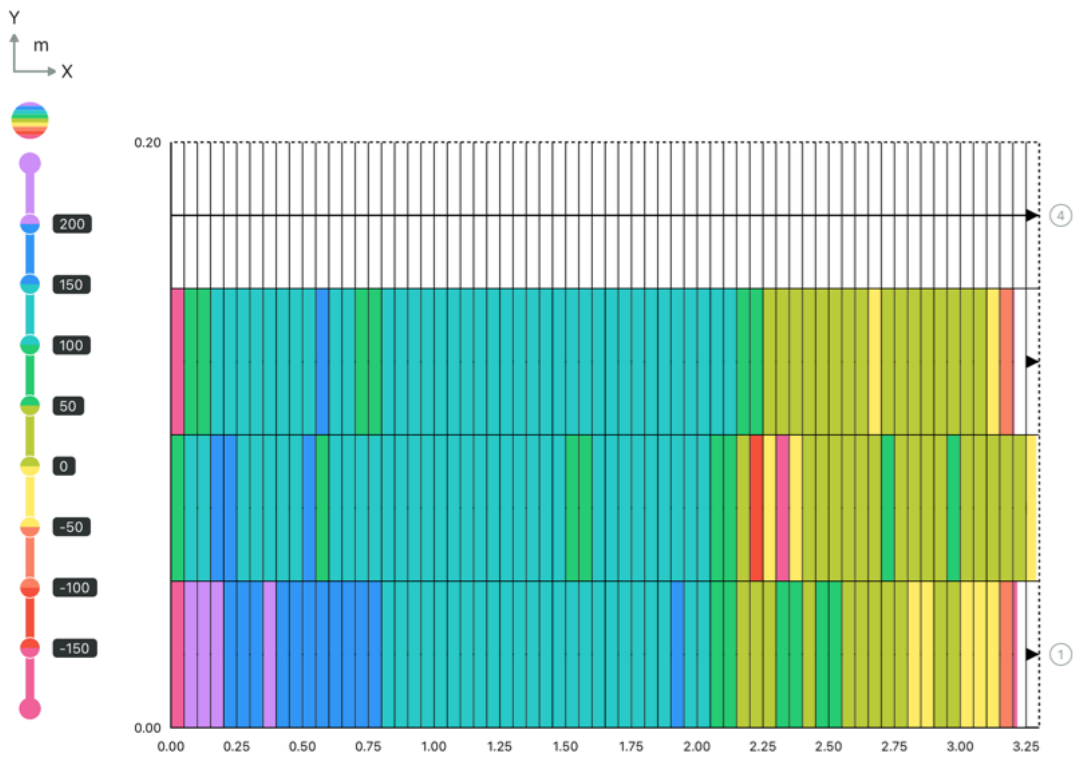
Figure F.28: Beam 13 west face half-cell potential map (2).
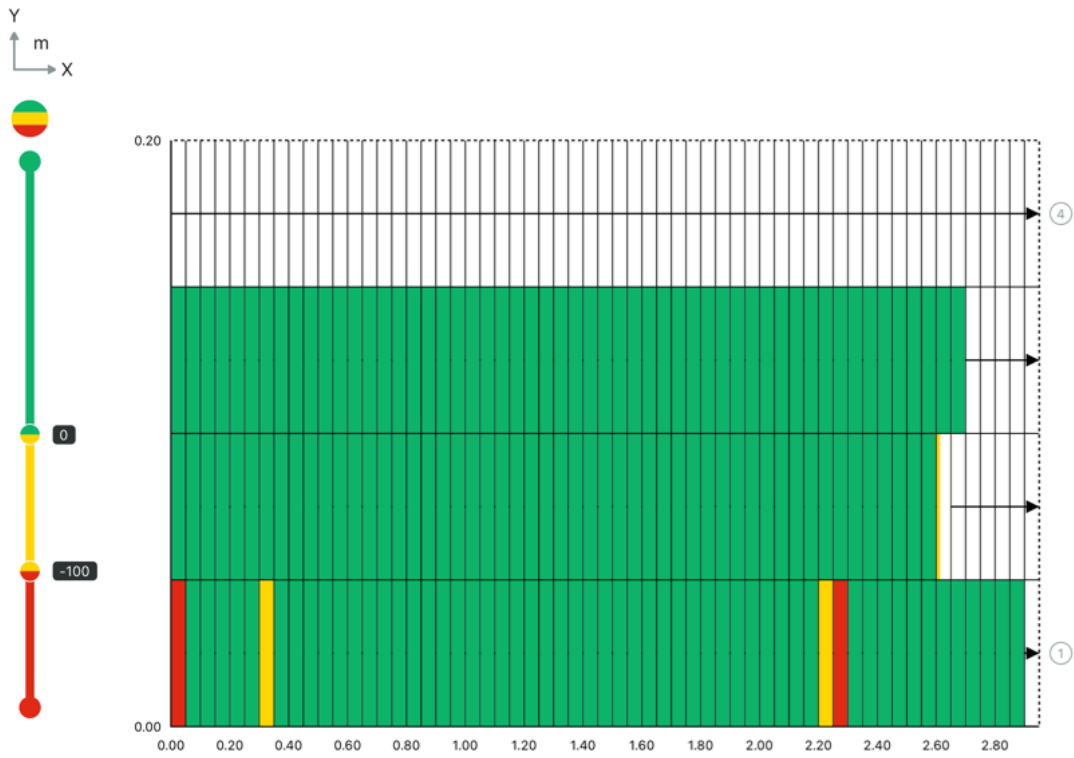
Figure F.29: Beam 13 bottom half-cell potential map (1).
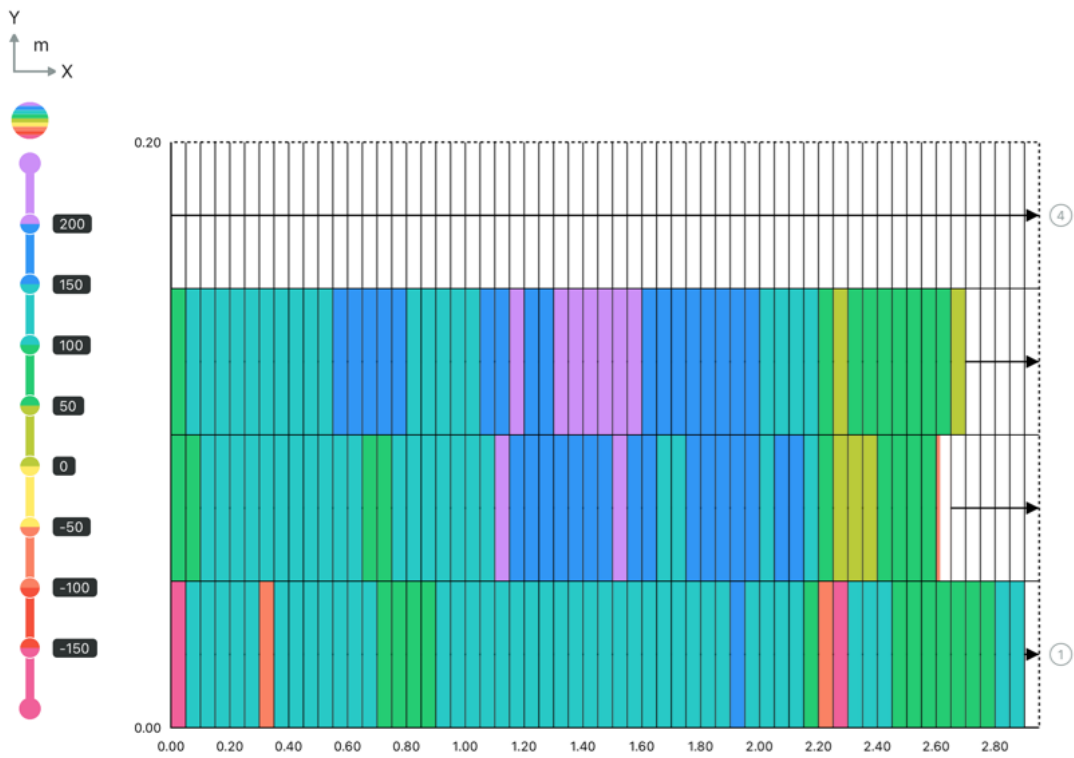
Figure F.30: Beam 13 bottom half-cell potential map (2).
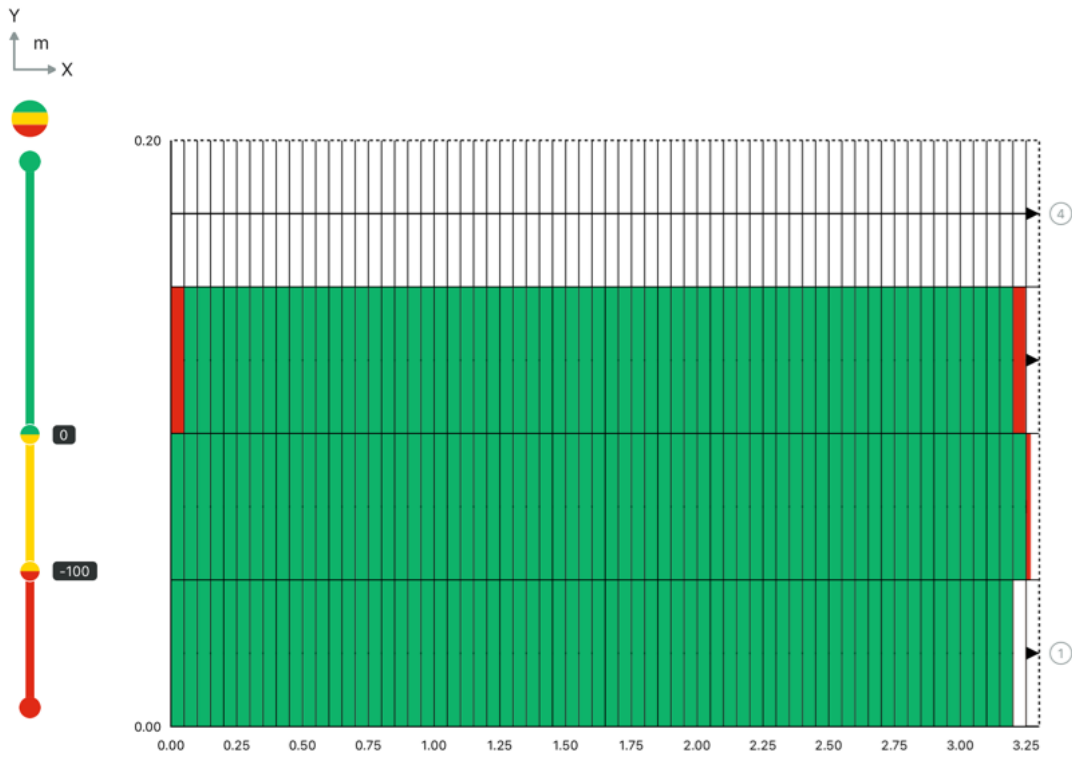
Figure F.31: Beam 18 east face half-cell potential map (1).
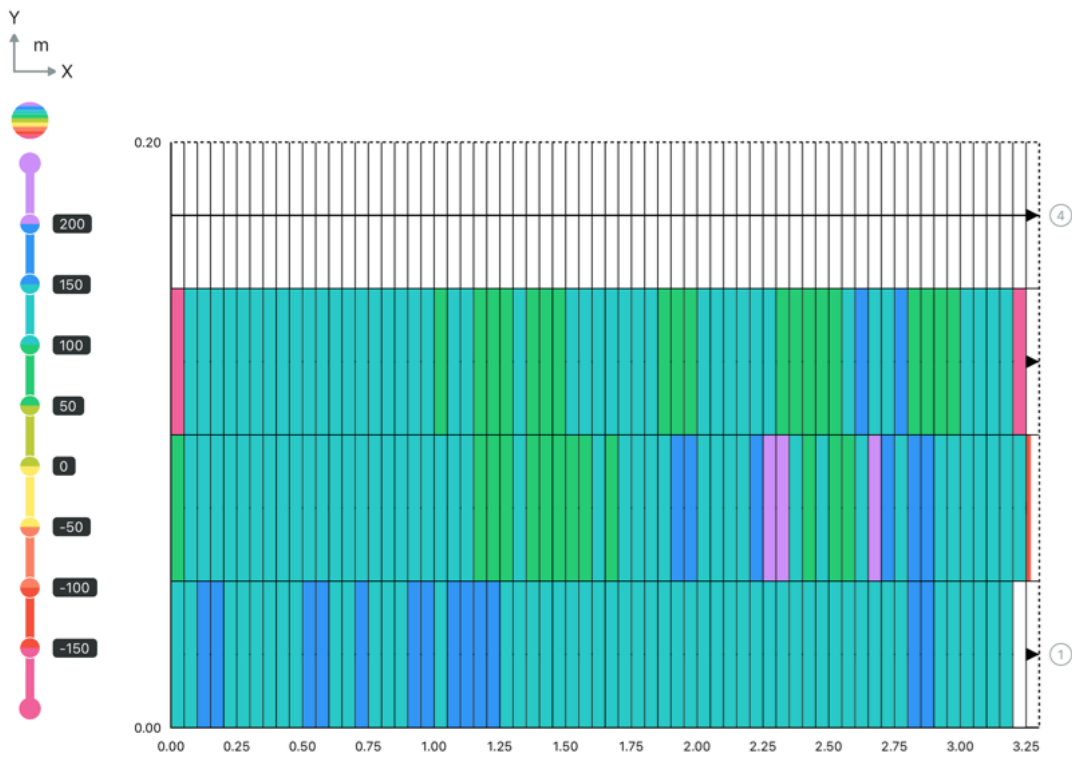
Figure F.32: Beam 18 east face half-cell potential map (2).
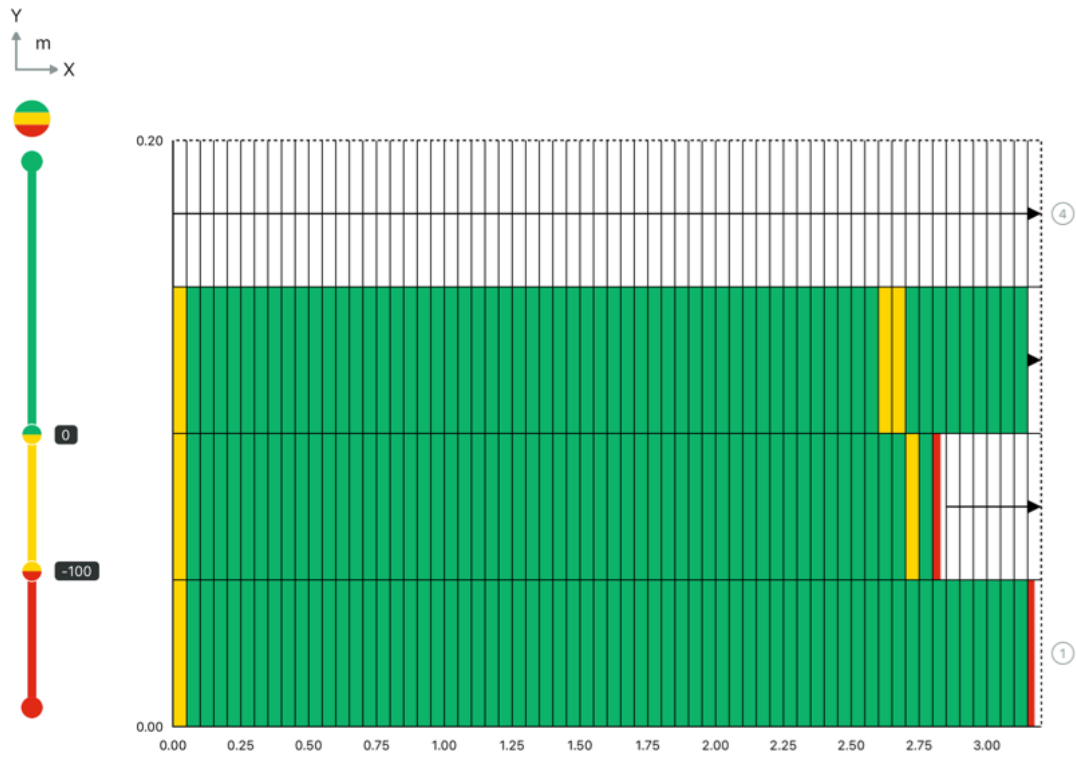
Figure F.33: Beam 18 west face half-cell potential map (1).
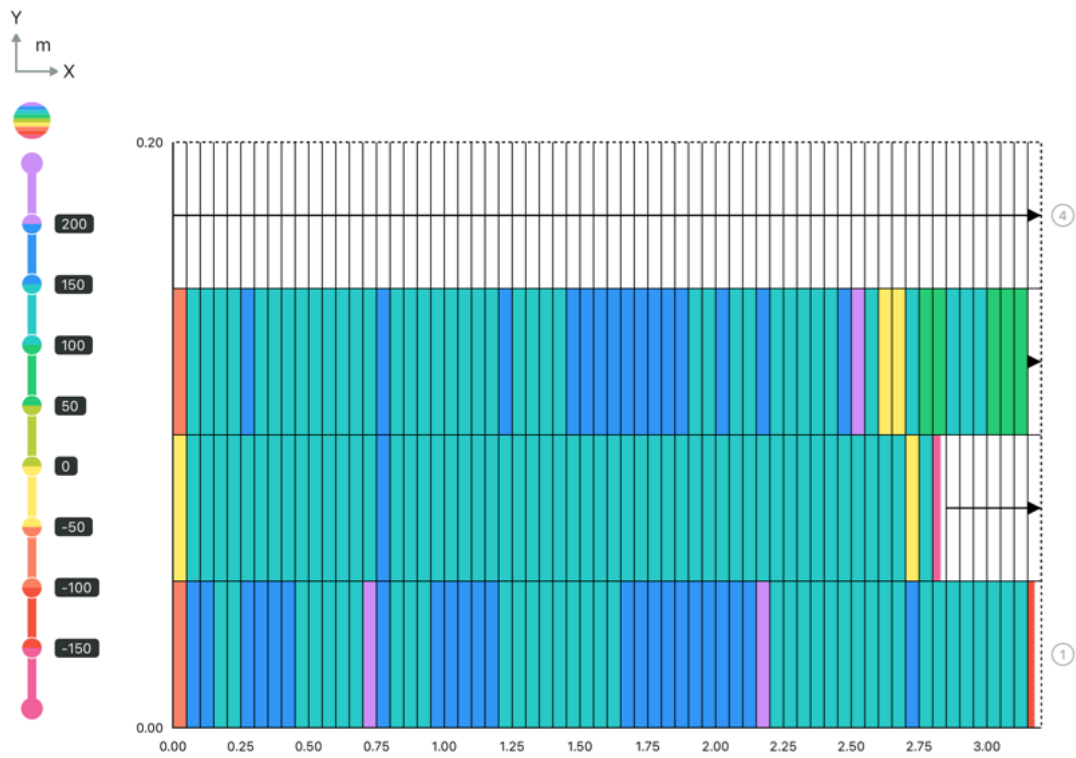
Figure F.34: Beam 18 west face half-cell potential map (2).
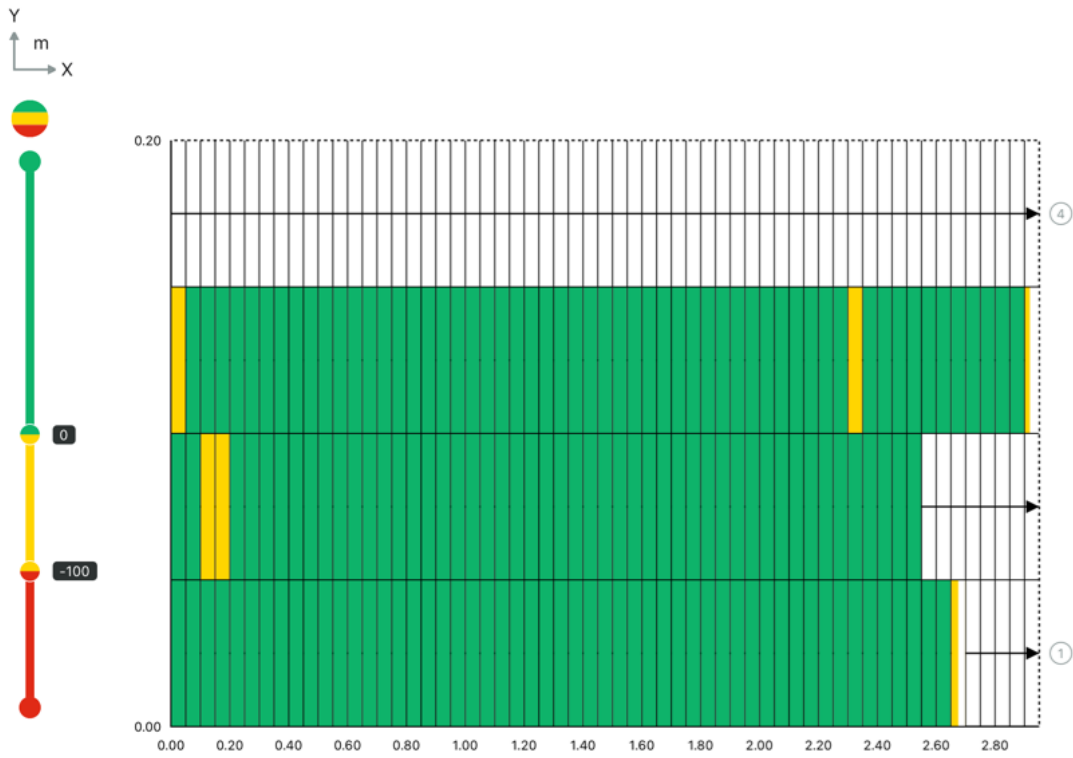
Figure F.35: Beam 18 bottom half-cell potential map (1).
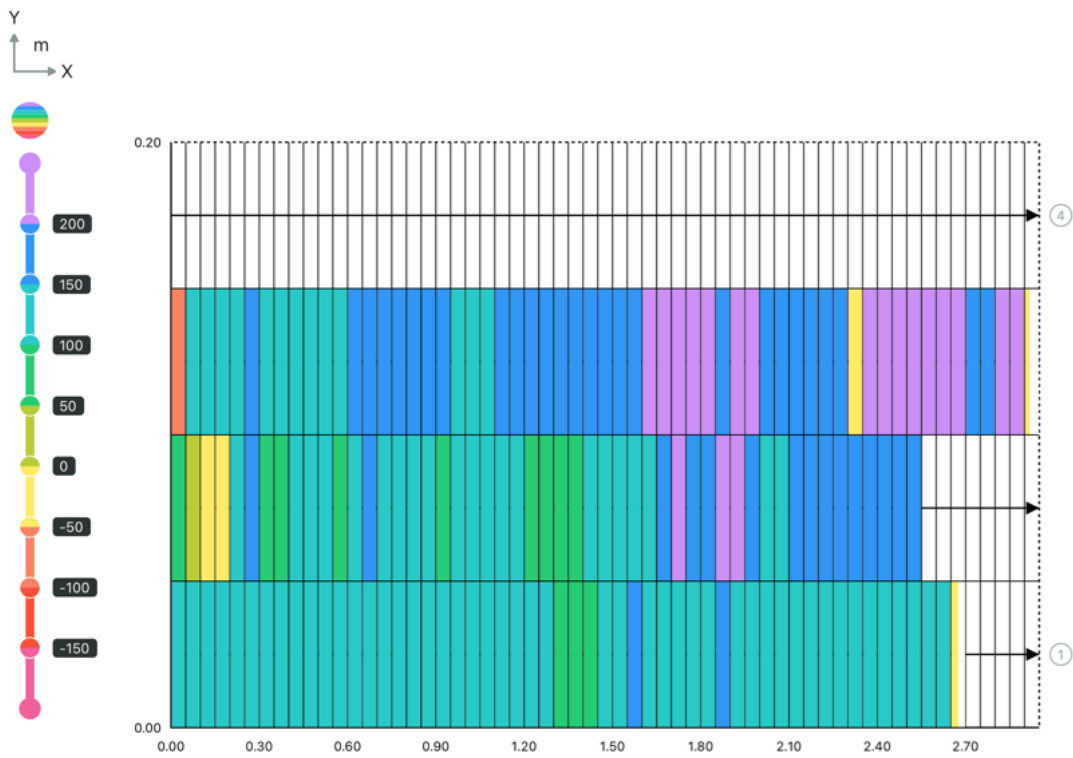
Figure F.36: Beam 18 bottom half-cell potential map (2).

Figure F.37: Beam 23 east face half-cell potential map (1).

Figure F.38: Beam 23 east face half-cell potential map (2).
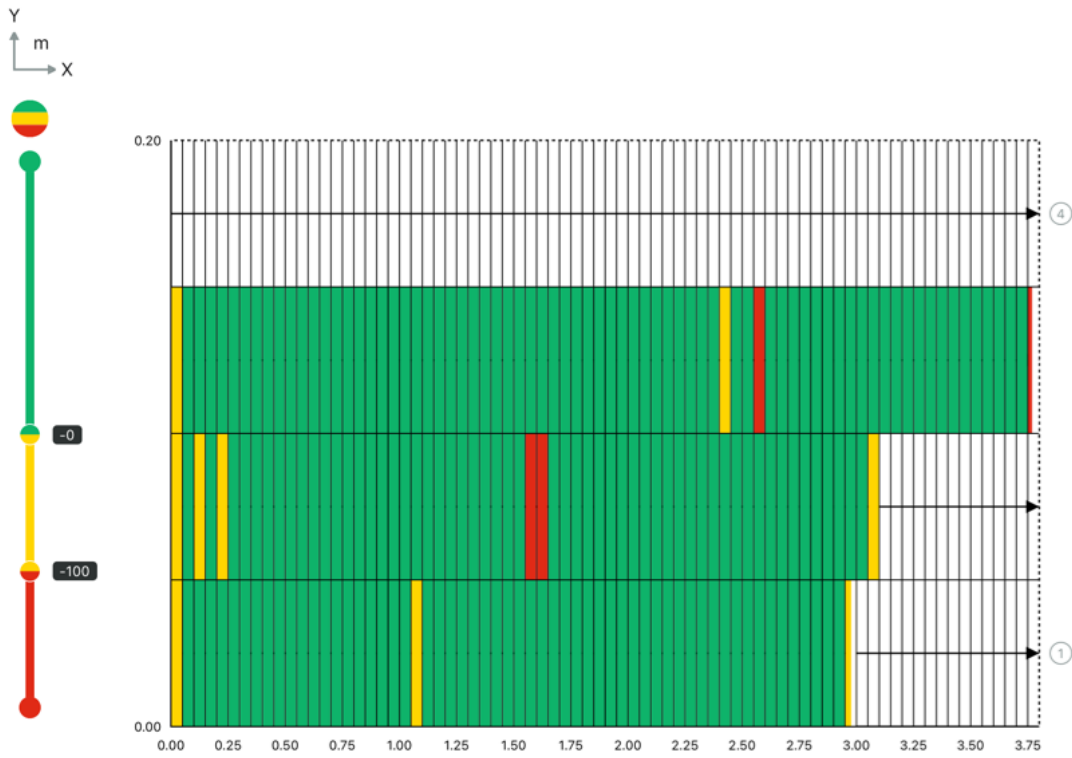
Figure F.39: Beam 23 bottom half-cell potential map (1).
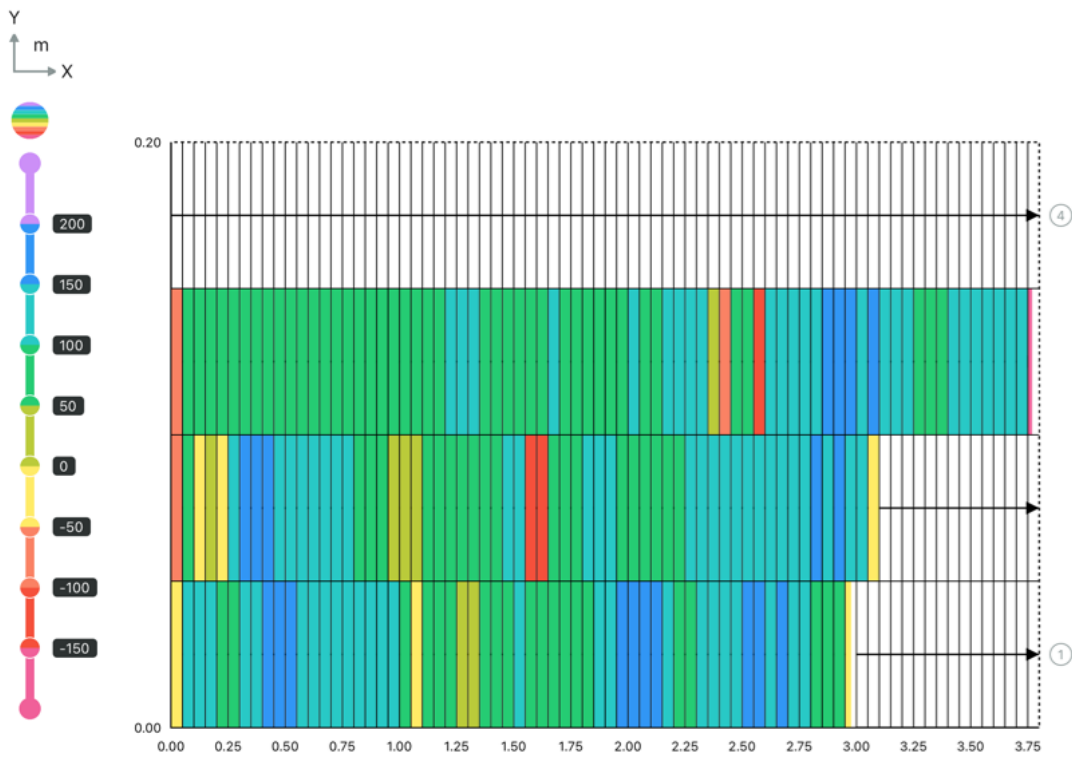
Figure F.40: Beam 23 bottom half-cell potential map (2).

F.4   Rebound hammer and UPV

Support beam
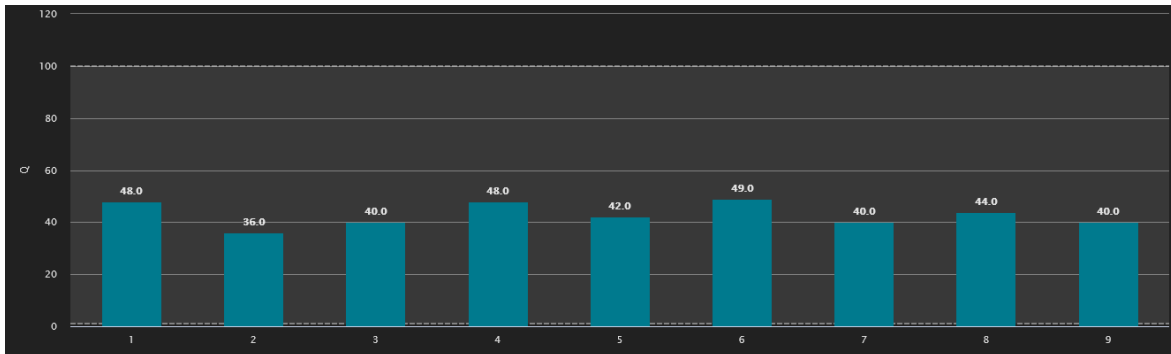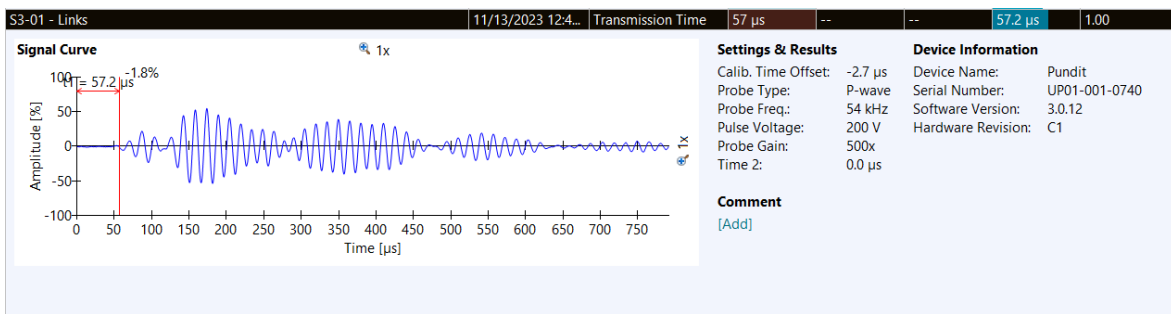

Figure F.41: Support beam S1 Q-values.
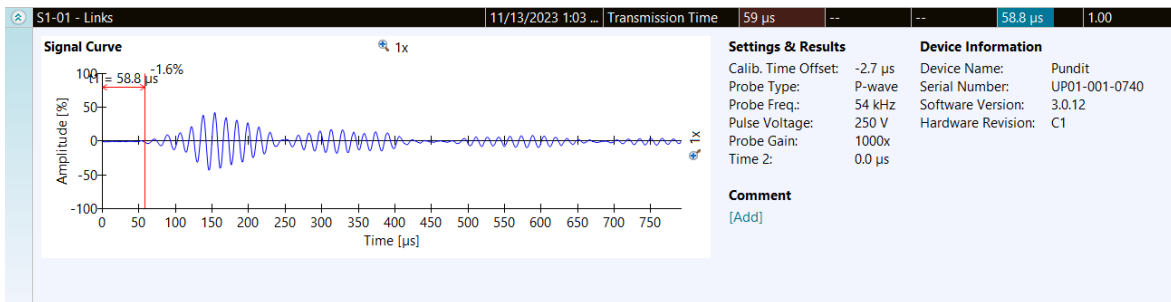
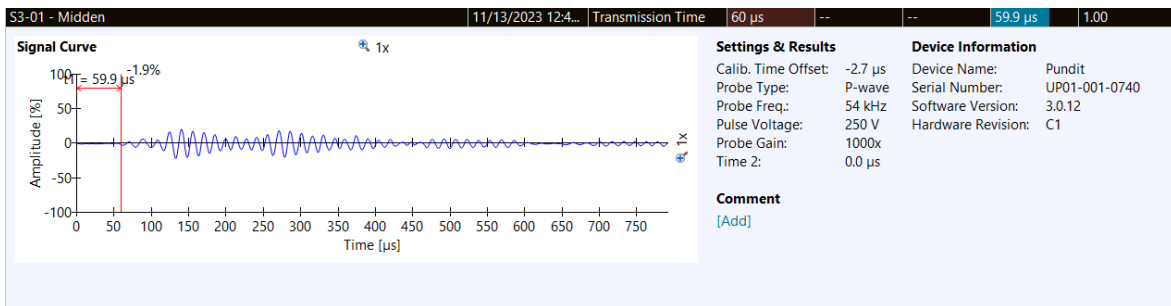Figure F.42: Support beam S1 UPV measurement 1.
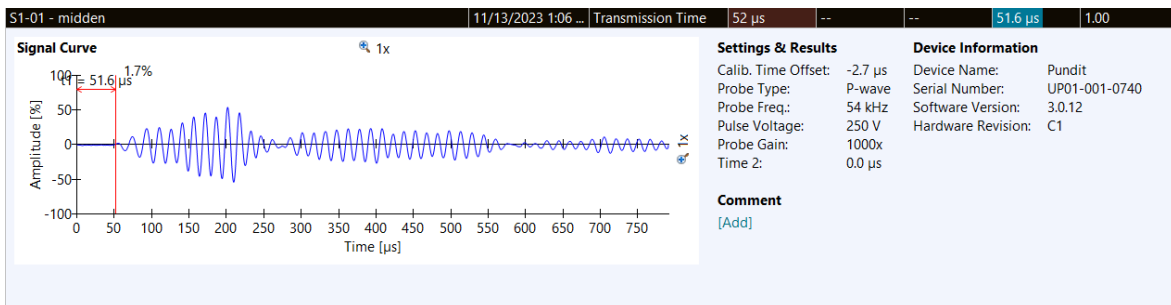
Figure F.43: Support beam S1 UPV measurement 2.
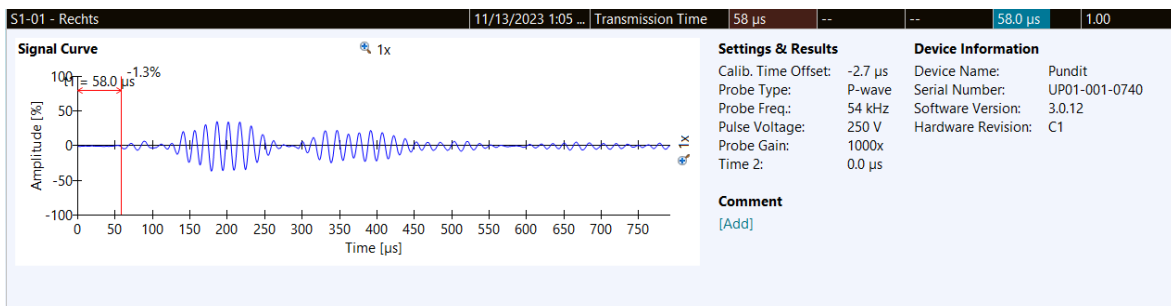
Figure F.44: Support beam S1 UPV measurement 3.
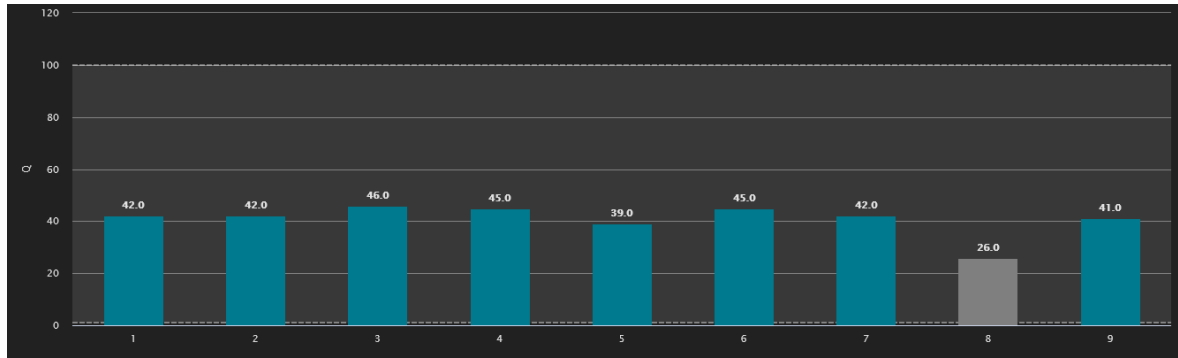
Figure F.45: Support beam S2 Q-values.
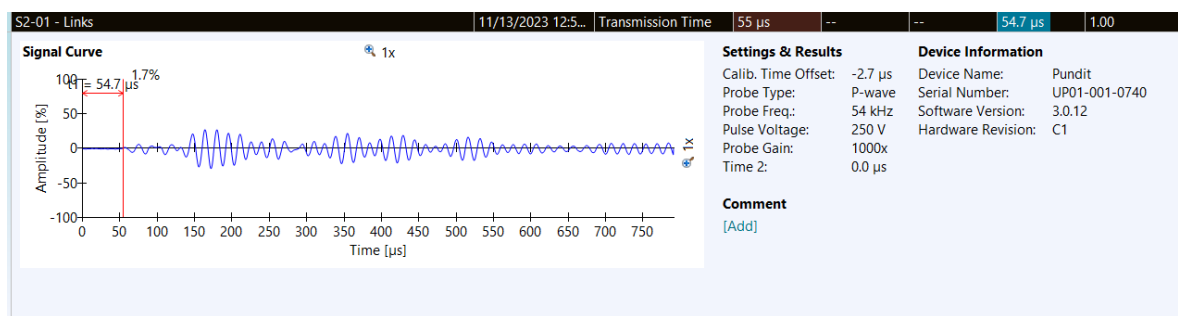
Figure F.46: Support beam S2 UPV measurement 1.
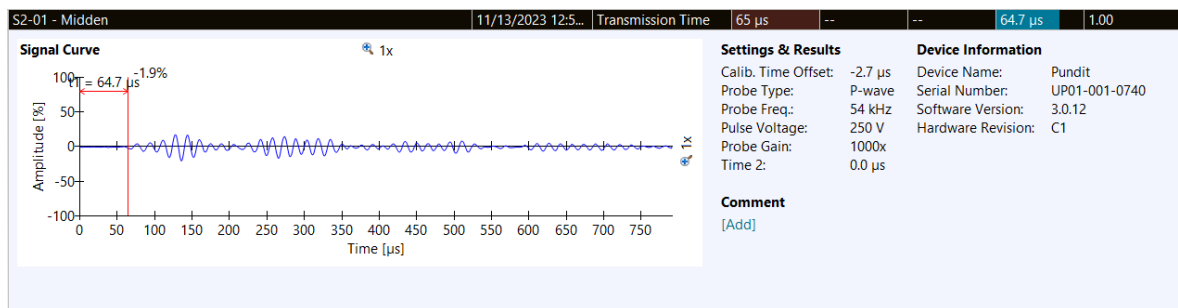
Figure F.47: Support beam S2 UPV measurement 2.
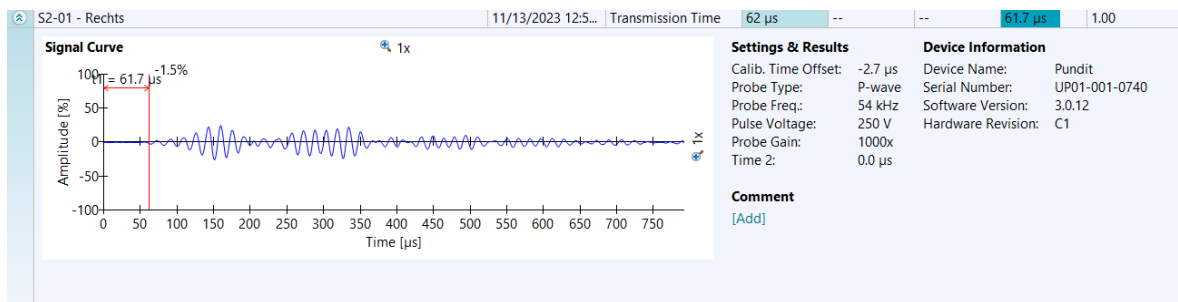
Figure F.48: Support beam S2 UPV measurement 3.
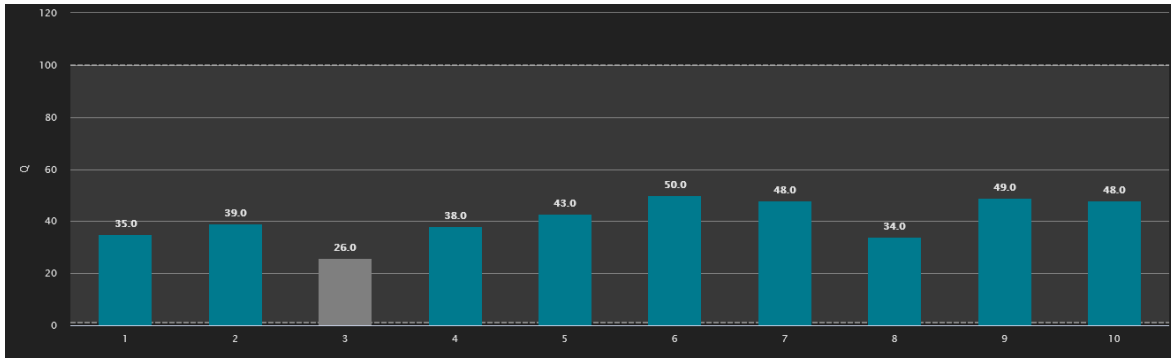
Figure F.49: Support beam S3 Q-values.

Figure F.50: Support beam S3 UPV measurement 1.

Figure F.51: Support beam S3 UPV measurement 2.

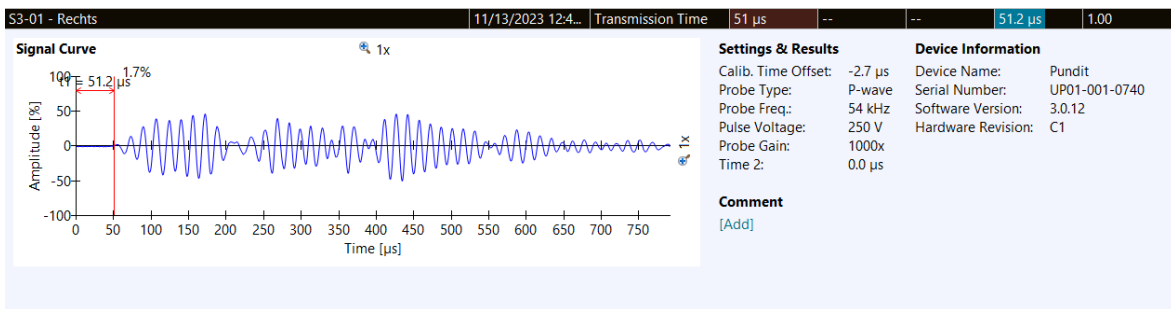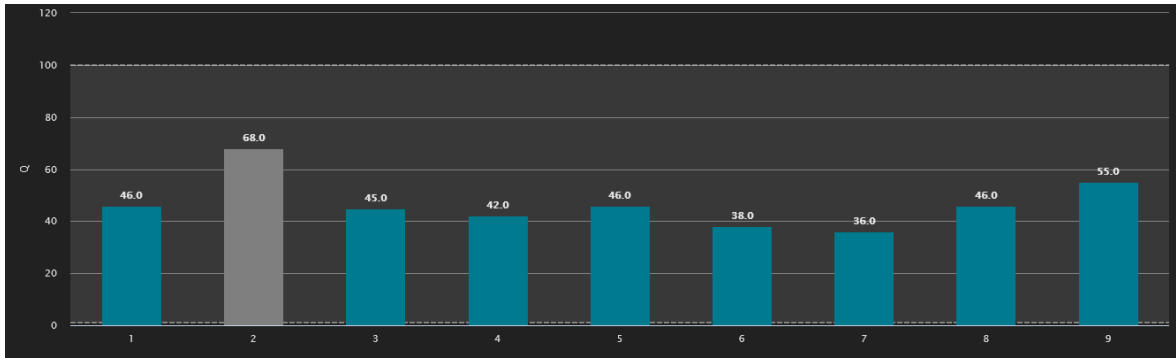Figure F.52: Support beam S3 UPV measurement 3.

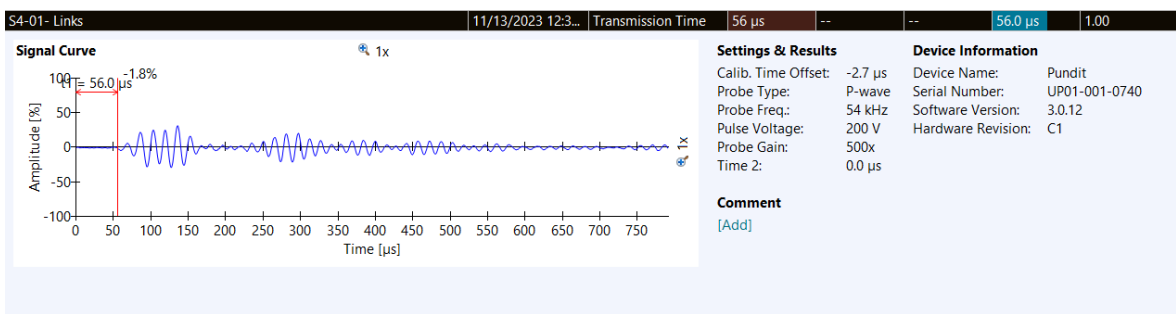Figure F.53: Support beam S4 Q-values.

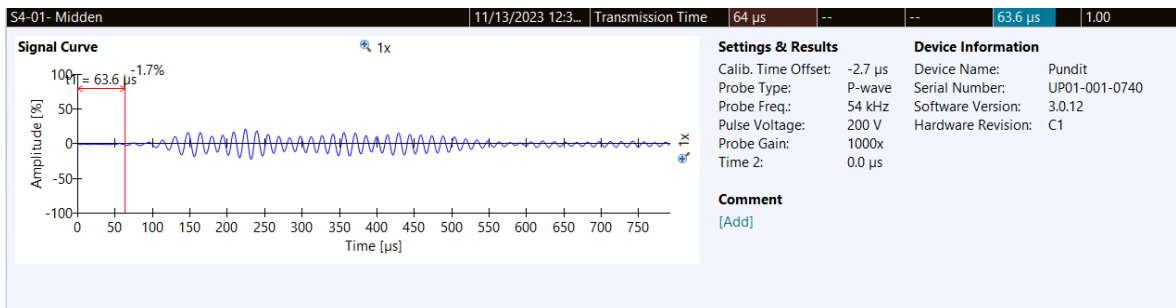Figure F.54: Support beam S4 UPV measurement 1.

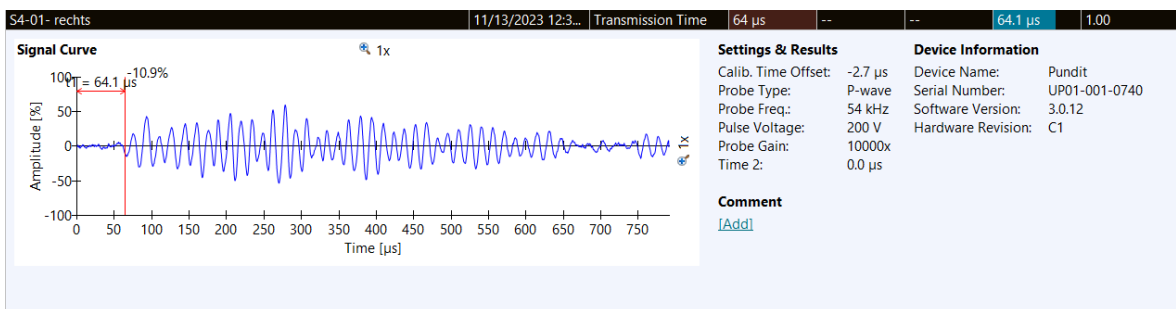Figure F.55: Support beam S4 UPV measurement 2.

Figure F.56: Support beam S4 UPV measurement 3.
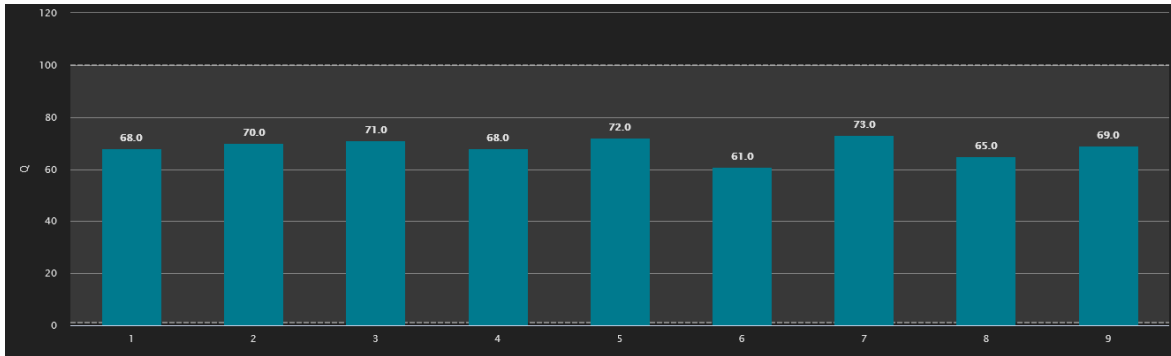
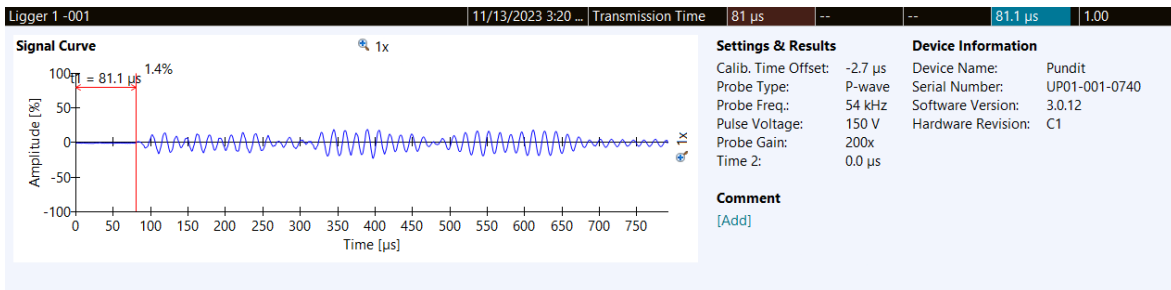**Beam 1**

Figure F.57: Beam 1 Q-values.

Figure F.58: Beam 1 UPV measurement 1.

Figure F.59: Beam 1 UPV measurement 2.

Figure F.60: Beam 1 UPV measurement 3.

Figure F.61: Beam 1 UPV measurement 4.

Figure F.62: Beam 1 UPV measurement 6.

Beam 7

Figure F.63: Beam 7 Q-values.

Figure F.64: Beam 7 UPV measurement 1.

Figure F.65: Beam 7 UPV measurement 2.

Figure F.66: Beam 7 UPV measurement 3.

Figure F.67: Beam 7 UPV measurement 4.
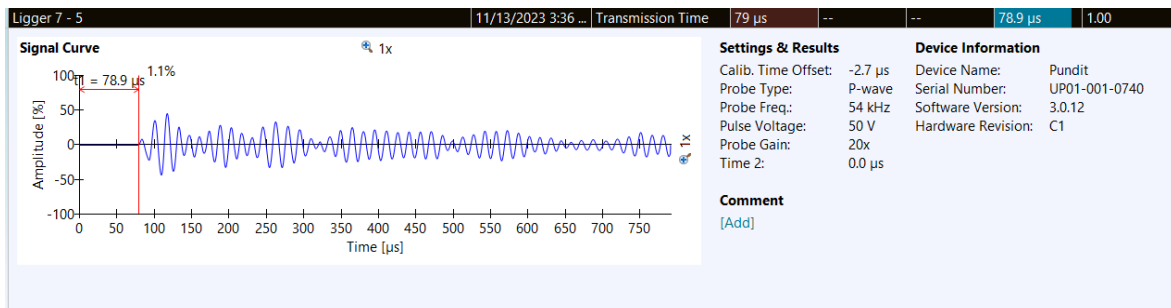
Figure F.68: Beam 7 UPV measurement 5.
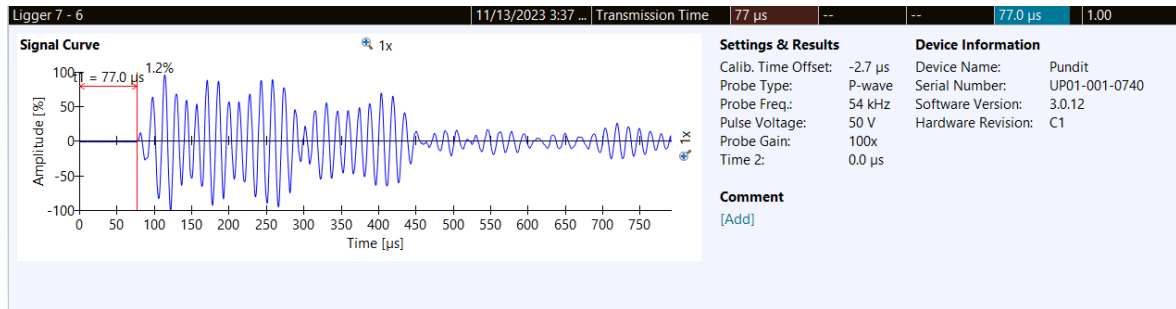
Figure F.69: Beam 7 UPV measurement 6.

Beam 13
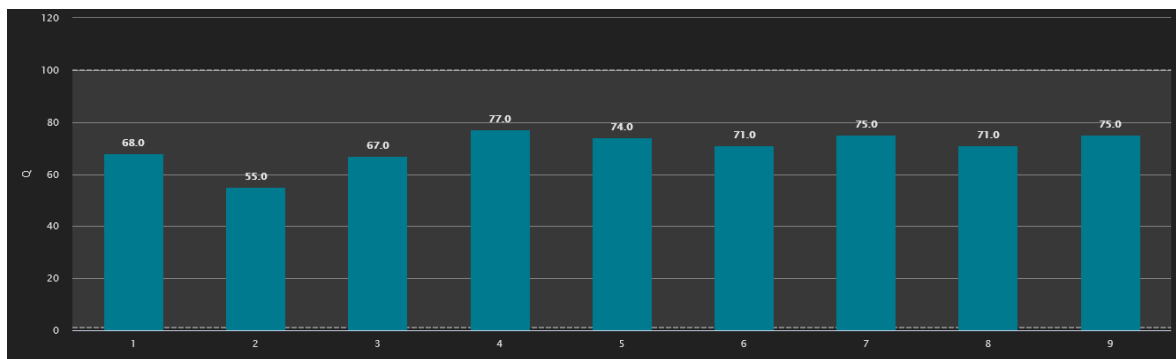
Figure F.70: Beam 13 Q-values.
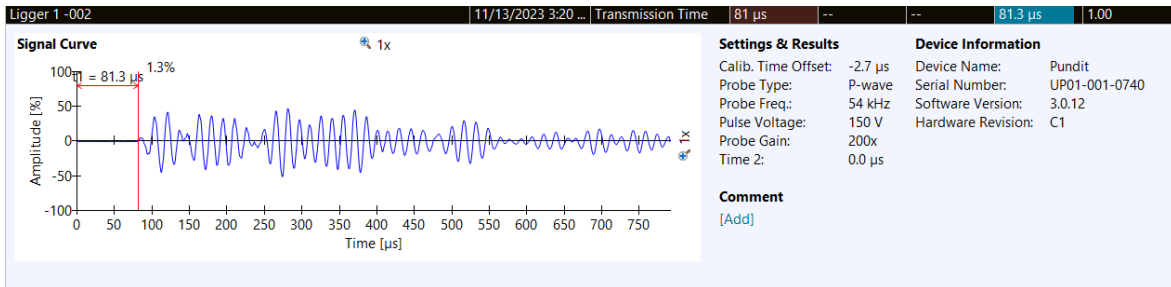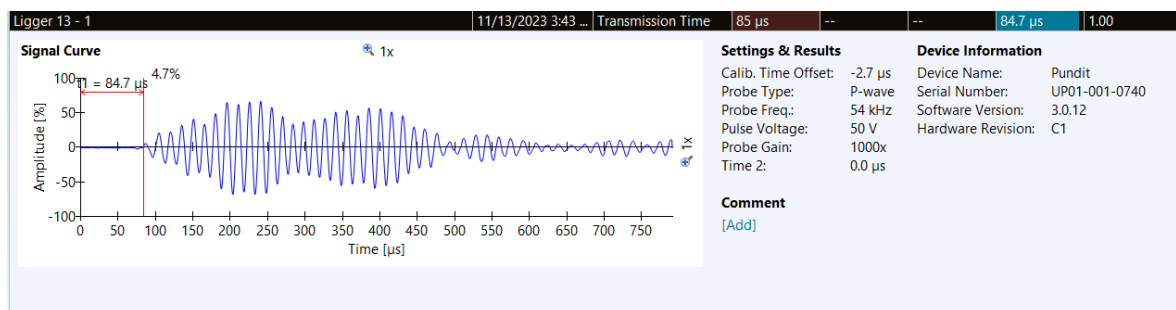

Figure F.71: Beam 13 UPV measurement 1.
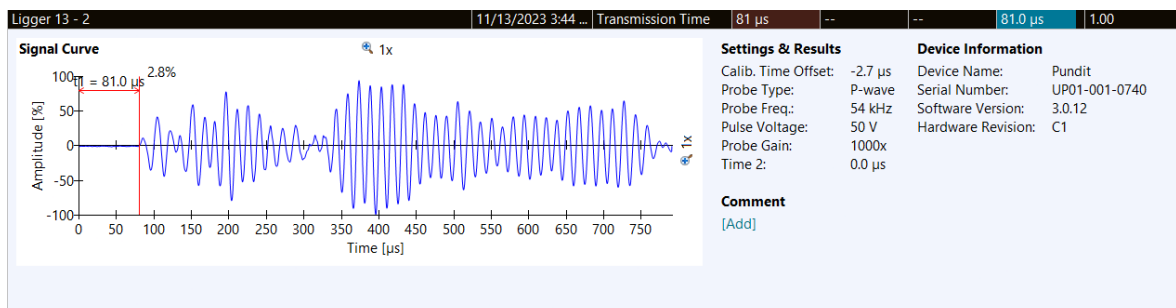
Figure F.72: Beam 13 UPV measurement 2.
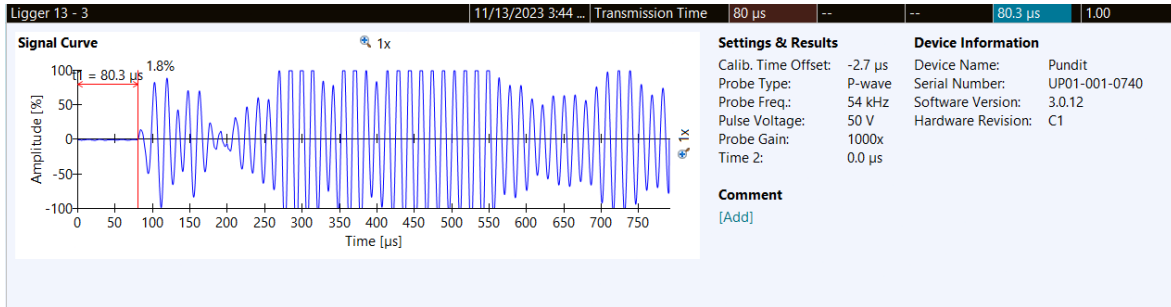
Figure F.73: Beam 13 UPV measurement 3.
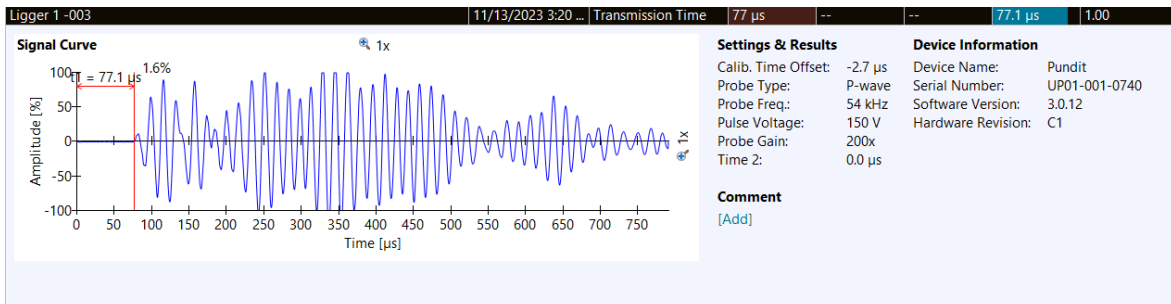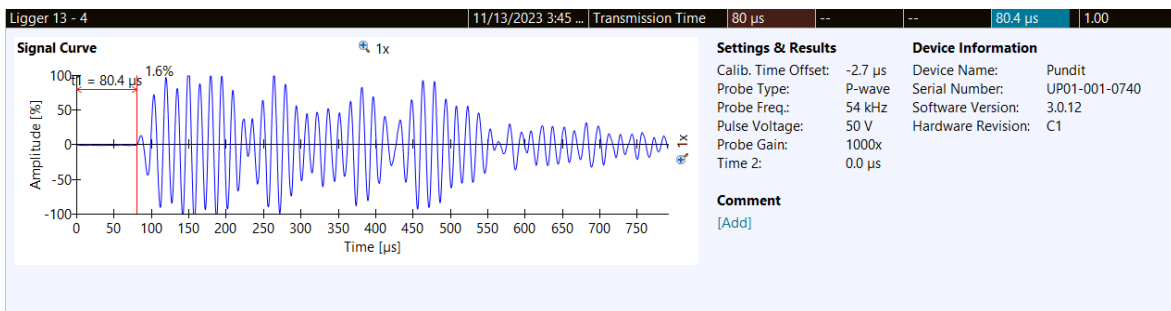

Figure F.74: Beam 13 UPV measurement 4.
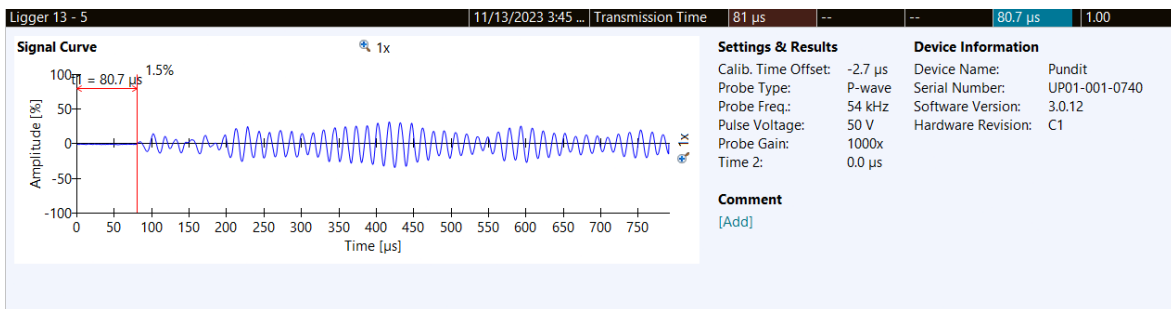
Figure F.75: Beam 13 UPV measurement 5.
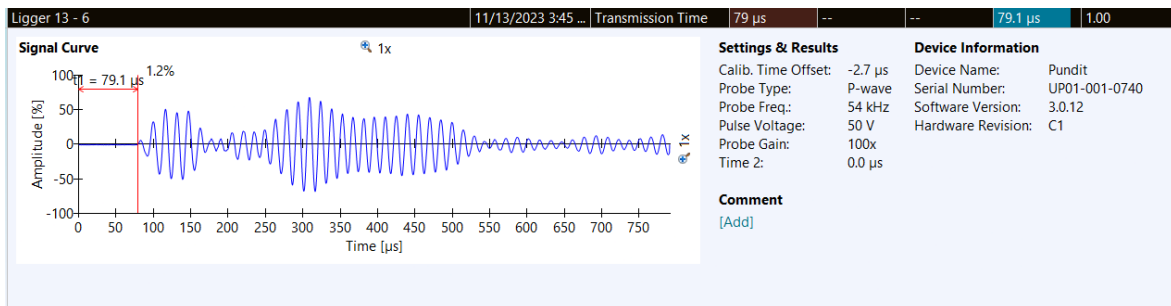
Figure F.76: Beam 13 UPV measurement 6.

Beam 18
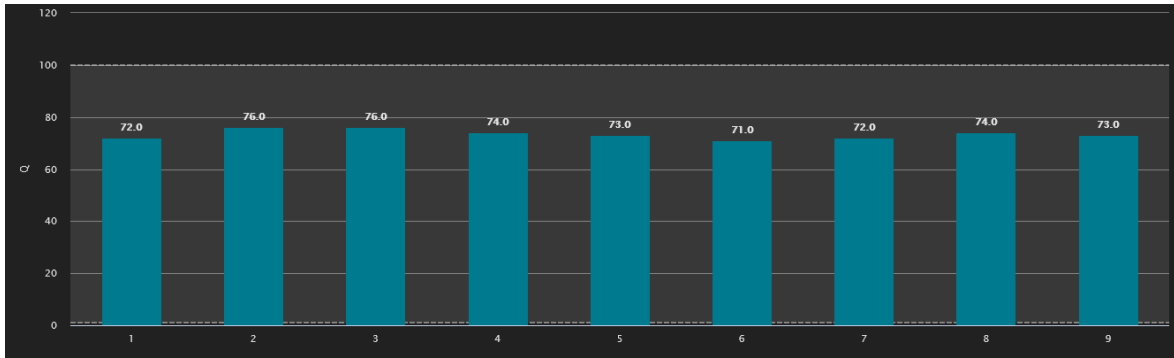
Figure F.77: Beam 18 Q-values.
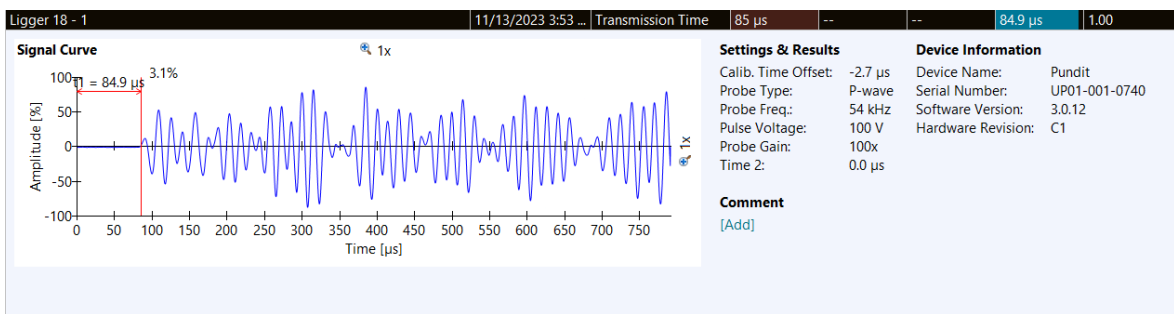
Figure F.78: Beam 18 UPV measurement 1.
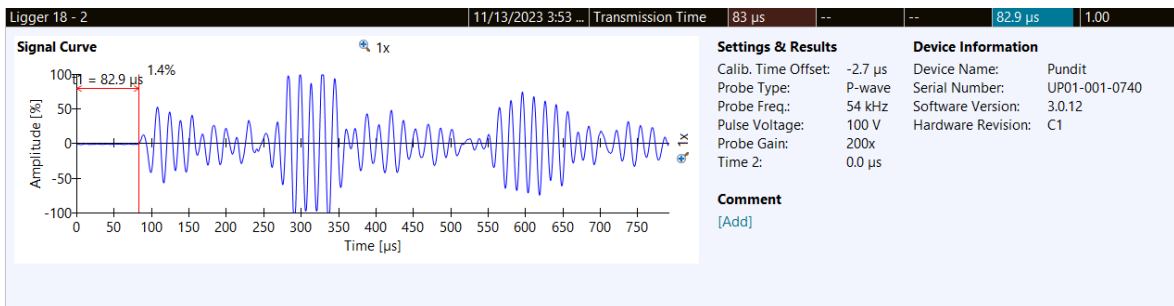
Figure F.79: Beam 18 UPV measurement 2.
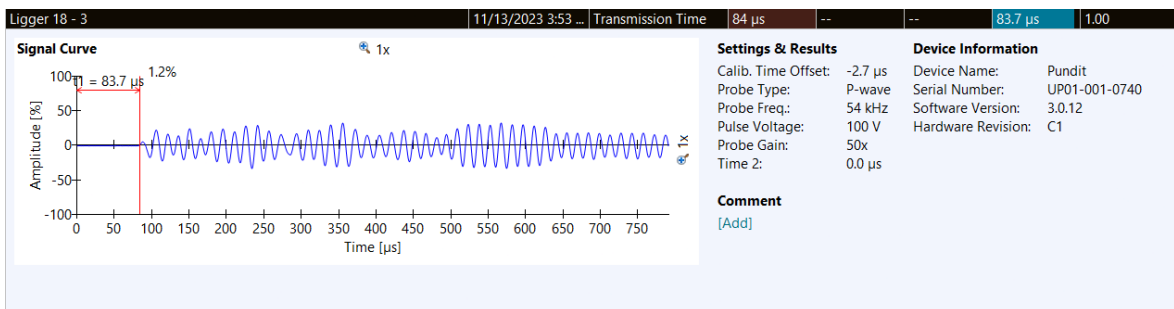
Figure F.80: Beam 18 UPV measurement 3.
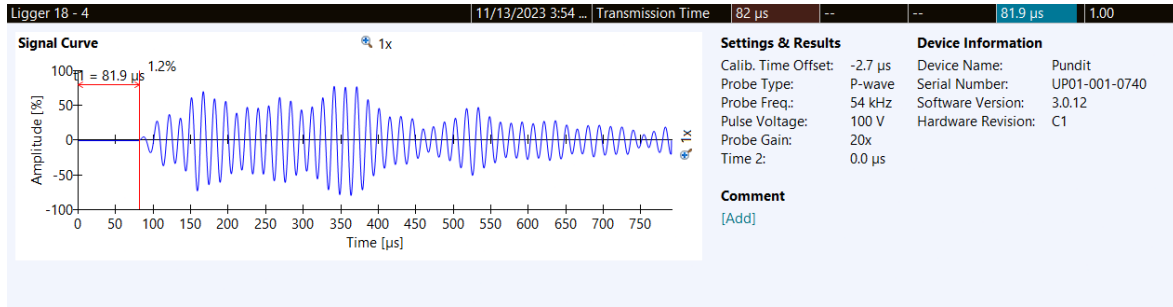
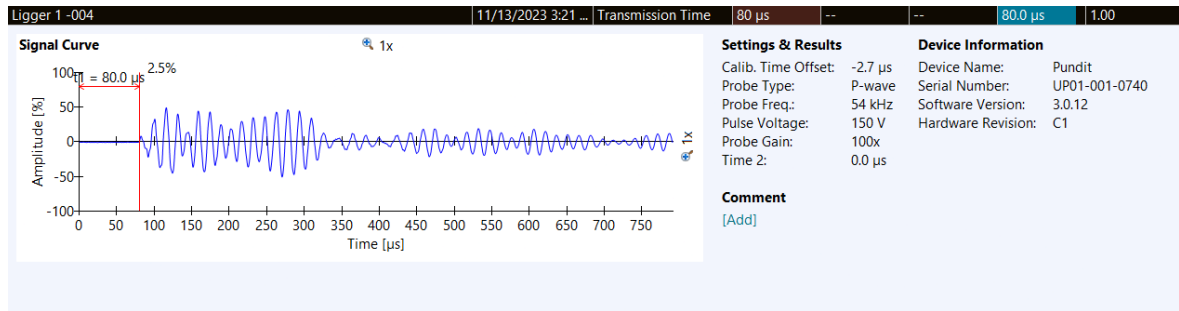Figure F.81: Beam 18 UPV measurement 4.
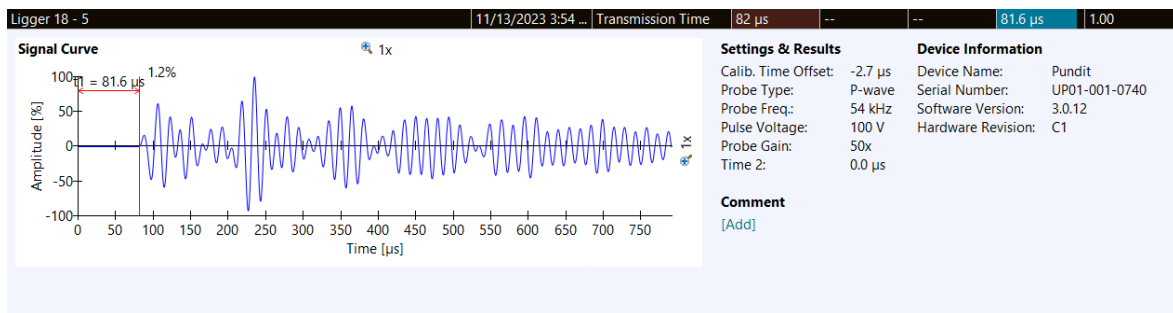
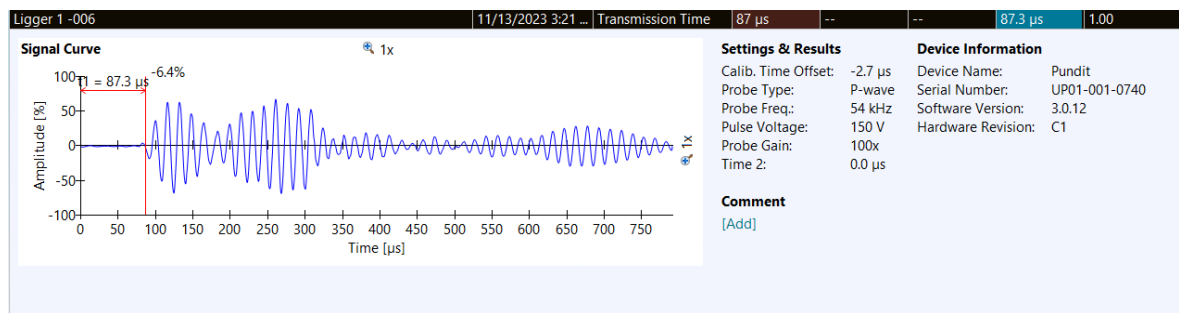Figure F.82: Beam 18 UPV measurement 5.
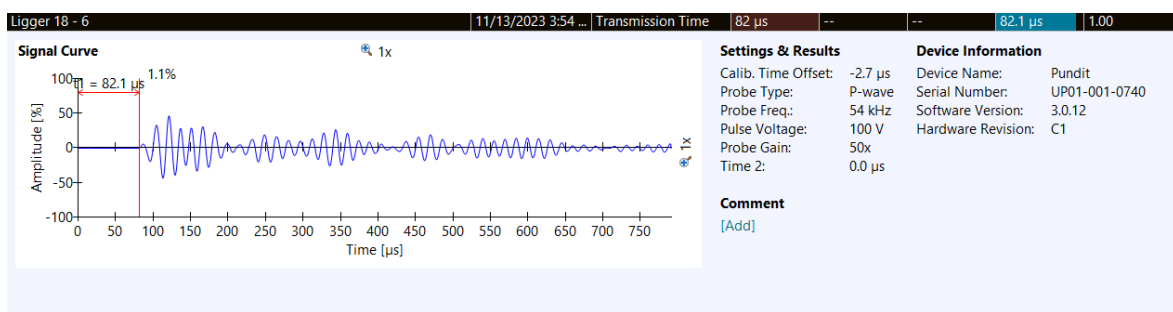
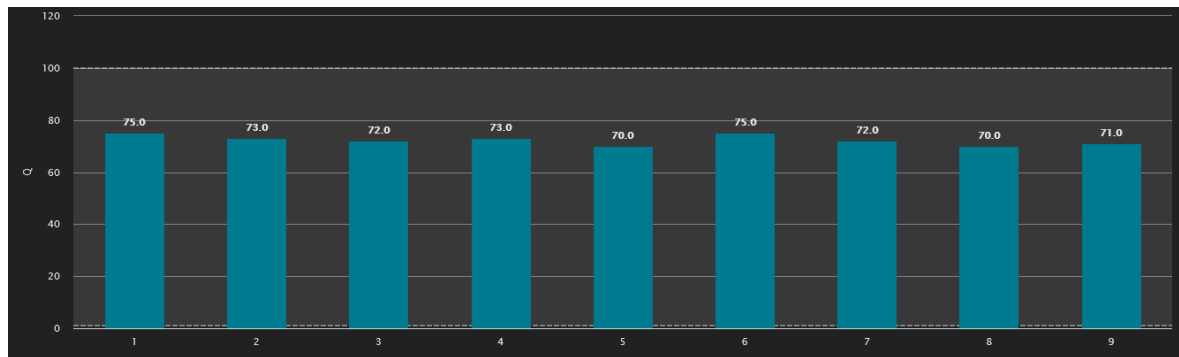Figure F.83: Beam 18 UPV measurement 6.

Beam 23
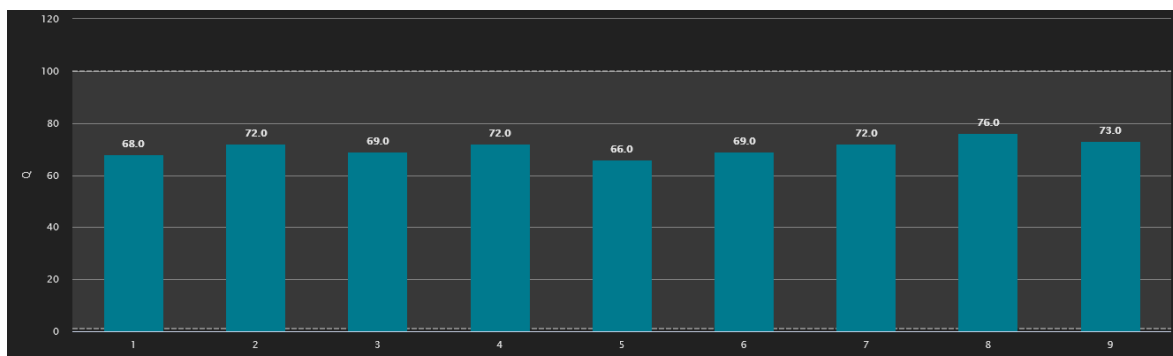
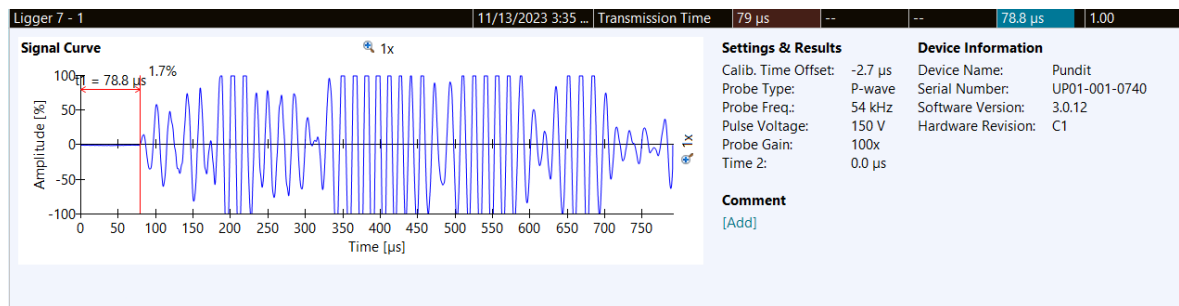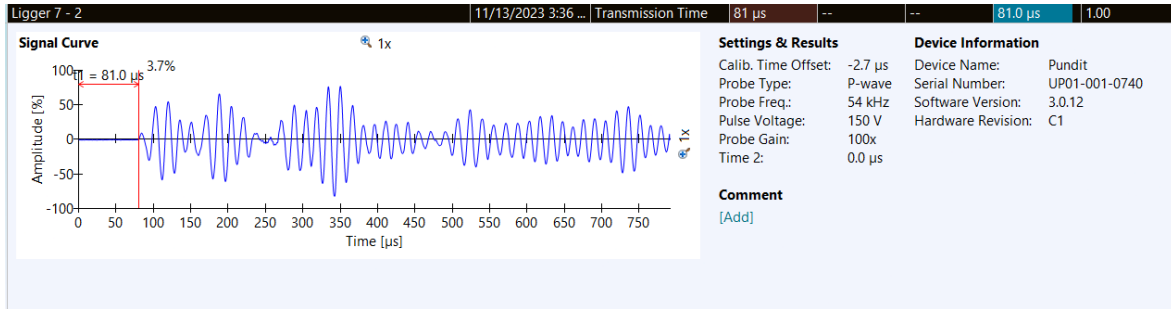Figure F.84: Beam 23 Q-values.
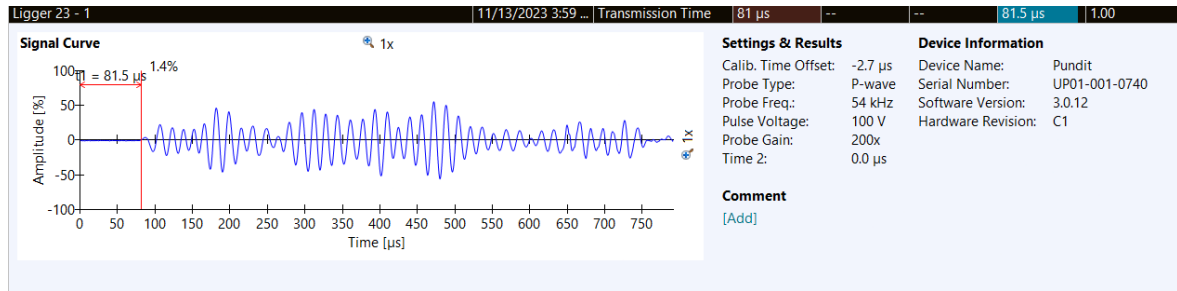
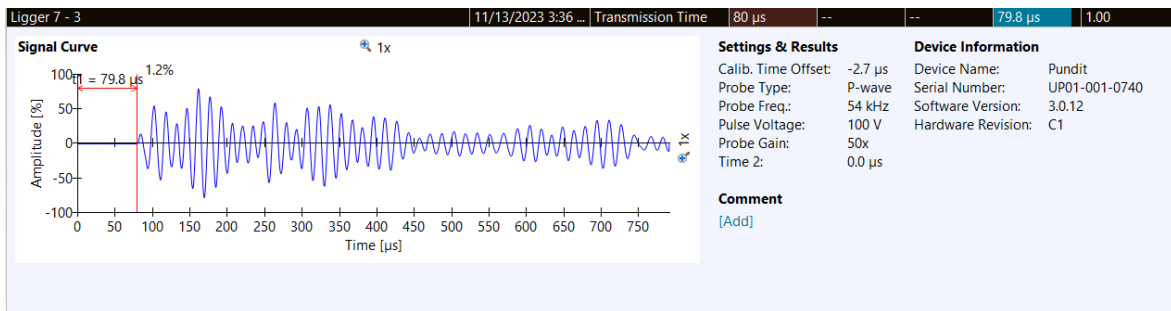Figure F.85: Beam 23 UPV measurement 1.
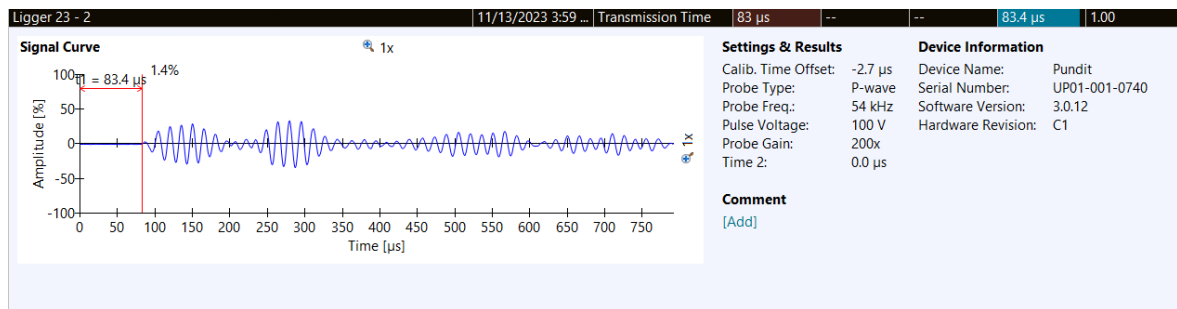
Figure F.86: Beam 23 UPV measurement 2.
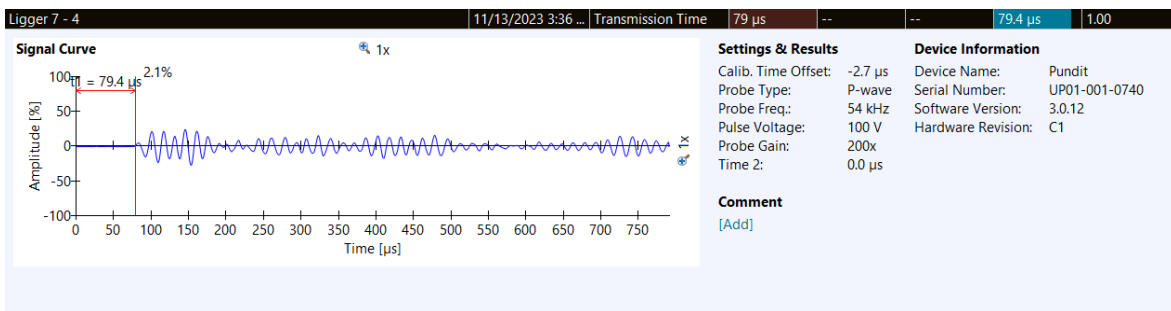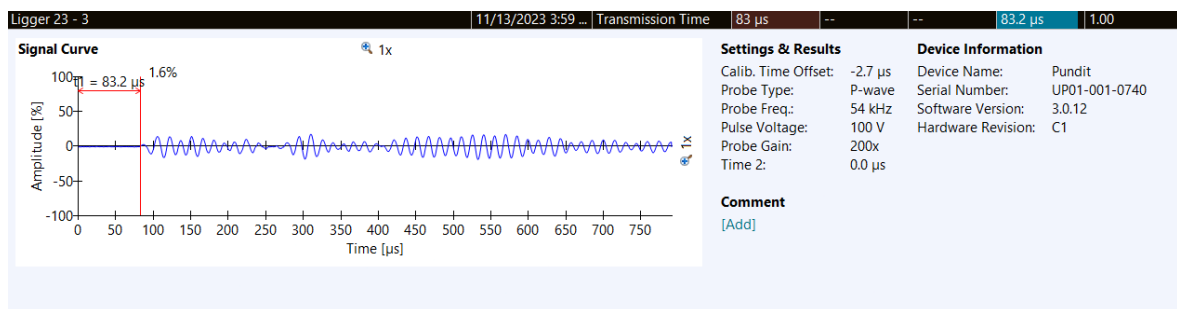

Figure F.87: Beam 23 UPV measurement 3.
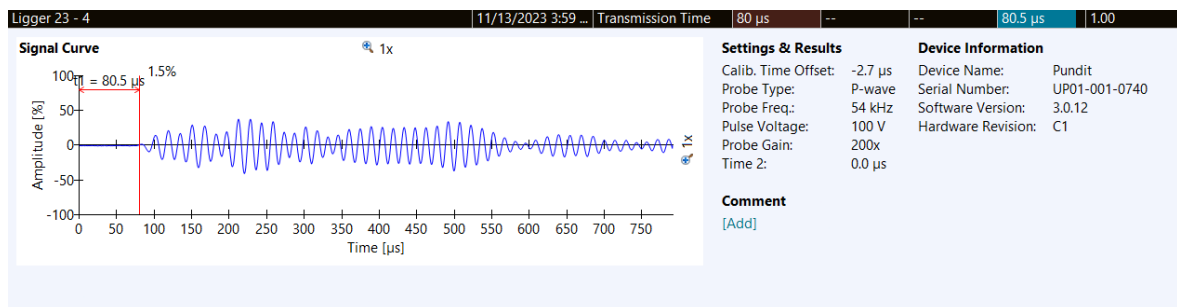
Figure F.88: Beam 23 UPV measurement 4.
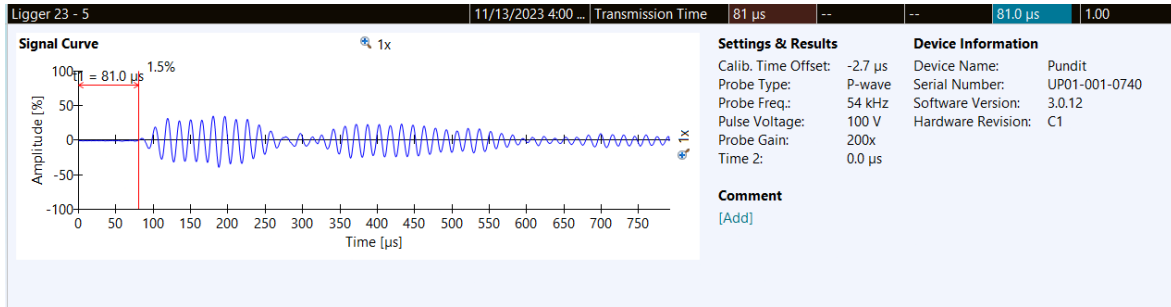
Figure F.89: Beam 23 UPV measurement 5.
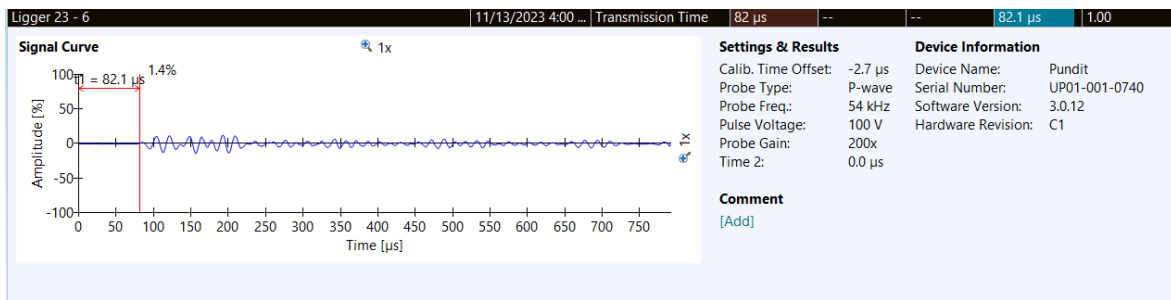
Figure F.90: Beam 23 UPV measurement 6.

Appendix G

Resistivity laboratory measurements

Resistivity measurements were conducted within a controlled laboratory environment on a reinforced concrete OPC slab measuring 60x60 centimeters, which was cast in 2018 (Figure G.1). The slab contains two rebars with a diameter of 12 mm and a cover depth of 25 mm. Notably, the top portion of the slab was subjected to a 5% NaCl solution, resulting in corrosion of the top rebar, while the bottom half was solely exposed to water. Using the Gecor-10 half-cell potential probe to measure the potential yielded the values listed in Table G.1. This underscores the fact that the top rebar is indeed corroding.

Figure G.1: Reinforced concrete OPC slab pre-wetting.

Table G.1: Potentials measured on the reinforced concrete OPC slab.

Measurement	Non-corroded OCP (mV)	Corroded OCP (mV)
1	-192.7	-426.8
2	-190.9	-417.2
3	-190.6	-415.1
Mean	**-191.4**	**-419.7**

The testing procedure involved wetting the slab with 2 liters of water and allowing it to soak for 15 minutes. Subsequently, measurements were taken using both the Gecor-10 and Resipod Wenner probes, perpendicular to the rebar, moving from left to right. Measurements with both devices were carried out at the same location immediately following each other. The distribution across the length of the slab is presented in Table G.2, the statistical data is summarised in Figure G.3 and Table G.2.
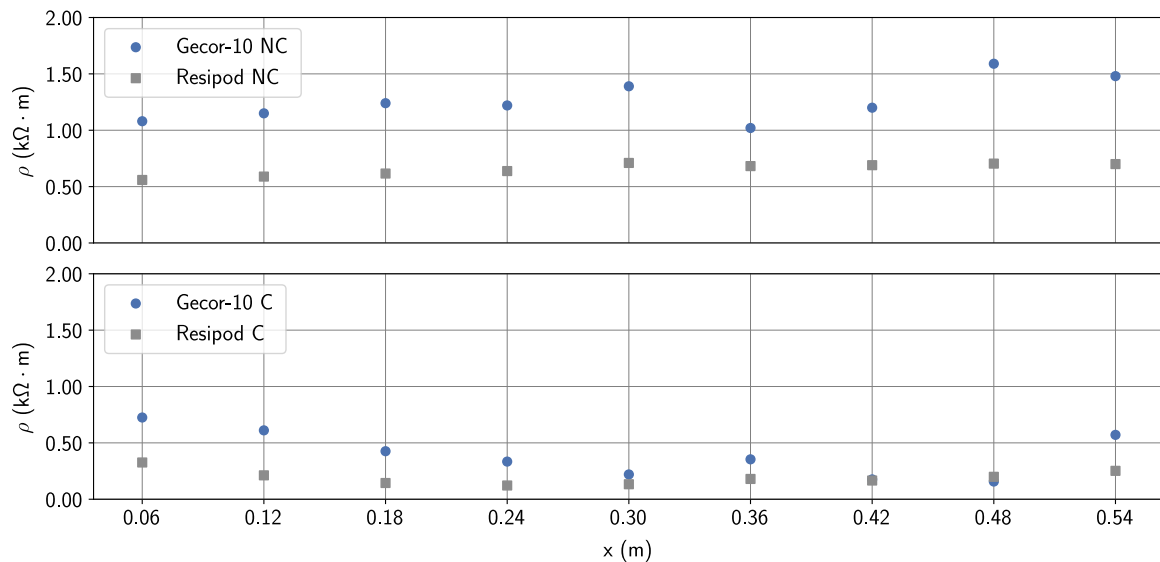
Figure G.2: Distribution of resistivity measurements across the length of the slab for the non-corroded and corroded rebar.
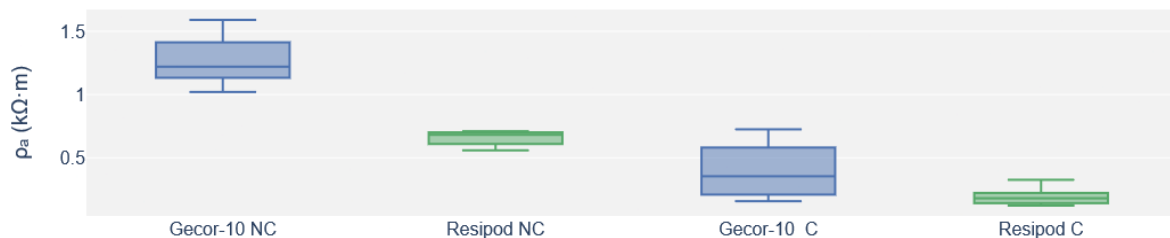
Figure G.3: Boxplots for the laboratory resistivity measurements for the non-corroded and corroded rebar.

Table G.2: Statistical data of laboratory resistivity measurements in k$\Omega \cdot$ m
for the non-corroded and corroded rebar.

Device	N	Quartile 1	Quartile 3	IQR	Median	Mean	Std
Gecor-10 NC	9	1.13	1.41	0.28	1.22	1.26	0.19
Resipod NC	9	0.61	0.70	0.09	0.68	0.65	0.056
Gecor-10 C	9	0.21	0.58	0.37	0.35	0.40	0.20
Resipod C	9	0.14	0.22	0.08	0.18	0.19	0.065

Appendix H

Practical methodology

This methodology distinguishes four distinct phases: preparation, execution, reporting, and monitoring, as illustrated in Figure H.1. During the preparation phase, the objectives are clearly defined, an inspection plan is formulated, and risk assessment and safety protocols are established. The execution phase involves carrying out the inspection itself. In the reporting phase, data analysis is conducted, and the findings are documented in a report. The monitoring phase entails determining any necessary follow-up actions based on the inspection results. Decisions made in this phase can impact the course of future inspections, making it closely interconnected with the preparation phase.

```
┌─────────────────────────┐
│  Phase I: Preparation   │◄──┐
└─────────────────────────┘   │
            │                 │
            ▼                 │
┌─────────────────────────┐   │
│  Phase II: Execution     │  │
└─────────────────────────┘   │
            │                 │
            ▼                 │
┌─────────────────────────┐   │
│  Phase III: Reporting    │  │
└─────────────────────────┘   │
            │                 │
            ▼                 │
┌─────────────────────────┐   │
│  Phase IV: Monitoring    │──┘
└─────────────────────────┘
```
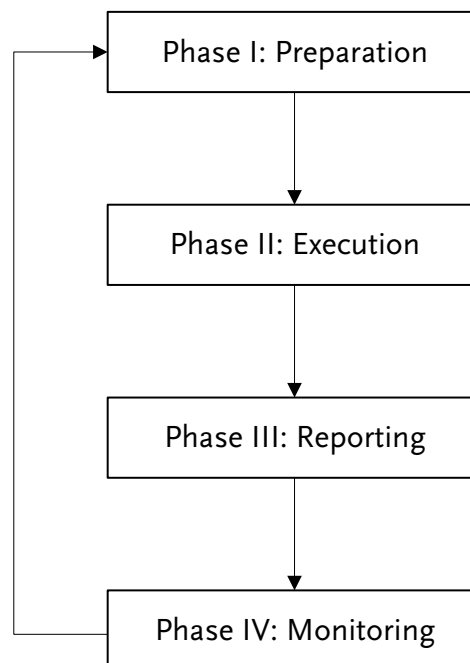
Figure H.1: Phases of an inspection.

The execution phase based on this research can be presented using the simplified flowchart provided on the next page. The flowchart should always be consulted alongside the practical considerations presented in Section 7.2.

```
Start execution phase
        │
        ▼
In-situ preparations
        │
        ▼
Visual inspection
        │
        ▼
Encountered suspicious areas? ──Yes──> Mark suspicious areas and make photos
        │ No
        ▼
Reinforced and/or prestressed concrete? ──Yes──> GPR ──> Investigating grouting defects? ──Yes──> Combined GPR, UPE and endoscopy
        │ No                                                        │ No
        ▼                                                           │
Assessing compressive strength? <─────────────────────────────────┘
        │ Yes──> Rebound hammer ──Yes──> Doubts about the quality of the concrete? ──Yes──> UPV
        │                                         │ No
        │ No                                      │
        ▼                                         │
Assessing probability of corrosion? <────────────┘
        │ Yes──> Half-cell potential ──> Any suspicious areas? ──Yes──> Resistivity and/or corrosion current density
        │                                         │ No
        │ No                                      │
        ▼                                         │
Destructive verification? <──────────────────────┘
        │ Yes──> Define test regions and test locations and take the necessary cores
        │              ──> Are these cores sufficient? ──No──> Apply heavier destructive methods such as hydrodemolition
        │                         │ Yes
        │ No                      │
        ▼                         ▼
Cleaning site <───────────────────┘
        │
        ▼
End of execution phase
```

Bibliography

[1] R.P.H. Vergoossen (2011). *Overkoepelende rapportage Liggerkoppen*. (In Dutch).

[2] G.H. Wilgenburg (2023). "Non-destructive testing of reinforced concrete structures - a literature review". (Unpublished).

[3] N.B. Winter (2012). *Understanding Cement: An Introduction to Cement Production, Cement Hydration and Deleterious Processes in Concrete*. Microanalysis Consultants Ltd. isbn: 9780957104525.

[4] T.E. Brown et al. (2019). *Chemistry: The Central Science (13th Edition)*. Pearson. isbn: 9780321910417.

[5] T.D. Marcotte (2001). "Characterization of chloride-induced corrosion products that form in steel-reinforced cementitious materials". PhD thesis. University of Waterloo.

[6] N. Perez (2016). *Electrochemistry and Corrosion Science*. Springer International Publishing. https://doi.org/10.1007/978-3-319-24847-9.

[7] C.G. Berrocal (2017). "Corrosion of Steel Bars in Fibre Reinforced Concrete: Corrosion mechanisms and structural performance". PhD thesis. Chalmers University of Technology.

[8] Z. Jiang et al. (2021). "Macrocell Corrosion of Steel in Concrete under Carbonation, Internal Chloride Admixing and Accelerated Chloride Penetration Conditions". In: *Materials* 14. https://doi.org/10.3390/ma14247691.

[9] U. Angst et al. (2011). "Chloride induced reinforcement corrosion: Rate limiting step of early pitting corrosion". In: *Electrochimica Acta* 56, pp. 5877–5889. https://doi.org/10.1016/j.electacta.2011.04.12.

[10] L. Bertolini et al. (2013). *Corrosion of steel in concrete: Prevention, diagnosis, repair, 2nd Edition*. Wiley – VCH Verlag GmbH Co. KGaA. https://doi.org/10.1002/3527603379.

[11] C.M. Hansson, A. Poursaee, and S.J. Jaffer (2012). "Corrosion of Reinforcing Bars in Concrete". In: *The Masterbuilder*.

[12] P. Liu et al. (2019). "Effect of Temperature on Concrete Carbonation Performance". In: *Advances in Materials Science and Engineering*. https://doi.org/10.1155/2019/9204570.

[13] National Oceanic and Atmospheric Administration (2022). *Trends in Atmospheric Carbon Dioxide*. url: https://gml.noaa.gov/ccgg/trends/global.html#global.

[14] Z. Liu et al. (2023). "Carbonation of blast furnace slag concrete at different CO2 concentrations: Carbonation rate, phase assemblage, microstructure and thermodynamic modelling". In: *Cement and Concrete Research* 169. https://doi.org/10.1016/j.cemconres.2023.107161.

[15] G.K. Glass, C.L. Page, and N.R. Short (1991). "Factors affecting the corrosion rate of steel in carbonated mortars". In: *Corrosion Science* 32. https://doi.org/10.1016/0010-938X(91)90048-T.

[16] B. Cherry and W. Green (2021). *Corrosion and Protection of Reinforced Concrete*. CRC Press. isbn: 9780367517618.

[17] E.J.F. Dickinson and A.J. Wain (2020). "The Butler-Volmer equation in electrochemical theory: Origins, value, and practical application". In: *Journal of Electroanalytical Chemistry* 872. https://doi.org/10.1016/j.jelechem.2020.114145.

[18] Betonvereniging (2019). *Dictaat Kathodische Bescherming*. (In Dutch). url: https://www.betonvereniging.nl/media/16656/dictaat-kathodische-bescherming-09-2019.pdf.

[19] M. Stern and A.L. Geary (1957). "Electrochemical Polarization: I . A Theoretical Analysis of the Shape of Polarization Curves". In: *Journal of The Electrochemical Society* 104. https://doi.org/10.1149/1.2428496.

[20] C. Andrade (2019). "Propagation of reinforcement corrosion: principles, testing and modelling". In: *Materials and Structures* 52. https://doi.org/10.1617/s11527-018-1301-1.

[21] C. Andrade and N. Rebolledo (2009). *Corrosion of reinforced concrete made with different binders and exposed for 20 years in natural sea water*. RILEM Publications SARL, pp. 173–180. isbn: 9782351580745.

[22] C. Andrade and I. Martínez (2005). "Calibration by gravimetric losses of electrochemical crrosion rate measurement using modulated confinement of the current". In: *Materials and Structures* 38, pp. 833–841. https://doi.org/10.1007/BF02481656.

[23] E. Poulsen and L. Mejlbro (2006). *Diffusion of Chloride in Concrete: Theory and Application*. CRC Press. https://doi.org/10.1201/9781482295108.

[24] J. Crank (1975). *The mathematics of diffusion*. Oxford university press.

[25] R. Cai et al. (2020). "Skin effect of chloride ingress in marine concrete: A review on the convection zone". In: *Construction and Building Materials* 262. https://doi.org/10.1016/j.conbuildmat.2020.120566.

[26] S. Kashif-ur-Rehman et al. (2016). "Nondestructive test methods for concrete bridges: A review". In: *Construction and Building Materials* 107. https://doi.org/10.1016/j.conbuildmat.2015.12.011.

[27] C. Maierhofer, H.-W. Reinhardt, and G. Dobmann (2010). *Non-Destructive Evaluation of Reinforced Concrete Structures Volume 2: Non Destructive Testing Methods*. Woodhead Publishing. isbn: 9781845699604.

[28] K. Tesic et al. (2022). "Characterization of ground penetrating radar signal during simulated corrosion of concrete reinforcement". In: *Automation in Construction* 143. https://doi.org/10.1016/j.autcon.2022.104548.

[29] W.M. Haynes, ed. (2014). *CRC Handbook of Chemistry and Physics, 95th Ed.* CRC Press, pp. 6–188. isbn: 9781482208689.

[30] American Society for Testing and Materials (2019). *ASTM D6432-19: Standard Guide for Using the Surface Ground Penetrating Radar Method for Subsurface Investigation*. ASTM International. https://doi.org/10.1520/D6432-19.

[31] W. Zatar, T.T. Nguyen, and H. Nguyen (2022). "Environmental effects on condition assessments of concrete structures with ground penetrating radar". In: *Journal of Applied Geophysics* 203. https://doi.org/10.1016/j.jappgeo.2022.104713.

[32] Z.M. Sbartaï et al. (2016). "Effect of Concrete Moisture on Radar Signal Amplitude". In: *ACI Materials Journal* 103, pp. 419–426. https://doi.org/10.14359/18219.

[33] S.F. Senin and R. Hamid (2016). "Ground penetrating radar wave attenuation models for estimation of moisture and chloride content in concrete slab". In: *Construction and Building Materials* 106, pp. 659–669. https://doi.org/10.1016/j.conbuildmat.2015.12.156.

[34] D. Breysse and J.-P. Balayssac, eds. (2021). *Non-Destructive In Situ Strength Assessment of Concrete - Practical Application of the RILEM TC 249-ISC Recommendations*. Springer International Publishing. https://doi.org/10.1007/978-3-030-64900-5.

[35] X. Derobert, G. Villain, and J.-P. Balayssac (2018). "Influence of Concrete Carbonation on Electromagnetic Permittivity Measured by GPR and Capacitive Techniques". In: *Journal of Environmental and Engineering Geophysics* 23. http://dx.doi.org/10.2113/JEEG23.4.443.

[36] American Society for Testing and Materials (2022a). *ASTM D6087-22: Standard Test Method for Evaluating Asphalt-Covered Concrete Bridge Decks Using Ground Penetrating Radar*. ASTM International. https://doi.org/10.1520/D6087-22.

[37] American Association of State Highway and Transportation Officials (2004). *AASHTO R 37: Standard Practice for Application of Ground Penetrating Radar (GPR) to Highways*.

[38] International Atomic Energy Agency (2002). *Guidebook on non-destructive testing of concrete structures*. IAEA. url: http://www-pub.iaea.org/MTCD/publications/PDF/TCS-17_web.pdf.

[39] E. Estévez et al. (2020). "Ultrasonic Pulse Velocity — Compressive Strength Relationship for Portland Cement Mortars Cured at Different Conditions". In: *Crystals* 10. https://doi.org/10.3390/cryst10020133.

[40] R. Jones and I. Facaoaru (1969). "Recommendations for testing concrete by the ultrasonic pulse method". In: *Materials and Structures* 2, pp. 275–284. https://doi.org/10.1007/BF02475162.

[41] Z. Lafhaj et al. (2006). "Correlation between porosity, permeability and ultrasonic parameters of mortar with variable water/cement ratio and water content". In: *Cement and Concrete Research* 36. https://doi.org/10.1016/j.cemconres.2005.11.009.

[42] RILEM (1993). *RILEM Technical Recommendations for the testing and use of construction materials*. E. F.N. Spon. https://doi.org/10.1201/9781482271362.

[43] D. Corbett (2022). *Harness The Power of Ultrasonic Pulse Echo Technology in Concrete Tests*. (Webinar by Screening Eagle Technologies). url: https://www.screeningeagle.com/en/academy/webinars/Pundit-pd8050-ultrasonic-pulse-echo.

[44] A. Jiang and D. Corbett (2020). *NDT imaging technology for assessment of concrete defects and faults*. (Webinar by Screening Eagle Technologies).

[45] European Committee for Standardization (2021a). *Testing concrete in structures - Part 2: Determination of rebound number (EN 12504-2)*.

[46] —   (2019a). *Assessment of in-situ compressive strength in structures and precast concrete components (EN 13791)*.

[47] S. Winkler and J.A. Matthews (2014). "Comparison of electronic and mechanical Schmidt hammers in the context of exposure-age dating: are Q- and R-values interconvertible?" In: *Earth Surface Processes and Landforms* 39. https://doi.org/10.1002/esp.3584.

[48] A. Brencich et al. (2020). "Rebound Hammer Test: An Investigation into Its Reliability in Applications on Concrete Structures". In: *Advances in Materials Science and Engineering* 2020, pp. 5877–5889. https://doi.org/10.1155/2020/6450183.

[49] K. Szilágyi and A. Borosnyói (2009). "50 Years of experience with the Schmidt rebound hammer". In: *Concrete Structures* 10, pp. 46–56.

[50] J. Brozovsky and L. Bodnarova (2016). "Contribution to the issue of evaluating the compressive strength of concrete exposed to high temperatures using the Schmidt rebound hammer". In: *Russian Journal of Nondestructive Testing* 52. https://doi.org/10.1134/S1061830916010046.

[51] D. Breysse (2012). "Nondestructive evaluation of concrete strength: An historical review and a new perspective by combining NDT methods". In: *Construction and Building Materials* 33, pp. 139–163. https://doi.org/10.1016/j.conbuildmat.2011.12.103.

[52] N. Olsson et al. (2013). "Non-saturated ion diffusion in concrete – A new approach to evaluate conductivity measurements". In: *Cement and Concrete Composites* 40, pp. 40–47. https://doi.org/10.1016/j.cemconcomp.2013.04.001.

[53] R. Polder et al. (2000). "Test methods for on site measurement of resistivity of concrete". In: *Materials and Structures* 33, pp. 603–611. https://doi.org/10.1007/BF02480599.

[54] S.G. Millard (1991). "Reinforced concrete resistivity measurement techniques". In: *Proceedings of the Institution of Civil Engineers* 91, pp. 71–88. https://doi.org/10.1680/iicep.1991.13583.

[55] C.-T. Chen and W.-C. Yeih J.-J. Chang (2014). "The effects of specimen parameters on the resistivity of concrete". In: *Construction and Building Materials* 71, pp. 35–43. https://doi.org/10.1016/j.conbuildmat.2014.08.009.

[56] J.A. Jones (1991). *Principles and prevention of corrosion*. Prentice Hall.

[57] P. Pedeferri (2018). *Corrosion Science and Engineering*. Springer International Publishing. https://doi.org/10.1007/978-3-319-97625-9.

[58] B. Elsener et al. (2003). "Half-cell potential measurements - Potential mapping on reinforced concrete structures". In: *Materials and Structures* 36, pp. 461–471. https://doi.org/10.1007/BF02481526.

[59] Z.H. Zou et al. (2016). "Relationship between half-cell potential and corrosion level of rebar in concrete". In: *Corrosion Engineering, Science and Technology* 51. https://doi.org/10.1080/1478422X.2016.1167304.

[60] W. Yodsudjai and T. Pattarakittam (2017). "Factors influencing half-cell potential measurement and its relationship with corrosion level". In: *Measurement* 104. https://doi.org/10.1016/j.measurement.2017.03.027.

[61] C. Andrade et al. (2004). "Test methods for on-site corrosion rate measurement of steel reinforcement in concrete by means of the polarization resistance method". In: *Materials and Structures* 37. http://dx.doi.org/10.1007/BF02483292.

[62] J.E. Ramón, Á. Castillo, and I. Martínez (2021). "On-site corrosion monitoring experience in concrete structures: Potential improvements on the current-controlled polarization resistance method". In: *Materiales de Construcción* 71. https://doi.org/10.3989/mc.2021.11221.

[63] C. Andrade (2020). "Electrochemical methods for on-site corrosion detection". In: *Structural Concrete* 21. https://doi.org/10.1002/suco.201900426.

[64] L.S. Gómez Jaramillo (2023). "In-Situ Appraisal and Classification of Concrete Structures Prior Demolition: Chemical Composition Analysis Using Handheld X-ray Fluorescence Analyzer with Cement Type-Driven Separation". PhD thesis. Delft University of Technology.

[65] G.F. Kheder (1999). "A two stage procedure for assessment of in situ concrete strength using combined non-destructive testing". In: *Materials and Structures* 32, pp. 410–417.

[66] G. Menditto et al. (2004). "Metodo combinato ultrasuoni-sclerometro (SonReb): considerazioni e riflessioni". In: *15o Congresso CTE Collegio dei Tecnici della*. (In Italian).

[67] B. Hobbs and M.T. Kebir (2007). "Non-destructive testing techniques for the forensic engineering investigation of reinforced concrete buildings". In: *Forensic Science International* 167, pp. 167–172. http://dx.doi.org/10.1016/j.forsciint.2006.06.065.

[68] G. Faella et al. (2011). "Calibrazione sperimentale del metodo SonReb per costruzioni della Provincia di Caserta degli anni '60÷'80". In: *Atti del XIV Convegno Nazionale L'Ingegneria Sismica in Italia*. (In Italian).

[69] Y.-F. Shih et al. (2015). "Improving Non-Destructive Concrete Strength Tests Using Support Vector Machines". In: *Materials* 8, pp. 7169–7178. https://doi.org/10.3390/ma8105368.

[70] K.A. Benyahia et al. (2017). "Analysis of the relationship between nondestructive and destructive testing of low concrete strength in new structures". In: *Asian Journal of Civil Engineering* 18, pp. 191–205.

[71] H. Abbaszadeh, S. Karatosun, and S. Baran (2018). "The Effect of Different Equations and Methods on R-Square Values of Ndt Correlations". In: *Proceedings of the International conference on Applied Research in Engineering, Science and Technology*, pp. 53–62. https://doi.org/10.33422/icarest.2018.09.41.

[72] S. Bingöl and A. Çavdar (2018). "A New Nomogram Proposal to Determine Concrete Compressive Strength by Combined Non-Destructive Test Methods". In: *Research in Nondestructive Evaluation* 29, pp. 1–17. https://doi.org/10.1080/09349847.2016.1195466.

[73] N.R. Chandak and H.R. Kumavat (2018). "SonReb Method for Evaluation of Compressive Strength of Concrete". In: *IOP Conference Series: Materials Science and Engineering* 810. https://doi.org/10.1088/1757-899X/810/1/012071.

[74] M.T. Cristofaro and S. Viti M. Tanganelli (2020). "New predictive models to evaluate concrete compressive strength using the SonReb method". In: *Journal of Building Engineering* 27. https://doi.org/10.1016/j.jobe.2019.100962.

[75] F. Al-Neshawy, M. Ferreira, and J. Puttonen (2023). "Combined NDT methods to determine the variations in compressive strength throughout concrete structures". In: *Proceedings of the International Conference on Non-destructive Evaluation of Concrete in Nuclear Applications - NDE NucCon 2023*.

[76] ACI Committee 214 (2011). *Guide to Evaluation of Strength Test Results of Concrete (ACI PRC-214-11)*. (Reapproved 2019). American Concrete Institute. isbn: 9780870314230.

[77] Rijkswaterstaat (2022). *RTD 1006 - Richtlijnen Beoordeling Kunstwerken 1.2.1*. url: https://standaarden.rws.nl/link/standaard/1059.

[78] European Committee for Standardization (2006). *Determination of carbonation depth in hardened concrete by the phenolphthalein method (EN 14630)*.

[79]   American Society for Testing and Materials (2022b). *ASTM C1202-22: Standard Test Method for Electrical Indication of Concrete's Ability to Resist Chloride Ion Penetration*. ASTM International. https://doi.org/10.1520/C1202-22E01.

[80]   P.M. Chess (2018). *Cathodic Protection for Reinforced Concrete Structures*. CRC Press. https://doi.org/10.1201/9781351045834.

[81]   R. Polder and A.W.M. Van den Hondel (2022). "Cathodic Protection Of Reinforcement In Concrete – Overview And Experience Over 30+ Years". In: *MATEC Web of Conferences* 364. https://doi.org/10.1051/matecconf/202236401001.

[82]   International Organization for Standardization (2022). *Cathodic protection of steel in concrete (EN-ISO 12696)*.

[83]   European Committee for Standardization (2021b). *Testing concrete in structures - Part 4: Determination of ultrasonic pulse velocity (EN 12504-4)*.

[84]   Rijkswaterstaat (2013). *RTD 1007-1: Meerkeuzematrix (MKM) voegovergangen*. (In Dutch).

[85]   W. Schwarz (2020). *21 Years Composite Anode System for the Economic, Reliable Cathodic Sustainable Corrosion Protection of Steel in Concrete*.

[86]   K.M.J.T. Van Deurzen and L.C.B. De Mooij (2020). *Inspectie en onderzoek Sluinerweg (de Sluiner)*. (In Dutch).

[87]   J.C. Verhage, A.J. Van den Hondel, and R.N. Ter Maten (2022). *KW03: Sluinerweg - Liggerkoppen MJO - Inspectie jaar 9*. (In Dutch).

[88]   European Committee for Standardization (2019b). *Testing concrete in structures - Part 1: Cored specimens - Taking, examining and testing in compression (EN 12504-1)*.

[89]   ——   (2019c). *Testing hardened concrete - Part 3: Compressive strength of test specimens (EN 12390-3)*.

[90]   M.W. Van Zandwijk and R. Van Osch (2023). *Proeftuin RWS Meettechnieken - Ultrasoononderzoek Sluinerweg*. (In Dutch).

[91]   M. Nedeljkovic et al. (2023). "Energy consumption of a laboratory jaw crusher during normal and high strength concrete recycling". In: *Mineral Engineering* 204. https://doi.org/10.1016/j.mineng.2023.108421.

[92]   European Committee for Standardization (2020). *Further guidance on the application of EN 13791:2019 and background to the provisions (CEN/TR 17086)*.

[93]   B.A. Turkoglu (2024). "Towards the full utilization of RCA in Dutch infrastructure by 2030". (Unpublished).